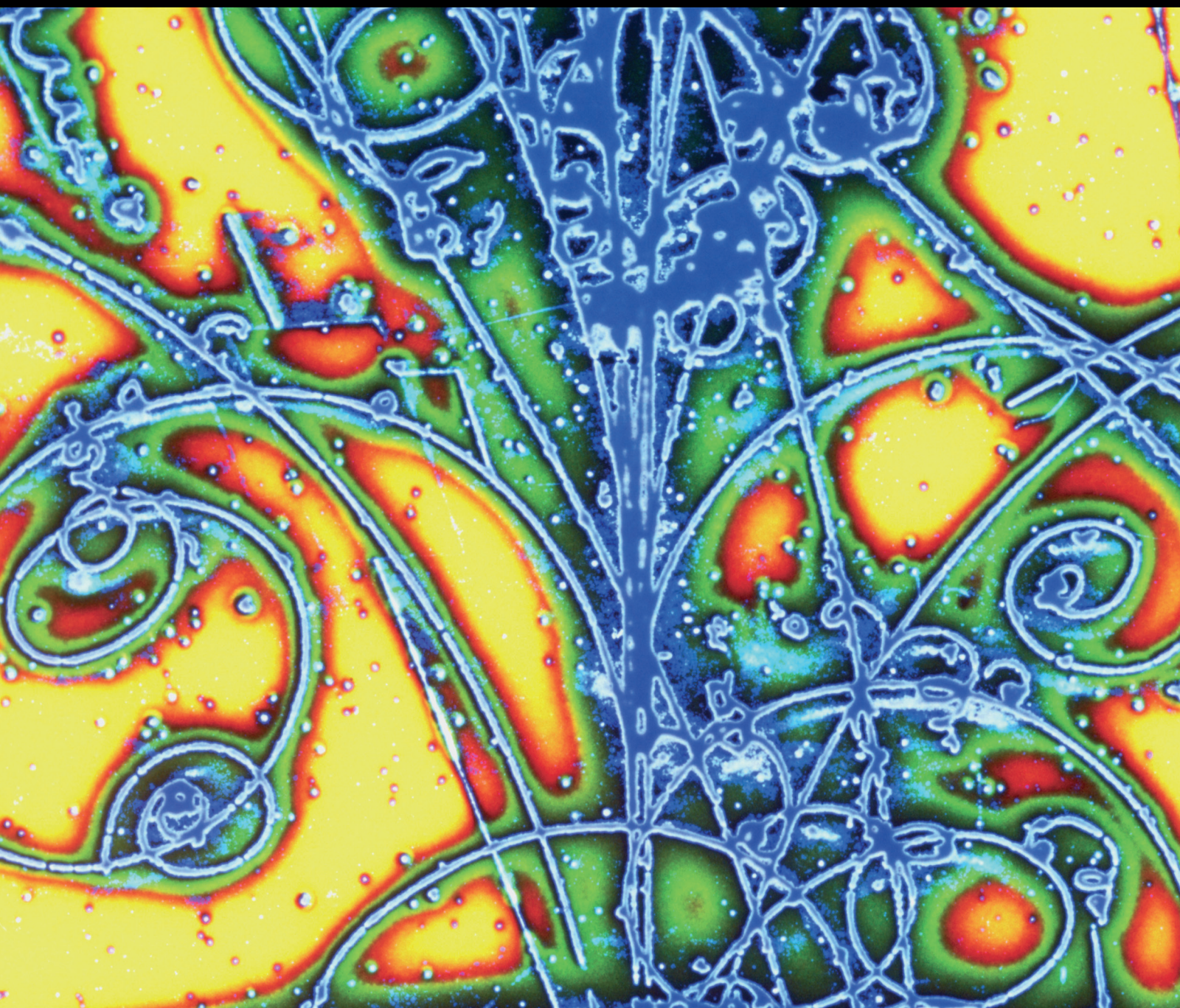


Advances in High Energy Physics

Nonperturbative Approaches in Field Theory

Lead Guest Editor: Ralf Hofmann

Guest Editors: Thierry Grandou and Mario Gattobigio





Nonperturbative Approaches in Field Theory

Advances in High Energy Physics

Nonperturbative Approaches in Field Theory

Lead Guest Editor: Ralf Hofmann

Guest Editors: Thierry Grandou and Mario Gattobigio



Copyright © 2018 Hindawi. All rights reserved.

This is a special issue published in “Advances in High Energy Physics.” All articles are open access articles distributed under the Creative Commons Attribution License, which permits unrestricted use, distribution, and reproduction in any medium, provided the original work is properly cited.

Editorial Board

Antonio J. Accioly, Brazil
Giovanni Amelino-Camelia, Italy
Luis A. Anchordoqui, USA
Michele Arzano, Italy
T. Asselmeyer-Maluga, Germany
Alessandro Baldini, Italy
Marco Battaglia, Switzerland
Lorenzo Bianchini, Switzerland
Roelof Bijker, Mexico
Burak Bilki, USA
Adrian Buzatu, UK
Rong-Gen Cai, China
Anna Cimmino, Belgium
Osvaldo Civitarese, Argentina
Andrea Coccaro, Italy
Shi-Hai Dong, Mexico
Lorenzo Fortunato, Italy
Mariana Frank, Canada

Ricardo G. Felipe, Portugal
Chao-Qiang Geng, Taiwan
Philippe Gras, France
Xiaochun He, USA
Luis Herrera, Spain
Filipe R. Joaquim, Portugal
Aurelio Juste, Spain
Theocharis Kosmas, Greece
Ming Liu, USA
Enrico Lunghi, USA
Salvatore Mignemi, Italy
Omar G. Miranda, Mexico
Bogdan Mitrica, Romania
Grégory Moreau, France
Piero Nicolini, Germany
Carlos Pajares, Spain
Sergio Palomares-Ruiz, Spain
Giovanni Pauletta, Italy

Yvonne Peters, UK
Anastasios Petkou, Greece
Alexey A. Petrov, USA
Thomas Rössler, Sweden
Diego Saez-Gomez, Spain
Takao Sakaguchi, USA
Juan José Sanz-Cillero, Spain
Edward Sarkisyan-Grinbaum, USA
Sally Seidel, USA
George Siopsis, USA
Luca Stanco, Italy
Jouni Suhonen, Finland
Mariam Tórtola, Spain
Smarajit Triambak, South Africa
Jose M. Udías, Spain
Elias C. Vagenas, Kuwait
Sunny Vagnozzi, Sweden
Yau W. Wah, USA

Contents

Nonperturbative Approaches in Field Theory

Ralf Hofmann , Thierry Grandou , and Mario Gattobigio
Editorial (3 pages), Article ID 2423459, Volume 2018 (2018)

On How QCD Gauge Invariance Gets Realized in the Context of Effective Locality

H. M. Fried, T. Grandou , and R. Hofmann
Review Article (6 pages), Article ID 2686507, Volume 2018 (2018)

Color Confinement, Hadron Dynamics, and Hadron Spectroscopy from Light-Front Holography and Superconformal Algebra

Stanley J. Brodsky 
Review Article (16 pages), Article ID 7236382, Volume 2018 (2018)

Hamiltonian Approach to QCD in Coulomb Gauge: A Survey of Recent Results

H. Reinhardt , G. Burgio, D. Campagnari, E. Ebadati, J. Heffner, M. Quandt, P. Vastag, and H. Vogt
Review Article (21 pages), Article ID 2312498, Volume 2018 (2018)

A Renormalisation Group Approach to the Universality of Wigner's Semicircle Law for Random Matrices with Dependent Entries

Thomas Krajewski
Research Article (7 pages), Article ID 4098720, Volume 2017 (2018)

Relativistic Localizing Processes Bespeak an Inevitable Projective Geometry of Spacetime

Jacques L. Rubin
Research Article (18 pages), Article ID 9672417, Volume 2017 (2018)

Cosmic Microwave Background as a Thermal Gas of SU(2) Photons: Implications for the High- z Cosmological Model and the Value of H_0

Steffen Hahn and Ralf Hofmann
Research Article (9 pages), Article ID 7525121, Volume 2017 (2018)

Massive Fluctuations in Deconfining SU(2) Yang-Mills Thermodynamics

Ingolf Bischer
Research Article (9 pages), Article ID 8593678, Volume 2017 (2018)

Asymptotic Behaviour of the QED Perturbation Series

Idrish Huet, Michel Rausch de Traubenberg, and Christian Schubert
Review Article (12 pages), Article ID 6214341, Volume 2017 (2018)

Supersymmetry across the Hadronic Spectrum

Hans Günter Dosch
Research Article (6 pages), Article ID 8627918, Volume 2017 (2018)

Exact Computations in Topological Abelian Chern-Simons and BF Theories

Philippe Mathieu
Research Article (6 pages), Article ID 2878949, Volume 2017 (2018)



Charges and Electromagnetic Radiation as Topological Excitations

Manfried Faber

Research Article (9 pages), Article ID 9340516, Volume 2017 (2018)

Emerging Translational Variance: Vacuum Polarization Energy of the ϕ^6 Kink

H. Weigel

Research Article (10 pages), Article ID 1486912, Volume 2017 (2018)

Radiative Decay Widths of Ground and Excited States of Vector Charmonium and Bottomonium

Hluf Negash and Shashank Bhatnagar

Research Article (8 pages), Article ID 7306825, Volume 2017 (2018)

On the Emergence of the Coulomb Forces in Quantum Electrodynamics

Jan Naudts

Research Article (4 pages), Article ID 7232798, Volume 2017 (2018)

Editorial

Nonperturbative Approaches in Field Theory

Ralf Hofmann ¹, Thierry Grandou ², and Mario Gattobigio²

¹Universität Heidelberg and Karlsruhe Institute of Technology, Heidelberg, Eggenstein-Leopoldshafen, Germany

²Institut de Physique de Nice, Sophia Antipolis, France

Correspondence should be addressed to Ralf Hofmann; ralf.hofmann2@kit.edu

Received 26 April 2018; Accepted 26 April 2018; Published 29 May 2018

Copyright © 2018 Ralf Hofmann et al. This is an open access article distributed under the Creative Commons Attribution License, which permits unrestricted use, distribution, and reproduction in any medium, provided the original work is properly cited. The publication of this article was funded by SCOAP³.

Perturbation theory has long been the method of choice in addressing the S -matrix and related observables predicted by quantum field theories subject to well defined asymptotic scattering states and an accordingly local and sufficiently weak interaction, suggesting an analysis in terms of powers of a small coupling. Gauge theories like Quantum Electrodynamics (QED), the electroweak sector of the Standard Model (SM) of particle physics as a whole, and the primary perturbative vertices of Quantum Chromodynamics (QCD) describing, e.g., the creation of jets of hadrons from electron-positron annihilation at large center-of-mass energies thanks to asymptotic freedom are empirically very successful applications of this approach. Among many other important results, they gave us a quantitative description of radiative effects such as the deviation of the electron's spin induced magnetic moment (the g -factor) from the value predicted by the Dirac equation, a quantitative explanation of the Lamb shift, and the precise evolution of the strength of the electromagnetic and strong couplings α and α_s in dependence of the momentum transfer in given scattering processes. On the conceptual side, a major accomplishment of the perturbative approach is the demonstration by 't Hooft and Veltman of renormalizability of quantum gauge theory in four space-time dimensions with and without spontaneous gauge-symmetry breaking through a (renormalizable) Higgs-field sector, implying the intactness of the predictivity of these theories under the renormalization programme: the subtraction of loop-inherent infinities to dress only the parameters of the tree-level theory under physically imposed conditions and this to all loop orders. The thus enabled precise predictions of electroweak observables in the SM were impressively confirmed by experiments performed at the Large Electron-Positron Collider (LEP).

A genuine testing of the $U(1) \times SU(2) \times SU(3)$ gauge dynamics of the perturbatively understood SM beyond perturbation theory must, however, avoid model assumptions such as suggestively parameterized parton distribution functions and the associated factorization of soft-momentum, nonperturbative contributions to hadronic polarization tensors. One usually argues that lattice gauge theory—a first-principle approach to QCD based on an ultraviolet (UV) and infrared (IR) cutoff formulation on a finite 4D Euclidean space-time lattice—produces results which do not rely on such assumptions and this increasingly well as computational resources become more and more abundant and the available conceptual and computational techniques more and more refined. But even for the pure Yang-Mills case (no fermions which couple to the gauge fields), there are various issues inherent to this approach: (i) problems in the direct simulation of dynamical processes (form factors at time-like momentum transfer, certain decay amplitudes) due to formulation of lattice gauge theory in Euclidean space-time, (ii) finite-size scaling at finite temperature and its profound impact on infrared sensitive thermodynamical quantities, and (iii) customary simulations of the Euclidean Yang-Mills partition function subject to the Wilson discretization of the fundamental Yang-Mills action with the UV cutoff dependence (lattice spacing) and coarsening effects usually parameterized in terms of the *perturbative* Yang-Mills β function. A nonperturbative, perfect quantum lattice action by definition does not exhibit any cutoff dependence at finite lattice spacing. It is, however, prohibitively expensive to construct by successions of numerical block-spin transformations. Apart from these technical problems, the determination of static observables (which do not depend on the Euclidean formulation), like the mass spectrum of light

hadrons, is the result of black-box numerical experiments and as such does not openly provide insights into the underlying physics of ground-state structure, confinement, chiral symmetry breaking, and excitability. There is activity in lattice gauge theory, however, which poses these questions about mechanisms directly, thus providing valuable guidance to analytical approaches to nonperturbative Quantum Yang-Mills theory.

Some of the contributions to this present special issue focus on just such nonperturbative approaches to pure Yang-Mills theory, QCD, and Yang-Mills thermodynamics. Namely, the work of H. Reinhardt et al. investigates the nonperturbative vacuum functional in the Hamiltonian formulation of SU(2) and SU(3) QCD in Weyl-Coulomb gauge both at finite and at zero temperature and for both situations, pure Yang-Mills and fluctuating quark fields. The task is to solve the functional Schrödinger equation with a duly gauge-fixed Hamiltonian for the ground-state functional. This is done in an approximate form in terms of minimizing energy in a well-motivated Gaussian-variational ansatz (and cubic plus quartic generalizations thereof) for the ground-state functional. The associated kernels can be expressed as solutions to Dyson-Schwinger and to gap equations which can be solved subject to simplifying assumptions and boundary (horizon) conditions to implement confinement (a highly nonperturbative feat). Interesting quantities to compute are the Wilson and Coulomb string tension. One then is led to ask about the field configurations that mainly induce them. This is done in comparison of the present continuum approach to lattice results in discussing the role of center-vortex loops and the magnetic monopoles that associate with them. Finite temperature is introduced by compactification of the *spatial dimension* after $O(4)$ rotation, and the Polyakov loop as an order parameter for deconfinement is computed with the according ground-state functional used to compute the expectation of the A_0 field in Polyakov gauge. Again, the results are compared to lattice results yielding a good agreement. Approaches like the one pursued by H. Reinhardt et al. in this special issue have helped to elucidate a number of important nonperturbative mechanisms in non-Abelian gauge theory. Exemplarily, we now sketch the content of some of the papers.

There are two interesting contributions in this special issue, one by S. J. Brodsky and the other one by H. G. Dosch, who base their nonperturbative approach to QCD on the so-called AdS-QCD conjecture which is believed to be related to the AdS-CFT holography correspondence, conjectured by J. Maldacena to hold between 4D SU($N \rightarrow \infty$), $\mathcal{N} = 4$ SUSY Yang-Mills theory, and the corresponding 5D supergravity dual theory on anti-de-Sitter background space-time (AdS₅). In particular, S. J. Brodsky first introduces a mass scale into the QCD light-front Hamiltonian by adding a term proportional to the special conformal operator which then gives rise to a confining potential. This does not break conformal invariance on the level of the QCD action. This somewhat ad hoc procedure can be shown to follow from the conjectured duality between light-front QCD and AdS₅ if one introduces the AdS₅ action by the dilaton along the fifth dimension. Generalizing this by appealing to the full

superconformal algebra, Brodsky obtains, among interesting insights about the light-front vacuum structure, a unified hadron spectroscopy for mesons, baryons, and tetraquarks with supersymmetric relations between meson and baryon masses. H. G. Dosch (in collaboration with S. J. Brodsky and G. de Teramont) makes the case for supersymmetry across the light hadron spectrum very explicit in appealing to the superconformal algebra to fix the form of the light-front potential. On the other hand, heavy-quark symmetry seems to ensure the survival of supersymmetry even though conformal symmetry is strongly broken in the heavy-quark limit.

A long-standing question about the asymptotic behavior of perturbative expansions, here in QED, is pursued by I. Huet et al. There are good, classical arguments that this expansion does not converge. However, in particular, the leading large- N photon amplitude in the effective Euler-Heisenberg (E-H) theory can be constructed from a conjectured all-loop expression of the imaginary part of the E-H Lagrangian for scalar and spinor QED by Borel dispersion, suggesting the usefulness of a perturbative approach in expanding this amplitude in powers of α in a convergent way. However, an explicit example in 1 + 1 dimension does not support such a possibility.

P. Mathieu discusses the possibility of performing exact nonperturbative computations of functional integrals related to the partition function and observables in 3D U(1) Chern-Simons theory thanks to the Deligne cohomology classes of its fiber bundles.

H. Weigel reports about his development of an efficient method, based on scattering data (spectral method) about a scalar field configuration of given topology (static solution to the classical equation of motion), to compute its one-loop effective potential (or vacuum polarization energy, VPE) in a 1 + 1D ϕ^6 (nonrenormalizable) theory where fluctuations do not naturally decompose into parity eigenstates since the background field may connect inequivalent vacua (not related by a parity transformation). Still, at the one-loop level, the VPE can be fixed unambiguously by UV subtractions. As a consequence, such a soliton may exhibit a VPE which no longer exhibits the breaking of translational invariance it had introduced on the classical level. This is an interesting, quantum induced, emergent phenomenon. Quantifying VPEs for even more general potentials may turn out to be insightful regarding quantum effects in soliton binding.

T. Krajewski presents a beautiful discussion on an extension of validity of the Wigner semicircle law for the probability distribution of eigenvalues of $N \times N$ Hermitian, independent Gaussian, or Wigner random matrices (off-diagonal entries independent and identically distributed with zero mean, diagonal entries identically distributed with finite mean and independent of off-diagonal entries) in the large- N limit to the case of correlated entries. Namely, assuming a certain scaling bound for the cumulants of entries, he shows by means of a renormalization-group equation for the effective action of the replica that bounds on effective cumulants are implied. In the large- N limit, this, in turn, guarantees that only Gaussian terms contribute such that one is back at the semicircle law. Krajewski's work is an important contribution

in showing the universality of eigenvalue distributions in a large class of high-dimensional random matrices.

The contribution by J. L. Rubin is a bit off the main theme of the special issue, yet highly interesting: insights derived from relativistic positioning systems for the structure of space-time. Namely, he shows how causal axiomatics and certain local 1D and 2D projective structures attached to emitters are sufficient to deduce the 4D projective structure of space-time. This allows, e.g., for a modification of Newton's force law on large distances.

M. Faber in his paper proposes a model of the electron along the lines of a Skyrme-model-like construction (but with a different potential term). The basic quantity, a spatial dreibein, parameterizes unit quaternions, that is, group elements of $SU(2)$ with nontrivial winding on its group manifold S_3 which give rise to a connection, in turn, defining the curvature tensor. Solving the static field equations, this yields solitons whose topological charge can be matched to electric charge after a reduction of the non-Abelian curvature to the 't Hooft tensor is performed. The extent of this static field configuration essentially matches the classical electron radius. There are two more topological quantum numbers which relate to spin and photon number. The model allows for magnetic currents which should make this description of classical electrodynamics nonlocal. The ideas presented here are very interesting because they may help to demystify the electron. It would be welcome if the emergence of the Compton wavelength, a more intuitive grasp of electron spin, and the apparent pointlikeness of the electron in high-energy scattering experiments could be understood, possibly in extensions of the model incorporating quantum effects from the outset and doing justice to L. de Broglie's work on the thermodynamics of the isolated particle.

The paper by T. Grandou et al. addresses an effective formulation of QCD which exhibits locality in fermionic Green's functions upon a sophisticated and highly nonperturbative functional integration (actually, functional differentiation) of gluonic gauge-field fluctuations, using the Halpern quadrature of the QCD partition function for the gauge field A_μ . In the present paper, the emergence of gauge-fixing independence (the fundamental formulation of the QCD partition function is subjected to gauge fixing) of nonperturbative, fermionic Green's functions is discussed in a sequence of relaxed high-energy approximations (quenching, eikonal, Fradkin's representation of fermionic Green's functions and, finally, no Fradkin's representation) to scattering of quarks off quarks. This result is put into perspective by a very instructive comparison with conventional, perturbatively minded approaches to quark scattering in QCD and electron scattering in QED.

Finally, there are two papers, one by I. Bischer and one by S. Hahn and R. Hofmann, which explore consequences of deconfining $SU(2)$ Yang-Mills thermodynamics. The former contribution addresses certain (nonperturbative) radiative corrections to the pressure, arising from massive quasi-particle fluctuations. It is shown that fixed-order dihedral diagrams exhibit a high-temperature dependence starkly exceeding the Stefan-Boltzmann behavior. However, it is demonstrated that an all-order resummation cures

this apparent problem and leads to well-bounded, purely imaginary contributions at leading order (implying that these radiative corrections do not admit a thermodynamical interpretation). The second paper investigates the consequences of the postulate that an $SU(2)$ rather than a $U(1)$ gauge principle governs thermal photon gases, e.g., the Cosmic Microwave Background (CMB), for the high- z cosmological model. Specifically, a modification of the T - z relation implies that the high- z cosmological model has to contain less dark matter than the Λ CDM standard model posits. This is argued to resolve the tension in H_0 between fits to the power spectra of the CMB and its cosmologically local extraction.

All papers of this special issue have undergone peer review by one or two high-calibre referees. A substantial fraction of manuscripts submitted had to be rejected.

*Ralf Hofmann
Thierry Grandou
Mario Gattobigio*

Review Article

On How QCD Gauge Invariance Gets Realized in the Context of Effective Locality

H. M. Fried,¹ T. Grandou ,² and R. Hofmann³

¹Physics Department, Brown University, Providence, RI 02912, USA

²Institut de Physique de Nice, UMR CNRS 7010, Université de Nice-Sophia Antipolis, 1361 route des Lucioles, 06560 Valbonne, France

³Institut für Theoretische Physik, Universität Heidelberg, Philosophenweg 16, 69120 Heidelberg, Germany

Correspondence should be addressed to T. Grandou; thierry.grandou@inphyni.cnrs.fr

Received 23 August 2017; Accepted 29 March 2018; Published 22 May 2018

Academic Editor: Enrico Lunghi

Copyright © 2018 H. M. Fried et al. This is an open access article distributed under the Creative Commons Attribution License, which permits unrestricted use, distribution, and reproduction in any medium, provided the original work is properly cited. The publication of this article was funded by SCOAP³.

The fermionic Green's functions of QCD exhibit an unexpected property of *effective locality*, which appears to be exact, involving no approximation. This property is nonperturbative, resulting from a full integration of the elementary gluonic degrees of freedom of QCD. Recalling, correcting, and extending the derivations of effective locality, focus is put on the way nonabelian gauge invariance gets realized in the fermionic nonperturbative regime of QCD.

1. Introduction

In some recent articles [1–5], a property, which bears on the nonperturbative fermionic Green's functions of QCD, has been put forth under the name of *effective locality* (EL). This property can be summarized as follows.

For any fermionic 2n-point Green's functions and related amplitudes, the full gauge-fixed sum of cubic and quartic gluonic interactions, with fermionic loops included, results in a local contact-type interaction. This local interaction is mediated by a tensorial field which is antisymmetric both in Lorentz and color indices. Moreover, the resulting sum appears to be fully gauge-fixing independent, that is, gauge-invariant.

This is an unexpected result because integrations of elementary degrees of freedom ordinarily result in highly nonlocal structures. The “effective locality” denomination, which sounds like an *oxymoron*, accounts for this unusual circumstance. It is worth pointing out that in the pure euclidean Yang Mills case and up to the first nontrivial orders of a semiclassical expansion, effective locality was observed as a welcome property in an attempt to construct a formulation dual to the original Yang Mills theory [6–8].

Now, apart from a *supersymmetric* extension, QCD is not known for possessing any dual formulation and the full

EL functional expressions certainly attest to this difficulty. It remains that, like in the pure Yang Mills situation of [6, 7], the EL property may allow one to learn something about the nonperturbative regime of QCD and this from first principles.

In the next section a comparison of the QED and QCD Green's functions generating functional is given, while Section 3 displays the property of effective locality in the simpler situation of eikonal and quenching approximations where it was first noticed and then in full generality. Eventually, Section 4 presents some concluding remarks.

2. Contrasting Generating Functionals

In QED it has been known for quite a long time that manifest covariance and manifest gauge invariance are competing aspects of a generating functional construction. For short, starting from a photonic Lagrangian density of

$$\mathcal{L}_0 = -\frac{1}{4} f^{\mu\nu} f_{\mu\nu} = -\frac{1}{4} (\partial^\mu A^\nu - \partial^\nu A^\mu) (\partial_\mu A_\nu - \partial_\nu A_\mu), \quad (1)$$

and corresponding action (at $\lambda = 1$),

$$\int d^4x \mathcal{L}_0 = -\frac{1}{2} \int A^\mu (-\partial^2) A_\mu + \frac{\lambda}{2} \int (\partial^\mu A_\mu)^2, \quad (2)$$

one may use the ‘‘inconvenient’’ (in Fermi’s words [1]) term of $(\partial \cdot A)^2$ to generate any relativistic gauge (manifest covariance), treating, for example, $(\lambda/2) \int (\partial^\mu A_\mu)^2$ as a kind of ‘‘interaction.’’ Gauge invariance is then guaranteed by enforcing charge conservation: clearly not a manifest way.

The construction can be summarized through the following steps. Starting from the free-field case ($\lambda = e = 0$), one has, with $D_{F\mu\nu}^{(0)} = g_{\mu\nu}D_F$, $(-\partial^2)D_F = 1$, the free-field generating functional

$$Z_0^{(0)} \{j\} = \exp \left\{ \frac{i}{2} \int j \cdot D_F^{(0)} \cdot j \right\}. \quad (3)$$

Then one can proceed in Schwinger’s way with the ‘‘gauge-interaction term’’:

$$\begin{aligned} Z_0^{(\zeta)} \{j\} &= e^{i(\lambda/2) \int (\partial^\mu A_\mu)^2} \Big|_{A \rightarrow (1/i)(\delta/\delta j)} \cdot e^{(i/2) \int j \cdot D_F^{(0)} \cdot j} \\ &= e^{-(i/2) \text{Tr} \ln [1 - \lambda(\partial \otimes \partial^2)]} e^{(i/2) \int j \cdot D_F^{(\zeta)} \cdot j}, \end{aligned} \quad (4)$$

with

$$D_{F\mu\nu}^{(\zeta)} = \left[g_{\mu\nu} - \frac{\zeta \partial_\mu \partial_\nu}{\partial^2} \right] D_F, \quad \zeta = \frac{\lambda}{1 - \lambda}. \quad (5)$$

The full Green’s functions generating functional now reads as ($\lambda \neq 0$, $e \neq 0$)

$$\begin{aligned} Z_{\text{QED}}^{(\zeta)} [j, \eta, \bar{\eta}] \\ = \mathcal{N} e^i \int \bar{\eta} \cdot G_F [A] \cdot \eta + L[A] + (i/2) \lambda \int (\partial^\mu A_\mu)^2 \Big|_{A \rightarrow (1/i)(\delta/\delta j)} \\ \cdot e^{(i/2) \int j \cdot D_F^{(0)} \cdot j} \end{aligned} \quad (6)$$

with (the phase factor appearing in the second line of (4) is absorbed into the normalization constant \mathcal{N})

$$\begin{aligned} G_F [A] &= [\gamma \cdot (\partial - ieA) - m]^{-1}, \\ L[A] &= \text{Tr} \ln [1 - ie\gamma \cdot AS_F], \quad S_F = G_F [0]. \end{aligned} \quad (7)$$

This is the standard Schwinger solution for the QED generating functional. For any polynomial and/or exponential functional $\mathcal{F}[A]$, the following *differential* functional identity holds:

$$\mathcal{F} \left[\frac{1}{i} \frac{\delta}{\delta j} \right] \cdot e^{(i/2) \int j \cdot D_F^{(\zeta)} \cdot j} \equiv e^{(i/2) \int j \cdot D_F^{(\zeta)} \cdot j} \cdot e^{\mathfrak{D}_A} \cdot \mathcal{F}[A] \Big|_{A = \int D_F^{(\zeta)} \cdot j} \quad (8)$$

with the so-called *linkage operator*

$$\mathfrak{D}_A^{(\zeta)} = -\frac{i}{2} \int d^4x \int d^4y \frac{\delta}{\delta A(x)} \cdot D_F^{(\zeta)}(x-y) \cdot \frac{\delta}{\delta A(y)}. \quad (9)$$

This identity can be used to write eventually

$$\begin{aligned} Z_{\text{QED}}^{(\zeta)} [j, \eta, \bar{\eta}] &= \mathcal{N} e^{(i/2) \int j \cdot D_F^{(\zeta)} \cdot j} \\ &\cdot e^{\mathfrak{D}_A^{(\zeta)}} \cdot e^i \int \bar{\eta} \cdot G_F [A] \cdot \eta + L[A] \Big|_{A = \int D_F^{(\zeta)} \cdot j}. \end{aligned} \quad (10)$$

Of course, this is the QED generating functional that would result from linear and covariant gauge fixing of $(-1/2(1 - \lambda))(\partial \cdot A)^2$. However, $\lambda = 1$ cannot be chosen as $D_{F\mu\nu}^{(\zeta)}$ would not be defined. It is at $\lambda = 1$ though that manifest gauge invariance is maintained. As a result, Green’s functions cannot display gauge invariance. As shown in (10), the bare photon propagator remains explicitly gauge-dependent, and through Ward-Takahashi identities, its radiative corrections are checked to be gauge-invariant. For the whole set of physical processes described by QED, the LSZ reduction formula and *equivalence theorem* [9] allow one to pass from nongauge-invariant Green’s functions to gauge-invariant S-matrix elements. Recovering gauge invariance is therefore a circuitous procedure and it seems that the nonabelian structure of QCD offers a different possibility.

In the case of QCD, the same canonical steps can be taken. To sum up and within concise notations (color degrees being understood)

$$\begin{aligned} Z_{\text{QCD}}^{(\zeta)} [j, \bar{\eta}, \eta] &= \mathcal{N} e^i \int \mathcal{L}'_{\text{QCD}} [(1/i)(\delta/\delta j)] e^{(i/2) \int j \cdot D_F^{(0)} \cdot j}, \\ \mathcal{L}'_{\text{QCD}} [A] &= \bar{\eta} G_F [A] \eta + L[A] + \mathcal{L}' [A], \end{aligned} \quad (11)$$

where the following propagator, of course, does not exist:

$$\left(D_F^{(\zeta)-1} \right)_{\mu\nu}^{ab} = -i\delta^{ab} [g_{\mu\nu} \partial^2 - \partial_\mu \partial_\nu]. \quad (12)$$

However, in QCD, unlike QED, one has

$$\begin{aligned} \int \mathcal{L}' [A] &= -\frac{1}{4} \int F^2 - \frac{1}{2} \int A_\mu^a (\partial^2) A_\mu^a \\ &\quad - \frac{1}{2} \int (\partial^\mu A_\mu^a)^2, \end{aligned} \quad (13)$$

that is, omitting fermionic variables momentarily,

$$\begin{aligned} Z^{(\zeta)} [j] &= \mathcal{N} e^{-(i/4) \int F^2 + (i/2) \int A_\mu^a (D_F^{(\zeta)})^{-1} A_\mu^a} \Big|_{A \rightarrow (1/i)(\delta/\delta j)} \\ &\cdot e^{(i/2) \int j \cdot D_F^{(0)} \cdot j}. \end{aligned} \quad (14)$$

Now, simply adding and subtracting a linear covariant gauge-fixing term of $(1/2\zeta)(\partial \cdot A)^2$, it is elementary to proceed and pass from an undefined $D_F^{(\zeta)}$ to the well-defined and covariant propagator $D_F^{(\zeta)}$:

$$\left(D_F^{(\zeta)-1} \right)_{\mu\nu}^{ab} = -i\delta^{ab} \left[g_{\mu\nu} \partial^2 + \left(\frac{1}{\zeta} - 1 \right) \partial_\mu \partial_\nu \right] \quad (15)$$

and to a Green’s function QCD generating functional of

$$\begin{aligned} Z_{\text{QCD}} [j, \bar{\eta}, \eta] &= \mathcal{N} e^{(i/2) \int j \cdot D_F^{(\zeta)} \cdot j} e^{-(i/2) \int (\delta/\delta A) \cdot D_F^{(\zeta)} \cdot (\delta/\delta A)} \\ &\times e^{-(i/4) \int F^2 + (i/2) \int A \cdot (D_F^{(\zeta)})^{-1} \cdot A} \\ &\cdot e^i \int \bar{\eta} \cdot G_F [A] \cdot \eta + L[A] \Big|_{A = \int D_F^{(\zeta)} \cdot j}, \end{aligned} \quad (16)$$

where fermionic dependence has been restored and the differential functional identity (8) used again.

However, likewise, adding and subtracting a gauge fixing of $(1/2\xi)(n \cdot A)^2$, with n being a lightlike vector, $n^2 = 0$, one gets (in the limit $\xi \rightarrow 0$, [9])

$$(D_F^{(n)})_{\mu\nu}^{ab}(K) = -i\delta^{ab} \left(\frac{g_{\mu\nu}}{K^2 + i\varepsilon} - \frac{K_\mu n_\nu + K_\nu n_\mu}{(K^2 + i\varepsilon)(K \cdot n)} \right) \quad (17)$$

and a Green's function QCD generating functional of

$$\begin{aligned} Z_{\text{QCD}}[j, \bar{\eta}, \eta] &= \mathcal{N} e^{(i/2) \int j \cdot D_F^{(n)} \cdot j} e^{-(i/2) \int (\delta/\delta A) \cdot D_F^{(n)} \cdot (\delta/\delta A)} \\ &\times e^{-(i/4) \int F^2 + (i/2) \int A \cdot (D_F^{(n)})^{-1} \cdot A} \\ &\cdot e^i \int \bar{\eta} \cdot G_F[A] \cdot \eta + L[A] \Big|_{A=\int D_F^{(n)} \cdot j}. \end{aligned} \quad (18)$$

As many identical forms as desired can be obtained for $Z_{\text{QCD}}[j, \bar{\eta}, \eta]$, differing only in the *intermediate* gluonic field function, $D_F^{(n)}$, $D_F^{(\zeta)}$, and so forth.

In conclusion, the following points can be proposed.

(i) In QED (where $\lambda = 1$ cannot be chosen), these standard functional operations amount to a quantization in a given covariant gauge. Manifest Lorentz covariance is maintained while manifest gauge invariance is not. Gauge invariance is the matter of indirect recovering.

(ii) In QCD, surprisingly and explicitly due to the non-abelian structure, manifest Lorentz covariance and manifest gauge invariance can be preserved at a time.

(iii) Since no gauge fixing is really achieved, none of the several forms of the QCD generating functional, with $D_F^{(n)}$, $D_F^{(\zeta)}$, or any other free-field function, do indeed correspond to the usual QCD generating functional in the associated gauge.

(iv) There is but one possibility. Gauge field functions (i.e., propagators) must show up as *necessary intermediates* and not affect the fermionic *momenta* of the QCD generating functionals (16) and (18).

(v) Now, this is guaranteed by the property of effective locality.

3. Effective Locality

The property of effective locality will be first displayed in a simplified situation corresponding to the use of eikonal and quenching approximations.

3.1. Effective Locality in a Small Example: Eikonal and Quenching Approximations. With the help of the representation [10],

$$e^{-(i/4) \int F^2} = \mathcal{N}' \int d[\chi] e^{(i/4) \int (\chi_{\mu\nu}^a)^2 + (i/2) \int \chi_a^{\mu\nu} F_{\mu\nu}^a} \quad (19)$$

any D_F -dependent form of $Z_{\text{QCD}}[j, \bar{\eta}, \eta]$ can be used; for example,

$$\begin{aligned} &\mathcal{N} e^{(i/2) \int j \cdot D_F^{(0)} \cdot j} \int d[\chi] \\ &\cdot e^{(i/4) \int \chi^2} e^{\mathfrak{D}_A^{(0)}} e^{-(i/2) \int \chi \cdot F + (i/2) \int A \cdot (-\partial^2) \cdot A} \\ &\cdot e^i \int \bar{\eta} \cdot G_F[A] \cdot \eta + L[A] \Big|_{A=\int D_F^{(0)} \cdot j}. \end{aligned} \quad (20)$$

However, representation (19) breaks the manifest gauge invariance. This can be remedied either by *gauging* the χ -field [6, 7] or by means of an exact integration of the χ -field dependence. In the latter instance, the powerful *Random Matrix* theory allows one to do it in the “small case” at least [4]. So long as gauge invariance is concerned, however, none of the above possibilities is necessary as effective locality brings about a remarkable simplification.

Let there be a Fradkin's representation of the functional $G_F[A]$ [11]:

$$\begin{aligned} \langle p | G_F[A] | y \rangle &= e^{-ip \cdot y} i \int_0^\infty ds e^{-ism^2} e^{-(1/2)\text{Tr} \ln(2h)} \\ &\times \int d[u] \{ m - i\gamma \cdot [p - gA(y - u(s))] \} \\ &\cdot e^{(i/4) \int_0^s ds' [u'(s')]^2} e^{ip \cdot u(s)} \\ &\times \left(e^{g \int_0^s ds' \sigma \cdot \mathbf{F}(y - u(s'))} e^{-ig \int_0^s ds' u'(s') \cdot \mathbf{A}(y - u(s'))} \right)_+, \end{aligned} \quad (21)$$

where $u(s)$ is the 4-vector Fradkin's field variable, the subscript + stands for s -Schwinger proper-time ordering, and $h(s_1, s_2) = \int_0^s ds' \Theta(s_1 - s') \Theta(s_2 - s')$. This representation is exact but fairly involved. In *eikonal* approximation ($u(s) = sp$) the ordered exponential reduces to

$$\begin{aligned} &\left(e^{igp^\mu \int_{-\infty}^{+\infty} ds A_\mu^a(y-sp) T^a} \right)_+ \\ &= \mathcal{N} \int d[\alpha] \int d[\Omega] \\ &\times e^{-i \int_{-\infty}^{+\infty} ds \Omega^a(s) [\alpha^a(s) - gp^\mu A_\mu^a(y-sp)]} \\ &\times \left(e^i \int_{-\infty}^{+\infty} ds \alpha^a(s) T^a \right)_+. \end{aligned} \quad (22)$$

In (22), the α, Ω are auxiliary variables introduced to take A_μ^a -field dependence out of the ordered exponential; they are to be integrated out exactly so that dealing with the original time-ordered expressions is guaranteed. Again, this is doable at least in the strong coupling limit of $g \gg 1$ of a quenching approximation ($L[A] = 0$).

A 4-pt Green's function illustration can be given. One has basically the expression

$$\prod_{i=1}^2 \int ds_i \int d[u_i(s_i)] \int d[\alpha_i(s_i)] \int d[\Omega_i(s_i)] (\cdot \cdot) \int d[\chi] e^{(i/4) \int \chi^2 e^{\mathfrak{D}_A^{(0)}} e^{+(i/2) \int A_\mu^a K_{ab}^{\mu\nu} A_\nu^b} e^i \int Q_\mu^a A_\mu^a} \Big|_{A \rightarrow 0}, \quad (23)$$

$$K_{\mu\nu}^{ab} = gf^{abc} \chi_{\mu\nu}^c + \left(D_F^{(0)-1} \right)_{\mu\nu}^{ab}, \quad (24)$$

$$Q_\mu^a = -\partial^\nu \chi_{\mu\nu}^a + g [R_{1,\mu}^a + R_{2,\mu}^a],$$

$$R_{i,\mu}^a(z) = p_{i,\mu} \int ds_i \Omega_i^a(s_i) \delta^4(z - y_i + s_i p_i), \quad (25)$$

$i = 1, 2,$

where the dots in the first line of (23) account for the integrand

$$e^{-is_i m^2} e^{-(1/2) \text{Tr} \ln(2h)} e^{(i/4) \int_0^{s_i} ds'_i [u'_i(s'_i)]^2} \delta^{(4)}(x_i - y_i + u_i(s_i)) e^{-i \int ds'_i \Omega_i^a(s'_i) \alpha^a(s'_i)} \left(e^{i \int_{-\infty}^{+\infty} ds_i \alpha_i^a(s_i) \lambda^a} \right)_+. \quad (26)$$

$$\mathcal{N} \prod_{i=1}^2 \int ds_i \int d[u_i(s_i)] \int d[\alpha_i(s_i)] \int d[\Omega_i(s_i)] (\cdot \cdot) \int d[\chi] e^{(i/4) \int \chi^2} \cdot \frac{1}{\sqrt{\det(f \cdot \chi)}} \cdot e^{-(i/2) \int d^4 z Q(z) \cdot (gf \cdot \chi(z))^{-1} \cdot Q(z)}. \quad (30)$$

with $Q_\mu^a(z)$ being the ‘‘currents’’ given in (24).

(i) This result is obviously gauge-independent, that is, gauge-invariant. It cannot show up in the abelian QED case as long hoped (R. P. Feynman, quoted in [12]). It generalizes to the case of $2n$ -point fermionic Green's functions [13, 14]. When truncated to the YM case, the structure found in [6, 7] is basically reproduced. Eventually, this result lends itself to a (n analytically continued) *Random Matrix* exact calculation which takes care of the full integration of the χ -field dependence and displays the full algebraic dependence of fermionic Green's functions on the $SU_c(3)$ -Lie algebra invariants [13, 14].

3.2. Effective Locality in the General Case. It is possible to relax any of the approximations used in the ‘‘small case’’ and end up with the property of effective locality. Again this can be illustrated in the simpler case of a fermionic 4-point Green's function:

$$M(x_1, y_1; x_2, y_2) = \frac{\delta}{\delta \bar{\eta}(y_1)} \cdot \frac{\delta}{\delta \eta(x_1)} \cdot \frac{\delta}{\delta \bar{\eta}(y_2)} \cdot \frac{\delta}{\delta \eta(x_2)} \cdot \mathcal{Z} \{j, \bar{\eta}, \eta\} \Big|_{\eta=\bar{\eta}=0; j=0} = \mathcal{N} \int d[\chi] \cdot e^{(i/4) \int \chi^2 e^{\mathfrak{D}_A^{(0)}} e^{+(i/2) \int \chi \cdot \mathbf{F} + (i/2) \int A \cdot (D_F^{(0)})^{-1} \cdot A} G_F(x_1, y_1 | gA) G_F(x_2, y_2 | gA) e^{L[A]} \Big|_{A=0}. \quad (31)$$

Now,

$$e^{-(i/2) \int (\delta/\delta A) \cdot D_F^{(0)} \cdot (\delta/\delta A)} \cdot e^{+(i/2) \int A \cdot K \cdot A + i \int A \cdot Q} \Big|_{A \rightarrow 0} = e^{-(1/2) \text{Tr} \ln(1 - D_F^{(0)} \cdot K)} \cdot e^{(i/2) \int Q [D_F^{(0)} \cdot (1 - K \cdot D_F^{(0)})^{-1}] \cdot Q}, \quad (27)$$

with

$$D_F^{(0)} \cdot (1 - K \cdot D_F^{(0)})^{-1} = D_F^{(0)} \cdot \left(1 - [gf \cdot \chi + D_F^{(0)-1}] \cdot D_F^{(0)} \right)^{-1} = -(gf \cdot \chi)^{-1}, \quad (28)$$

and the *locality*

$$\langle x | (gf \cdot \chi)^{-1} | y \rangle = (gf \cdot \chi)^{-1}(x) \delta^{(4)}(x - y). \quad (29)$$

The 4-pt fermionic Green's function finally reads as

Gathering Gaussian A_μ^a dependence of $G_F(1 | A)$ and $G_F(2 | A)$,

$$\exp \left[\frac{i}{2} \int d^4 z A_\mu^a(z) K_{\mu\nu}^{ab}(z) A_\nu^b(z) + i \int d^4 z Q_\mu^a(z) A_\mu^a(z) \right], \quad (32)$$

requires 2 extra auxiliary variables; with

$$\Phi_{i,\mu\nu}^a(u_i; z) \equiv \int_0^{s_i} ds'_i \delta^{(4)}(z - y_i + u_i(s'_i)) \Phi_{i,\mu\nu}^a(s'_i), \quad (33)$$

a new piece of ‘‘interaction kernel’’ reads

$$K_{\text{spin } \mu\nu}^{ab}(z) = 2g^2 \int_0^{s_1} ds'_1 \delta^{(4)}(z - y_1 + u_1(s'_1)) f^{abc} \Phi_{\mu\nu,1}^c(s'_1) + 2g^2 \int_0^{s_2} ds'_2 \delta^{(4)}(z - y_2 + u_2(s'_2)) f^{abc} \Phi_{\mu\nu,2}^c(s'_2) \quad (34)$$

while ‘‘currents’’ $Q_{\mu\nu}^a(z)$ get completed into

$$Q_\mu^a(z) = -2g \partial^\nu \Phi_{1,\nu\mu}^a(z)$$

$$\begin{aligned}
& -g \int_0^{s_1} ds'_1 \delta^{(4)}(z - y_1 + u_1(s'_1)) u'_{1,\mu}(s'_1) \Omega_1^a(s'_1) \\
& - 2g \partial^\nu \Phi_{2,\nu\mu}^a(z) \\
& - g \int_0^{s_2} ds'_2 \delta^{(4)}(z - y_2 + u_2(s'_2)) u'_{2,\mu}(s'_2) \Omega_2^a(s'_2)
\end{aligned} \tag{35}$$

and generalized to a higher number of points of Green's functions in a formally similar way. Restoring the fermionic determinant (i.e., relaxing the quenching approximation), the needed functional operation is now

$$\begin{aligned}
& \exp \left[-\frac{i}{2} \int \frac{\delta}{\delta A} \cdot D_F^{(0)} \cdot \frac{\delta}{\delta A} \right] \\
& \cdot \exp \left[\frac{i}{2} \int A \cdot \bar{K} \cdot A + i \int \bar{Q} \cdot A \right] \cdot \exp(L[A]),
\end{aligned} \tag{36}$$

followed by the prescription of cancelling the potentials A_μ^a , where

$$\begin{aligned}
& \left\langle z \left| \bar{K}_{\mu\nu}^{ab} \right| z' \right\rangle \\
& = \left[K_{\text{spin}\mu\nu}^{ab}(z) + g f^{abc} \chi_{\mu\nu}^c(z) \right] \delta^{(4)}(z - z') \\
& + \left\langle z \left| (D_F^{(0)})^{-1} \right|_{\mu\nu}^{ab} \right| z' \right\rangle, \\
& \bar{Q}_\mu^a(z) = \partial^\nu \chi_{\nu\mu}^a(z) + Q_\mu^a(z).
\end{aligned} \tag{37}$$

Another differential functional identity is relevant to this operation [11]:

$$\boxed{e^{\mathfrak{D}^A} \mathcal{F}_1[A] \mathcal{F}_2[A] = (e^{\mathfrak{D}^A} \mathcal{F}_1[A]) e^{\overleftrightarrow{\mathfrak{D}}} (e^{\mathfrak{D}^{A'}} \mathcal{F}_2[A'])} \tag{38}$$

where the ‘‘cross-linkage’’ operator $\exp\{\overleftrightarrow{\mathfrak{D}}\}$ is given by

$$\overleftrightarrow{\mathfrak{D}} = -i \int \frac{\overleftarrow{\delta}}{\delta A} D_F^{(0)} \frac{\overrightarrow{\delta}}{\delta A'}, \tag{39}$$

and the limit of $A_\mu^a = A_\mu^{\prime a} = 0$ is to be taken in the end. After cumbersome, still standard, calculations, one gets (up to an irrelevant factor of $\exp((1/2)\text{Tr} \ln(-D_F^{(0)}))$) the functional statement of effective locality as

$$\begin{aligned}
& e^{\mathfrak{D}^A} \mathcal{F}_1[A] \mathcal{F}_2[A] \Big|_{A=0} \\
& = \mathcal{N} \exp \left[-\frac{i}{2} \int \bar{Q} \cdot \widehat{K}^{-1} \cdot \bar{Q} - \frac{1}{2} \text{Tr} \ln \widehat{K} \right] \\
& \cdot \exp \left[\frac{i}{2} \int \frac{\delta}{\delta A} \cdot \widehat{K}^{-1} \cdot \frac{\delta}{\delta A} - \int \bar{Q} \cdot \widehat{K}^{-1} \cdot \frac{\delta}{\delta A} \right] \\
& \cdot \exp(L[A]) \Big|_{A \rightarrow 0},
\end{aligned} \tag{40}$$

at $\widehat{K}_{\mu\nu}^{ab} = K_{\text{spin}\mu\nu}^{ab} + g f^{abc} \chi_{\mu\nu}^c$, that is, locality and gauge independence again, whatever the initial gauge field function

one begins with. However the famous duality relation of coupling constants $g \rightarrow 1/g$ is not verified in QCD contrarily to the pure YM case.

This is nontrivial result, the more so if auxiliary field integrations can be carried out exactly, as in the ‘‘small case.’’ Now these auxiliary field variables are those related to particular Fradkin's representations, and one may therefore wonder if such a property as effective locality is Fradkin's representation dependent, or not.

3.3. Effective Locality: Even More General. With the functional $L[A]$ being local and fully gauge-invariant, one may consider the case of a fermionic 2-point Green's function generalization to a higher number of points being trivial. One has thus to consider an expression like

$$\mathcal{N} \int ds \int d[u(s)] (\cdot \cdot) \int d[\chi] e^{(i/4) \int \chi^2} e^{\mathfrak{D}_A^{(0)} e^{+(i/2) \int \chi \cdot F + (i/2) \int A \cdot (D_F^{(0)})^{-1} \cdot A}} G_F(x, y | A) \Big|_{A \rightarrow 0}, \tag{41}$$

where, again, the dots in the first line stand for the integrand (26) and, this time, no particular representation is assumed for $G_F[A]$. Basically, this is

$$\begin{aligned}
& \mathcal{N} \int d[\chi] e^{(i/4) \int \chi^2} e^{\mathfrak{D}_A^{(0)} e^{+(i/2) \int A \cdot K \cdot A + i \int A_a^\mu \partial^\nu \chi_{\nu\mu}^a}} G_F(x, y | \\
& A) \Big|_{A \rightarrow 0}, \\
& K = g f^{abc} \chi_{\mu\nu}^c + (D_F^{(0)})^{-1} \Big|_{\mu\nu}^{ab},
\end{aligned} \tag{42}$$

$$\mathcal{F}_1[A] = \exp \left[\frac{i}{2} \int A \cdot K \cdot A + i \int A_a^\mu \partial^\nu \chi_{\nu\mu}^a \right],$$

$$\mathcal{F}_2[A] = G_F(x, y | A).$$

Up to a global factor of $\mathcal{N} e^{(1/2)\text{Tr} \ln(-D_F^{(0)})}$ the core expression, that is, the second line of (41), is

$$\begin{aligned}
& e^{\mathfrak{D}_A^{(0)} \mathcal{F}_1[A] \mathcal{F}_2[A]} \Big|_{A=0} = \exp \left[-\frac{i}{2} \int \nabla \chi \cdot (gf \cdot \chi)^{-1} \cdot \nabla \chi - \frac{1}{2} \text{Tr} \ln (gf \cdot \chi) \right] \\
& \cdot \exp \left[\frac{i}{2} \int \frac{\delta}{\delta A} \cdot (gf \cdot \chi)^{-1} \cdot \frac{\delta}{\delta A} \right] \\
& \cdot \exp \left[\int \nabla \chi \cdot (gf \cdot \chi)^{-1} \cdot \frac{\delta}{\delta A} \right] G_F(x, y | A) \Big|_{A \rightarrow 0}.
\end{aligned} \tag{43}$$

Effective locality is manifest in the first line. In the third line, $G_F[A]$ is not gauge-independent but acting upon it with the two functional differentiations, followed by the prescription $A \rightarrow 0$ yielding a manifestly gauge-independent result also. As stated above, it is trivial to check that the same applies to a product of n functionals, $\prod_{i=1}^n G_F(x_i, y_i | A)$, that is, to a $2n$ -point fermionic Green's function.

One may therefore conclude that while Fradkin's representations are useful to actual calculations and derivations of further remarkable properties, the gist of effective locality does not depend on them. This independence makes of effective locality a property sound enough to support the interpretation proposed in the current article.

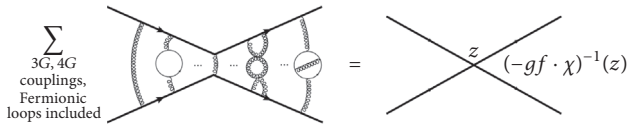


FIGURE 1: Effective Locality pictured in a rather symbolic way in which the sum of all possible QCD interactions between 2 scattering quarks “boils down” to a local contact-type interaction mediated by the structure $(-gf \cdot \chi)^{-1}(z)$.

Functional integrations (differentiations) reproduce the Feynman graphs perturbative expansions, so that, if not taken literally (analyticity in g on one side, nonanalyticity on the other side), one could propose that the pictorial representation of Figure 1 means effective locality in a symbolic way.

4. Conclusion

Decades of experience with the abelian case of QED have probably made us forget that *to calculate observables, it is intrinsically not necessary to select a gauge* [15]. To maintain an explicit covariance though, for both historical and practical reasons, one has admitted to break the manifest gauge invariance in QED.

The case of QCD seems to allow one to proceed in a different way, and this is explicitly due to the nonabelian structure of QCD, with its 3 and 4 linear gluonic self-couplings. The result is a generating functional which displays covariant and gauge-independent fermionic Green’s functions.

Originally derived on the basis of Fradkin’s representations for the closed fermionic loops and background field fermionic propagators, the property of effective locality appears to be more general indeed. The gist of effective locality seems essentially related to the way nonabelian gauge invariance gets realized in the nonperturbative regime of QCD, and this is most easily disclosed by using functional differentiation instead of functional integration.

This situation is new and very different from the abelian case of QED or the perturbative regime of QCD: Up to complications inherent to the nonabelian structure of QCD in effect, gauge invariance follows the same indirect pattern in either cases, *Slavnov-Taylor* identities playing the role of *Ward identities*. Reaching the nonperturbative regime of QCD (intense A_μ^a -fields and/or strong coupling $g \gg 1$) out of the perturbative sector is now recognized as a dead end because of the Gribov’s copy issue which opposes a violent obstruction to this attempt [16, 17].

Such a difficulty does not show up in the effective locality approach, and the fact that gauge invariance in this case is direct may have something to do with the fact that the only QCD states that are outright physical are those of the nonperturbative regime of QCD, that is, states of the hadronic spectrum.

Conflicts of Interest

The authors declare that there are no conflicts of interest regarding the publication of this paper.

References

- [1] H. M. Fried, Y. Gabellini, T. Grandou, and Y.-M. Sheu, “Phys. J,” C65, 395, 2010.
- [2] H. M. Fried, T. Grandou, and Y.-M. Sheu, “Ann. Phys.,” 327, 2666, 2012.
- [3] H. M. Fried, Y. Gabellini, T. Grandou, and Y.-M. Sheu, “Ann. Phys.,” 338, 107, 2013.
- [4] H. M. Fried, T. Grandou, and Y.-M. Sheu, “Ann. Phys.,” 344C, 78, 2014.
- [5] H. M. Fried, P. H. Tsang, Y. Gabellini, T. Grandou, and Y.-M. Sheu, “Ann. Phys.,” 359, 1, 2015.
- [6] H. Reinhardt, K. Langfeld, and L. V. Smekal, “Phys. Lett,” 300, 11, 1993.
- [7] H. Reinhardt, “Dual description of QCD,” in *Proceedings of the conference Quark Confinement and the Hadron Spectrum II*, Villa Olmo, Como, Italy, June 26-29, 1996.
- [8] M. Schaden, H. Reinhardt, P. A. Amundsen, and M. J. Lavelle, “Nucl. Phys.,” 339, 595, 1990.
- [9] C. Itzykson and J. B. Zuber, *Quantum Field Theory*, McGraw-Hill Inc., NY, USA, 1980.
- [10] M. B. Halpern, “Phys. Rev.,” 16, 1798, 1977.
- [11] H. M. Fried, *Functional Methods and Models in Quantum Field Theory*, the MIT Press, Cambridge, MA, USA, 1972.
- [12] A. Zee, *Quantum Field Theory in a Nutshell*, Princeton University Press, 2nd edition, 2010.
- [13] T. Grandou, “EPL,” Article ID 1650120, 107, 11001, 2014.
- [14] H. M. Fried, T. Grandou, and R. Hofmann, “Int. J. of Mod. Phys.,” 31, Nos. 20 & 21, 1650120, 25 pages, 2016.
- [15] A. Maas, “On gauge fixing,” in *Proceedings of the XXVIII International Symposium on Lattice Field Theory*, A. Maas, Ed., Villasimius, Italy, June 2010.
- [16] “XIIth Quark Confinement and the Hadron Spectrum,” Thessaloniki, Greece, 28 August-02 September 2016.
- [17] D. Zwanziger, private communication, 1st Winter Workshop in Non-Perturbative Quantum Field Theories, INLN, Valbonne, France, 18-20 January 2010, https://inis.iaea.org/search/search.aspx?orig_q=RN:45045764.

Review Article

Color Confinement, Hadron Dynamics, and Hadron Spectroscopy from Light-Front Holography and Superconformal Algebra

Stanley J. Brodsky 

SLAC National Accelerator Laboratory, Stanford University, Stanford, CA, USA

Correspondence should be addressed to Stanley J. Brodsky; sjbth@slac.stanford.edu

Received 12 June 2017; Accepted 31 January 2018; Published 16 April 2018

Academic Editor: Ralf Hofmann

Copyright © 2018 Stanley J. Brodsky. This is an open access article distributed under the Creative Commons Attribution License, which permits unrestricted use, distribution, and reproduction in any medium, provided the original work is properly cited. The publication of this article was funded by SCOAP³.

The QCD light-front Hamiltonian equation $H_{\text{LF}}|\Psi\rangle = M^2|\Psi\rangle$ derived from quantization at fixed LF time $\tau = t + z/c$ provides a causal, frame-independent method for computing hadron spectroscopy as well as dynamical observables such as structure functions, transverse momentum distributions, and distribution amplitudes. The QCD Lagrangian with zero quark mass has no explicit mass scale. de Alfaro, Fubini, and Furlan (dAFF) have made an important observation that a mass scale can appear in the equations of motion without affecting the conformal invariance of the action if one adds a term to the Hamiltonian proportional to the dilatation operator or the special conformal operator. If one applies the dAFF procedure to the QCD light-front Hamiltonian, it leads to a color-confining potential $\kappa^4 \zeta^2$ for mesons, where ζ^2 is the LF radial variable conjugate to the $q\bar{q}$ invariant mass squared. The same result, including spin terms, is obtained using light-front holography, the duality between light-front dynamics and AdS₅, if one modifies the AdS₅ action by the dilaton $e^{\kappa^2 z^2}$ in the fifth dimension z . When one generalizes this procedure using superconformal algebra, the resulting light-front eigensolutions provide a unified Regge spectroscopy of meson, baryon, and tetraquarks, including remarkable supersymmetric relations between the masses of mesons and baryons and a universal Regge slope. The pion $q\bar{q}$ eigenstate has zero mass at $m_q = 0$. The superconformal relations also can be extended to heavy-light quark mesons and baryons. This approach also leads to insights into the physics underlying hadronization at the amplitude level. I will also discuss the remarkable features of the Poincaré invariant, causal vacuum defined by light-front quantization and its impact on the interpretation of the cosmological constant. AdS/QCD also predicts the analytic form of the nonperturbative running coupling $\alpha_s(Q^2) \propto e^{-Q^2/4\kappa^2}$. The mass scale κ underlying hadron masses can be connected to the parameter $\Lambda_{\overline{\text{MS}}}$ in the QCD running coupling by matching the nonperturbative dynamics to the perturbative QCD regime. The result is an effective coupling $\alpha_s(Q^2)$ defined at all momenta. One obtains empirically viable predictions for spacelike and timelike hadronic form factors, structure functions, distribution amplitudes, and transverse momentum distributions. Finally, I address the interesting question of whether the momentum sum rule is valid for nuclear structure functions.

1. Introduction

A profound question in hadron physics is how the proton mass and other hadronic mass scales can be determined by QCD since there is no explicit parameter with mass dimensions in the QCD Lagrangian for vanishing quark mass. This dilemma is compounded by the fact that the chiral QCD Lagrangian has no knowledge of the conventions used for units of mass such as MeV. Thus QCD with $m_q = 0$ can

in principle only predict *ratios of masses* such as m_p/m_p , not their absolute values. Similarly, given that color is confined, how does QCD set its range without a parameter with dimensions of length? It is hard to see how this mass scale problem could be solved by “dimensional transmutation,” since the mass scale determined by perturbative QCD such as $\Lambda_{\overline{\text{MS}}}$ is renormalization scheme dependent, whereas hadron masses are independent of the conventions chosen to regulate the UV divergences.

A remarkable principle, first demonstrated by de Alfaro, Fubini, and Furlan (dAFF) [8] for conformal theory in $1 + 1$ quantum mechanics, is that a mass scale can appear in a Hamiltonian and its equations of motion without affecting the conformal invariance of the action. The essential step introduced by dAFF is to add to the conformal Hamiltonian terms proportional to the dilation operator D and the special conformal operator K . The unique result is the addition of a harmonic oscillator potential $V(x) = \kappa^4 x^2$ to the Hamiltonian. The group algebra is maintained despite the fact that D and K have dimensions. In fact, the new Hamiltonian has “extended dilatation invariance” since the mass scale κ can be rescaled arbitrarily. This implies that only ratios of the mass eigenvalues can be determined, not their absolute values.

Brodsky et al. [9] have shown that a mass gap and color confinement appears when one extends the dAFF procedure to relativistic, causal, Poincaré invariant, light-front Hamiltonian theory for QCD. The resulting predictions for both hadronic spectroscopy and dynamics provide an elegant description of meson and baryon phenomenology, including Regge trajectories with universal slopes in the principal quantum number n and the orbital angular momentum L . In addition, the resulting quark-antiquark bound-state equation predicts a massless pion for zero quark mass.

In this contribution, I will review a number of recent advances in holographic QCD, extending earlier reviews given in [10–12] with a new emphasis on the impact of superconformal algebra and new applications. As I will discuss, the resulting light-front eigensolutions provide a unified Regge spectroscopy of meson, baryon, and tetraquarks, including remarkable supersymmetric relations between the masses of mesons and baryons and a universal Regge slope. The combination of light-front holography with superconformal algebra thus leads to the novel prediction that hadron physics has supersymmetric properties in both spectroscopy and dynamics. It also predicts the form of the QCD running coupling at all scales and provides new insights into the physics underlying hadronization at the amplitude level. I will also discuss the remarkable features of the Poincaré invariant, causal vacuum defined by light-front quantization and its impact on the interpretation of the cosmological constant. Finally, I address the interesting question of whether the momentum sum rule is valid for nuclear structure functions.

Light-Front quantization is the natural formalism for relativistic quantum field theory. Measurements of hadron structure, such as deep inelastic lepton-proton scattering, are made at fixed light-front time $\tau = t + z/c$, analogous to a flash photograph, not at a single “instant time.” As shown by Dirac [13], boosts are kinematical in the “front form.” Thus all formulae using the front form are independent of the observer’s motion [14]; that is, they are Poincaré invariant. The eigenstates of the light-front Hamiltonian $H_{\text{LF}} = P^+ P^- - \vec{P}_\perp^2$ derived from the QCD Lagrangian encode the entire hadronic mass spectrum for both individual hadrons and the multihadron continuum. The eigenvalues of the LF Hamiltonian are the squares of the hadron masses M_H^2 : $H_{\text{LF}}|\Psi_H\rangle = M_H^2|\Psi_H\rangle$ [14]. The evaluation of the Wilson line

for gauge theories in the front form is discussed in [15]. In addition, I will discuss the advantages of perturbative QCD calculations using light-front-time-ordered perturbation theory, including the use of J^z conservation.

The eigenfunctions of the light-front Hamiltonian $H_{\text{LF}} = P^+ P^- - \vec{P}_\perp^2$ derived from the QCD Lagrangian correspond to the single hadron and multihadronic continuum eigenstates. The eigenvalues of the LF Hamiltonian are the squares of the hadron masses M_H^2 : $H_{\text{LF}}|\Psi_H\rangle = M_H^2|\Psi_H\rangle$ [14]. Here $P^- = i(d/d\tau)$ is the LF time evolution operator, and $P^+ = P^0 + P^z$ and \vec{P}_\perp are kinematical. The eigenfunctions of H_{LF} provide hadronic LF Fock state wavefunctions (LFWFs): $\psi_n^H(x_i, \vec{k}_\perp, \lambda_i) = \langle n | \Psi_H \rangle$, the projection of the hadronic eigenstate on the free Fock basis. The constituents’ physical momenta are $p_i^+ = x_i P^+$ and $\vec{p}_\perp = x_i \vec{P}_\perp + \vec{k}_\perp$, and the λ_i label the spin projections S_i^z . Remarkably one can reduce the LF Hamiltonian theory for $q\bar{q}$ mesons with $m_q = 0$ to an effective LF Schrödinger equation in a single variable, the LF radial variable $\zeta^2 = b_\perp^2 x(1-x)$.

The LFWFs are Poincaré invariant: they are independent of P^+ and P_\perp and are thus independent of the motion of the observer. Since the LFWFs are independent of the hadron’s momentum, there is no length contraction [16, 17]. Structure functions are essentially the absolute square of the LFWFs. One thus measures the same structure function in an electron-ion collider as in an electron-scattering experiment where the target hadron is at rest.

Light-front wavefunctions thus provide a direct link between the QCD Lagrangian and hadron structure. Since they are defined at a fixed τ , they connect the physical on-shell hadronic state to its quark and gluon parton constituents, not at off-shell energy, but off-shell in invariant mass squared $\mathcal{M}^2 = (\sum_i k_i^H)^2$. They thus control the transformation of the quarks and gluons in an off-shell intermediate state into the observed final on-shell hadronic state. See Figure 1.

One of the most elegant features of quantum field theory is supersymmetry, where fermionic and bosonic eigensolutions have the same mass. The conformal group has an elegant 2×2 Pauli matrix representation called superconformal algebra, originally discovered by Haag et al. [18] (1975). The conformal Hamiltonian operator and the special conformal operators can be represented as anticommutators of Pauli matrices $H = 1/2[Q, Q^\dagger]$ and $K = 1/2[S, S^\dagger]$. As shown by Fubini and Rabinovici [19], a nonconformal Hamiltonian with a mass scale and universal confinement can then be obtained by shifting $Q \rightarrow Q + \omega K$, the analog of the dAFF procedure. Thus the conformal algebra can be extended even though ω has dimension of mass. In effect one has generalized supercharges of the superconformal algebra [19]. The result of this shift of the Hamiltonian is a color-confining harmonic potential in the equations of motion. Remarkably the action remains conformally invariant, and only one mass parameter appears.

As shown by Guy de Téramond, Günter Dosch and myself, the bound-state equations of superconformal algebra are, in fact, Lorentz invariant, frame-independent, relativistic light-front Schrödinger equations, and the resulting eigensolutions are the eigenstates of a light-front Hamiltonian

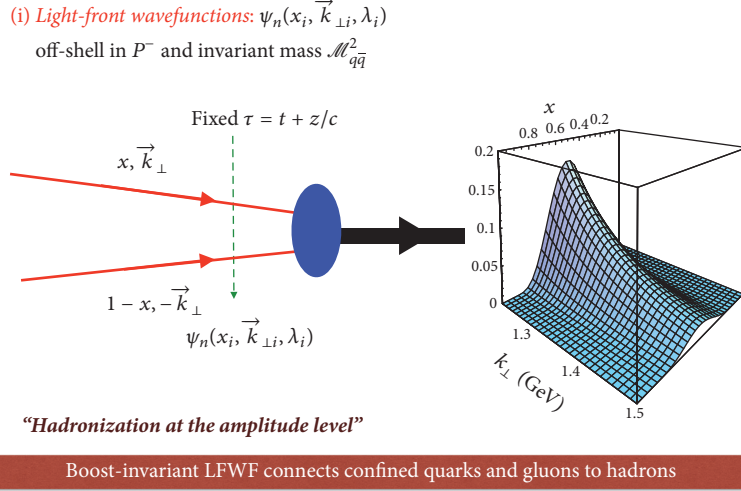


FIGURE 1: The meson LFWF connects the intermediate $q\bar{q}$ state, which is off of the P^- energy shell and thus off-the-invariant mass shell $\mathcal{M}^2 > m_H^2$ to the physical meson state with $\mathcal{M}^2 = m_H^2$. q and \bar{q} can be regarded as effective dressed fields.

LF holography

Baryon equation

$$\left(-\partial_{\zeta}^2 + \kappa^4 \zeta^2 + 2\kappa^2(L_B + 1) + \frac{4L_B^2 - 1}{4\zeta^2}\right) \psi_j^+ = M^2 \psi_j^+ \quad \text{G}_{22}$$

$$\left(-\partial_{\zeta}^2 + \kappa^4 \zeta^2 + 2\kappa^2 L_B + \frac{4(L_B + 1)^2 - 1}{4\zeta^2}\right) \psi_j^- = M^2 \psi_j^- \quad \text{G}_{11}$$

$M^2(n, L_B) = 4\kappa^2(n + L_B + 1)$

$S = 1/2, P = +$
both chiralities

Meson equation

$$\left(-\partial_{\zeta}^2 + \kappa^4 \zeta^2 + 2\kappa^2(J - 1) + \frac{4L_M^2 - 1}{4\zeta^2}\right) \phi_J = M^2 \phi_J \quad \text{G}_{11}$$

$M^2(n, L_M) = 4\kappa^2(n + L_M)$

Same $\kappa!$

$S = 0, I = 1$ Meson is superpartner of $S = 1/2, I = 1$ baryon
 Meson-baryon degeneracy for $L_M = L_B + 1$

FIGURE 2: The LF Schrödinger equations for baryons and mesons for zero quark mass derived from the Pauli 2×2 matrix representation of superconformal algebra. ψ^{\pm} are the baryon quark-diquark LFWFs where the quark spin $S_q^z = \pm 1/2$ is parallel or antiparallel to the baryon spin $J^z = \pm 1/2$. The meson and baryon equations are identical if one identifies a meson with internal orbital angular momentum L_M with its superpartner baryon with $L_B = L_M - 1$. See [1–3].

obtained from AdS₅ and light-front holography. Light-front quantization at fixed light-front time $\tau = t + z/c$ provides a physical, frame-independent formalism for hadron dynamics and structure.

Superconformal algebra leads to effective QCD light-front bound-state equations for both mesons and baryons [1–3]. The resulting set of bound-state equations for confined quarks are shown in Figure 2. The supercharges connect the baryon and meson spectra and their Regge trajectories to

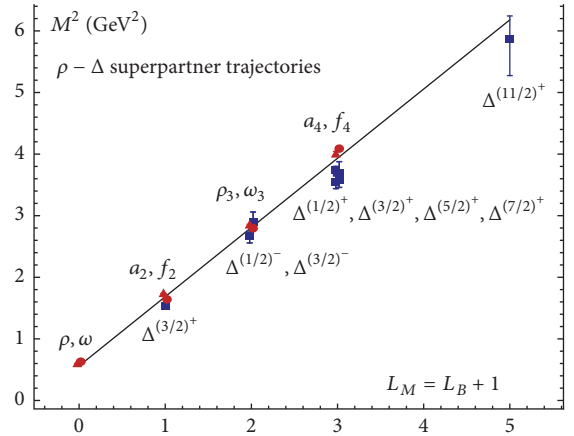


FIGURE 3: Comparison of the ρ/ω meson Regge trajectory with the $J = 3/2$ Δ baryon trajectory. Superconformal algebra predicts the degeneracy of the meson and baryon trajectories if one identifies a meson with internal orbital angular momentum L_M with its superpartner baryon with $L_M = L_B + 1$. See [1, 2].

each other in a remarkable manner: the superconformal algebra predicts that the bosonic meson and fermionic baryon masses are equal if one identifies each meson with internal orbital angular momentum L_M with its superpartner baryon with $L_B = L_M - 1$; the meson and baryon superpartners then have the same parity. Since $2 + L_M = 3 + L_B$, the twist-dimension of the meson and baryon superpartners are also the same. Superconformal algebra thus explains the phenomenological observation that Regge trajectories for both mesons and baryons have parallel slopes.

The comparison between the meson and baryon masses of the ρ/ω Regge trajectory with the spin-3/2 Δ trajectory is shown in Figure 3. The observed hadronic spectrum with $N_C = 3$ is seen to exhibit the supersymmetric features predicted by superconformal algebra.

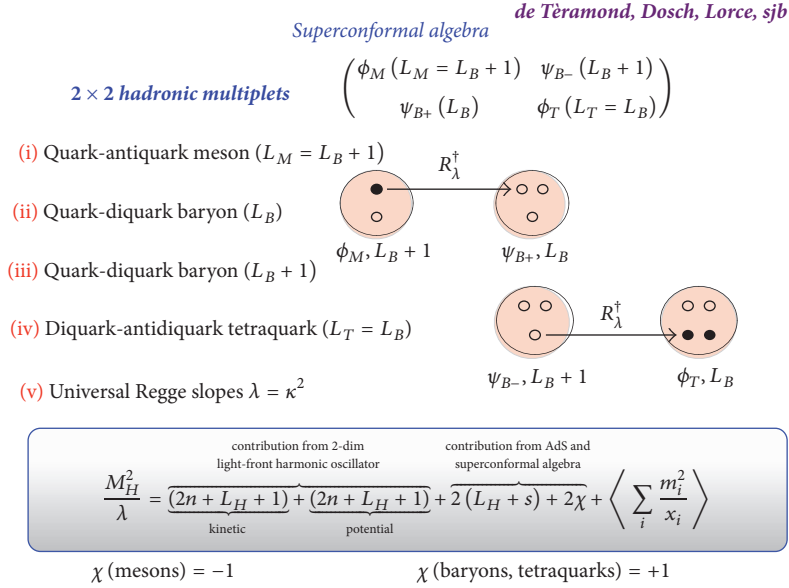


FIGURE 4: The eigenstates of superconformal algebra have a 2×2 representation of mass degenerate bosons and fermions: a meson with $L_M = L_B + 1$, a baryon doublet with $L_B, L_B + 1$ components, and a tetraquark with $L_T = L_B$. The breakdown of LF kinetic, potential, spin, and quark mass contributions to each hadron is also shown. The virial theorem predicts the equality of the LF kinetic and potential contributions.

As illustrated in Figure 4, the hadronic eigensolutions of the superconformal algebra are 2×2 matrices connected internally by the supersymmetric algebra operators. The eigensolutions of the supersymmetric conformal algebra thus have a 2×2 Pauli matrix representation, where the upper-left component corresponds to mesonic $q\bar{q}$ color-singlet bound states; the two off-diagonal eigensolutions ψ^\pm correspond to a pair of Fock components of baryonic quark-diquark states with equal weight, where the quark spin is parallel or antiparallel to the baryon spin, respectively. The fourth component corresponds to diquark-antidiquark (tetraquark) bound states. The resulting frame-independent color-confining bound-state LF eigensolutions can be identified with the hadronic eigenstates of confined quarks for SU(3) color. In effect, two of the quarks of the baryonic color-singlet qqq bound state bind to a color $\bar{3}_C$ diquark bound state, which then binds by the same color force to the remaining 3_C quark. As shown by 'tHooft in a string model [20], the Y configuration of three quarks is unstable and reduces to the quark-diquark configuration. The matching of the meson and baryon spectra is thus due to the fact that the same color-confining potential that binds two quarks to a diquark also binds a quark to an antiquark.

Note that the same slope controls the Regge trajectories of both mesons and baryons in both the orbital angular momentum L and the principal quantum number n . Only one mass parameter $\kappa = \omega^2$ appears; it sets the confinement scale and the hadron mass scale in the chiral limit, as well as the length scale which underlies hadron structure. We will also use the notation $\lambda = \kappa^2$. In addition to the meson and baryon eigenstates, one also predicts color-singlet *tetraquark* diquark-antidiquark bound states with the same mass as the baryon.

The LF Schrödinger equations for baryons and mesons derived from superconformal algebra are shown in Figure 2. As explained above, the baryons on the proton (Delta) trajectory are bound states of a quark with color 3_C and scalar (vector) diquark with color $\bar{3}_C$. The proton eigenstates labeled ψ^+ (parallel quark and baryon spins) and ψ^- (antiparallel quark and baryon spins) have equal Fock state probability, a feature of “quark chirality invariance.” Predictions for the static properties of the nucleons are discussed in [21].

Superconformal algebra also predicts that the LFWFs of the superpartners are related, and thus the corresponding elastic and transition form factors are identical. The resulting predictions for meson and baryon timelike form factors can be tested in $e^+e^- \rightarrow H\bar{H}'$ reactions.

One can generalize these results to heavy-light $[\bar{Q}q]$ mesons and $[Q[qq]]$ baryons [22]. The Regge slopes are found to increase for heavy m_Q as expected from heavy quark effective field theory; however, the supersymmetric connections between the heavy-light hadrons are predicted to be maintained.

The LFWFs thus play the same role in hadron physics as the Schrödinger wavefunctions which encode the structure of atoms in QED. The elastic and transition form factors of hadrons, weak-decay amplitudes, and distribution amplitudes are overlaps of LFWFs; structure functions, transverse momentum distributions, and other inclusive observables are constructed from the squares of the LFWFs. In contrast one cannot compute form factors of hadrons or other current matrix elements of hadrons from overlap of the usual “instant” form wavefunctions since one must also include contributions where the photon interacts with connected but acasual vacuum-induced currents. The calculation of deeply virtual Compton scattering using LFWFs is given in [23]. One

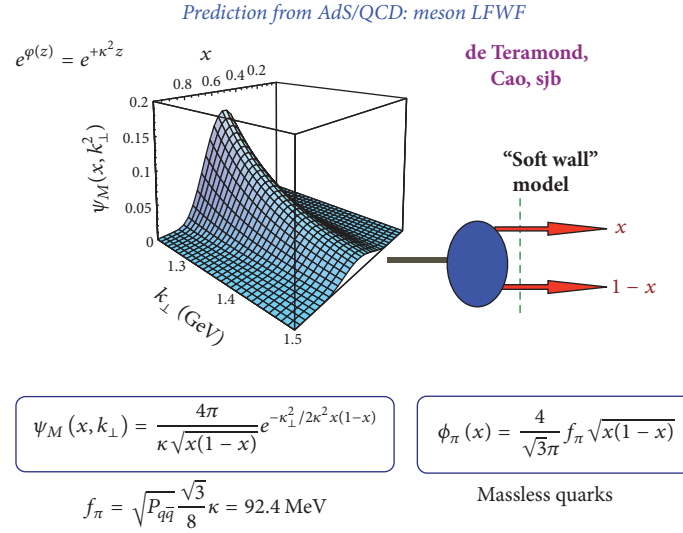


FIGURE 5: Prediction from AdS/QCD and Light-Front Holography for meson LFWFs $\psi_M(x, \vec{k}_\perp)$ and the pion distribution amplitude.

can also compute the gravitational form factors of hadrons. In particular, one can show that the anomalous gravitomagnetic moment $B(q^2 = 0)$ vanishes identically for any LF Fock state [24], in agreement with the equivalence theorem of gravity [25, 26].

The hadronic LFWFs predicted by light-front holography and superconformal algebra are functions of the LF kinetic energy $\vec{k}_\perp^2/x(1-x)$, the conjugate of the LF radial variable $\zeta^2 = b_\perp^2 x(1-x)$, times a function of $x(1-x)$. The hadronic LFWFs cannot be factorized as a function of \vec{k}_\perp^2 times a function of x . The resulting nonperturbative pion distribution amplitude $\phi_\pi(x) = \int d^2 \vec{k}_\perp \psi_\pi(x, \vec{k}_\perp) = (4/\sqrt{3}\pi) f_\pi \sqrt{x(1-x)}$, presented in Figure 5, which controls hard exclusive process, is consistent with the Belle data for the photon-to-pion transition form factor [27]. The AdS/QCD light-front holographic eigenfunction for the ρ meson LFWF $\psi_\rho(x, \vec{k}_\perp)$ gives excellent predictions for the observed features of diffractive ρ electroproduction $\gamma^* p \rightarrow \rho p'$, as shown by Forshaw and Sandapen [28].

2. Light-Front Holography

Five-dimensional AdS₅ space provides a geometrical representation of the conformal group. The color-confining light-front equation for mesons of arbitrary spin J can be derived [4] from the holographic mapping of the “soft-wall model” modification of AdS₅ space for the specific dilaton profile $e^{+\kappa^2 z^2}$, where one identifies the fifth dimension coordinate z with the light-front coordinate ζ . Remarkably, AdS₅ is holographically dual to 3 + 1 space-time at fixed light-front time $\tau = t + z/c$. The holographic dictionary is summarized in Figure 6. The combination of light-front dynamics, its holographic mapping to AdS₅ space, and the dAFF procedure provides new insight into the physics underlying color confinement, the nonperturbative QCD coupling, and the

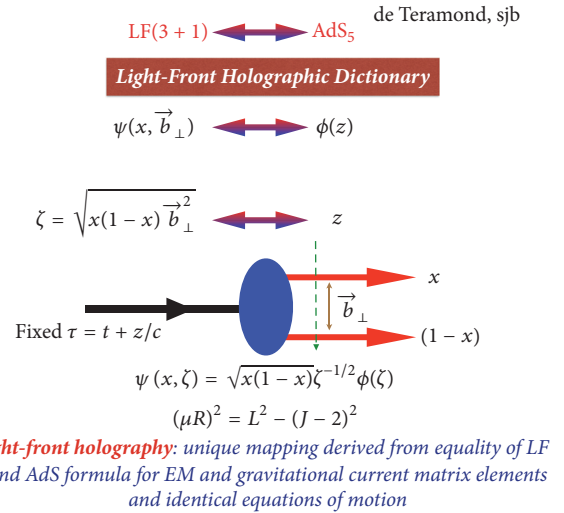


FIGURE 6: The holographic dictionary which maps the fifth dimension variable z of the five-dimensional AdS₅ space to the LF radial variable ζ where $\zeta^2 = b_\perp^2(1-x)$. The same physics transformation maps the AdS₅ and (3 + 1) LF expressions for electromagnetic and gravitational form factors to each other, from [4].

QCD mass scale. A comprehensive review is given in [29]. The $q\bar{q}$ mesons and their valence LF wavefunctions are the eigensolutions of the frame-independent relativistic bound state LF Schrödinger equation, the same meson equation that is derived using superconformal algebra. The mesonic $q\bar{q}$ bound-state eigenvalues for massless quarks are $M^2(n, L, S) = 4\kappa^2(n + L + S/2)$. The equation predicts that the pion eigenstate $n = L = S = 0$ is massless at zero quark mass. The Regge spectra of the pseudoscalar $S = 0$ and vector $S = 1$ mesons are predicted correctly, with equal slope in the principal quantum number n and the internal orbital angular momentum L . A comparison with experiment is shown in Figure 7.

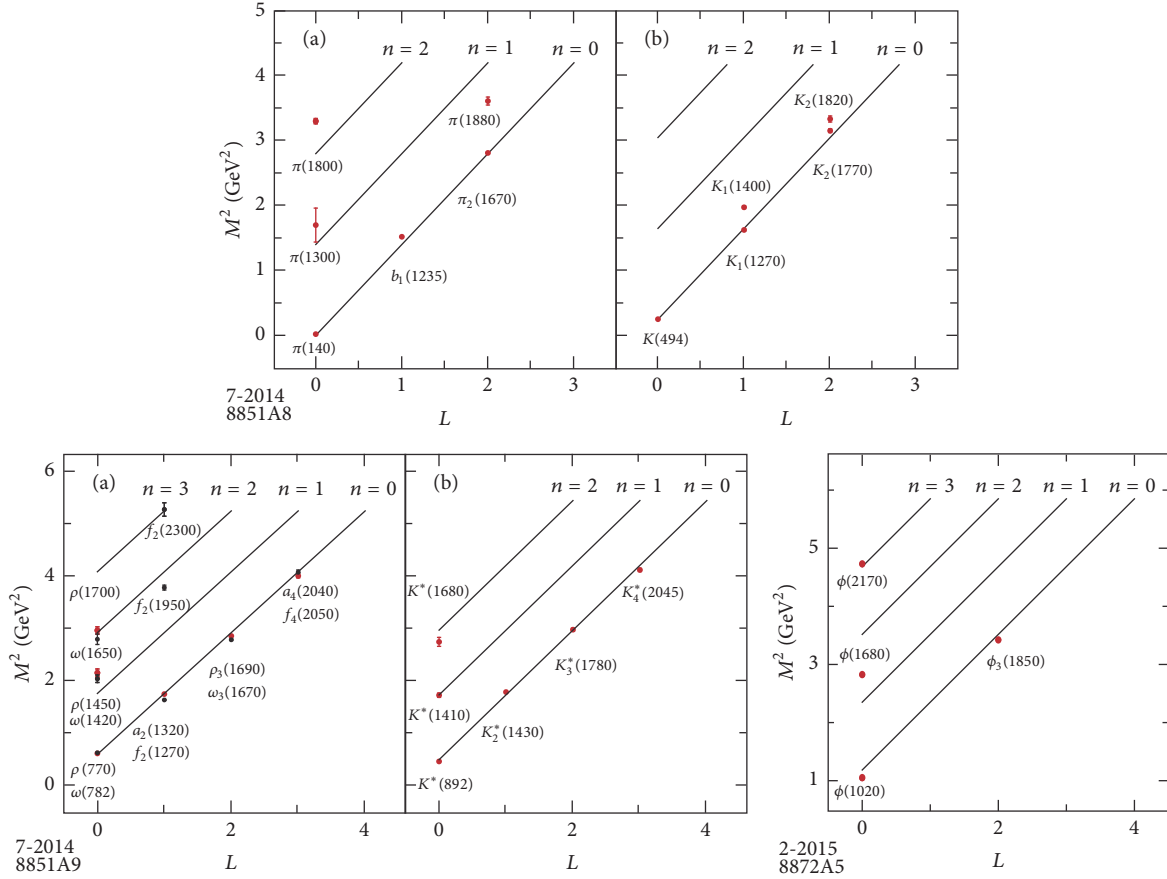


FIGURE 7: Comparison of the AdS/QCD prediction $M^2(n, L, S) = 4\kappa^2(n + L + S/2)$ for the orbital L and radial n excitations of the meson spectrum with experiment. The pion is predicted to be massless for zero quark mass. The u, d, s quark masses can be taken into account by perturbing in $\langle m_q^2/x \rangle$. The fitted value of $\kappa = 0.59$ GeV for pseudoscalar mesons, and $\kappa = 0.54$ GeV for vector mesons.

Light-Front Holography predicts not only meson and baryon spectroscopy successfully, but also hadron dynamics, including vector meson electroproduction, hadronic light-front wavefunctions, distribution amplitudes, form factors, and valence structure functions. The application to the deuteron elastic form factors and structure functions is given in [30, 31].

3. Color Confinement from LF Holography

Remarkably, the light-front potential using the dAFF procedure has the unique form of a harmonic oscillator $\kappa^4 \zeta^2$ in the light-front invariant impact variable ζ where $\zeta^2 = b_\perp^2 x(1-x)$. The result is a single-variable frame-independent relativistic equation of motion for $q\bar{q}$ bound states, a “Light-Front Schrödinger Equation” [32], analogous to the nonrelativistic radial Schrödinger equation in quantum mechanics. The same result, including spin terms, is obtained using light-front holography—the duality between the front form and AdS₅, the space of isometries of the conformal group—if one modifies the action of AdS₅ by the dilaton $e^{\kappa^2 z^2}$ in the fifth dimension z . The Light-Front Schrödinger Equation incorporates color confinement and other essential spectroscopic and dynamical features of hadron physics, including

a massless pion for zero quark mass and linear Regge trajectories with the same slope in the radial quantum number n and internal orbital angular momentum L . When one generalizes this procedure using superconformal algebra, the resulting light-front eigensolutions predict a unified Regge spectroscopy of meson, baryon, and tetraquarks, including remarkable supersymmetric relations between the masses of mesons and baryons of the same parity.

It is interesting to note that the contribution of the “ H ” diagram to $Q\bar{Q}$ scattering is IR divergent as the transverse separation between Q and \bar{Q} increases [33]. This is a signal that pQCD is inconsistent without color confinement. The sum of such diagrams could sum to the confinement potential $\kappa^4 \zeta^2$ dictated by the dAFF principle that the action remains conformally invariant despite the appearance of the mass scale κ in the Hamiltonian. The $\kappa^4 \zeta^2$ confinement interaction between a q and \bar{q} will induce a κ^4/s^2 correction to $R_{e^+e^-}$, replacing the $1/s^2$ signal usually attributed to a vacuum gluon condensate.

It should be emphasized that the value of the mass scale κ is not determined in an absolute sense by QCD. Only ratios of masses are determined, and the theory has dilation invariance under $\kappa \rightarrow C\kappa$. In a sense, chiral QCD has an “extended conformal invariance.” The resulting new time

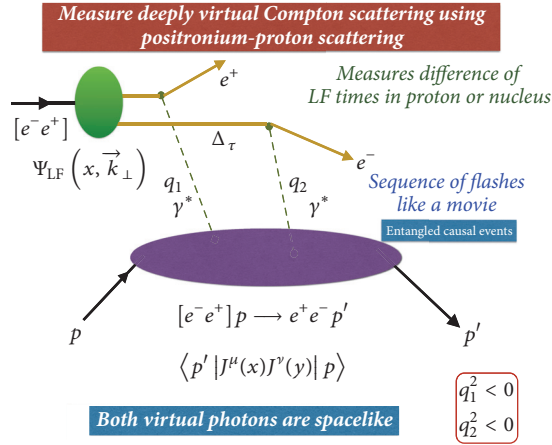


FIGURE 8: Doubly virtual Compton scattering on a proton (or nucleus) can be measured for two spacelike photons $q_1^2, q_2^2 < 0$ with minimal, tunable, skewness ξ using positronium-proton scattering $[e^+e^-]p \rightarrow e^+e^-p'$. One can also measure double deep inelastic scattering and elastic positronium-proton scattering. One can also create a beam of “true muonium” atoms $[\mu^-\mu^-]$ [5, 6] using Bethe-Heitler pair production just below threshold.

variable, which retains the conformal invariance of the action, has finite support, conforming to the fact that the LF time between the interactions with the confined constituents is finite. The finite time difference $\Delta\tau$ between the LF times τ of the quark constituents of the proton could be measured using positronium-proton scattering $[e^+e^-]p \rightarrow e^+e^-p'$. This process, which measures double diffractive deeply virtual Compton scattering for two spacelike photons, is illustrated in Figure 8. One can also study the dissociation of relativistic positronium atoms to an electron and positron with light-front momentum fractions x and $1-x$ and opposite transverse momenta in analogy to the E791 measurements of the diffractive dissociation of the pion to two jets [34]. The LFWF of positronium in the relativistic domain is the central input. One can produce a relativistic positronium beam using the collisions of laser photons with high energy photons or by using Bethe-Heitler pair production below the e^+e^- threshold. The production of parapositronium via the collision of photons is analogous to pion production in two-photon interactions and Higgs production via gluon-gluon fusion.

4. Light-Front Theory and QCD

One can derive the exact form of the light-front Hamiltonian H_{LF} directly from the QCD Lagrangian and avoid ghosts and longitudinal gluonic degrees of freedom by choosing the light-cone gauge $A^+ = 0$. Quark masses appear in the LF kinetic energy as $\sum_i(m^2/x_i)$. This can be derived from the Higgs theory quantized using LF dynamics [35]. The confined quark field ψ_q couples to the background Higgs field $g_{\bar{q}q}\langle H\rangle\Psi_q$ via its Yukawa scalar matrix element coupling $g_q\langle H\rangle\bar{u}(p)1u(p) = m_q \times (m_q/x) = m^2/x$. The usual Higgs vacuum expectation value $\langle H\rangle$ is replaced by a constant zero

mode when one quantizes the Standard Model using light-front quantization [35].

PQCD factorization theorems and the DGLAP [36–38] and ERL [39–42] evolution equations can also be derived using the light-front Hamiltonian formalism [40]. In the case of an electron-ion collider, one can represent the cross-section for $e-p$ collisions as a convolution of the hadron and virtual photon structure functions times the subprocess cross-section in analogy to hadron-hadron collisions. This nonstandard description of $\gamma^*p \rightarrow X$ reactions gives new insights into electroproduction physics, physics not apparent in the usual infinite-momentum frame description, such as the dynamics of heavy quark-pair production. Intrinsic heavy quarks at high x also play an important role [43].

The LF Heisenberg equation can in principle be solved numerically by matrix diagonalization using the “Discretized Light-Cone Quantization” (DLCQ) [44] method. Antiperiodic boundary conditions in x^- render the k^+ momenta discrete as well as limiting the size of the Fock basis. In fact, one can easily solve 1 + 1 quantum field theories such as QCD(1 + 1) [45] for any number of colors, flavors, and quark masses using DLCQ. Unlike lattice gauge theory, the nonperturbative DLCQ analysis is in Minkowski space, is frame-independent, and is free of fermion-doubling problems. AdS/QCD, based on the AdS₅ representation of the conformal group in five dimensions, maps to physical 3 + 1 space-time at fixed LF time; this correspondence, “light-front holography” [32], is now providing a color-confining approximation to H_{LF}^{QCD} for QCD(3 + 1). This method gives a remarkable first approximation to hadron spectroscopy and hadronic LFWFs. A new method for solving nonperturbative QCD “Basis Light-Front Quantization” (BLFQ) [46], uses the eigensolutions of a color-confining approximation to QCD (such as LF holography) as the basis functions, rather than the plane-wave basis used in DLCQ, thus incorporating the full dynamics of QCD. LFWFs can also be determined from the covariant Bethe-Salpeter wavefunction by integrating over k^- [47]. A review of the light-front formalism is given in [14].

5. Measuring LFWFs of Hadrons, Atoms, and Nuclei

One can in fact measure the LFWFs of QED atoms using diffractive dissociation.

For example, suppose one creates a relativistic positronium beam. It will dissociate by Coulomb exchange in a thin target: $[e^+e^-] + Z \rightarrow e^+e^-Z$. The momentum distribution of the leptons in the LF variables x and k_\perp will determine the first derivative of the atomic LFWF $(d/dk_\perp)\psi(x, \vec{k}_\perp)$. When $k_\perp^2/x(1-x) > 4m_e^2$ one can observe the transition from NR Schrödinger theory where $\psi(x, \vec{k}_\perp) \propto 1/k_\perp^4$ to the relativistic domain, where $\psi(x, \vec{k}_\perp) \propto 1/k_\perp^2$. One can thus test predictions from BLFQ (Basis Light-Front Quantization) [48]. Higher Fock states are also possible, such as $[e^+e^-] + Z \rightarrow e^+e^-\gamma Z$ and $[e^+e^-] + Z \rightarrow e^+e^-e^+e^-Z$.

Positronium dissociation is analogous to the Ashery measurements of the pion LFWF: $\pi A \rightarrow \text{JetJet}A$ [49], where

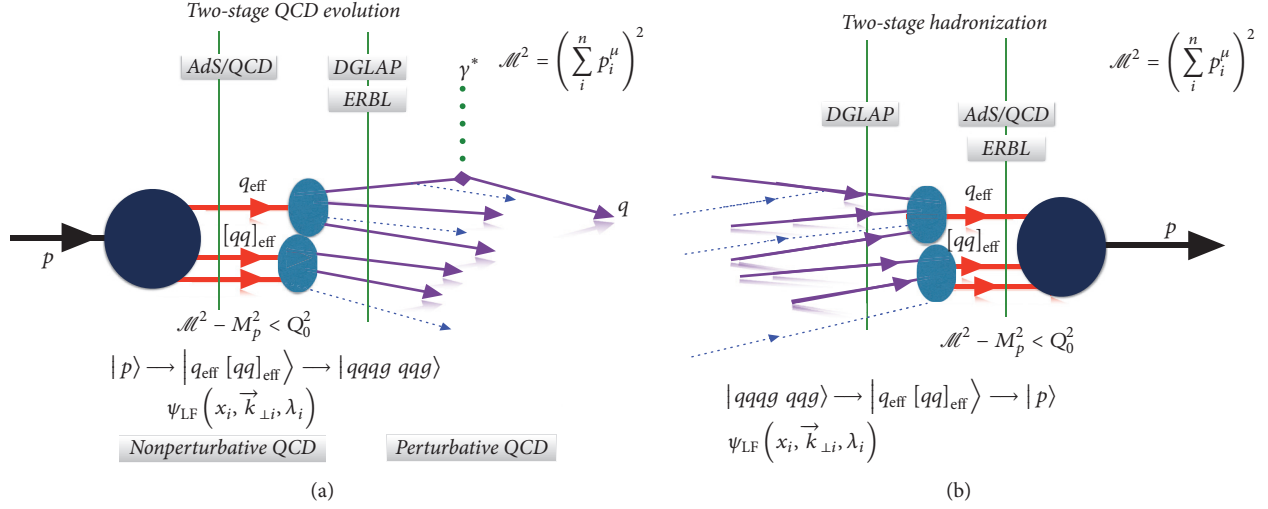


FIGURE 9: (a) A model for evolution starting with a nonperturbative hadronic LFWF. (b) Hadronization and evolution ending with a hadronic LFWF. The intermediate quark and gluon states are off the P^- energy shell and thus off-the-invariant mass shell $\mathcal{M}^2 > m_H^2$. In the off-shell domain $\mathcal{M}^2 - M_H^2 > \kappa^2$, the intermediate quarks and gluons obey the DGLAP and ERBL QCD evolution. If a cluster of quarks and antiquarks satisfies $\mathcal{M}^2 - M_H^2 < \kappa^2$, the intermediate state sees the color confinement interaction. The meson LFWF connects the intermediate $q\bar{q}$ state, which is off the P^- energy shell and thus off-the-invariant mass shell $\mathcal{M}^2 > m_H^2$ to the physical meson state with $\mathcal{M}^2 = m_H^2$. The LF angular momentum J^z is conserved at every vertex.

one observes the transition from Gaussian fall-off to power law fall-off at large $1/k_\perp^2$ as predicted by AdS/QCD. When $k_\perp^2/x(1-x) > 4m_e^2$ one can measure the transition from NR Schrödinger theory to the relativistic domain, where $\psi(x, \vec{k}_\perp) \propto 1/k_\perp^2$. Similarly, one could also measure the LFWF of a nucleus like a deuteron by dissociating relativistic ions $dA \rightarrow pnA$. At large $1/k_\perp^2$ one could observe the transition to the “hidden-color” Fock states predicted by QCD [50].

6. Calculations Using LF-Time-Ordered Perturbation Theory and Hadronization at the Amplitude Level

LF-time-ordered perturbation theory can be advantageous for perturbative QCD calculations. An excellent example of LF-time-ordered perturbation theory is the computation of multigluon scattering amplitudes by Cruz-Santiago et al. [51]. In this method, the propagating particles are on their respective mass shells: $k_\mu k^\mu = m^2$, and intermediate states are off-shell in invariant mass; that is, $P^- \neq \sum k_i^-$. Unlike instant form, where one must sum $n!$ frame-dependent amplitudes, only the τ -ordered diagrams where each propagating particle has positive $k^+ = k^0 + k^z$ can contribute. The number of nonzero amplitudes is also greatly reduced by noting that the total angular momentum projection $J^z = \sum_i^{n-1} L_i^z + \sum_i^n S_i^z$ and the total P^+ are conserved at each vertex. In a renormalizable theory, the change in orbital angular momentum is limited to $\Delta L^z = 0, \pm 1$ at each vertex [52].

A remarkable advantage of LF time-ordered perturbation theory (LFPth) is that the calculation of a subgraph of any order in pQCD only needs to be done once; the result can be stored in a “history” file. This is due to the fact

that in LFPth the numerator algebra is independent of the process; the denominator changes, but only by a simple shift of the initial P^- . Another simplification is that loop integrations are three dimensional: $\int d^2 \vec{k}_\perp \int_0^1 dx$. Unitarity and explicit renormalization can be implemented using the “alternate denominator” method which defines the required subtraction counterterms [53].

The new insights into color confinement given by AdS/QCD suggest that one could compute “hadronization at the amplitude level” [54] using the confinement interaction and the LFWFs predicted by AdS/QCD and Light-Front Holography. For example, as illustrated in Figure 1, the meson LFWF connects the off-the-invariant mass shell quark and antiquark to the on-shell asymptotic physical meson state.

The invariant mass of a color-singlet cluster \mathcal{M} is the key variable which separates perturbative and nonperturbative dynamics. For example, consider e^+e^- annihilation using LF τ -ordered perturbation theory. At an early stage in LF time, the annihilation will produce jets of quarks and gluons in an intermediate state off the P^- energy shell. If a color-singlet cluster of partons in a jet satisfies $\mathcal{M}^2 - M_H^2 < \kappa^2$, the cluster constituents are effective degrees of freedom which will be ruled by the $\kappa^4 \zeta^2$ color-confinement potential. At this stage, the LFWF ψ_H converts the off-shell partons to the asymptotic states, the on-shell hadrons. If $\mathcal{M}^2 > \kappa^2$ one can apply pQCD corrections, for example, from DGLAP and ERBL evolution [39–42].

A model for the two stages of hadronization and evolution is illustrated in Figure 9. In the off-shell domain $\mathcal{M}^2 - M_H^2 > \kappa^2$, the intermediate quarks and gluons obey DGLAP and ERBL evolution.

Thus quarks and gluons can appear in intermediate off-shell states, but only hadrons are produced asymptotically.

Thus the AdS/QCD Light-Front Holographic model suggests how one can implement the transition between perturbative and nonperturbative QCD. For a QED analog, see [5, 6].

7. Light-Front Spin and Light-Front J^z Conservation

A central, unique property of light-front quantization is J^z conservation [52]; the z -component of angular momentum remains unchanged under Lorentz transformations generated by the light-front kinematical boost operators. The spin along the \hat{z} direction defined by the light-front Lorentz transformation is preserved because $\langle J^3 \rangle_{\text{LF}} = s^z$ for all momenta p^μ . J^z conservation underlies the Jaffe spin sum rule [55].

Particles in the front form move with positive $k^+ = k^0 + k^z \geq 0$. The quantization axis for J^z for each particle is the same axis \hat{z} which defines LF time $\tau = t + z/c$. Thus S^z and L^z refer to angular momentum in the \hat{z} direction. As in nonrelativistic quantum mechanics, $J^z = \sum_{i=1}^n S_i^z + \sum_{i=1}^{n-1} L_i^z$ for any n -particle intermediate or Fock state. There are $n - 1$ relative orbital angular momenta. It is conserved at every vertex and is conserved overall for any process and ‘‘LF helicity’’ refers to the spin projection S^z of each particle and ‘‘LF chirality’’ is the spin projection S^z for massless particles. In a renormalizable theory L^z can only change by one unit at any vertex. This leads to a rigorous selection rule for amplitudes at fixed order in pQCD [52]: $|\Delta L^z| \leq n$ in an n th order perturbative expansion. This selection rule for the orbital angular momentum can be used to eliminate interaction vertices in QED and QCD and provides an upper bound on the change of orbital angular momentum in scattering processes at any fixed order in perturbation theory.

By definition, spin and helicity can be used interchangeably in the front form. LF chirality is conserved by the vector current in electrodynamics and the axial current of electroweak interactions. Each coupling conserves quark chirality when the quark mass is set to zero. A compilation of LF spinor matrix elements is given in [40].

Light-front spin is not the same as the usual ‘‘Wick helicity,’’ where spin is defined as the projection of the particle’s three-momentum \vec{k} . Wick helicity is thus not conserved unless all particles move in the same direction. Wick helicity can be frame dependent. For example, in the case of $gg \rightarrow H$, the Wick helicity assignment is $(+1) + (+1) \rightarrow 0$ in the CM frame, but it is $(+1) + (-1) \rightarrow 0$ for collinear gluons if the two gluons move in the same direction.

The twist of a hadronic interpolating operator corresponds to the number of fields plus $|L^z|$. The pion LF Fock state for $\pi \rightarrow q\bar{q}$ with twist-2 corresponds to $(J_\pi^z = 0) \rightarrow (S_q^z = +1/2) + (S_{\bar{q}}^z = -1/2)$ with zero relative orbital angular momentum $L_{q\bar{q}}^z$. This is the Fock state of the pion that decays to $\ell\nu$ via the LF chiral-conserving axial current $\gamma^\mu \gamma_5$. The twist-3 pion in the OPE corresponds to $J_\pi^z = 0 \rightarrow (S_q^z = +1/2) + (S_{\bar{q}}^z = +1/2) + (L^z = -1)$ or $J_\pi^z = 0 \rightarrow (S_q^z = -1/2) + (S_{\bar{q}}^z = -1/2) + (L_{q\bar{q}}^z = -1)$, where L^z is the relative orbital angular momentum between the quark and antiquark.

The twist-3 Fock state couples the pion to the chiral-flip pseudoscalar γ_5 operator. The GMOR relation connects the twist-2 and twist-3 Fock states when $m_q \neq 0$ [56]. The twist-3 proton with $J_p^z = +1/2$ in AdS/QCD is a bound state of a quark with $S_p^z = 1/2$ and a spin-zero diquark $[qq]$ with $L_{q[qq]}^z = 0$, and the twist-4 proton in AdS/QCD is a bound state of a quark with $S_p^z = -1/2$ and spin-zero diquark $[qq]$ with relative orbital angular momentum $L_{q[qq]}^z = +1$. LF holography predicts equal probability for the twist-3 and twist-4 Fock states in the nucleon for $m_q = 0$.

One can use LF J^z conservation to determine the contribution of Fock states of different twist in a scattering amplitude by using the fact that amplitudes with nonzero relative L^z between the outgoing particles vanish in the forward direction. For example, consider pion electroproduction $\gamma^* p \rightarrow \pi^0 p$ for a polarized photon with LF spin $S_\gamma^z = -1$. If the proton’s LF spin $S_p^z = -1/2$ is unchanged, then $J_{\text{tot}}^z = +1/2 : \gamma_T^*(S_\gamma^z = +1) + (S_p^z = -1/2) \rightarrow +(J_\pi^z = 0) + (S_p^z = -1/2) + (L_{\pi^0 p}^z = +1)$ vanishes at $t = 0$ for the twist-2 pion. However, the non-spin-flip proton amplitude $J_{\text{tot}}^z = 1/2 : \gamma_T^*(S_\gamma^z = +1) + S_p^z = (-1/2) \rightarrow [(S_q^z = -1/2) + (S_{\bar{q}}^z = -1/2) + (L_{q\bar{q}}^z = +1)]_{\pi^0} + S_p^z = (-1/2)$ for the twist-3 pion Fock state is finite at $t = 0$. A similar result holds for the contribution of the twist-2 pion and twist-4 proton. See Figure 10.

Similarly one can utilize the behavior of the amplitude $\gamma^* \text{He}^4 \rightarrow \pi^0 \text{He}^4$ on a spin-zero helium target. The pion twist-2 amplitude with $J_{\text{tot}}^z = +1 : \gamma_T^*(S_\gamma^z = +1) + (S_{\text{He}}^z = 0) \rightarrow [(S_q^z = +1/2) + (S_{\bar{q}}^z = -1/2) + (L_{q\bar{q}}^z = 0)]_{\pi^0} + (S_{\text{He}}^z = 0) + (L_{\pi^0 \text{He}^4}^z = 1)$ vanishes at $t = 0$, whereas the amplitude with a pion twist-3 amplitude $J_{\text{tot}}^z = +1 : \gamma_T^*(S_\gamma^z = +1) + (S_{\text{He}}^z = 0) \rightarrow [(S_q^z = +1/2) + (S_{\bar{q}}^z = -1/2) + (L_{q\bar{q}}^z = +1)]_{\pi^0} + (S_{\text{He}}^z = 0) + (L_{\pi^0 \text{He}^4}^z = 0)$ is finite at $t = 0$, thus discriminating between contributions using the twist-2 and twist-3 pion amplitudes.

8. The Light-Front Vacuum

It is important to distinguish the LF vacuum from the conventional instant-form vacuum. The eigenstates of the instant-form Hamiltonian describe a state defined at a single instant of time t over all space, and they are thus acausal as well as frame-dependent. The instant-form vacuum is defined as the lowest energy eigenstate of the instant-form Hamiltonian. As discussed by Zee [57], the cosmological constant is of order 10^{120} times larger than what is observed if one computes the effects of quantum loops from QED. Similarly, QCD instantons and condensates in the instant-form vacuum give a contribution of order 10^{42} . The contribution of the Higgs VEV computed in the instant-form vacuum is 10^{54} times too large.

In contrast, the vacuum in LF Hamiltonian theory is defined as the eigenstate of H_{LF} with lowest invariant mass. It is defined at fixed LF time τ within the causal horizon, and it is frame-independent; that is, it is independent of the observer’s motion. Vacuum loop diagrams from quantum field theory do not appear in the front-form vacuum since the + momenta

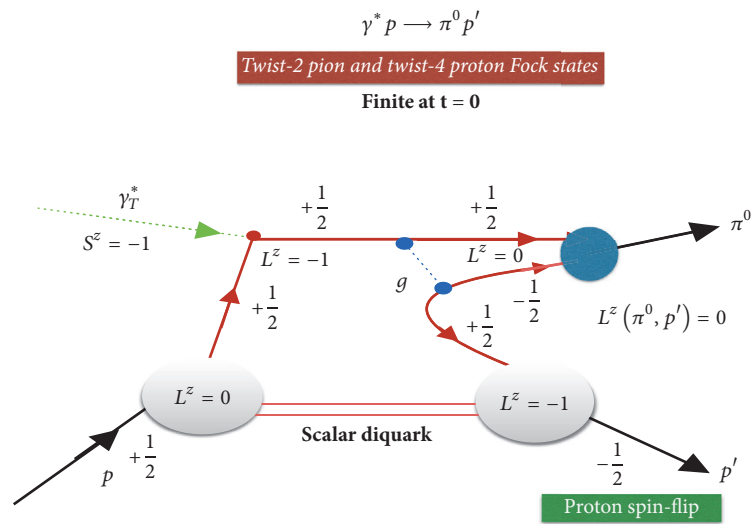
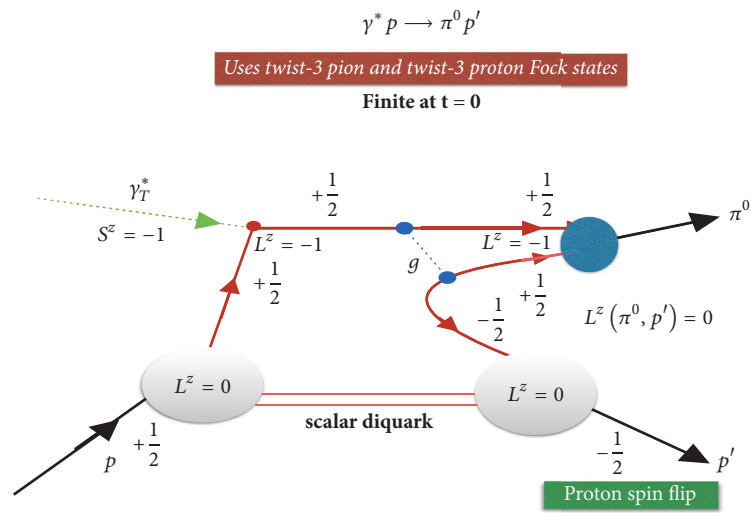
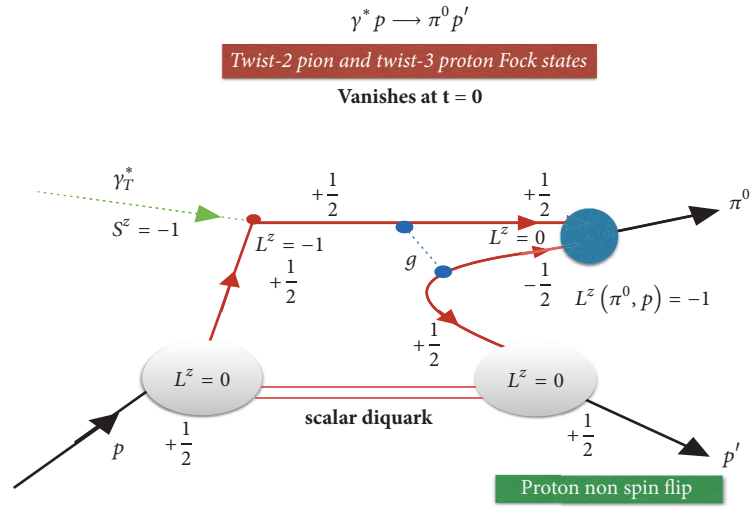


FIGURE 10: Illustration of spin flow in $\gamma^* p \rightarrow \pi^0 p$.

are positive: $k_i^+ = k_i^0 + k_i^z \geq 0$, and the sum of + momenta is conserved at every vertex. The creation of particles cannot arise from the LF vacuum since $\sum_i k^{+i} \neq P_{\text{vacuum}}^+ = 0$. Propagation with negative k^+ does not appear. The physical vacuum state can also have $k^+ = 0$ modes corresponding to a flat energy-momentum background, analogous to a classical scalar Stark or Zeeman field. For example, Reinhardt and Weigel [58] have shown that the Nambu-Jona-Lasino (NJL) model can lead to a nontrivial physical LF vacuum. In the case of the Higgs theory, the traditional Higgs vacuum expectation value (VEV) is replaced by a “zero mode” [35]. All phenomenological consequences of the Higgs theory in the Standard Model are unchanged in the LF formulation. As noted in Section 6, the m^2/x term in the LF kinetic energy ($k_{\perp}^2 + m^2)/x$ arises from the interaction of a quark within a hadron in QCD with its Yukawa interaction with the Higgs background zero mode.

The physics associated with quark and gluon QCD vacuum condensates of the instant form are replaced by physical effects contained within the hadronic LFWFs. This is referred to as “in-hadron” condensates [59–61]. For example, as discussed in Section 7, the GMOR relation relating the vacuum-to-pion matrix elements of the axial current and pseudoscalar operators is satisfied in LF theory as a relation between the twist-2 and twist-3 Fock states [56]. The usual properties of chiral symmetry are satisfied; for example, as discussed in Section 2, the mass of the pion eigenstate computed from LF holography vanishes for zero quark mass.

The universe is observed within the causal horizon, not at a single instant of time. The causal, frame-independent light-front vacuum can thus provide a viable match to the empty visible universe [61]. The huge contributions to the cosmological constant from quantum field theory loops thus do not appear if one notes that the causal, frame-independent light-front vacuum has no quantum fluctuations, in dramatic contrast to the acausal, frame-dependent instant-form vacuum; the cosmological constant arising from quantum field theory thus vanishes if one uses the front form. The Higgs LF zero mode [35] has no energy-momentum density, so it also gives zero contribution to the cosmological constant. The observed nonzero value could be a property of gravity itself, such as the “emergent gravity” postulated by Verlinde [62]. It is also possible that if one solves electroweak theory in a curved universe, the Higgs LF zero mode would be replaced with a field of nonzero curvature which could give a nonzero contribution to the cosmological constant.

9. The QCD Coupling at All Scales

The QCD running coupling $\alpha_s(Q^2)$ sets the strength of the interactions of quarks and gluons as a function of the momentum transfer Q . The dependence of the coupling Q^2 is needed to describe hadronic interactions at both long and short distances. The QCD running coupling can be defined [63] at all momentum scales from a perturbatively calculable observable, such as the coupling $\alpha_{g_1}^s(Q^2)$, which is defined from measurements of the Bjorken sum rule. At high momentum transfer, such “effective charges” satisfy

asymptotic freedom, obey the usual pQCD renormalization group equations, and can be related to each other without scale ambiguity by commensurate scale relations [64].

The dilaton $e^{+\kappa^2 z^2}$ soft-wall modification of the AdS₅ metric, together with LF holography, predicts the functional behavior of the running coupling in the small Q^2 domain [65]: $\alpha_{g_1}^s(Q^2) = \pi e^{-Q^2/4\kappa^2}$. Measurements of $\alpha_{g_1}^s(Q^2)$ are remarkably consistent [66] with this predicted Gaussian form; the best fit gives $\kappa = 0.513 \pm 0.007$ GeV. See Figure 11. Brodsky et al. [7, 65, 67] have also shown how the parameter κ , which determines the mass scale of hadrons and Regge slopes in the zero quark mass limit, can be connected to the mass scale Λ_s controlling the evolution of the perturbative QCD coupling. The high momentum transfer dependence of the coupling $\alpha_{g_1}(Q^2)$ is predicted by pQCD. The matching of the high and low momentum transfer regimes of $\alpha_{g_1}(Q^2)$, both its value and its slope, then determines a scale $Q_0 = 0.87 \pm 0.08$ GeV which sets the interface between perturbative and nonperturbative hadron dynamics. This connection can be done for any choice of renormalization scheme, such as the $\overline{\text{MS}}$ scheme, as seen in Figure 11. The result of this perturbative/nonperturbative matching is an effective QCD coupling defined at all momenta. The predicted value of $\Lambda_{\overline{\text{MS}}} = 0.339 \pm 0.019$ GeV from this analysis agrees well the measured value [68] $\Lambda_{\overline{\text{MS}}} = 0.332 \pm 0.017$ GeV. These results, combined with the AdS/QCD superconformal predictions for hadron spectroscopy, allow one to compute hadron masses in terms of $\Lambda_{\overline{\text{MS}}}$: $m_p = \sqrt{2}\kappa = 3.21\Lambda_{\overline{\text{MS}}}$, $m_\rho = \kappa = 2.2\Lambda_{\overline{\text{MS}}}$, and $m_p = \sqrt{2}m_\rho$, meeting a challenge proposed by Zee [69]. The value of Q_0 can be used to set the factorization scale for DGLAP evolution of hadronic structure functions and the ERBL evolution of distribution amplitudes. Deur, de Téramond, and I have also computed the dependence of Q_0 on the choice of the effective charge used to define the running coupling and the renormalization scheme used to compute its behavior in the perturbative regime. The use of the scale Q_0 to resolve the factorization scale uncertainty in structure functions and fragmentation functions, in combination with the scheme-independent *principle of maximum conformality* (PMC) [70] for setting renormalization scales, can greatly improve the precision of pQCD predictions for collider phenomenology.

10. Is the Momentum Sum Rule Valid for Nuclear Structure Functions?

Sum rules for deep inelastic scattering are usually analyzed using the operator product expansion of the forward virtual Compton amplitude, assuming it depends in the limit $Q^2 \rightarrow \infty$ on matrix elements of local operators such as the energy-momentum tensor. The moments of structure functions and other distributions can then be evaluated as overlaps of the target hadron’s light-front wavefunction, as in the Drell-Yan-West formulae for hadronic form factors [71–74]. The real phase of the resulting DIS amplitude and its OPE matrix elements reflects the real phase of the stable target hadron’s wavefunction.

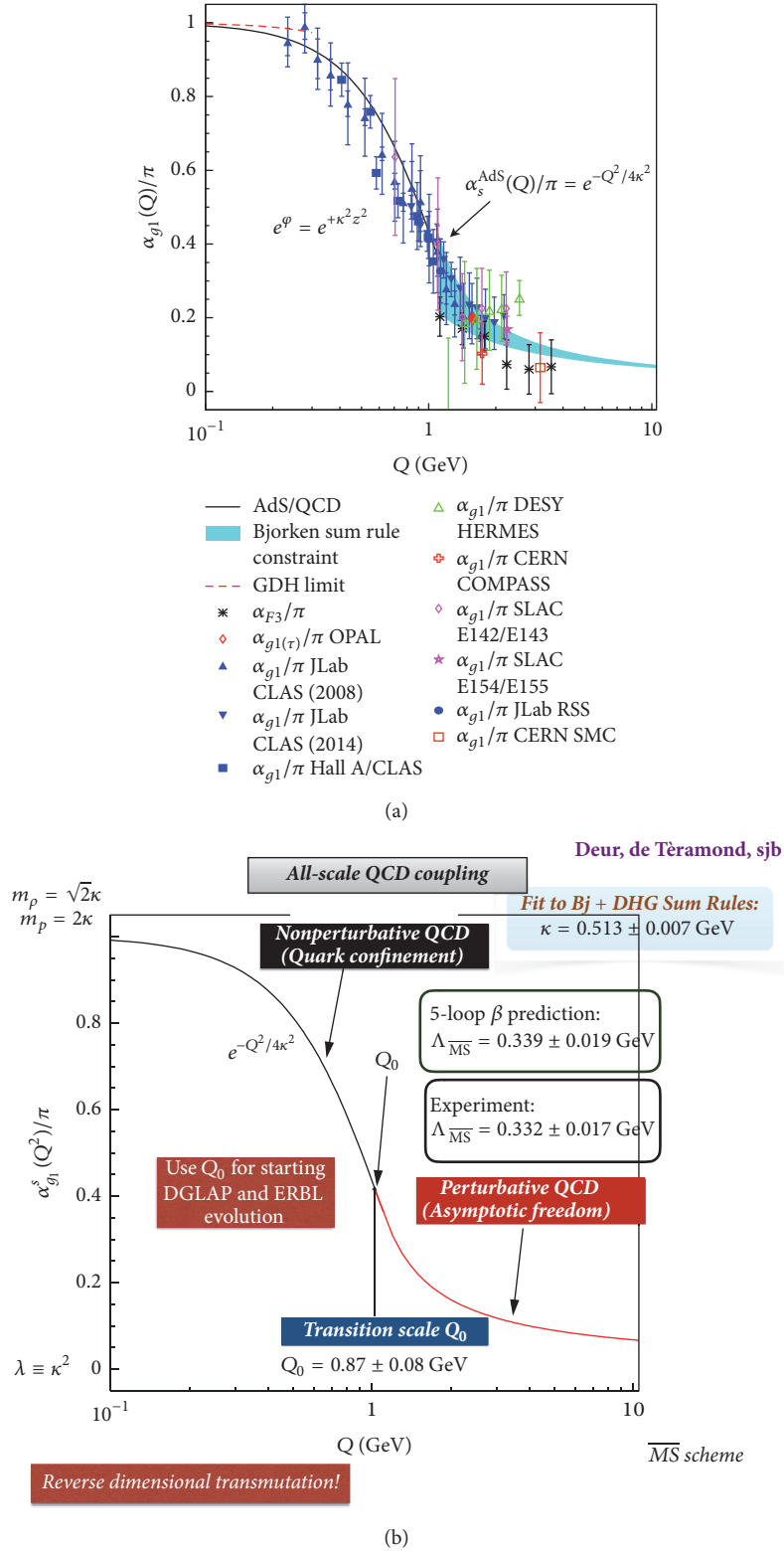


FIGURE 11: (a) Comparison of the predicted nonperturbative coupling, based on the dilaton $\exp(+\kappa^2 z^2)$ modification of the AdS_5 metric, with measurements of the effective charge $\alpha_{g_1}^s(Q^2)$, as defined from the Bjorken sum rule. (b) Prediction from LF holography and pQCD for the QCD running coupling $\alpha_{g_1}^s(Q^2)$ at all scales. The magnitude and derivative of the perturbative and nonperturbative coupling are matched at the scale Q_0 . This matching connects the perturbative scale $\Lambda_{\overline{\text{MS}}}$ to the nonperturbative scale κ which underlies the hadron mass scale. See [7].

The “handbag” approximation to deeply virtual Compton scattering also defines the “static” contribution [75, 76] to the measured parton distribution functions (PDF), transverse momentum distributions, and so on. The resulting momentum, spin, and other sum rules reflect the properties of the hadron’s light-front wavefunction. However, the final-state interactions which occur *after* the lepton scatters on the quark can give nontrivial contributions to deep inelastic scattering processes at leading-twist and thus survive at high Q^2 and high $W^2 = (q + p)^2$. For example, the pseudo- T -odd Sivers effect [77] is directly sensitive to the rescattering of the struck quark. Similarly, diffractive deep inelastic scattering (DDIS) involves the exchange of a gluon after the quark has been struck by the lepton [78]. In each case the corresponding DVCS amplitude is not given by the handbag diagram since interactions between the two currents are essential. These “lensing” corrections survive when both W^2 and Q^2 are large since the vector gluon couplings grow with energy. Part of the final-state phase can be associated with a Wilson line as an augmented LFWF [79] which does not affect the moments.

The Glauber propagation of the vector system V produced by the DDIS interaction on the nuclear front face and its subsequent inelastic interaction with the nucleons in the nuclear interior $V + N_b \rightarrow X$ occurs after the lepton interacts with the struck quark. The corresponding amplitude for deeply virtual Compton scattering is not given by the handbag diagram alone since interactions between the two currents are essential. Because of the rescattering dynamics, the DDIS amplitude acquires a complex phase from Pomeron and Regge exchange; thus final-state rescattering corrections lead to nontrivial “dynamical” contributions to the measured PDFs; that is, they are a consequence of the scattering process itself [80]. The $I = 1$ Reggeon contribution to DDIS on the front-face nucleon then leads to flavor-dependent antishadowing [81, 82]. This could explain why the NuTeV charged current measurement $\mu A \rightarrow \nu X$ scattering does not appear to show antishadowing, in contrast to deep inelastic electron-nucleus scattering as discussed in [83].

Diffractive deep inelastic scattering is leading-twist, and it is an essential component of the two-step amplitude which causes shadowing and antishadowing of the nuclear PDF. It is important to analyze whether the momentum and other sum rules derived from the OPE expansion in terms of local operators remain valid when these dynamical rescattering corrections to the nuclear PDF are included. The OPE is derived assuming that the LF time separation between the virtual photons in the forward virtual Compton amplitude $\gamma^* A \rightarrow \gamma^* A$ scales as $1/Q^2$. However, the propagation of the vector system V produced by the DDIS interaction on the front face and its inelastic interaction with the nucleons in the nuclear interior $V + N_b \rightarrow X$ are characterized by a nonvanishing LF time interval in the nuclear rest frame. Note also that shadowing in deep inelastic lepton scattering on a nucleus involves nucleons facing the incoming lepton beam. The geometrical orientation of the shadowed nucleons is not a property of the nuclear LFWFs used to evaluate the matrix elements of local currents. Thus leading-twist shadowing and antishadowing appear to invalidate the sum rules for nuclear PDFs. The

same complications occur in the leading-twist analysis of deeply virtual Compton scattering $\gamma^* A \rightarrow \gamma^* A$ on a nuclear target. Thus the leading-twist multinucleon processes which produce shadowing and antishadowing in a nucleus are not accounted for using the $Q^2 \rightarrow \infty$ OPE analysis.

11. Summary

The light-front Hamiltonian equation $H_{\text{LF}}|\Psi\rangle = M^2|\Psi\rangle$ derived from quantization at fixed LF time $\tau = t+z/c$ provides a causal, Poincaré-invariant method for solving QCD. The eigenvalues M_H^2 are the squares of the hadronic masses, and the eigensolutions provide the LF Fock state wavefunctions $\Psi_n(x_i, \vec{k}_{\perp i}, \lambda_i)$ controlling hadron dynamics. The LFWFs Ψ_n are independent of the hadron’s momentum; that is, they are boost invariant and satisfy momentum and spin sum rules. Light-Front Quantization thus provides a physical, frame-independent formalism for hadron dynamics and structure. Observables such as structure functions, transverse momentum distributions, and distribution amplitudes are defined from the hadronic light-front wavefunctions.

The full QCD LF equation can be reduced for massless quarks to an effective LF Schrödinger radial equation for the valence $|q\bar{q}\rangle$ Fock state of $q\bar{q}$ mesons

$$\left[-\frac{d^2}{d\zeta^2} + \frac{4L^2 - 1}{4\zeta^2} + U(\zeta^2) \right] \psi = M^2 \psi \quad (1)$$

and similar bound-state equations for baryons, represented as quark + diquark-cluster $|q[qq]\rangle$ eigenstates. The “radial” LF variable $\zeta^2 = b_{\perp}^2 x(1-x)$ of LF theory is conjugate to the LF kinetic energy. The identical equation is derived from AdS₅, where the fifth coordinate z is identified with ζ (Light-Front Holography).

The color-confining potential $U(\zeta^2) = \kappa^4 \zeta^2 + 2\kappa^2(J-1)$ can be derived from soft-wall AdS₅ by incorporating the remarkable dAFF principle that a mass scale can appear in the Hamiltonian while retaining the conformal invariance of the action. The result is a color-confining LF potential which depends on a single universal constant κ with mass dimensions. In addition, by utilizing superconformal algebra [3], the resulting hadronic color-singlet eigenstates have a 2×2 representation of mass degenerate bosons and fermions: a $|q\bar{q}\rangle$ meson with $L_M = L_B + 1$, a baryon doublet $|q[qq]\rangle$ with L_B and $L_B + 1$ components of equal weight, and a tetraquark $|[qq][\bar{q}\bar{q}]\rangle$ with $L_T = L_B$. See Figure 4. Thus ratios of hadron masses such as $m_\rho = M_\rho/\sqrt{2}$ are predicted. The individual contributions LF kinetic energy, potential energy, spin-interactions, and the quark mass to the mass squared of each hadron are also shown. The virial theorem for harmonic oscillator confinement predicts the equality of the LF kinetic and potential contributions to M_H^2 for each hadron.

One obtains new insights into the hadronic spectrum, light-front wavefunctions, and the $e^{-Q^2/4\kappa^2}$ Gaussian functional form of the QCD running coupling in the nonperturbative domain using light-front holography—the duality between the front form and AdS₅, the space of isometries

of the conformal group. AdS/QCD also predicts the analytic form of the nonperturbative running coupling $\alpha_s(Q^2) \propto e^{-Q^2/4\kappa^2}$, in agreement with the effective charge measured from measurements of the Bjorken sum rule. This analysis also provides a connection between nonperturbative QCD and PQCD at a scale Q_0 and a prediction for $\Lambda_{\overline{\text{MS}}}$ from the proton or ρ mass.

Other LF Holographic predictions include the following:

- (1) Universal Regge slopes in n and L for mesons: $M^2(n, L) = 4\kappa^2(n + L)$ for mesons and $M^2(n, L) = 4\kappa^2(n + L + 1)$ for baryons, consistent with measurements.
- (2) The pion eigenstate is a massless $q\bar{q}$ bound state for chiral QCD ($m_q = 0$).
- (3) Empirically viable predictions for spacelike and timelike hadronic form factors, structure functions, distribution amplitudes, and transverse momentum distributions [84].
- (4) Superconformal extensions to heavy-light quark mesons and baryons.

In addition, superconformal algebra leads to remarkable supersymmetric relations between mesons and baryons of the same parity. The mass scale κ underlying confinement and hadron masses can be connected to the parameter $\Lambda_{\overline{\text{MS}}}$ in the QCD running coupling by matching the nonperturbative dynamics, as described by the effective conformal theory mapped to the light-front and its embedding in AdS space, to the perturbative QCD regime. The result is an effective coupling defined at all momenta. This matching of the high and low momentum transfer regimes determines a scale Q_0 which sets the interface between perturbative and nonperturbative hadron dynamics. The use of Q_0 to resolve the factorization scale uncertainty for structure functions and distribution amplitudes, in combination with the principle of maximal conformality (PMC) for setting the renormalization scales [70], can greatly improve the precision of perturbative QCD predictions for collider phenomenology. The absence of vacuum excitations of the causal, frame-independent front-form vacuum has important consequences for the cosmological constant. I have also discussed evidence that the antishadowing of nuclear structure functions is non-universal, that is, flavor dependent, and why shadowing and antishadowing phenomena may be incompatible with sum rules for nuclear parton distribution functions.

Future work will include the extension of superconformal representations to pentaquark and other exotic hadrons, comparisons with lattice gauge theory predictions, the construction of an AdS/QCD orthonormal basis to diagonalize the QCD light-front Hamiltonian, hadronization at the amplitude level, and the computation of intrinsic heavy quark higher Fock states.

Conflicts of Interest

The author declares that they have no conflicts of interest.

Acknowledgments

The author thanks Ralf Hofmann for organizing an outstanding 5th Winter Workshop on Nonperturbative Quantum Field Theory at the Université de Nice. The results presented here are based on collaborations and discussions with Kelly Chiu, Alexandre Deur, Guy de Téraumont, Guenter Dosch, Susan Gardner, Fred Goldhaber, Paul Hoyer, Dae Sung Hwang, Rich Lebed, Simonetta Liuti, Cedric Lorcé, Valery Lyubovitskij, Matin Mojaza, Michael Peskin, Craig Roberts, Robert Shrock, Ivan Schmidt, Peter Tandy, and Xing-Gang Wu. This research was supported by the Department of Energy, Contract DE-AC02-76SF00515. SLAC-PUB-17012.

References

- [1] G. F. de Téraumont, H. G. Dosch, and S. J. Brodsky, “Baryon spectrum from superconformal quantum mechanics and its light-front holographic embedding,” *Physical Review D*, vol. 91, no. 4, article 045040, 2015.
- [2] H. G. Dosch, G. F. de Téraumont, and S. J. Brodsky, “Superconformal baryon-meson symmetry and light-front holographic QCD,” *Physical Review D: Particles, Fields, Gravitation and Cosmology*, vol. 91, no. 8, article 085016, 2015.
- [3] H. G. Dosch, G. F. de Téraumont, and S. J. Brodsky, “Supersymmetry across the light and heavy-light hadronic spectrum,” *Physical Review D: Particles, Fields, Gravitation and Cosmology*, vol. 92, no. 7, article 074010, 2015.
- [4] G. F. de Téraumont, H. G. Dosch, and S. J. Brodsky, “Kinematical and dynamical aspects of higher-spin bound-state equations in holographic QCD,” *Physical Review D: Particles, Fields, Gravitation and Cosmology*, vol. 87, no. 7, article 075005, 2013.
- [5] S. J. Brodsky and R. F. Lebed, “Production of the smallest QED atom: True Muonium ($\mu^+ \mu^-$),” *Physical Review Letters*, vol. 102, article 213401, 2009.
- [6] A. Banburski and P. Schuster, “Production and discovery of true muonium in fixed-target experiments,” *Physical Review D: Particles, Fields, Gravitation and Cosmology*, vol. 86, article 093007, 2012.
- [7] S. J. Brodsky, G. F. de Téraumont, A. Deur, and H. G. Dosch, “The light-front schrödinger equation and determination of the perturbative QCD scale from color confinement,” *Few-Body Systems*, vol. 56, no. 6-9, article 621, 2015.
- [8] V. de Alfaro, S. Fubini, and G. Furlan, “Conformal invariance in quantum mechanics,” *Il Nuovo Cimento A*, vol. 34, no. 4, pp. 569–612, 1976.
- [9] S. J. Brodsky, G. F. de Téraumont, and H. G. Dosch, “Threefold complementary approach to holographic QCD,” *Physics Letters B*, vol. 729, pp. 3–8, 2014.
- [10] S. J. Brodsky, “Advances in light-front QCD: supersymmetric properties of hadron physics from light-front holography and superconformal algebra,” *Few-Body Systems*, vol. 58, no. 133, 2017.
- [11] S. J. Brodsky, “Light-front holography, color confinement, and supersymmetric features of QCD,” *Few-Body Systems*, vol. 57, no. 8, 2016.
- [12] S. J. Brodsky, “New insights into color confinement, hadron dynamics, spectroscopy, and jet hadronization from light-front holography and superconformal algebra,” *Russian Physics Journal*, vol. 60, no. 3, pp. 399–416, 2017.

- [13] P. A. Dirac, “Forms of relativistic dynamics,” *Reviews of Modern Physics*, vol. 21, pp. 392–399, 1949.
- [14] S. J. Brodsky, H.-C. Pauli, and S. S. Pinsky, “Quantum chromodynamics and other field theories on the light cone,” *Physics Reports*, vol. 301, no. 4-6, pp. 299–486, 1998.
- [15] H. Reinhardt, “Wilson loop in light-front quantization,” *Physical Review D*, vol. 95, no. 4, article 045015, 2017.
- [16] J. Terrell, “Invisibility of the Lorentz contraction,” *Physical Review A: Atomic, Molecular and Optical Physics*, vol. 116, no. 4, pp. 1041–1045, 1959.
- [17] R. Penrose, “The apparent shape of a relativistically moving sphere,” *Proceedings of the Cambridge Philosophical Society*, vol. 55, pp. 137–139, 1959.
- [18] R. Haag, J. T. Lopuszanski, and M. Sohnius, “All possible generators of supersymmetries of the S-matrix,” *Nuclear Physics B*, vol. 88, pp. 257–274, 1975.
- [19] S. Fubini and E. Rabinovici, “Superconformal quantum mechanics,” *Nuclear Physics B*, vol. 245, no. C, pp. 17–44, 1984.
- [20] G. 't Hooft, “Minimal Strings for Baryons,” <https://arxiv.org/abs/hep-th/0408148>.
- [21] T. Liu and B. Q. Ma, “Baryon properties from light-front holographic QCD,” *Physical Review D*, vol. 92, no. 9, article 096003, 2015.
- [22] H. G. Dosch, G. F. de Téramond, and S. J. Brodsky, “Supersymmetry across the light and heavy-light hadronic spectrum II,” *Physical Review D*, vol. 95, no. 3, article 034016, 2017.
- [23] S. J. Brodsky, M. Diehl, and D. S. Hwang, “Light-cone wavefunction representation of deeply virtual compton scattering,” *Nuclear Physics B*, vol. 596, no. 1-2, pp. 99–124, 2001.
- [24] S. J. Brodsky, D. S. Hwang, B. Q. Ma, and I. Schmidt, “Light-cone representation of the spin and orbital angular momentum of relativistic composite systems,” *Nuclear Physics B*, vol. 593, pp. 311–335, 2001.
- [25] I. Y. Kobzarev and L. B. Okun, “Gravitational interaction of fermions,” *Soviet Physics—Journal of Experimental and Theoretical Physics*, vol. 16, pp. 1343–1346, 1963.
- [26] O. V. Teryaev, “Spin structure of nucleon and equivalence principle,” <https://arxiv.org/abs/hep-ph/9904376>.
- [27] S. J. Brodsky, F. Cao, and G. F. de Téramond, “Evolved QCD predictions for the meson-photon transition form factors,” *Physical Review D: Particles, Fields, Gravitation and Cosmology*, vol. 84, no. 3, article 075012, 2011.
- [28] J. R. Forshaw and R. Sandapen, “AdS/QCD holographic wave function for the ρ Meson and diffractive ρ Meson electroproduction,” *Physical Review Letters*, vol. 109, no. 8, article 081601, 2012.
- [29] S. J. Brodsky, G. F. de Téramond, H. G. Dosch, and J. Erlich, “Light-front holographic QCD and emerging confinement,” *Physics Reports*, vol. 584, pp. 1–105, 2015.
- [30] T. Gutsche, V. E. Lyubovitskij, I. Schmidt, and A. Vega, “Nuclear physics in soft-wall AdS/QCD: deuteron electromagnetic form factors,” *Physical Review D*, vol. 91, no. 11, article 114001, 2015.
- [31] T. Gutsche, V. E. Lyubovitskij, and I. Schmidt, “Deuteron electromagnetic structure functions and polarization properties in soft-wall AdS/QCD,” *Physical Review D*, vol. 94, no. 11, article 116006, 2016.
- [32] G. F. de Téramond and S. J. Brodsky, “Light-front holography: a first approximation to QCD,” *Physical Review Letters*, vol. 102, no. 8, article 081601, 2009.
- [33] A. V. Smirnov, V. A. Smirnov, and M. Steinhauser, “Three-loop static potential,” *Physical Review Letters*, vol. 104, no. 11, article 112002, 2010.
- [34] D. Ashery, “Measurement of light-cone wave functions by diffractive dissociation,” *Nuclear Physics B—Proceedings Supplements*, vol. 108, pp. 321–326, 2002.
- [35] P. P. Srivastava and S. J. Brodsky, “Light-front formulation of the standard model,” *Physical Review D: Particles, Fields, Gravitation and Cosmology*, vol. 66, no. 4, article 045019, 2002.
- [36] V. N. Gribov and L. N. Lipatov, “Deep inelastic ep scattering in perturbation theory,” *Soviet Journal of Nuclear Physics*, vol. 15, no. 4, pp. 438–450, 1972.
- [37] G. Altarelli and G. Parisi, “Asymptotic freedom in parton language,” *Nuclear Physics B*, vol. 126, no. 2, pp. 298–318, 1977.
- [38] Y. L. Dokshitzer, “Calculation of the structure functions for deep inelastic scattering and e^+e^- annihilation by perturbation theory in quantum chromodynamics,” *Journal of Experimental and Theoretical Physics*, vol. 73, pp. 1216–1240, 1977.
- [39] G. P. Lepage and S. J. Brodsky, “Exclusive processes in quantum chromodynamics: evolution equations for hadronic wave functions and the form-factors of mesons,” *Physics Letters*, vol. 87B, no. 359, 1979.
- [40] G. P. Lepage and S. J. Brodsky, “Exclusive processes in perturbative quantum chromodynamics,” *Physical Review D: Particles, Fields, Gravitation and Cosmology*, vol. 22, article 2157, 1980.
- [41] A. V. Efremov and A. V. Radyushkin, “Factorization and asymptotical behavior of pion form-factor in QCD,” *Physics Letters*, vol. 94B, no. 245, 1980.
- [42] A. V. Efremov and A. V. Radyushkin, “Asymptotical behavior of pion electromagnetic form-factor in QCD,” *Theoretical and Mathematical Physics*, vol. 42, no. 147, 1980.
- [43] S. J. Brodsky and S. Gardner, “Comment on ‘New limits on intrinsic charm in the nucleon from global analysis of parton distributions,’” *Physical Review Letters*, vol. 116, no. 1, article 019101, 2016.
- [44] H.-C. Pauli and S. J. Brodsky, “Solving field theory in one space and one time dimension,” *Physical Review D: Particles, Fields, Gravitation and Cosmology*, vol. 32, no. 8, pp. 1993–2000, 1985.
- [45] K. Hornbostel, S. J. Brodsky, and H.-C. Pauli, “Light-cone-quantized QCD in $1 + 1$ dimensions,” *Physical Review D: Particles, Fields, Gravitation and Cosmology*, vol. 41, no. 12, pp. 3814–3821, 1990.
- [46] J. P. Vary, X. Zhao, A. Ilderton, H. Honkanen, P. Maris, and S. J. Brodsky, “Applications of basis light-front quantization to QED,” *Nuclear Physics B—Proceedings Supplements*, vol. 251-252, no. 10, 2014.
- [47] S. J. Brodsky, A. L. Deshpande, H. Gao, R. D. McKeown, C. A. Meyer et al., “QCD and hadron physics,” <https://arxiv.org/abs/1502.05728>.
- [48] J. P. Vary, X. Zhao, A. Ilderton, H. Honkanen, P. Maris, and S. J. Brodsky, “Basis light-front quantization: a new approach to non-perturbative scattering and time-dependent production processes,” *Acta Physica Polonica B Proceedings Supplement*, vol. 6, no. 257, 2013.
- [49] D. Ashery, “Measurement of the photon light-cone wave function by diffractive dissociation,” *Nuclear Physics B—Proceedings Supplements*, vol. 161, pp. 8–14, 2006.
- [50] S. J. Brodsky, C. Ji, and G. P. Lepage, “Quantum chromodynamic predictions for the deuteron form factor,” *Physical Review Letters*, vol. 51, no. 83, 1983.

- [51] C. Cruz-Santiago, P. Kotko, and A. M. Staśto, “Scattering amplitudes in the light-front formalism,” *Progress in Particle and Nuclear Physics*, vol. 85, pp. 82–131, 2015.
- [52] K. Y. J. Chiu and S. J. Brodsky, “Angular momentum conservation law in light-front quantum field theory,” *Physical Review D*, vol. 95, no. 6, article 065035, 2017.
- [53] S. J. Brodsky, R. Roskies, and R. Suaya, “Quantum electrodynamics and renormalization theory in the infinite-momentum frame,” *Physical Review D: Particles, Fields, Gravitation and Cosmology*, vol. 8, no. 12, pp. 4574–4594, 1973.
- [54] S. J. Brodsky and G. F. de Téramond, “Light-front holography and QCD hadronization at the amplitude level,” <https://arxiv.org/abs/0901.0770>.
- [55] R. L. Jaffe, “The axial anomaly and the sum rules for spin dependent electroproduction,” *Physics Letters B*, vol. 193, no. 101, 1987.
- [56] S. J. Brodsky, C. D. Roberts, R. Shrock, and P. C. Tandy, “Confinement contains condensates,” *Physical Review C: Nuclear Physics*, vol. 85, article 065202, 2012.
- [57] A. Zee, “Dark energy and the cosmological constant paradox,” *Modern Physics Letters A*, vol. 23, no. 1336, 2008.
- [58] H. Reinhardt and H. Weigel, “Vacuum nature of the QCD condensates,” *Physical Review D*, vol. 85, no. 7, article 074029, 2012.
- [59] A. Casher and L. Susskind, “Chiral magnetism (or magneto-hydrochironics),” *Physical Review D: Particles, Fields, Gravitation and Cosmology*, vol. 9, article 436, 1974.
- [60] S. J. Brodsky and R. Shrock, “Condensates in quantum chromodynamics and the cosmological constant,” *Proceedings of the National Academy of Sciences*, vol. 108, pp. 45–50, 2011.
- [61] S. J. Brodsky, C. D. Roberts, R. Shrock, and P. C. Tandy, “New perspectives on the quark condensate,” *Physical Review C: Nuclear Physics*, vol. 82, article 022201, 2010.
- [62] E. P. Verlinde, “Emergent gravity and the dark universe,” 2017, <https://arxiv.org/abs/1611.02269>.
- [63] G. Grunberg, “Renormalization scheme independent QCD and QED: the method of effective charges,” *Physical Review D*, vol. 29, no. 10, pp. 2315–2338, 1984.
- [64] S. J. Brodsky and H. J. Lu, “Commensurate scale relations in quantum chromodynamics,” *Physical Review D: Particles, Fields, Gravitation and Cosmology*, vol. 51, pp. 3652–3668, 1995.
- [65] S. J. Brodsky, G. F. de Téramond, and A. Deur, “Nonperturbative QCD coupling and its β function from light-front holography,” *Physical Review D: Particles, Fields, Gravitation and Cosmology*, vol. 81, article 096010, 2010.
- [66] A. Deur, V. Burkert, J. Chen, and W. Korsch, “Experimental determination of the effective strong coupling constant,” *Physics Letters B*, vol. 650, pp. 244–248, 2007.
- [67] A. Deur, S. J. Brodsky, and G. F. de Téramond, “Connecting the hadron mass scale to the fundamental mass scale of quantum chromodynamics,” *Physics Letters B*, vol. 750, pp. 528–532, 2015.
- [68] K. A. Olive, K. Agashe, C. Amsler, and Particle Data Group, “Review of particle physics,” *Chinese Physics C*, vol. 38, no. 9, Article ID 090001, 2014.
- [69] A. Zee, “Quantum field theory in a nutshell,” Princeton, UK: Princeton University Pr. 576 p, 2010.
- [70] M. Mojaza, S. J. Brodsky, and X. Wu, “Systematic all-orders method to eliminate renormalization-scale and scheme ambiguities in Perturbative QCD,” *Physical Review Letters*, vol. 110, article 192001, 2013.
- [71] S. J. Brodsky and S. D. Drell, “Anomalous magnetic moment and limits on fermion substructure,” *Physical Review D: Particles, Fields, Gravitation and Cosmology*, vol. 22, no. 9, article 2236, 1980.
- [72] S. Liuti, A. Rajan, A. Courtoy, G. R. Goldstein, and J. O. G. Hernandez, “Partonic picture of generalized transverse momentum distributions,” *International Journal of Modern Physics: Conference Series*, vol. 25, article 1460009, 2014.
- [73] C. Mondal and D. Chakrabarti, “Generalized parton distributions and transverse densities in a light-front quark-diquark model for the nucleons,” *The European Physical Journal C*, vol. 75, no. 6, article 261, 2015.
- [74] C. Lorcé, B. Pasquini, and M. Vanderhaeghen, “Unified framework for generalized and transverse-momentum dependent parton distributions within a 3Q light-cone picture of the nucleon,” *Journal of High Energy Physics*, vol. 1105, no. 041, 2011.
- [75] S. J. Brodsky, “Dynamic versus static structure functions and novel diffractive effects in QCD,” *AIP Conference Proceedings*, vol. 1105, no. 315, 2009.
- [76] S. J. Brodsky, “Dynamic versus static hadronic structure functions,” *Nuclear Physics A*, vol. 827, no. 327C, 2009.
- [77] S. J. Brodsky, D. S. Hwang, and I. Schmidt, “Final-state interactions and single-spin asymmetries in semi-inclusive deep inelastic scattering,” *Physics Letters B*, vol. 530, pp. 99–107, 2002.
- [78] S. J. Brodsky, P. Hoyer, N. Marchal, S. Peigné, and F. Sannino, “Structure functions are not parton probabilities,” *Physical Review D: Particles, Fields, Gravitation and Cosmology*, vol. 65, article 114025, 2002.
- [79] S. J. Brodsky, B. Pasquini, B. Xiao, and F. Yuan, “Phases of augmented hadronic light-front wave functions,” *Physics Letters B*, vol. 687, pp. 327–330, 2010.
- [80] S. J. Brodsky, D. S. Hwang, Y. V. Kovchegov, I. Schmidt, and M. D. Sievert, “Single-spin asymmetries in semi-inclusive deep inelastic scattering and Drell-Yan processes,” *Physical Review D: Particles, Fields, Gravitation and Cosmology*, vol. 88, no. 1, article 014032, 2013.
- [81] S. J. Brodsky and H. J. Lu, “Shadowing and antishadowing of nuclear structure functions,” *Physical Review Letters*, vol. 64, article 1342, 1990.
- [82] S. J. Brodsky, I. Schmidt, and J. Yang, “Nuclear antishadowing in neutrino deep inelastic scattering,” *Physical Review D: Particles, Fields, Gravitation and Cosmology*, vol. 70, article 116003, 2004.
- [83] I. Schienbein, J. Y. Yu, C. Keppel, J. G. Morfin, F. Olness, and J. F. Owens, “Nuclear parton distribution functions from neutrino deep inelastic scattering,” *Physical Review D: Particles, Fields, Gravitation and Cosmology*, vol. 77, article 054013, 2008.
- [84] R. S. Fufian, G. F. de Téramond, S. J. Brodsky, A. Deur, and H. G. Dosch, “Analysis of nucleon electromagnetic form factors from light-front holographic QCD: The spacelike region,” *Physical Review D: Particles, Fields, Gravitation and Cosmology*, vol. 95, no. 1, article 014011, 2017.

Review Article

Hamiltonian Approach to QCD in Coulomb Gauge: A Survey of Recent Results

H. Reinhardt , **G. Burgio**, **D. Campagnari**, **E. Ebadati**, **J. Heffner**, **M. Quandt**,
P. Vastag, and **H. Vogt**

Institut für Theoretische Physik, Universität Tübingen, Auf der Morgenstelle 14, 72076 Tübingen, Germany

Correspondence should be addressed to H. Reinhardt; h.reinhardt@uni-tuebingen.de

Received 6 June 2017; Revised 4 September 2017; Accepted 2 October 2017; Published 19 February 2018

Academic Editor: Ralf Hofmann

Copyright © 2018 H. Reinhardt et al. This is an open access article distributed under the Creative Commons Attribution License, which permits unrestricted use, distribution, and reproduction in any medium, provided the original work is properly cited. The publication of this article was funded by SCOAP³.

We report on recent results obtained within the Hamiltonian approach to QCD in Coulomb gauge. Furthermore this approach is compared to recent lattice data, which were obtained by an alternative gauge-fixing method and which show an improved agreement with the continuum results. By relating the Gribov confinement scenario to the center vortex picture of confinement, it is shown that the Coulomb string tension is tied to the spatial string tension. For the quark sector, a vacuum wave functional is used which explicitly contains the coupling of the quarks to the transverse gluons and which results in variational equations which are free of ultraviolet divergences. The variational approach is extended to finite temperatures by compactifying a spatial dimension. The effective potential of the Polyakov loop is evaluated from the zero-temperature variational solution. For pure Yang–Mills theory, the deconfinement phase transition is found to be second order for SU(2) and first order for SU(3), in agreement with the lattice results. The corresponding critical temperatures are found to be 275 MeV and 280 MeV, respectively. When quarks are included, the deconfinement transition turns into a crossover. From the dual and chiral quark condensate, one finds pseudocritical temperatures of 198 MeV and 170 MeV, respectively, for the deconfinement and chiral transition.

1. Introduction

One of the most challenging problems in particle physics is the understanding of the phase diagram of strongly interacting matter. By means of ultrarelativistic heavy ion collisions the properties of hadronic matter at high temperature and/or density can be explored. From the theoretical point of view we have access to the finite-temperature behavior of QCD by means of lattice Monte-Carlo calculations. Due to the sign problem, this method fails, however, to describe baryonic matter at high density or, more technically, QCD at large chemical baryon potential [1]. Therefore, alternative, nonperturbative approaches to QCD which do not rely on the lattice formulation and hence do not suffer from the notorious sign problem are desirable. In recent years, much effort has been devoted to develop nonperturbative continuum approaches. These are based on either Dyson–Schwinger equations [2–7] or functional renormalization group flow equations [8, 9], or

they exploit the variational principle in either the Hamiltonian [10, 11] or covariant [12, 13] formulation of gauge theory. There are also semiphenomenological approaches assuming a massive gluon propagator [14] or the Gribov–Zwanziger action [15]; see [16].

In this talk, I will review some recent results obtained within the Hamiltonian approach to QCD in Coulomb gauge both at zero and at finite temperatures; for earlier reviews, see [17, 18]. After a short introduction to the basic features of this approach, I will summarize the essential zero-temperature results for pure Yang–Mills theory and compare them to recent lattice data which were obtained by an alternative gauge-fixing method, which is expected to yield results closer to the continuum theory. After that, I will show by means of lattice calculations that the so-called Coulomb string tension is linked not to the temporal but to the spatial string tension. In this context, I will demonstrate that the Gribov–Zwanziger confinement scenario is related to the

center vortex picture of confinement. I will then report on new variational calculations carried out for the quark sector of QCD. After that I will extend the Hamiltonian approach to QCD in Coulomb gauge to finite temperatures by compactifying a spatial dimension [19]. Numerical results will be given for the Polyakov loop and the chiral and dual quark condensates. Finally, I will give some outlook on future research within the Hamiltonian approach.

2. Variational Hamiltonian Approach to Yang–Mills Theory

For pedagogical reason let me first summarize the basic features of the Hamiltonian approach in Coulomb gauge for pure Yang–Mills theory. The Hamiltonian approach to Yang–Mills theory starts from Weyl gauge $A_0(\mathbf{x}) = 0$ and considers the spatial components of the gauge field $A_i^a(\mathbf{x})$ as coordinates. The momenta are introduced in the standard fashion $\Pi_i^a(\mathbf{x}) = \delta S_{\text{YM}}[A]/\delta \dot{A}_i^a(\mathbf{x}) = -E_i^a(\mathbf{x})$ and turn out to be the color electric field $\mathbf{E}^a(\mathbf{x})$. The classical Yang–Mills Hamiltonian is then obtained as

$$H = \frac{1}{2} \int d^3x (\mathbf{E}^2(\mathbf{x}) + \mathbf{B}^2(\mathbf{x})), \quad (1)$$

where

$$B_k^a(\mathbf{x}) = \varepsilon_{klm} \left(\partial_l A_m^a(\mathbf{x}) - \frac{g}{2} f^{abc} A_l^b(\mathbf{x}) A_m^c(\mathbf{x}) \right) \quad (2)$$

is the non-Abelian color magnetic field with g being the coupling constant. The theory is quantized by replacing the classical momentum Π_i^a with the operator $\Pi_i^a(\mathbf{x}) = -i\delta/\delta A_i^a(\mathbf{x})$. The central issue is then to solve the Schrödinger equation $H\phi[A] = E\phi[A]$ for the vacuum wave functional $\phi[A]$. Due to the use of Weyl gauge, Gauß's law $\widehat{\mathbf{D}} \cdot \mathbf{\Pi}\phi[A] = 0$ (with $\widehat{\mathbf{D}} = \partial + g\mathbf{A}$ being the covariant derivative in the adjoint representation) has to be put as a constraint on the wave functional, which ensures the gauge invariance of the latter. Instead of working with explicitly gauge invariant states, it is more convenient to fix the gauge and explicitly resolve Gauß's law in the chosen gauge. This has the advantage that any (normalizable) wave functional $\phi[A]$ is physically admissible for a variational approach, while the price to pay is a significant complication of the gauge-fixed Hamiltonian. A particular convenient choice of gauge for this method turns out to be Coulomb gauge $\partial \cdot \mathbf{A} = 0$.

After canonical quantization in Weyl gauge $A_0 = 0$ and resolution of Gauß's law in Coulomb gauge $\partial \cdot \mathbf{A} = 0$ one finds the following gauge-fixed Hamiltonian [20]:

$$H = H_T + H_C \quad (3)$$

with

$$H_T = \frac{1}{2} \int d^3x \left(J^{-1}[A] \mathbf{\Pi}^a(\mathbf{x}) \cdot J[A] \mathbf{\Pi}^a(\mathbf{x}) + \mathbf{B}^a(\mathbf{x}) \cdot \mathbf{B}^a(\mathbf{x}) \right), \quad (4)$$

where

$$J[A] = \text{Det}(-\widehat{\mathbf{D}} \cdot \partial) \quad (5)$$

is the Faddeev–Popov determinant and

$$H_C = \frac{g^2}{2} \int d^3x \int d^3y J[A]^{-1} \rho^a(\mathbf{x}) J[A] \cdot \left[(-\widehat{\mathbf{D}} \cdot \partial)^{-1} (-\partial^2) (-\widehat{\mathbf{D}} \cdot \partial)^{-1} \right]^{ab}(\mathbf{x}, \mathbf{y}) \rho^b(\mathbf{y}) \quad (6)$$

is the so-called Coulomb term with the color charge density

$$\begin{aligned} \rho^a(\mathbf{x}) &= f^{abc} \mathbf{A}^b(\mathbf{x}) \cdot \mathbf{\Pi}^c(\mathbf{x}) + \rho_m^a(\mathbf{x}) \\ &\equiv \rho_{\text{YM}}^a(\mathbf{x}) + \rho_m^a(\mathbf{x}). \end{aligned} \quad (7)$$

This expression contains besides the charge density of the matter fields ρ_m^a also a purely gluonic part. Due to the implementation of Coulomb gauge, the scalar product in the Hilbert space of wave functionals $\phi[A] = \langle A | \phi \rangle$ is defined by

$$\langle \phi | \cdots | \psi \rangle = \int \mathcal{D}AJ[A] \phi^*[A] \cdots \psi[A]. \quad (8)$$

Here, the functional integration is over transverse spatial gauge fields and the Faddeev–Popov determinant $J[A]$ appears due to Coulomb gauge fixing with the standard Faddeev–Popov method. The Faddeev–Popov determinant (5) in the integration measure represents the Jacobian of the change of variables from “Cartesian” to “curvilinear” variables in Coulomb gauge. With the gauge-fixed Hamiltonian (3) one has to solve the stationary Schrödinger equation $H\phi[A] = E\phi[A]$ for the vacuum wave functional $\phi[A]$. Once $\phi[A]$ is known, all observables and correlation functions can, in principle, be calculated. This has been attempted by means of the variational principle using Gaussian type ansatz for the vacuum wave functional [21, 22]. However, the first attempts did not properly include the Faddeev–Popov determinant, which turns out to be crucial in order to describe the confinement properties of the theory. Below, I will discuss the variational approach developed in [10, 11], which differs from previous attempts by the ansatz for the vacuum wave functional, the treatment of the Faddeev–Popov determinant and, equally important, by the renormalization; see [23] for further details.

2.1. Variational Solution of the Schrödinger Equation. The ansatz for the vacuum wave functional is inspired by the quantum mechanics of a particle in a spherically symmetric potential for which the ground state wave function is given by $\phi(r) = u(r)/r$, where the radial wave functional $u(r)$ satisfies a standard one-dimensional Schrödinger equation and r represents (the square root of the radial part of) the Jacobian of the transformation from the Cartesian to spherical coordinates. Our ansatz for the vacuum wave functional is given by

$$\begin{aligned} \phi_{\text{YM}}[A] &= \frac{1}{\sqrt{J[A]}} \\ &\cdot \exp \left[-\frac{1}{2} \int d^3x \int d^3y A_k^a(\mathbf{x}) \omega(\mathbf{x}, \mathbf{y}) A_k^a(\mathbf{y}) \right] \\ &\equiv \frac{1}{\sqrt{J[A]}} \tilde{\phi}_{\text{YM}}[A]. \end{aligned} \quad (9)$$



FIGURE 1: Dyson–Schwinger equation for the ghost propagator.

The inclusion of the preexponential factor has the advantage that it eliminates the Faddeev–Popov determinant from the integration measure in the scalar product (8). Furthermore, for the wave function (9), the gluon propagator is given up to a factor of 1/2 by the inverse of the variational kernel $\omega(\mathbf{x}, \mathbf{y})$. As the numerical calculation shows [24] in the Yang–Mills sector the Coulomb term H_C (6) can be ignored. The reason is the presence of the Faddeev–Popov determinant in the pure Yang–Mills term of H_C (see (6)), which ensures that in the numerator of the expectation value the gluon energy $\omega(\mathbf{p})$ occurs only in the combination $\omega(\mathbf{p}) - \chi(\mathbf{p})$ (see [10]), which is infrared vanishing. The Faddeev–Popov determinant $J[A]$, however, drops out from H_C in the quark sector, since $J[A]$ commutes with the charge density $\rho_m^a(\mathbf{x})$ of the quarks; see (31).

Calculating the expectation value of the remaining parts of the Yang–Mills Hamiltonian (4) with the wave functional (9) up to two loops, the minimization of the energy density with respect to $\omega(\mathbf{x}, \mathbf{y})$ yields the following gap equation in momentum space (Due to translational and rotational invariance, kernels such as $\omega(\mathbf{x}, \mathbf{y})$ can be Fourier transformed as $\omega(\mathbf{x}, \mathbf{y}) = \int (d^3k/(2\pi)^3) e^{i\mathbf{k}\cdot(\mathbf{x}-\mathbf{y})} \omega(k)$ where the new kernel in momentum space depends on $k = |\mathbf{k}|$ only. For simplicity, we will use the same symbol for the kernel in position and momentum space and go back and forth between both representations with impunity.):

$$\omega^2(k) = \mathbf{k}^2 + \chi^2(k) + c, \quad (10)$$

where c is a finite renormalization constant resulting from the tadpole and

$$\begin{aligned} \chi_{kl}^{ab}(\mathbf{x}, \mathbf{y}) &= -\frac{1}{2} \left\langle \phi \left| \frac{\delta^2 \ln J[A]}{\delta A_k^a(\mathbf{x}) \delta A_l^b(\mathbf{y})} \right| \phi \right\rangle \\ &= \delta^{ab} t_{kl}(\mathbf{x} - \mathbf{y}) \chi(\mathbf{x} - \mathbf{y}) \end{aligned} \quad (11)$$

represents the ghost loop ($t_{kl}(\mathbf{x}) = \delta_{kl} - \partial_k \partial_l / \partial^2$ is the transverse projector). This can be expressed in terms of the ghost propagator:

$$G(\mathbf{x}, \mathbf{y}) = \left\langle \phi \left| (-\widehat{\mathbf{D}} \cdot \partial)^{-1}(\mathbf{x}, \mathbf{y}) \right| \phi \right\rangle, \quad (12)$$

which is evaluated with the vacuum wave functional (9) in the rainbow-ladder approximation, resulting in a Dyson–Schwinger equation for the form factor

$$d(\mathbf{k}) = g\mathbf{k}^2 G(\mathbf{k}) \quad (13)$$

of the ghost propagator which is diagrammatically illustrated in Figure 1. This equation has to be solved together with the gap equation (10).

Dyson–Schwinger equations are functional differential equations and their solutions are uniquely determined only

after providing appropriate boundary conditions. In the present case, the so-called horizon condition

$$d^{-1}(0) = 0 \quad (14)$$

is assumed, which is the key point in Gribov’s confinement scenario. Its physical implications will be discussed later. The equations given in (10) and Figure 1 can be studied analytically in the infrared using power law ansatz:

$$\begin{aligned} \omega(p) &= Ap^{-\alpha}, \\ d(p) &= Bp^{-\beta}. \end{aligned} \quad (15)$$

Assuming a bare ghost-gluon vertex and the horizon condition (14), one finds, for the IR exponents of gluon and ghost form factor (15), the sum rule

$$\alpha = 2\beta - (d - 2), \quad (16)$$

where d is the number of spatial dimensions (i.e., $d = 3$ is our real world). The coupled gluon gap equation (10) and ghost DSE (Figure 1) allow for a single solution in $d = 2$,

$$\beta = 0.4, \quad (17)$$

and for two solutions in $d = 3$,

$$\begin{aligned} \beta &= 1, \\ \beta &= 0.796. \end{aligned} \quad (18)$$

The numerical solutions of the gluon gap and ghost DSE are shown in Figure 2. The numerical solutions reproduce the result (18) of the IR analysis. At large momenta, the gluon energy $\omega(p)$ approaches the photon energy $|\mathbf{p}|$ in agreement with asymptotic freedom, while $\omega(p)$ diverges like $\sim 1/|\mathbf{p}|$ in the IR, which implies the absence of free gluons in the IR and signals confinement.

Alternative to the variational approach, one can indirectly determine the vacuum wave functional by solving the functional renormalization group flow equations for the various propagators and vertex functions of the Hamiltonian approach. Restricting the flow equations to those for the ghost and gluon propagators, one finds for the ghost form factor the result shown in Figure 3. Starting with a constant ghost form factor in the ultraviolet, the ghost form factor develops an infrared singularity as the momentum cutoff of the flow equation tends to zero. This is nicely seen in Figure 3(b), which shows a cut through Figure 3(a) at fixed renormalization group scale k .

Let us also mention that it is not necessary to assume the horizon condition (14) in the case of $D = 2 + 1$ dimensions, where it is a direct consequence of the coupled equations for the ghost and gluon propagators obtained from the variational principle. Finally, the horizon condition (14) is also seen in the lattice data for the ghost form factor; see Section 3.

2.2. Physical Implications of the Ghost Form Factor. As can be seen from its definition (13), the ghost form factor expresses the deviation of Yang–Mills theory from QED, where the

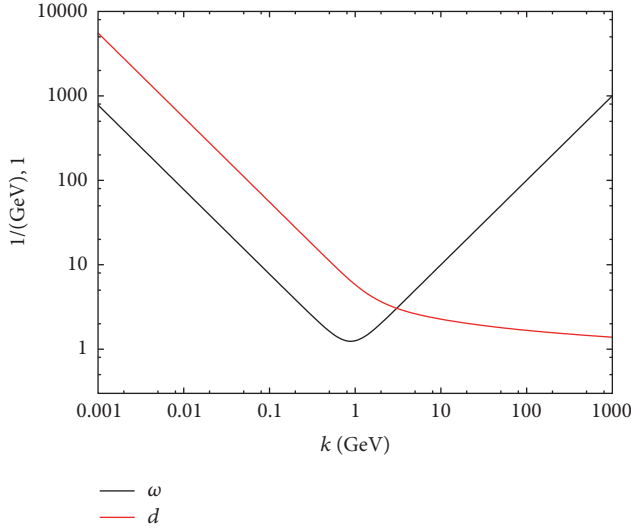


FIGURE 2: Numerical solution of the coupled gap equation for ω (10) and Dyson–Schwinger equation for the ghost form factor d (13) for the renormalization constant $c = 0$ for $d = 3$ spatial dimensions [25]. The scale is fixed by the Coulomb string tension; see Section 4.

Faddeev–Popov operator in Coulomb gauge is given by the Laplacian, that is, the ghost propagator is $G(p) = 1/p^2$.

Coulomb gauge is called a physical gauge since in QED the remaining transverse components are the gauge invariant degrees of freedom. This is not the case for Yang–Mills theory. However, Coulomb gauge can be viewed as a physical gauge also in the case of Yang–Mills theory in the sense that the inverse ghost form factor in Coulomb gauge represents the dielectric function of the Yang–Mills vacuum [32]:

$$\epsilon(k) = d^{-1}(k). \quad (19)$$

The horizon condition (14) guarantees that this function vanishes in the infrared, $\epsilon(k = 0) = 0$. This implies that the Yang–Mills vacuum is a perfect color dielectric, that is, a dual superconductor. In this way, the Hamiltonian approach in Coulomb gauge relates Gribov’s confinement scenario to the dual Meißner effect, a confinement mechanism realized through the condensation of magnetic monopoles and proposed by Mandelstam and ’t Hooft [33, 34]. The dielectric function obtained here as inverse ghost form factor is also in accord with the phenomenological bag model picture of hadrons. Inside the hadron, that is, at small distance, the dielectric function is that of a normal vacuum while outside the physical hadrons the vanishing of the dielectric constant implies the absence of free color charges by Gauß’s law.

3. Comparison with Lattice Calculation

Let us now compare the results of the variational solution with lattice calculations. Figure 4 shows the gluon energy and the ghost form factor in $d = 2$ spatial dimension obtained in the variational approach [27] together with the lattice data [28]. The agreement is in general quite satisfactory, in particular, in the IR and the UV. There are, however, significant deviations in the mid-momentum regime. A similar picture

is obtained in $d = 3$ [35]. Figure 5 shows the static gluon propagator $D = 1/(2\omega)$ in Coulomb gauge obtained in SU(2) gauge theory in $d = 3$. It is remarkable that the lattice data can be nicely fitted by Gribov’s formula [15] (see Figure 7):

$$\omega(p) = \sqrt{p^2 + \frac{M^4}{p^2}}, \quad (20)$$

where M is the so-called Gribov mass. Using a Wilsonian string tension of $\sigma_W = (440 \text{ MeV})^2$ one finds $M \approx 880 \text{ MeV}$. The variational calculations reproduce the infrared behavior of the lattice propagator perfectly and are also in reasonably agreement with the lattice data in the ultraviolet. However, in the mid-momentum regime, some strength is missing in the variational calculation. This missing strength is the result of the Gaussian type ansatz for the vacuum wave functional. In [36], the ansatz for the vacuum wave functional was extended to include also cubic and quartic terms of the gauge field in the exponent of the vacuum wave functional:

$$\phi[A] \sim \exp[-S[A]], \quad (21a)$$

$$S[A] = \frac{1}{2} \int A\omega A + \frac{1}{3!} \int \gamma^{(3)} AAA + \frac{1}{4!} \int \gamma^{(4)} AAAA, \quad (21b)$$

and one finds the full curve in Figure 5, which gives a much better agreement with the lattice data in the mid-momentum regime. Let us stress that the inclusion of the cubic and quartic terms in the exponent of the vacuum wave functional does not change the IR behavior of the gluon propagator, which is determined exclusively by the ghost loop $\chi(\mathbf{p})$.

The lattice calculation of the ghost form factor $d(p)$ (13) is more involved than that of the gluon propagator since it requires the inversion of the Faddeev–Popov operator $(-\hat{\mathbf{D}} \cdot \partial)$, which requires high numerical accuracy for field configurations near the Gribov horizon, where the Faddeev–Popov operator has a very small eigenvalue. It turns out that the lattice results for the ghost form factor depend on how the Coulomb gauge is implemented on the lattice. In principle, this is done by maximizing the gauge-fixing functional

$$F_t[g] = \sum_{\mathbf{x}, i} \text{Re tr } U_i^g(t, \mathbf{x}) \longrightarrow \max \quad (22)$$

with respect to all spatial gauge transformations $g(\mathbf{x})$. In (22) the summation is over all spatial links at a fixed time t and the maximization is performed at all lattice times. In the continuum limit the extremum condition $\delta F[g]/\delta g(\mathbf{x}) = 0$ yields the Coulomb gauge $\partial \cdot \mathbf{A} = 0$.

The lattice gauge-fixing condition yields a gauge copy which lies within the first Gribov region, but usually not within the fundamental modular region composed of those copies which give the *absolute* maximum of the functional (22). Therefore, in practice, one repeatedly performs random gauge transformations and selects in the end, that is, after Coulomb gauge fixing, the gauge copy which yields the largest maximum of the gauge-fixing functional (22). This copy is

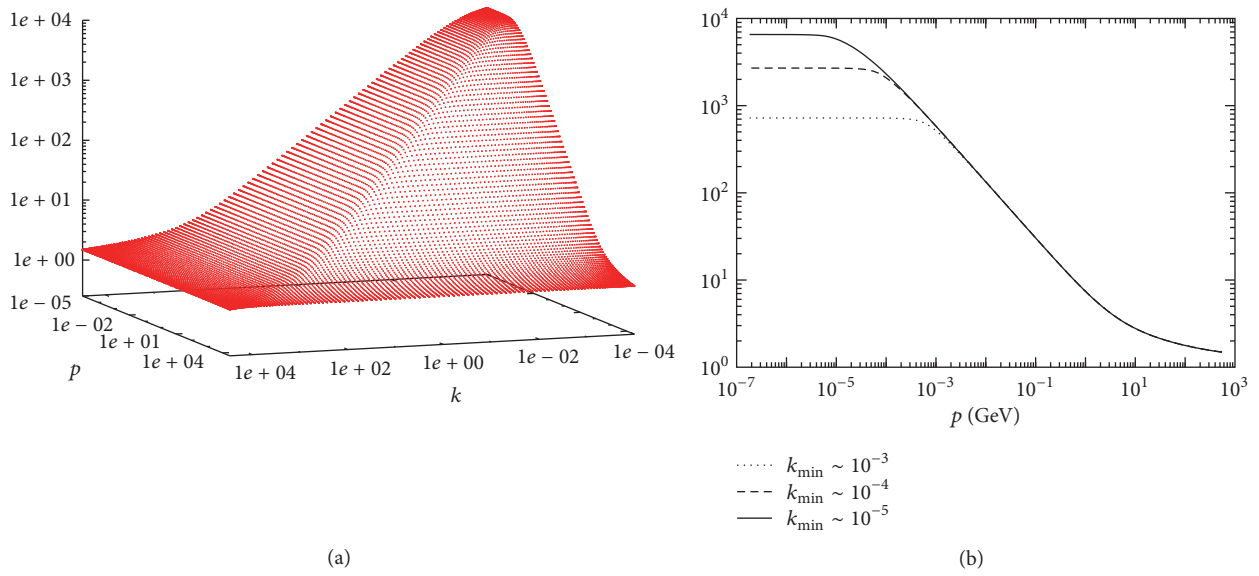


FIGURE 3: (a) The ghost form factor obtained in [26] from the solution of the renormalization group flow equations. Here, p represents the momentum variable of the ghost form factor while k is the infrared momentum cutoff of the flow equations. (b) Cuts through subfigure (a) at various values of the momentum scale k of the flow equations.

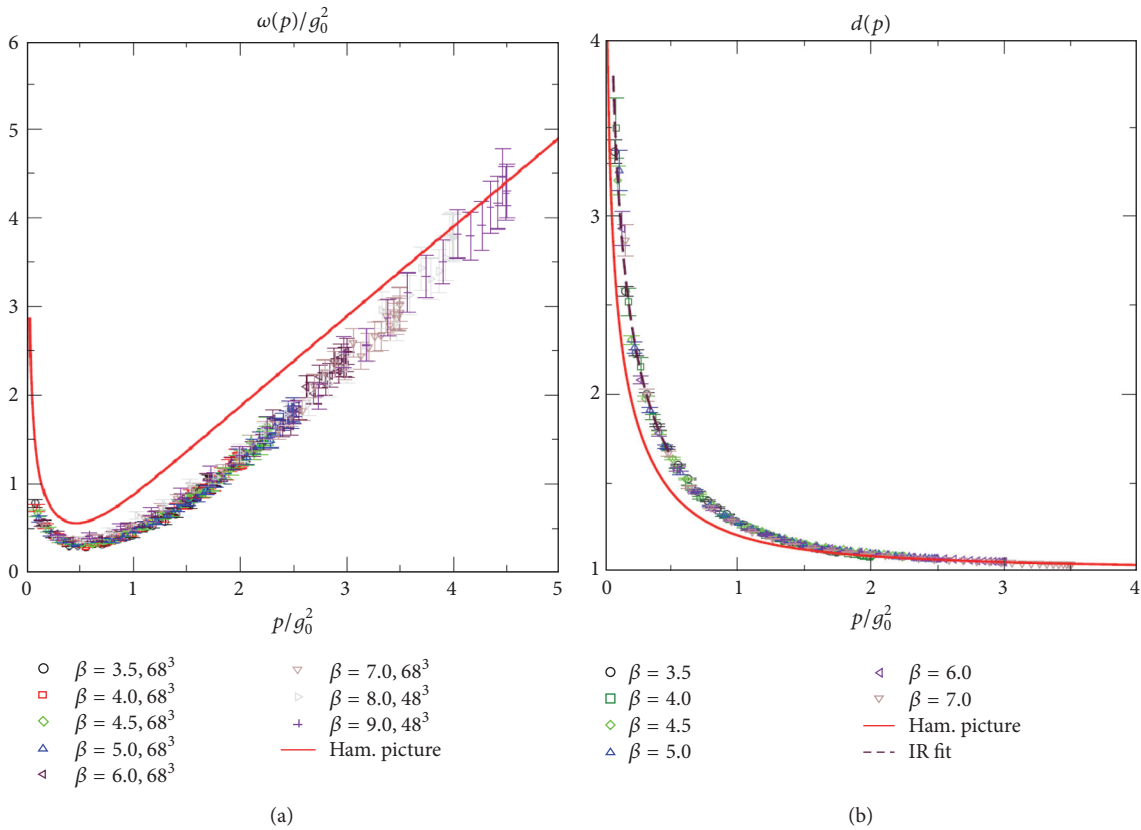


FIGURE 4: Comparison of the variational approach to $(2 + 1)$ -dimensional Yang–Mills theory in Coulomb gauge [27] with the lattice data [28]: (a) gluon energy and (b) ghost form factor.

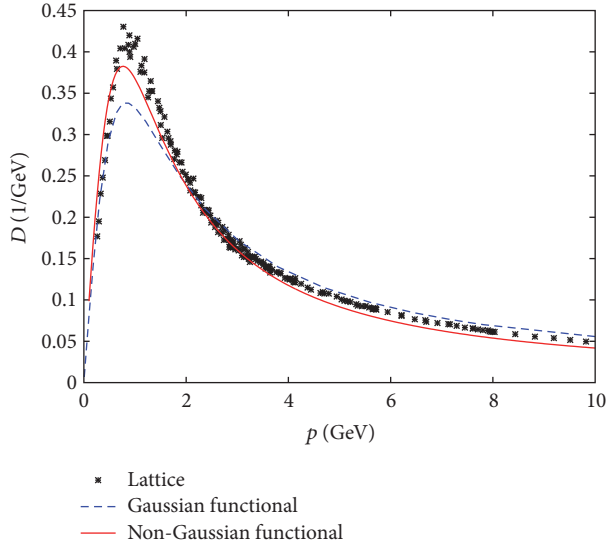


FIGURE 5: The static gluon propagator in Coulomb gauge calculated on the lattice for SU(2) gauge theory (crosses). The dashed and the full curves show the result of the variational calculation using, respectively, a Gaussian and non-Gaussian ansatz for the vacuum wave functional.

called “best copy” since it is assumed that this method yields a gauge copy which is the best representative of the global maximum. Figure 6 shows the result for the ghost form factor using the “best copy” gauge fixing. The obtained ghost form factor has an IR exponent of $\beta \approx 0.5$, which is at odds with the sum rule (16) given that an IR exponent of $\alpha = 1$ is obtained for the lattice gluon propagator; see (20). This result is puzzling since the sum rule is considered incontrovertible as it is obtained under quite mild assumptions. However, in [37], it was shown that for the $U(1)$ lattice gauge theory on S^2 the “best copy” method does not necessarily provide the best approximation to the fundamental modular region. An alternative lattice gauge-fixing method consists in choosing not the “best” Gribov copy but that gauge copy which minimizes the lowest eigenvalue of the Faddeev–Popov operator [38]. This configuration is referred to as the “lowest” Gribov copy. As argued in [39], the “lowest copy” method should yield results closer to the continuum theory. We have used the “lowest copy” (lc) method to recalculate the ghost and gluon propagator; see [40]. While the gluon propagator is basically the same as obtained with the “best copy” (bc) method (see Figure 7), the ghost form factor gets further enhanced in the IR as the number of gauge-fixing attempts increases (see Figure 8). (To find the absolute extremum in the bc and lc approach, we have repeated the gauge-fixing procedure a large number $N_r = 10, \dots, 10000$ of times, starting each time from a different random gauge transformation of the original configuration. In general, the number N_r of gauge-fixing trials is indicative of the number of Gribov copies included, even though the exact relation is complicated and nonlinear [40].) Although we did not find a strict saturation for a sufficiently large number of gauge-fixing attempts, the IR exponent of the ghost form factor is compatible with the

continuum result of $\beta \approx 1$ (see Figure 9), in agreement with the sum rule (16).

4. The Coulomb String Tension

The Coulomb term H_C (6) plays an important role in the Gribov–Zwanziger confinement scenario. Its Yang–Mills vacuum expectation value

$$V_C = g^2 \langle (-\widehat{\mathbf{D}} \cdot \partial)^{-1} (-\partial^2) (-\widehat{\mathbf{D}} \cdot \partial)^{-1} \rangle \quad (23)$$

provides an upper bound for the potential between static point-like color charges and is referred to as (non-Abelian) Coulomb potential. The Coulomb potential found within the variational approach [10, 11, 25] is shown in Figure 10(a). At small distances it behaves like an ordinary Coulomb potential, $V_C(r) \sim 1/r$, and increases linearly at large distances with a coefficient given by the so-called Coulomb string tension σ_C . It was shown in [41] that this quantity is an upper bound to the Wilsonian string tension σ_W . On the lattice one finds $\sigma_C/\sigma_W \approx 2 \dots 4$ [29, 42, 43]. Due to the constraint $\sigma_C \geq \sigma_W$ in the Gribov–Zwanziger confinement scenario a necessary condition for confinement is that the non-Abelian Coulomb potential (23) rises at least linearly at large distances.

One may now ask, what field configurations induce the horizon condition, $d^{-1}(0) = 0$, and the linearly rising Coulomb potential V_C (23) and thus confinement? Given the relation of Gribov’s confinement scenario to the dual superconductor, we expect magnetic monopoles to play a substantial role. Lattice calculations carried out in the so-called indirect maximum center gauge, which contains the maximum Abelian gauge in an intermediate step, showing that magnetic monopoles are tied to center vortices [44]. This can be also understood in the continuum [45]. Center vortices are string-like gauge field configurations in $D = 3$ or world surfaces in $D = 4$, for which the Wilson loop equals a nontrivial center element of the gauge group, provided the loop has nontrivial linking with the center vortices. (By the Bianchi identity center vortices form closed loops in $D = 3$ and closed surfaces in $D = 4$.)

Lattice calculations provide strong evidence that confinement is due to center vortices. Indeed, when the center vortex content of the gauge field configurations is removed, one finds that the Wilsonian string tension and thus confinement disappears [46].

On the lattice center vortices can be detected as follows [47]: one first brings the gauge field configurations into the so-called maximal center gauge:

$$\sum_{x,\mu} |\text{tr} U_\mu^2(x)| \longrightarrow \max, \quad (24)$$

which rotates a link as close as possible to a center element, for example, $Z_\mu(x) = \pm 1 \in Z(2)$ for the gauge group SU(2). Subsequently, one performs a so-called center projection:

$$U_\mu(x) \longrightarrow Z_\mu(x) \quad (25)$$

which replaces each link with its nearest center element. One is then left with $Z(2)$ links, which form closed center

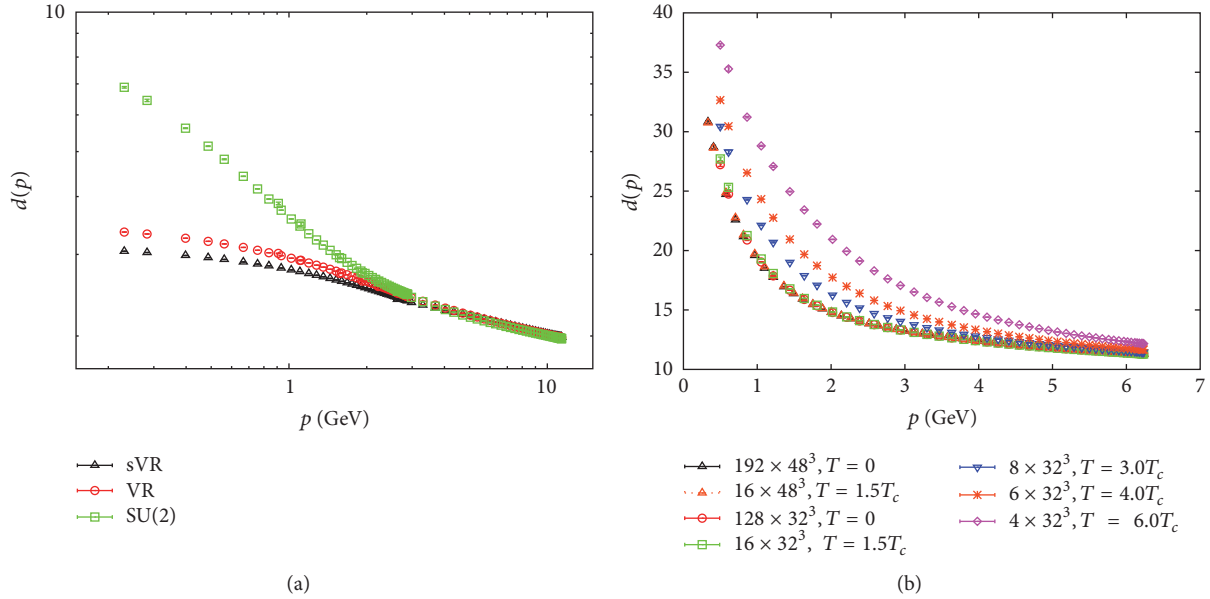


FIGURE 6: (a) The ghost form factor in Coulomb gauge calculated on the lattice in [29] (green squares). The red circles and black triangles show the results obtained for the ghost form factor when all center vortices or only the spatial center vortices are removed from the ensemble of gauge field configurations; see main text. (b) Ghost form factor calculated on the lattice for different temperatures.

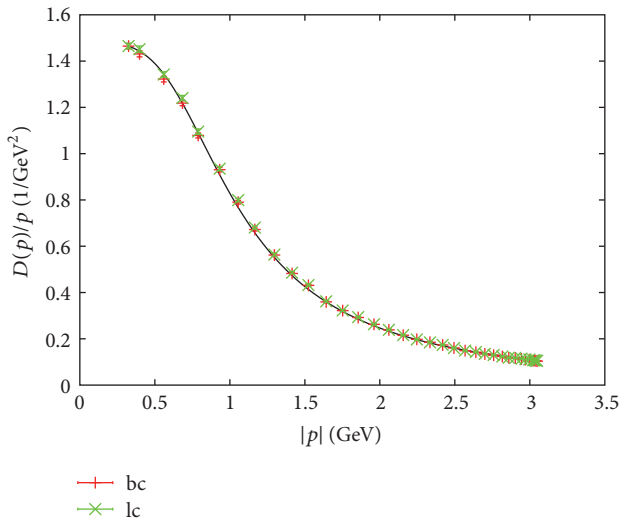


FIGURE 7: The gluon propagator with the bc and the lc approach from 1000 gauge-fixing attempts. The solid line is a fit to the Gribov formula (20). The choice of Gribov copies apparently makes no visible difference.

vortices, the only nontrivial field configurations in a $Z(2)$ theory. When a center vortex pierces a Wilson loop it contributes a nontrivial center element to the latter. It was shown in [48] that the center vortices obtained in this way are physical objects in the sense that they show the proper scaling behavior; that is, their area density survives the continuum limit. This property distinguishes the center vortices found after center projection in the maximal center gauge from other gauges like, for example, the Laplacian center gauge [44].

The center vortex content of a gauge field configuration can be removed [46] by multiplying the original link variable $U_\mu(x)$ by its center projection $Z_\mu(x)$:

$$U_\mu(x) \longrightarrow U_\mu(x) \cdot Z_\mu(x). \quad (26)$$

Figure 6 shows the ghost form factor obtained on the lattice when the center vortices are removed from the ensemble of gauge field configurations as described above [29]. The ghost form factor becomes infrared flat and the horizon condition is lost. This shows that center vortices induce the horizon condition which is the cornerstone of Gribov's confinement scenario. This also shows that Gribov's confinement scenario is tied to the center vortex picture of confinement. This is in accord with the observation that center vortices and magnetic monopoles are located on the Gribov horizon of Coulomb gauge [42].

When center vortices are removed as described above, the static color potential extracted from a Wilson loop loses its linearly rising part; that is, the Wilsonian string tension σ_W disappears after center vortex removal. Since $\sigma_C \geq \sigma_W$ this does not necessarily imply that elimination of center vortices also removes the Coulomb string tension. In [29], the non-Abelian Coulomb potential was calculated after center projection and center vortex removal. Removing the center vortices also eliminates the Coulomb string tension while center vortex projection keeps only the linearly rising part of the non-Abelian Coulomb potential; see Figure 10(b). This result is perhaps not so surprising since center vortices live on the Gribov horizon (more precisely on the common boundary between the Gribov horizon and the fundamental modular region [42]), which represents the domain of the infrared dominant field configurations in the Gribov-Zwanziger confinement scenario.

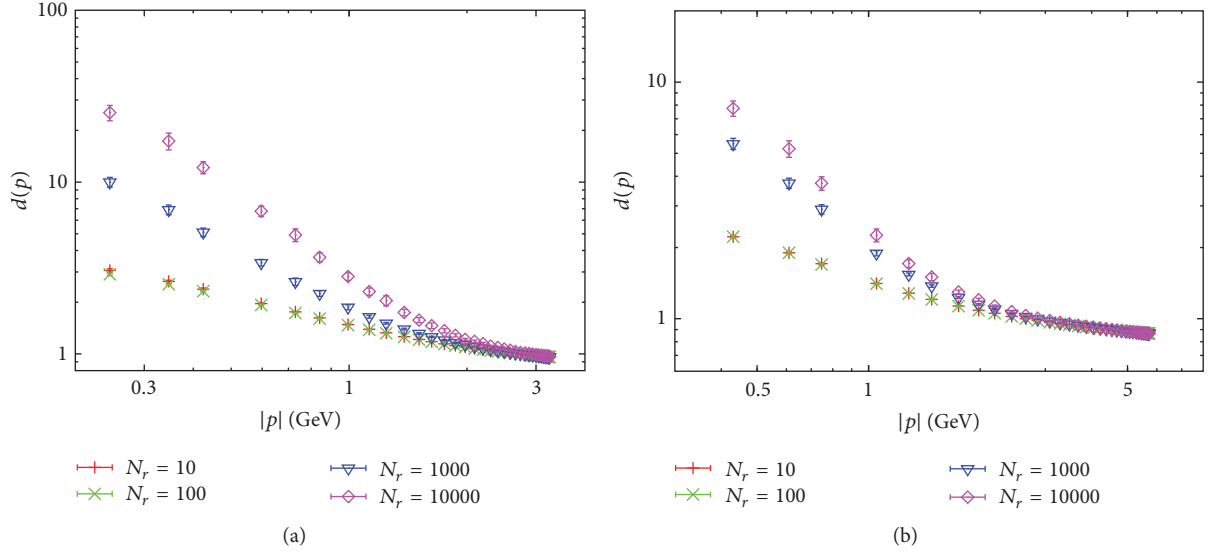


FIGURE 8: The ghost form factor after gauge fixing to the lowest-eigenvalue copy with increasing number of trials from 10 to 10000 on 24^4 lattices at (a) $\beta = 2.2$ and (b) $\beta = 2.4$, where β is the (inverse) lattice coupling constant.

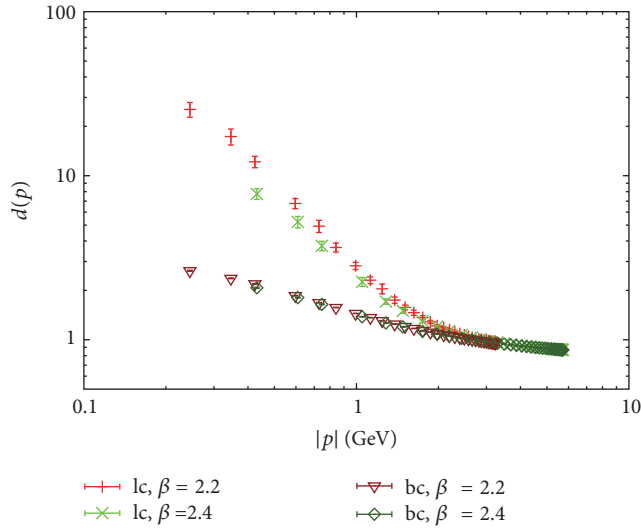


FIGURE 9: The ghost form factor after 10000 copies of bc and lc strategy.

At finite temperature different Wilsonian string tensions are measured from temporal and spatial Wilson loops referred to as temporal and spatial string tension, respectively. Above the deconfinement phase transition these two Wilsonian string tensions decouple. While the spatial string tension increases above the critical temperature, the temporal string tension disappears. On the lattice it is not difficult to see that in the center projected $Z(2)$ theory the temporal and spatial Wilsonian string tensions, that is, the area law in the temporal and spatial Wilson loop, are produced by temporal and spatial center vortices, respectively. The latter are formed exclusively by spatial center-valued links:

$$U_i(x) \longrightarrow Z_i(x), \quad (27)$$

which will be referred to as spatial center projection in the following. (In $D = 3$, spatial center vortices are closed lines formed by a “stack” of spatial plaquettes with nontrivial value after center projection. Geometrically, they extend in the time direction (on the dual lattice) and can thus link with spatial Wilson loops. The terminology in $D = 4$ is similar; that is, spatial center vortices are hypersurfaces on the dual lattice which are composed of spatial plaquettes on the original lattice, which are nontrivial after center projection. Geometrically, such spatial vortices extend in one space and one time direction and may hence link with spatial Wilson loops.) Analogously multiplying the spatial link by its nearest center projected $Z(2)$ element,

$$U_i(x) \longrightarrow U_i(x) \cdot Z_i(x), \quad (28)$$

removes all spatial center vortices and thus the spatial string tension while the temporal links are unaffected. Therefore, the temporal string tension, which can be calculated from the correlator of Polyakov loops and hence from temporal links exclusively, will not be affected by the spatial center vortex removal. Figure 11(a) shows the quantity $p^4 V_C(p)$ whose infrared limit gives the Coulomb string tension, $\lim_{p \rightarrow 0} p^4 V_C(p) = 8\pi\sigma_C$. As one observes, the Coulomb string tension disappears already when only the spatial center vortices are removed. This clearly shows that the Coulomb string tension is related to the spatial string tension and not to the temporal one. This explains also the finite-temperature behavior of the Coulomb string tension, which increases with the temperature above the deconfinement phase transition just like the spatial string tension; see Figure 11(b).

A necessary condition for the Gribov–Zwanziger confinement scenario to be realized is that the ghost form factor is infrared divergent, which is indeed found in the variational approach and also on the lattice; see Figure 6(b). However,

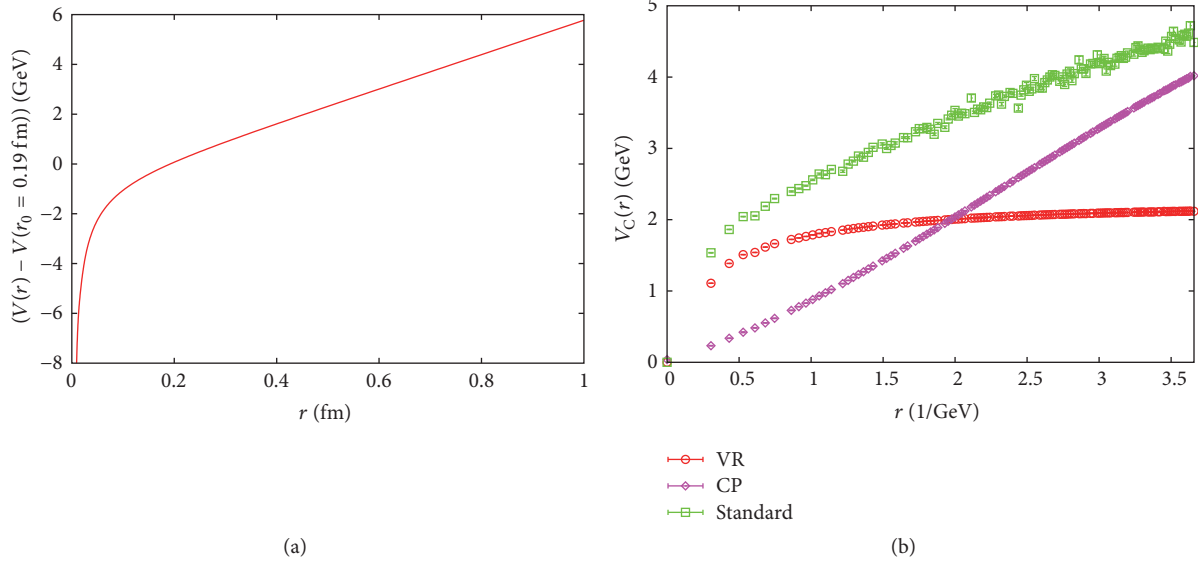


FIGURE 10: (a) Non-Abelian Coulomb potential (23) obtained within the variational approach [25]. (b) Standard non-Abelian Coulomb potential (green boxes) compared to the potential obtained after vortex removal (red circles) and center projection (violet diamonds) [29].

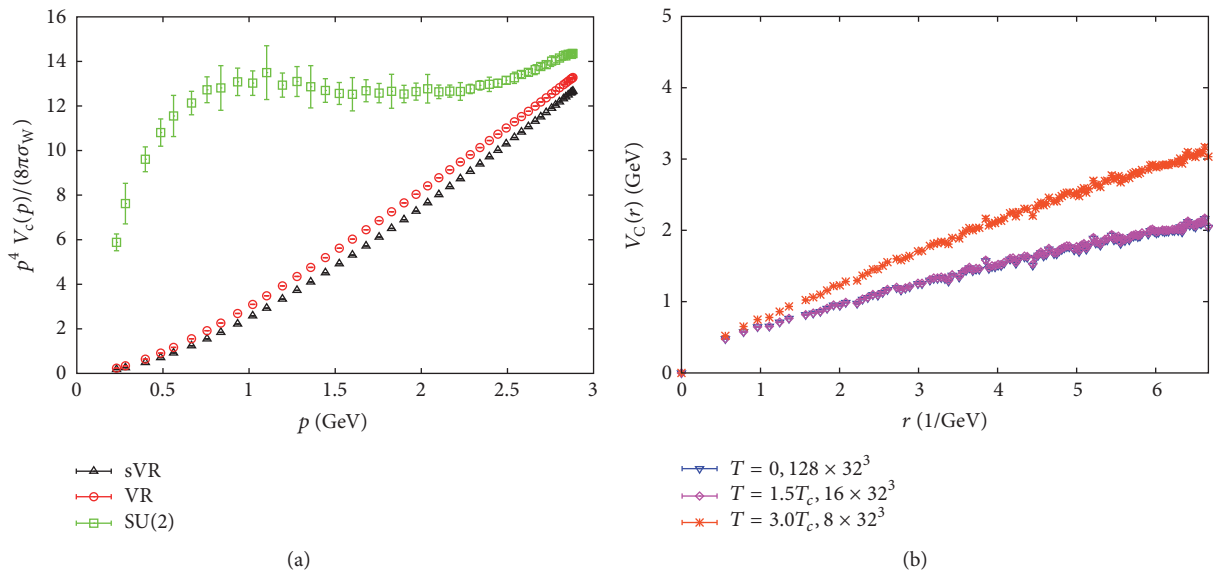


FIGURE 11: (a) Non-Abelian Coulomb potential in momentum space (green boxes) compared to the result obtained after removing just the spatial (black triangles) or all center vortices (red circles). (b) Non-Abelian Coulomb potential for different temperatures (T_c denotes the critical temperature).

the infrared divergence disappears when one removes the center vortices or the spatial center vortices only as can be seen in Figure 6(a). Also, the spatial center vortex projection produces the same ghost form factor as full center projection. This also explains why the infrared divergence of the ghost form factor does not disappear above the deconfinement phase transition. Thus both features of the Gribov–Zwanziger confinement scenario, the infrared divergent ghost form

factor and the linearly rising Coulomb potential, are caused by spatial center vortices and are thus tied to the spatial string tension, which increases above the deconfinement transition.

5. Variational Approach to the Quark Sector

The variational approach to Yang–Mills theory in Coulomb gauge presented in Section 2 has been extended to full QCD

in [30, 49, 50]. The Hamiltonian of full QCD in Coulomb gauge is given by

$$H_{\text{QCD}} = H_{\text{T}} + H_{\text{Q}} + H_{\text{C}}, \quad (29)$$

where H_{T} is the Hamiltonian of the transverse gluon degrees of freedom (4), H_{C} is the Coulomb interaction (6), and

$$H_{\text{Q}} = \int d^3x \psi^\dagger(\mathbf{x}) [\boldsymbol{\alpha} \cdot (-i\nabla + g t^a \mathbf{A}^a(\mathbf{x})) + \beta m_0] \psi(\mathbf{x}) \quad (30)$$

is the Hamiltonian of the quarks coupling to the transverse gluon field. Here, $\boldsymbol{\alpha}$, β are the usual Dirac matrices, t^a denotes the generator of the color group in the fundamental representation, and m_0 is the bare current quark mass (of electroweak origin) which will be neglected in the following. Furthermore, when the quarks are included, the matter charge density in the Coulomb Hamiltonian H_{C} (7) is given by

$$\rho_m^a(\mathbf{x}) = \psi^\dagger(\mathbf{x}) t^a \psi(\mathbf{x}). \quad (31)$$

In [30, 50], the quark sector of QCD has been treated within the variational approach using the following ansatz for the QCD wave functional

$$|\phi[A]\rangle = \mathcal{N} \frac{1}{\sqrt{I[A]}} \phi_{\text{YM}}[A] |\phi_{\text{Q}}[A]\rangle, \quad (32)$$

where ϕ_{YM} is the Yang–Mills vacuum functional (9) and

$$|\phi_{\text{Q}}[A]\rangle = \exp \left[- \int d^3x \int d^3y \psi_+^\dagger(\mathbf{x}) K(\mathbf{x}, \mathbf{y}) \psi_-(\mathbf{y}) \right] |0\rangle, \quad (33)$$

with

$$K(\mathbf{x}, \mathbf{y}) = \beta S(\mathbf{x}, \mathbf{y}) \quad (34)$$

$$+ g \int d^3z [V(\mathbf{x}, \mathbf{y}; \mathbf{z}) + \beta W(\mathbf{x}, \mathbf{y}; \mathbf{z})] \boldsymbol{\alpha} \cdot \mathbf{A}^a(\mathbf{z}) t^a$$

being the quark wave functional. Here, S , V , and W are variational kernels. Furthermore, $|0\rangle$ is the Fock vacuum of the quarks which represents the bare Dirac sea. Finally,

$$I[A] = \langle \phi_{\text{Q}}[A] | \phi_{\text{Q}}[A] \rangle = \det(\text{id} + K^\dagger K) \quad (35)$$

is the quark determinant. The ansatz (32) treats the quark determinant $I[A]$ and the Faddeev–Popov determinant (5) on equal footing.

The ansatz (33) reduces for $W = 0$ to the quark wave functional used in [49] while for $V = W = 0$ it becomes the BCS-type wave functional considered in [51–53]. A comment is here in order concerning the choice of the Dirac structures in the ansatz for the vacuum wave functional (33), (34). The first coupling term ($\sim V$) is the usual quark–gluon coupling, which also occurs in the QCD Hamiltonian (30). This coupling form is mandatory to capture the quark–gluon coupling of the QCD Hamiltonian in the vacuum expectation value. The second coupling term ($\sim W$) was included for technical reasons. With these two coupling terms all UV divergences cancel in the variational equations; see below. There exist, of course, more Dirac structures for the quark–gluon couplings. The variational principle guarantees that the inclusion of further Dirac structures with additional variational kernels can only improve the quality of the description. With the wave functional (32) the expectation value of the QCD Hamiltonian was calculated up to two loops. Variation with respect to the two kernels V and W , which describe the coupling of the quarks to the transverse gluons, gives two equations, which can be solved explicitly in terms of the scalar kernel S and the gluon energy ω yielding

$$V(\mathbf{p}, \mathbf{q}) = \frac{1 + S(p)S(q)}{pP(p)(1 - S^2(p) + 2S(p)S(q)) + qP(q)(1 - S^2(q) + 2S(p)S(q)) + \omega(|\mathbf{p} + \mathbf{q}|)}, \quad (36)$$

$$W(\mathbf{p}, \mathbf{q}) = \frac{S(p) + S(q)}{pP(p)(1 - S^2(p) - 2S(p)S(q)) + qP(q)(1 - S^2(q) - 2S(p)S(q)) + \omega(|\mathbf{p} + \mathbf{q}|)}, \quad (37)$$

where we have defined the quantity

$$P(p) = \frac{1}{1 + S^2(p)}. \quad (38)$$

The variational equation for the scalar kernel S , referred to as *gap equation*, is highly nonlocal and can only be solved numerically. However, one can show analytically that all UV divergences in this equation cancel: the UV-divergent

contributions to $S(k)$ induced by the kernels V and W are given, respectively, by

$$\frac{C_{\text{F}}}{16\pi^2} g^2 S(k) \left[-2\Lambda + k \ln \frac{\Lambda}{\mu} \left(-\frac{2}{3} + 4P(k) \right) \right], \quad (39)$$

$$\frac{C_{\text{F}}}{16\pi^2} g^2 S(k) \left[2\Lambda + k \ln \frac{\Lambda}{\mu} \left(\frac{10}{3} - 4P(k) \right) \right].$$

Here, $C_{\text{F}} = (N_{\text{C}}^2 - 1)/2N_{\text{C}}$ is the quadratic Casimir, Λ is the UV cutoff, and μ is an arbitrary momentum scale. In the sum

of the two terms given by (39), the linear UV divergences obviously cancel. Furthermore, the sum of the logarithmic UV divergences of these two terms cancels against the asymptotic contribution to the gap equation induced by the Coulomb kernel,

$$-\frac{C_F}{6\pi^2}g^2kS(k)\ln\frac{\Lambda}{\mu}. \quad (40)$$

Due to the exact cancellation of all UV divergences no renormalization of the gap equation is required. This is certainly a big advantage of the present ansatz (33) for the quark wave functional. Using the gluon propagator $\sim 1/\omega$ obtained in the Yang–Mills sector as input, the quark gap equation can be solved within a quenched calculation. In this approach, the coupling constant g is determined by fixing the chiral quark condensate to its phenomenological value [30]. Figure 12 shows the vector kernels $V(\mathbf{p}, \mathbf{q})$, $W(\mathbf{p}, \mathbf{q})$ obtained in this way, as function of the modulus $p = q$ of the ingoing quark momenta and the cosine of the angle between them, $z = \cos \angle(\mathbf{p}, \mathbf{q})$. These kernels are peaked in the mid-momentum regime. Furthermore, the vector kernel V is about a factor of two larger than the kernel W . Figure 13 shows the scalar kernel $S(p)$ and the mass function

$$M(p) = \frac{2pS(p)}{1 - S^2(p)} \quad (41)$$

on a logarithmic scale. For the sake of comparison we also quote the curves obtained when the coupling to the transverse gluons is neglected. More precisely, this corresponds to putting $g = 0$ in the ansatz (34) and discarding the second (perturbative) part in the approximation

$$V_C(p) \approx \frac{8\pi\sigma_C}{p^4} + \frac{g^2}{p^2} \quad (42)$$

for the Coulomb potential (see (23)). As one observes, the inclusion of the coupling to the transverse gluon changes only the mid- and large-momentum regime while the infrared behavior is not changed at all. This is perhaps a little bit surprising but should have been expected in view of the fact that the non-Abelian Coulomb term [the first part in (42)], which gives rise to a linearly rising potential at large distances and dominates the infrared behavior of the gap equation. Let us also mention that we do not find chiral symmetry breaking from our equations when the linearly rising part of the Coulomb potential is neglected.

6. Hamiltonian Approach to Finite-Temperature QCD by Compactifying a Spatial Dimension

In [24, 54] the variational approach to Yang–Mills theory in Coulomb gauge was extended to finite temperatures by making a quasiparticle ansatz for the density matrix of the grand canonical ensemble where the quasiparticle energy was determined by minimizing the free energy. The resulting variational equations could be solved analogously to the

ones at zero-temperature. There is, however, a more efficient way to treat Yang–Mills theory at finite temperature within the Hamiltonian approach. The motivation comes from the Polyakov loop

$$P[A_0](\mathbf{x}) = \frac{1}{d_r} \text{tr} \mathcal{P} \exp \left[ig \int_0^L dx^0 A_0(x^0, \mathbf{x}) \right], \quad (43)$$

where $A_0 = A_0^a t^a$ is the temporal gauge field in the fundamental representation, \mathcal{P} is the path ordering prescription, d_r denotes the dimension of the representation of the gauge group, and $L = 1/T$ is the length of the compactified Euclidean time axis which represents the inverse temperature. The Polyakov loop cannot be calculated straightforwardly in the Hamiltonian approach due to the unrestricted time interval and the use of the Weyl gauge $A_0 = 0$. Both problems are overcome in the more efficient Hamiltonian approach to finite-temperature quantum field theory developed in [19]. This approach does not require an ansatz for the density matrix of the grand canonical ensemble and allows the evaluation of the Polyakov loop. In this novel approach, one exploits the $O(4)$ invariance to interchange the Euclidean time axis with one spatial axis. The temporal (anti)periodic boundary conditions to the fields become then spatial boundary conditions, while the new (Euclidean) time axis has infinite extent as is required within the Hamiltonian approach (see below). The upshot is that the partition function at finite temperature L^{-1} is entirely given by the ground state calculated on the spatial manifold $\mathbb{R}^2 \times S^1(L)$, where $S^1(L)$ is a circle with length L . The whole thermodynamics of the theory is then encoded in the vacuum calculated on the partially compactified spatial manifold $\mathbb{R}^2 \times S^1(L)$. This approach was used in [55] to study Yang–Mills theory at finite temperature and in [31] to calculate the Polyakov loop within the Hamiltonian approach. Furthermore, in [56], the so-called dual quark condensate was evaluated using this approach. Let us briefly sketch its main properties.

Consider finite-temperature quantum field theory in the standard functional integral approach. Here the finite temperature is introduced by going to Euclidean space and compactifying the Euclidean time dimension by imposing periodic and antiperiodic boundary conditions for Bose and Fermi fields, respectively,

$$A\left(x^0 = \frac{L}{2}\right) = A\left(x^0 = -\frac{L}{2}\right), \quad (44a)$$

$$\psi\left(x^0 = \frac{L}{2}\right) = -\psi\left(x^0 = -\frac{L}{2}\right). \quad (44b)$$

The length of the compactified dimension L represents then the inverse temperature $T^{-1} = L$. One can now exploit the $O(4)$ invariance of the Euclidean Lagrangian to rotate the Euclidean time axis into a space axis and, correspondingly, one spatial axis into the Euclidean time axis. Of course,

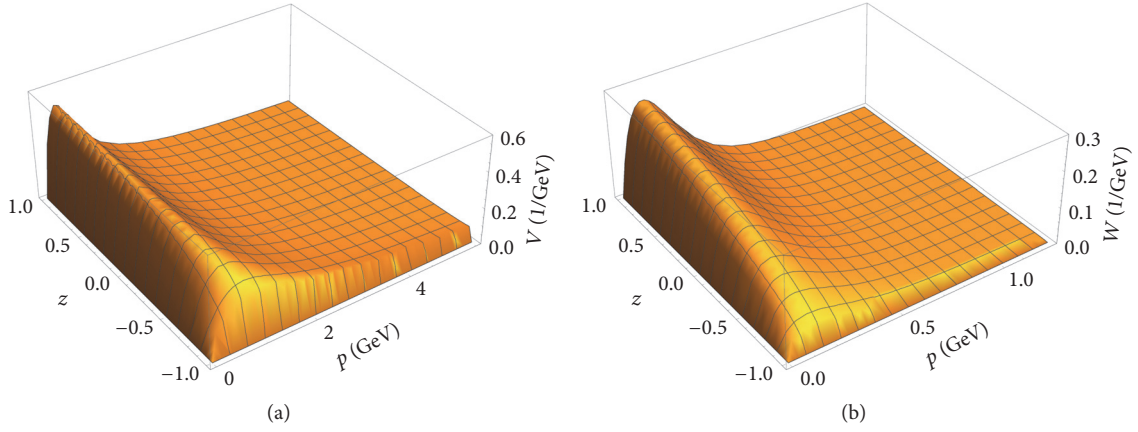


FIGURE 12: The vector kernel (a) $V(\mathbf{p}, \mathbf{q})$ (36) and (b) $W(\mathbf{p}, \mathbf{q})$ (37) obtained from the solution of the quark gap equation for $g \approx 2.1$ as function of $p = q$ and $z = \cos \angle(\mathbf{p}, \mathbf{q})$ [30].

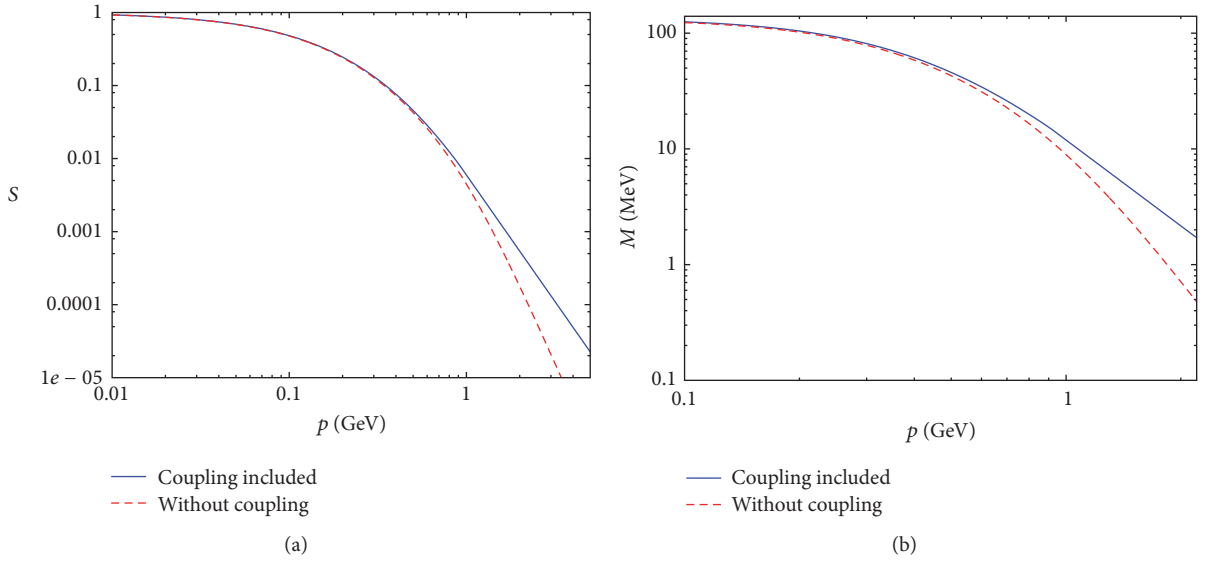


FIGURE 13: (a) Scalar form factor and (b) mass function obtained from the (quenched) solution of the quark gap equation. Results are presented for $g \approx 2.1$ (full curve) and $g = 0$ (dashed curve).

thereby all vectorial quantities transform in the same way; that is, we can choose the transformation:

$$\begin{aligned} x^0 &\longrightarrow x^3, \\ A^0 &\longrightarrow A^3, \\ \gamma^0 &\longrightarrow \gamma^3, \\ x^1 &\longrightarrow x^0, \\ A^1 &\longrightarrow A^0, \\ \gamma^1 &\longrightarrow \gamma^0, \\ x^2 &\longrightarrow x^1, \\ A^2 &\longrightarrow A^1, \end{aligned}$$

$$\begin{aligned} \gamma^2 &\longrightarrow \gamma^1, \\ x^3 &\longrightarrow x^2, \\ A^3 &\longrightarrow A^2, \\ \gamma^3 &\longrightarrow \gamma^2. \end{aligned} \tag{45}$$

After this rotation we are left with the spatial periodic and antiperiodic boundary conditions:

$$\begin{aligned} A\left(x^3 = \frac{L}{2}\right) &= A\left(x^3 = -\frac{L}{2}\right), \\ \psi\left(x^3 = \frac{L}{2}\right) &= -\psi\left(x^3 = -\frac{L}{2}\right). \end{aligned} \tag{46a}$$

As a consequence of the $O(4)$ rotation our spatial manifold is now $\mathbb{R}^2 \times S^1(L)$ instead of \mathbb{R}^3 while the temporal manifold is \mathbb{R} independent of the temperature; that is, the temperature is now encoded in one spatial dimension while time has infinite extension. We can now apply the usual canonical Hamiltonian approach to this rotated space-time manifold. As the new time axis has infinite extension $\ell \rightarrow \infty$, the partition function is now given by

$$Z(L) = \lim_{\ell \rightarrow \infty} \text{tr} \exp(-\ell H(L)), \quad (47)$$

where $H(L)$ is the usual Hamiltonian obtained after canonical quantization, however, now defined on the spatial manifold $\mathbb{R}^2 \times S^1(L)$. Taking the trace in the basis of the exact eigenstates of the Hamiltonian $H(L)$, we obtain for the partition function (47):

$$\begin{aligned} Z(L) &= \lim_{\ell \rightarrow \infty} \sum_n \exp(-\ell E_n(L)) \\ &= \lim_{\ell \rightarrow \infty} \exp(-\ell E_0(L)). \end{aligned} \quad (48)$$

The full partition function is now obtained from the ground state energy calculated on the spatial manifold $\mathbb{R}^2 \times S^1(L)$. Introducing the energy density $e(L)$ on $\mathbb{R}^2 \times S^1(L)$ by separating the volume $L\ell^2$ of the spatial manifold from the energy, we have

$$E_0(L) = L\ell^2 e(L). \quad (49)$$

For the physical pressure

$$P = \frac{1}{L} \frac{\partial \ln Z}{\partial V}, \quad V = \ell^3 \quad (50)$$

one finds from (48)

$$P = -e(L), \quad (51)$$

while the physical energy density ε is obtained as

$$\varepsilon = \frac{\partial (Le(L))}{\partial L} - \mu \frac{\partial e(L)}{\partial \mu}. \quad (52)$$

To distinguish this quantity from the (negative) Casimir pressure $e(L)$ [see (51)], which also appears as an energy density in our formalism after the transformation [see (45)], we will denote $e(L)$ as *pseudo energy density*. Finally, after the $O(4)$ rotation (45), the finite chemical potential μ enters the single-particle Dirac Hamiltonian h in the following form:

$$h(\mu) = h(\mu = 0) + i\mu\alpha^3, \quad (53)$$

where α^3 is the third Dirac matrix and $h(\mu = 0)$ the standard Dirac operator coupled to the gauge field.

6.1. Free Bose and Fermi Gases. To illustrate the above approach let us first consider a relativistic Bose gas with dispersion relation $\omega(p) = \sqrt{\mathbf{p}^2 + m^2}$, where we assume for

simplicity a vanishing chemical potential. The thermodynamical pressure obtained from the grand canonical ensemble for such a system is given by

$$P = \frac{2}{3} \int \frac{d^3 p}{(2\pi)^3} \frac{p^2}{\omega(p)} n(p), \quad (54)$$

$$n(p) = \frac{1}{\exp(\beta\omega(p)) - 1},$$

where $n(p)$ are the finite temperature Bose occupation numbers. On the other hand, one finds for the ideal Bose gas with dispersion relation $\omega(p) = \sqrt{\mathbf{p}^2 + m^2}$ the pseudo energy density on the spatial manifold $\mathbb{R}^2 \times S^1(L)$ [19]:

$$e(L) = \frac{1}{2} \int \frac{d^2 p_\perp}{(2\pi)^2} \frac{1}{L} \sum_{n=-\infty}^{\infty} \sqrt{\mathbf{p}_\perp^2 + p_n^2 + m^2}, \quad (55)$$

$$p_n = \frac{2n\pi}{L},$$

where p_n are the bosonic Matsubara frequencies. This quantity does not look at all like the negative of the pressure (54), as it should by (51). In fact, as it stands it is ill-defined: the integral and the sum are both divergent. To make it mathematically well defined, we first use the proper-time regularization of the square root:

$$\begin{aligned} \sqrt{A} &= \frac{1}{\Gamma(-1/2)} \\ &\cdot \lim_{\Lambda \rightarrow \infty} \left[\int_{1/\Lambda^2}^{\infty} d\tau \tau^{-3/2} \exp(-\tau A) - 2\Lambda + \mathcal{O}(\Lambda^{-1}) \right]. \end{aligned} \quad (56)$$

The divergent constant appears because the limit $\Lambda \rightarrow \infty$ of the incomplete Γ -function is not smooth; it drops out when taking the difference to the zero-temperature case after (59) below. With this replacement, the momentum integral in (55) can be carried out in closed form. For the remaining Matsubara sum, we use the Poisson resummation formula:

$$\frac{1}{2\pi} \sum_{k=-\infty}^{\infty} \exp(ikx) = \sum_{n=-\infty}^{\infty} \delta(x - 2\pi n), \quad (57)$$

by whose means we obtain

$$\frac{1}{2\pi} \int_{-\infty}^{\infty} dz f(x) \sum_{k=-\infty}^{\infty} e^{ik\beta z} = \frac{1}{\beta} \sum_{n=-\infty}^{\infty} f(\omega_n) \quad (58)$$

for any function $f(z)$. The term with $k = 0$ on the r.h.s. represents the zero-temperature limit of the l.h.s. After use of (58) the proper-time integral can also be carried out, yielding for the pseudo energy density (55):

$$e(L) = -\frac{1}{2\pi^2} \sum_{k=-\infty}^{\infty} \left(\frac{m}{kL} \right)^2 K_2(kLm), \quad (59)$$

where $K_\nu(z)$ is the modified Bessel function. The term with $k = 0$ is divergent and represents the pseudo energy density of the zero-temperature vacuum, which should be eliminated

from the pressure. The remaining terms $k \neq 0$ are all finite and also the remaining sum converges. This sum, however, cannot be carried out analytically for massive bosons (the same applies to the integral in the grand canonical expression (54) for the pressure). In the zero-mass limit, we find from (59) for the pressure (51)

$$P = \frac{\zeta(4)}{\pi^2} T^4 = \frac{\pi^2}{90} T^4, \quad (60)$$

which is Stefan–Boltzmann law, the correct result also obtained from the grand canonical ensemble. For massive bosons the evaluation of the sum in (59) as well as the evaluation of the integral in (54) has to be done numerically. The result is shown in Figure 14(a). As expected the pressure calculated from the compactified spatial dimension reproduces the result of the usual grand canonical ensemble. Figure 14(b) shows the various contributions to the pressure. It is seen that only a few terms in the sum of (59) are necessary to reproduce the result of the grand canonical ensemble to good accuracy.

In the case of the relativistic *Fermi* gas with dispersion relation $\omega(p) = \sqrt{\mathbf{p}^2 + m^2}$ the energy density on $\mathbb{R}^2 \times S^1(L)$ is given by

$$e(L) = -2 \int \frac{d^2 p_{\perp}}{(2\pi)^2} \frac{1}{L} \sum_{n=-\infty}^{\infty} \sqrt{\mathbf{p}_{\perp}^2 + (p_n + i\mu)^2 + m^2}, \quad (61)$$

$$p_n = \frac{2n+1}{L} \pi,$$

where we have now included a nonvanishing chemical potential μ . To make this expression mathematically well defined one has to resort again to the proper-time regularization and Poisson resummation technique sketched above. The result is

$$e(L) = \frac{2}{\pi^2} \sum_{n=0}^{\infty} \cos \left[nL \left(\frac{\pi}{L} - i\mu \right) \right] \left(\frac{m}{nL} \right)^2 K_{-2}(nLm). \quad (62)$$

Again, the term with $n = 0$ represents the zero-temperature vacuum energy density, which is divergent and has to be removed. As before, this expression can only be calculated in closed form for massless particles. For the remaining sum to converge, an analytic continuation $i\mu L \rightarrow \bar{\mu} \in \mathbb{R}$ is required to carry out the sum

$$\sum_{n=1}^{\infty} (-1)^n \frac{\cos(n\bar{\mu})}{n^4} = \frac{1}{48} \left[-\frac{7}{15} \pi^2 + 2\pi^2 \bar{\mu}^2 - \bar{\mu}^4 \right]. \quad (63)$$

Continuing back to real chemical potentials one finds through (51) for the pressure

$$P = \frac{1}{12\pi^2} \left[\frac{7}{15} \pi^4 T^4 + 2\pi^2 T^2 \mu^2 + \mu^4 \right], \quad (64)$$

which is the correct result obtained also from the usual grand canonical ensemble.

In [55], the above approach was used to study Yang–Mills theory at finite temperature. For this purpose, it is merely required to repeat the variational Hamiltonian approach on

the spatial manifold $\mathbb{R}^2 \times S^1(L)$. Due to the one compactified spatial dimension the three-dimensional integral equations of the zero-temperature case are replaced with a set of two-dimensional integral equations distinguished by different Matsubara frequencies. Below, I will use this approach to calculate the effective potential of the Polyakov loop, the order parameter of confinement.

6.2. The Polyakov Loop. Consider $SU(N)$ gauge theory at finite temperature, where the temperature is introduced by the usual periodic boundary condition in the temporal directions (44a) and (44b). Gauge transformations preserving this boundary conditions need to be periodic only up to an element z of the center $Z(N)$ of the gauge group,

$$U(x^0 = L) = zU(x^0 = 0), \quad z \in Z(N). \quad (65)$$

Since there are N center elements, this theory has a residual global $Z(N)$ symmetry, which remains after gauge fixing. However, there are quantities which are sensitive to such a $Z(N)$ symmetry transformation. The most prominent example is the Polyakov loop (43). A gauge transformation of the form (65) multiplies the Polyakov loop by the center element z , that is,

$$P[A_0^U] = zP[A_0]. \quad (66)$$

The expectation value of the Polyakov loop

$$\langle P[A_0](\mathbf{x}) \rangle \sim \exp(-F_{\infty}(\mathbf{x})L) \quad (67)$$

can be shown to be related to the free energy $F_{\infty}(\mathbf{x})$ of a static color point charge located at \mathbf{x} [57]. In a confining theory this quantity has to be infinite since there are no free color charges, while in a deconfined phase it is finite. Accordingly we find for the expectation value of the Polyakov loop

$$\langle P[A_0](\mathbf{x}) \rangle \begin{cases} = 0 & \text{confined phase,} \\ \neq 0 & \text{deconfined phase.} \end{cases} \quad (68)$$

From (66), it follows that the Polyakov loop vanishes in a center symmetric state. Hence, in the deconfined phase the $Z(N)$ center symmetry must be obviously broken. In the continuum theory the Polyakov loop can be most easily calculated in the Polyakov gauge:

$$\partial_0 A_0 = 0, \quad A_0 \text{ color diagonal.} \quad (69)$$

In this gauge, one finds, for example, for the $SU(2)$ gauge group, that the Polyakov loop

$$P[A_0](\mathbf{x}) = \cos \left(\frac{1}{2} g A_0(\mathbf{x}) L \right) \quad (70)$$

is a one-to-one function of the gauge field, at least in the fundamental modular region of this gauge. It can be shown, see [14, 58–60], that instead of the expectation value of the Polyakov loop $\langle P[A_0] \rangle$ one may alternatively use the Polyakov loop of the expectation value, $P[\langle A_0 \rangle]$, or the expectation value of the temporal gauge field itself, $\langle A_0 \rangle$, as order

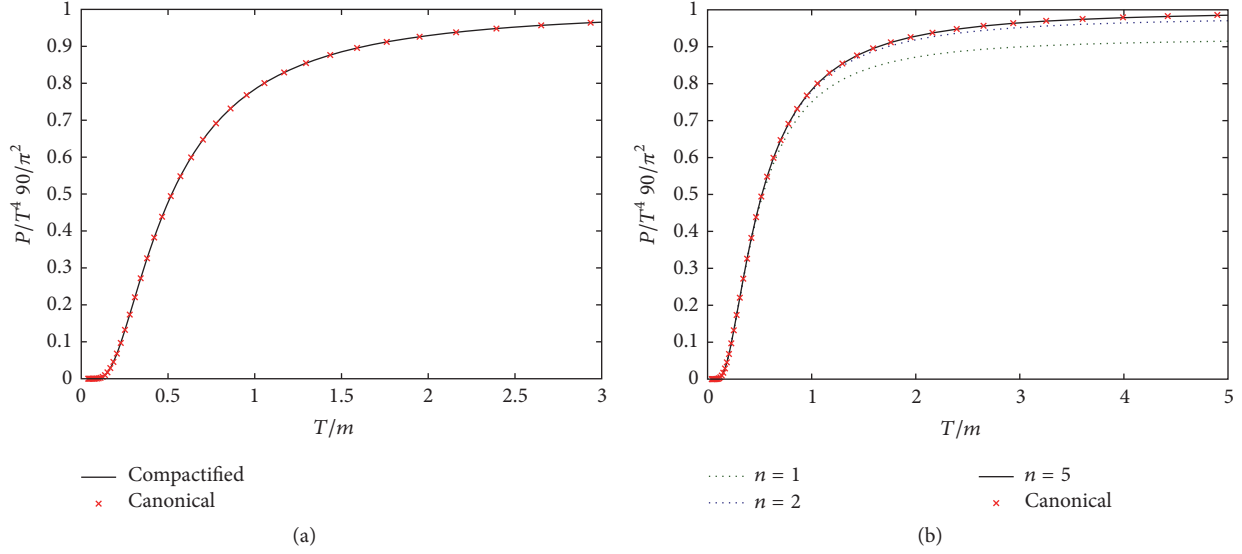


FIGURE 14: The pressure of a free massive Bose gas (a) calculated from equation (59) (full curve) and from the grand canonical ensemble (54) (crosses). (b) The pressure when the summation index in equation (59) is restricted to $|n| = 1, 2$ and 5.

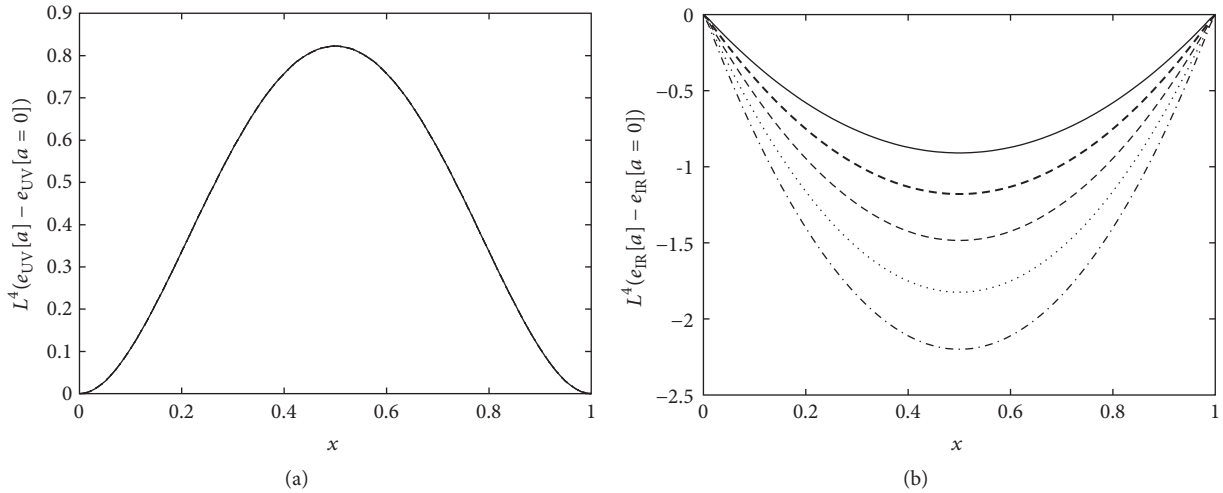


FIGURE 15: The effective potential of the Polyakov loop $e(a, L)$ (71) as function of the background field $x = a_3 L / 2\pi$. The curvature is neglected ($\chi = 0$) and the gluon energy assumed to be (a) $\omega(p) = p$ (UV form) and (b) $\omega(p) = M^2/p$ (IR form), respectively; see [31] for more details.

parameter of confinement in the gauge (69). This analysis also shows that the most efficient way to obtain the Polyakov loop is to carry out a so-called background field calculation with a temporal background field $a_0(\mathbf{x}) = \langle A_0(\mathbf{x}) \rangle$ chosen in the Polyakov gauge and then calculate the effective potential $e[a_0]$ of that background field. From the minimum \bar{a}_0 of this potential one evaluates the Polyakov loop $P[\langle A_0 \rangle] = P[\bar{a}_0]$, which can then serve as the order parameter of confinement.

Such a calculation was done a long time ago in [61], where the effective potential $e[a_0]$ was calculated in one-loop perturbation theory. The result is shown in Figure 15(a). The potential is periodic due to center symmetry. The minimum of the potential occurs at the vanishing background field, which gives $P[a_0 = 0] = 1$ corresponding to the deconfined phase.

This is, of course, expected due to the use of perturbation theory. Below, I present the results of a nonperturbative evaluation of $e[a_0]$ in the Hamiltonian approach in Coulomb gauge.

At first sight it seems that the Polyakov loop cannot be calculated in the Hamiltonian approach due to the use of the Weyl gauge $A_0 = 0$. However, we can now use the alternative Hamiltonian approach to finite temperature introduced above, where the temperature is introduced by compactifying a spatial dimension. Here, we compactify the x_3 -axis and consequently put also the background field along this axis, $\mathbf{a} = a e_3$. In the Hamiltonian approach, the effective potential of a spatial background field \mathbf{a} can be easily calculated by minimizing the expectation value of the Hamiltonian under the constraint $\langle \mathbf{A} \rangle = \mathbf{a}$. The resulting energy $\langle H \rangle_{\mathbf{a}} = L^2 l e(\mathbf{a})$ is then (up to the spatial volume factor) the effective potential.

So the effective potential $e(\mathbf{a})$ is nothing but the pseudo energy density considered earlier, but now calculated in a background gauge with the constraint $\langle \mathbf{A} \rangle = \mathbf{a}$.

6.3. The Effective Potential of the Polyakov Loop. After lengthy calculations exploiting the gluon gap equation (10), one finds for the effective potential of the Polyakov loop the following expression:

$$e(a, L) = \sum_{\sigma} \frac{1}{L} \sum_{n=-\infty}^{\infty} \int \frac{d^2 p_{\perp}}{(2\pi)^2} (\omega(\mathbf{p}^{\sigma}) - \chi(\mathbf{p}^{\sigma})), \quad (71)$$

where $\omega(p)$ is the gluon energy and $\chi(p)$ is the ghost loop. These quantities have to be taken with the momentum variable

$$\mathbf{p}^{\sigma} = \mathbf{p}_{\perp} + (p_n - \sigma \cdot \mathbf{a}) \mathbf{e}_3, \quad (72)$$

where \mathbf{p}_{\perp} is the momentum corresponding to the two uncompactified space dimensions while $p_n = 2\pi n/L$ is the Matsubara frequency resulting from the compactification of the third dimension. Furthermore, $\sigma \cdot \mathbf{a} \equiv \sigma^b a^b$ denotes the product of the color background field with the root vectors σ^b of the gauge group. Equation (71) includes also the summation over the roots σ of the gauge group. In [31, 62], the effective potential (71) was explicitly calculated using for $\omega(p)$ and $\chi(p)$, the results from the variational calculation in Coulomb gauge at zero-temperature [25]. This represents certainly an approximation since, in principle, one should use the finite-temperature solutions obtained in [55].

Before I present the full results let me ignore the ghost loop $\chi(p)$ in (71) and consider the ultraviolet and infrared limit of the gluon energy. If we choose the ultraviolet limit $\omega(p) = p$, we obtain from (71) with $\chi(p) = 0$ precisely the Weiss potential, shown in Figure 15(a), which corresponds to the deconfined phase. Choosing for the gluon energy its infrared limit $\omega(p) = M^2/p$, one finds from (71) with $\chi(p) = 0$ the (center symmetric) potential shown in Figure 15(b). From its center symmetric minimum $\bar{a} = \pi/L$ one finds a vanishing Polyakov loop $P[\bar{a}] = 0$ corresponding to the confined phase. Obviously, the deconfining phase transition results from the interplay between the confining infrared and the deconfining ultraviolet potentials. Choosing for the gluon energy the sum of the UV- and IR-parts $\omega(p) = p + M^2/p$, which can be considered as an approximation to the Gribov formula (20), one has to add the UV and IR potentials and finds a phase transition at a critical temperature $T_c = \sqrt{3}M/\pi$. With the Gribov mass $M \approx 880$ MeV this gives a critical value of $T_c \approx 485$ MeV for the color group SU(2), which is much too high as compared to the lattice value of 312 MeV [63]. One can show analytically [31, 62] that the neglect of the ghost loop $\chi(p) = 0$ shifts the critical temperature to higher values. If one uses for the gluon energy $\omega(p)$ the Gribov formula (20) and includes the ghost loop $\chi(p)$, one finds the effective potential shown in Figure 16(a), which shows a second-order phase transition and gives a transition temperature of $T_c \approx 269$ MeV for the gauge group SU(2), which is in the right ballpark. The Polyakov loop $P[\bar{a}]$ calculated from the minimum \bar{a} of the effective potential $e(a, L)$ (71) is plotted in Figure 17(a)

as function of the temperature. After the phase transition it approaches rather rapidly (at about $T/T_c \sim 1.1$) its limiting value $\langle P \rangle = 1$ contrary to the lattice results. Such behavior is also observed in analogous calculations in the path-integral approach in Landau gauge; see, for example, [13, 14]. As shown in [14], the Polyakov loop approaches less rapidly its limiting value when two-loop contributions are included. This refers also to the Polyakov loop obtained for the gauge group SU(3) shown in Figure 16(b).

The effective potential for the gauge group SU(3) can be reduced to that of the SU(2) group by noticing that the SU(3) algebra consists of three SU(2) subalgebras characterized by the three positive roots $\sigma = (1, 0), (1/2, \sqrt{3}/2), (1/2, -\sqrt{3}/2)$. One finds

$$e_{\text{SU}(3)}(a, L) = \sum_{\sigma > 0} e_{\text{SU}(2)}[\sigma](a, L). \quad (73)$$

The resulting effective potential for SU(3) is shown in Figure 18 as function of the components of the background field in the Cartan algebra, a_3 and a_8 . Above and below T_c the absolute minima of the potential occur in both cases for $a_8 = 0$ because of charge conjugation invariance. Cutting the two-dimensional potential surface at $a_8 = 0$, one finds the effective potential shown in Figure 16(b), which shows a first-order phase transition with a critical temperature of $T_c \approx 283$ MeV. The first-order nature of the SU(3) phase transition is also seen in Figure 17(b), where the Polyakov loop $P[\bar{a}]$ is shown as function of the temperature.

6.4. The Dual Quark Condensate. The dual quark condensate was originally introduced in [64] and was discussed in a more general context in [65]. This quantity has been calculated on the lattice [66, 67], in the functional renormalization group approach [68] and in the Dyson–Schwinger approach [69]. The dual condensate is defined by

$$\Sigma_n = \int_0^{2\pi} \frac{d\varphi}{2\pi} \exp(-in\varphi) \langle \bar{\psi}\psi \rangle_{\varphi}, \quad (74)$$

where $\langle \bar{\psi}\psi \rangle_{\varphi}$ is the quark condensate calculated with the U(1)-valued boundary condition:

$$\psi\left(x^0 + \frac{L}{2}, \mathbf{x}\right) = e^{i\varphi} \psi\left(x^0 - \frac{L}{2}, \mathbf{x}\right). \quad (75)$$

For $\varphi = \pi$ these boundary conditions reduce to the usual finite-temperature boundary conditions of the quark field in the functional integral representation of the partition function; see (44a) and (44b). On the lattice it is not difficult to show that the quantity Σ_n (74) represents the vacuum expectation value of the sum of all closed Wilson loops winding precisely n -times around the compactified time axis. In particular, the quantity Σ_1 represents the expectation value of all closed loops winding precisely once around the compactified time axis and is therefore called the dressed Polyakov loop. The phase in the boundary condition (75) can be absorbed into an imaginary chemical potential:

$$\mu = i \frac{\pi - \varphi}{L} \quad (76)$$

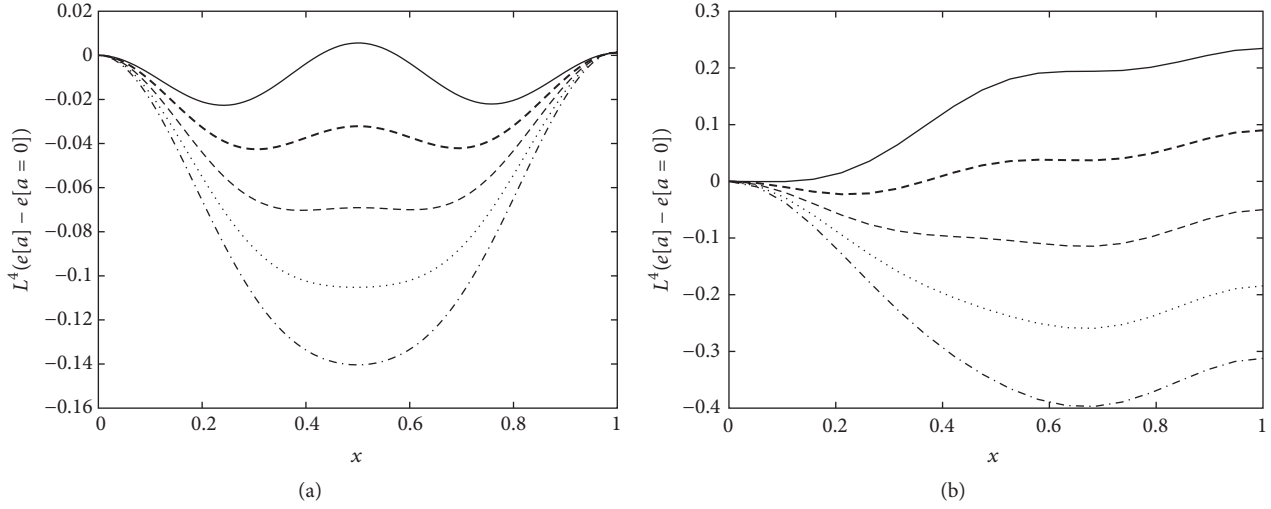


FIGURE 16: Effective potential of the Polyakov loop (71) as function of the background field $x = a_3 L / 2\pi$ at various temperatures, for the gauge groups (a) SU(2) and (b) SU(3).

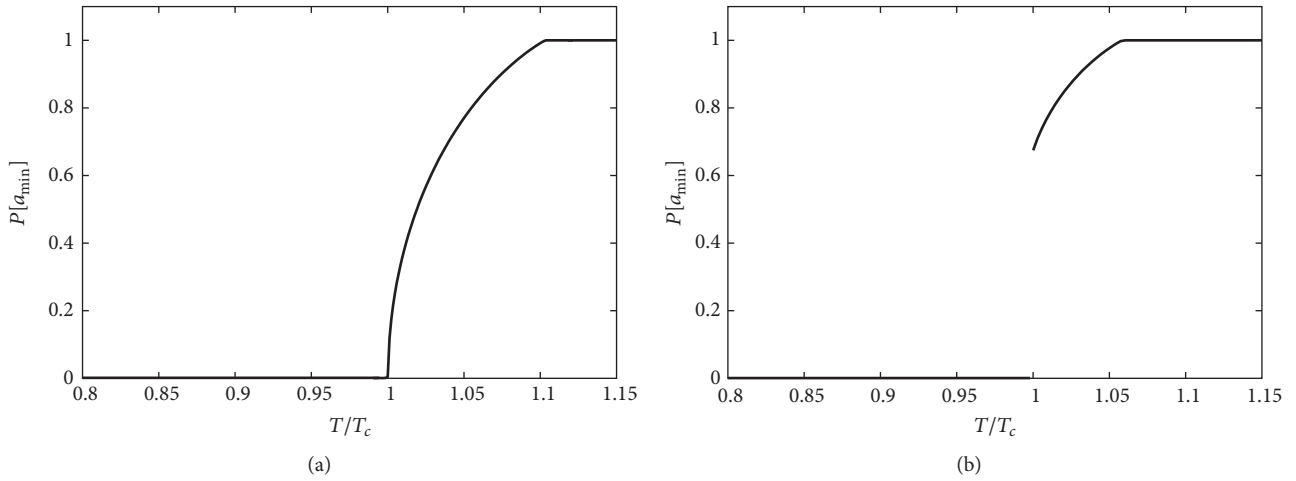


FIGURE 17: The Polyakov loop as function of the temperature (a) for SU(2) and (b) for SU(3).

for fermion fields satisfying the usual antisymmetric boundary condition $\psi(x^0 + L/2, \mathbf{x}) = -\psi(x^0 - L/2, \mathbf{x})$. In the Hamiltonian approach to finite temperatures of [19], where the compactified time axis has become the third spatial axis, the phase-dependent boundary condition (75) or equivalently the imaginary chemical potential (76) manifests itself in the momentum variable along the (compactified) three axes, which reads

$$p_3 = p_n + i\mu = \frac{2\pi n + \varphi}{L}, \quad p_n = \frac{2n+1}{L}\pi, \quad (77)$$

where p_n is the usual fermionic Matsubara frequency [see (61)]. Using the zero-temperature quark mass function $M(p)$ calculated in [30], one finds in the Hamiltonian approach

to QCD of [50] for the dual quark condensate after Poisson resummation the leading expression [56]:

$$\Sigma_n = -\frac{N}{\pi^2} \int_0^\infty dp \frac{p^2 M(p)}{\sqrt{p^2 + M^2(p)}} \left[\delta_{n0} + \frac{\sin(n\beta p)}{n\beta p} \right], \quad (78)$$

where N denotes the number of colors. In the same way, one can compute the quark condensate $\langle \bar{\psi}\psi \rangle_\varphi$ shown in Figure 19(a). For the dressed Polyakov loop one finds the temperature behavior shown in Figure 19(b), where we also compare with the result obtained when the coupling to the transverse gauge field degrees of freedom is neglected ($g = 0$). As one observes there is no difference at small temperatures in accord with the fact that the mass function $M(p)$ has the same infrared behavior, whether the coupling to the transverse

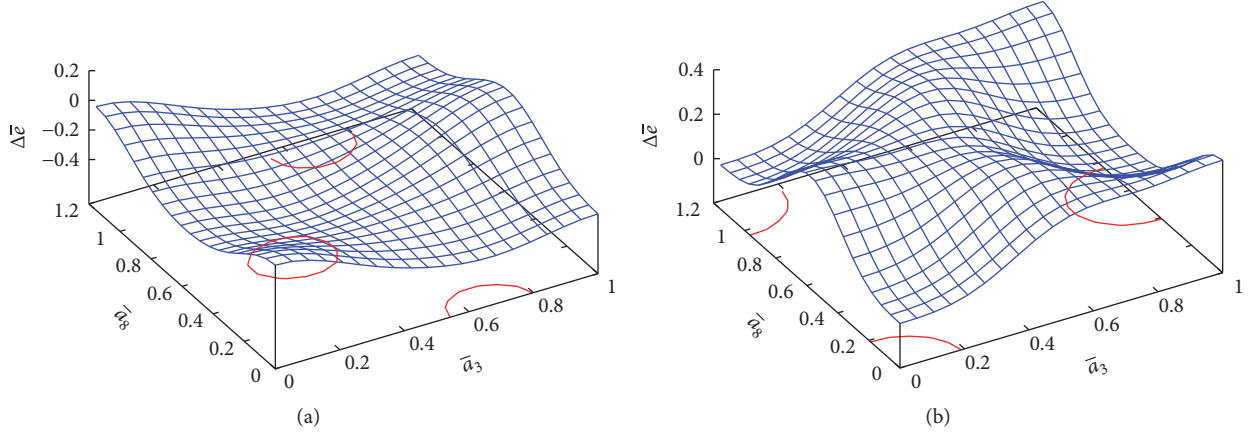


FIGURE 18: The effective potential of the Polyakov loop for the gauge group SU(3) as function of the two Cartan components of the background field $x = a_3 L/2\pi$ and $y = a_8 L/2\pi$ for (a) $T < T_c$ and (b) $T > T_c$.

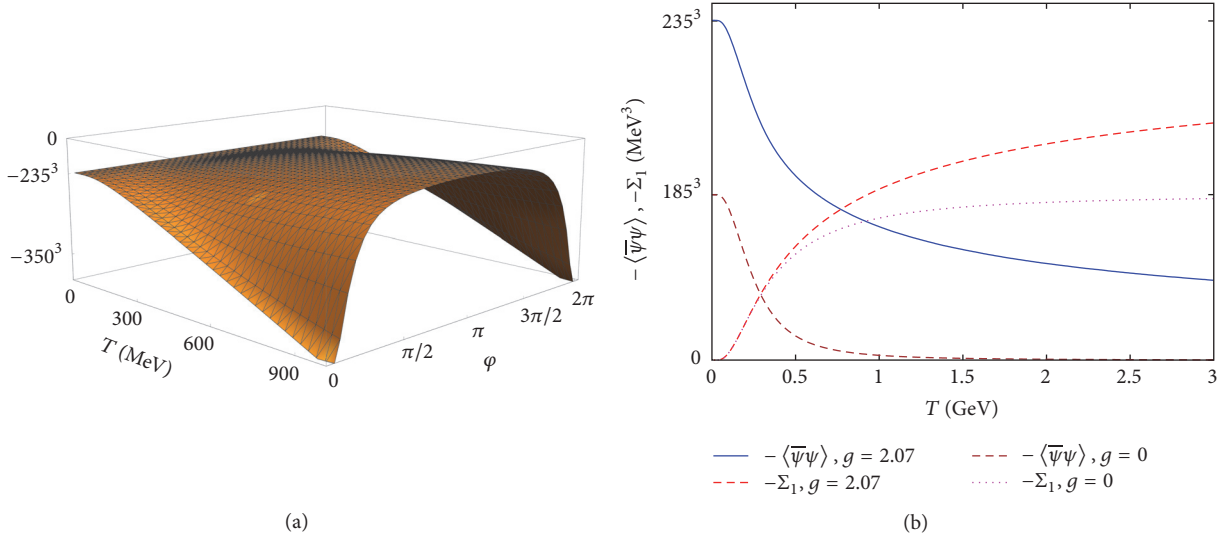


FIGURE 19: (a) Chiral quark condensate $\langle \bar{\psi}\psi \rangle_\varphi$ as function of the temperature T and the phase φ of the boundary condition (75). (b) Chiral and dual quark condensate as function of the temperature. Results are presented for both a coupling of $g \approx 2.1$ and $g = 0$.

gluons is included or not. The slower UV decrease of the full mass function causes the dual condensate to reach its high-temperature limit:

$$\begin{aligned} \lim_{L \rightarrow 0} \Sigma_1 &= -\frac{N}{\pi^2} \int_0^\infty dp \frac{p^2 M(p)}{\sqrt{p^2 + M^2(p)}} \\ &= \lim_{L \rightarrow \infty} \langle \bar{\psi}\psi \rangle_{\varphi=\pi} \end{aligned} \quad (79)$$

only very slowly. We expect, however, that this limit is reached faster when the finite-temperature solutions are used. This will presumably also convert the crossover obtained for the chiral condensate, see Figure 19(b), into a true phase transition as expected for chiral quarks. From the inflexion points of the chiral and dual condensate one extracts the values of $T_\chi^{\text{pc}} \approx 170$ MeV and $T_c^{\text{pc}} \approx 198$ MeV for the pseudocritical temperatures of the chiral and deconfinement

transition, respectively. For comparison, one finds on the lattice for realistic quark masses $T_\chi^{\text{pc}} \approx 155$ MeV and $T_c^{\text{pc}} \approx 165$ MeV [70, 71].

7. Conclusions

In my talk, I have presented some recent results obtained within the Hamiltonian approach to QCD in Coulomb gauge. I have first shown that the so-called Coulomb string tension is not related to the temporal but to the spatial string tension. This relation explains the finite-temperature behavior of the Coulomb string tension, namely, the fact that it does not disappear but even increases above the deconfinement transition. I have then studied the quark sector of QCD in Coulomb gauge using a Slater determinant ansatz for the quark wave functional, which includes in particular the quark-gluon coupling by two different Dirac structures. Our calculations show that there is no spontaneous breaking of chiral symmetry

when the (linearly rising) infrared part of the Coulomb potential is excluded. Furthermore, choosing the Coulomb string tension from the lattice data we can reproduce the phenomenological value of the quark condensate when the coupling of the quarks to the transverse gluon is included.

I have then extended the Hamiltonian approach to QCD in Coulomb gauge to finite temperatures by compactifying a spatial dimension. Within this approach, I have calculated the effective potential of the Polyakov loop as well as the chiral and dual quark condensate as function of the temperature. Using our zero-temperature solution as input, from the Polyakov loop we predict a critical temperature for the deconfinement phase transition of about $T_c \sim 275$ MeV for SU(2), and $T_c \sim 280$ MeV for SU(3). Furthermore, the correct order of the phase transition was found for SU(2) and SU(3). For full QCD our calculations of the dual and chiral quark condensate predict pseudocritical temperatures of $T_c^{\text{pc}} \approx 170$ MeV for the chiral and $T_c^{\text{pc}} \approx 198$ MeV for the deconfinement transition. In all these finite-temperature calculations the zero-temperature variational solutions were used as input, which is likely the reason that the critical temperatures currently obtained are too high as compared to lattice data. The solution of the variational principle at finite temperature will be the next step in our investigation of the QCD phase diagram.

Disclosure

This talk was given by H. Reinhardt at “5th Winter Workshop on Non-Perturbative Quantum Field Theory,” 22–24 March 2017, Sophia-Antipolis, France.

Conflicts of Interest

The authors declare that there are no conflicts of interest regarding the publication of this paper.

Acknowledgments

This work was supported in part by DFG-RE856/9-2 and by DFG-RE856/10-1.

References

- [1] C. Gattringer and K. Langfeld, “Approaches to the sign problem in lattice field theory,” *International Journal of Modern Physics A*, vol. 31, no. 22, Article ID 1643007, 2016.
- [2] C. S. Fischer, “Infrared properties of QCD from Dyson-Schwinger equations,” *Journal of Physics G: Nuclear and Particle Physics*, vol. 32, no. 8, article no. R02, pp. R253–R291, 2006.
- [3] R. Alkofer and L. von Smekal, “The infrared behaviour of QCD Green’s functions: confinement, dynamical symmetry breaking, and hadrons as relativistic bound states,” *Physics Reports*, vol. 353, no. 5-6, pp. 281–465, 2001.
- [4] D. Binosi and J. Papavassiliou, “Pinch technique: Theory and applications,” *Physics Reports*, vol. 479, no. 1-6, pp. 1–152, 2009.
- [5] P. Watson and H. Reinhardt, “Propagator Dyson-Schwinger equations of Coulomb gauge Yang-Mills theory within the first order formalism,” *Physical Review D: Particles, Fields, Gravitation and Cosmology*, vol. 75, no. 4, Article ID 045021, 2007.
- [6] P. Watson and H. Reinhardt, “Two-point functions of Coulomb gauge Yang-Mills theory,” *Physical Review D: Particles, Fields, Gravitation and Cosmology*, vol. 77, no. 2, Article ID 025030, 2008.
- [7] P. Watson and H. Reinhardt, “Slavnov-Taylor identities in Coulomb gauge Yang-Mills theory,” *The European Physical Journal C*, vol. 65, no. 3, pp. 567–585, 2010.
- [8] J. M. Pawłowski, “Aspects of the functional renormalisation group,” *Annals of Physics*, vol. 322, no. 12, pp. 2831–2915, 2007.
- [9] H. Gies, *Introduction to the Functional RG and Applications to Gauge Theories*, vol. 852 of *Lecture Notes in Physics*, Springer, Heidelberg, Berlin, Germany, 2012.
- [10] C. Feuchter and H. Reinhardt, “Variational solution of the Yang-Mills Schrödinger equation in Coulomb gauge,” *Physical Review D: Particles, Fields, Gravitation and Cosmology*, vol. 70, Article ID 105021, 2004.
- [11] H. Reinhardt and C. Feuchter, “Yang-Mills wave functional in Coulomb gauge,” *Physical Review D: Particles, Fields, Gravitation and Cosmology*, vol. 71, no. 10, Article ID 105002, 6 pages, 2005.
- [12] M. Quandt, H. Reinhardt, and J. Heffner, “Covariant variational approach to Yang-Mills theory,” *Physical Review D: Particles, Fields, Gravitation and Cosmology*, vol. 89, no. 6, Article ID 065037, 2014.
- [13] M. Quandt and H. Reinhardt, “Covariant variational approach to Yang-Mills theory at finite temperatures,” *Physical Review D: Particles, Fields, Gravitation and Cosmology*, vol. 92, no. 2, Article ID 025051, 18 pages, 2015.
- [14] U. Reinosa, J. Serreau, M. Tissier, and N. Wschebor, “Deconfinement transition in SU(2) Yang-Mills theory: A two-loop study,” *Physical Review D: Particles, Fields, Gravitation and Cosmology*, vol. 91, no. 4, Article ID 045035, 2015.
- [15] V. N. Gribov, “Quantization of non-Abelian gauge theories,” *Nuclear Physics B*, vol. 139, no. 1-2, pp. 1–19, 1978.
- [16] F. E. Canfora, D. Dudal, I. F. Justo, P. Pais, L. Rosa, and D. Vercauteren, “Effect of the Gribov horizon on the Polyakov loop and vice versa,” *The European Physical Journal C*, vol. 75, no. 7, article no. 326, 2015.
- [17] H. Reinhardt, D. Campagnari, J. Heffner, M. Quandt, and P. Vastag, “Hamiltonian approach to QCD in Coulomb gauge: From the vacuum to finite temperatures,” in *Proceedings of the 4th International Conference on New Frontiers in Physics, ICNFP 2015*, Greece, August 2015.
- [18] H. Reinhardt, G. Burgio, D. Campagnari et al., “Hamiltonian approach to QCD in Coulomb gauge at zero and finite temperature,” in *Proceedings of the 12th Quark Confinement and the Hadron Spectrum*, Greece, September 2017.
- [19] H. Reinhardt, “Hamiltonian finite-temperature quantum field theory from its vacuum on partially compactified space,” *Physical Review D: Particles, Fields, Gravitation and Cosmology*, vol. 94, no. 4, Article ID 045016, 2016.
- [20] N. H. Christ and T. D. Lee, “Operator ordering and Feynman rules in gauge theories,” *Physical Review D: Particles, Fields, Gravitation and Cosmology*, vol. 22, no. 4, pp. 939–958, 1980.
- [21] D. Schütte, “Nonperturbative many-body techniques applied to a Yang-Mills field theory,” *Physical Review D: Particles, Fields, Gravitation and Cosmology*, vol. 31, no. 4, pp. 810–821, 1985.
- [22] A. P. Szczepaniak and E. S. Swanson, “Coulomb gauge QCD, confinement, and the constituent representation,” *Physical Review D: Particles, Fields, Gravitation and Cosmology*, vol. 65, no. 2, Article ID 025012, 2002.

- [23] J. Greensite, H. Matevosyan, S. Olejnik, M. Quandt, H. Reinhardt, and A. P. Szczepaniak, "Testing proposals for the Yang-Mills vacuum wavefunctional by measurement of the vacuum," *Physical Review D: Particles, Fields, Gravitation and Cosmology*, vol. 83, no. 11, Article ID 114509, 2011.
- [24] J. Heffner, H. Reinhardt, and D. R. Campagnari, "Deconfinement phase transition in the Hamiltonian approach to Yang-Mills theory in Coulomb gauge," *Physical Review D: Particles, Fields, Gravitation and Cosmology*, vol. 85, no. 12, Article ID 125029, 2012.
- [25] D. Epple, H. Reinhardt, and W. Schleifenbaum, "Confining solution of the Dyson-Schwinger equations in Coulomb gauge," *Physical Review D: Particles, Fields, Gravitation and Cosmology*, vol. 75, no. 4, Article ID 045011, 2007.
- [26] M. Leder, J. M. Pawłowski, H. Reinhardt, and A. Weber, "Hamiltonian flow in Coulomb gauge Yang-Mills theory," *Physical Review D: Particles, Fields, Gravitation and Cosmology*, vol. 83, no. 2, Article ID 025010, 2011.
- [27] C. Feuchter and H. Reinhardt, "The Yang-Mills vacuum in Coulomb gauge in $D = 2 + 1$ dimensions," *Physical Review D: Particles, Fields, Gravitation and Cosmology*, vol. 77, no. 8, Article ID 085023, 2008.
- [28] L. Moyaerts, *A Numerical Study of Quantum Forces: Casimir Effect, Vortices and Coulomb Gauge Yang-Mills Theory [PhD thesis]*, 2004.
- [29] G. Burgio, M. Quandt, H. Reinhardt, and H. Vogt, "Coulomb versus physical string tension on the lattice," *Physical Review D: Particles, Fields, Gravitation and Cosmology*, vol. 92, no. 3, Article ID 034518, 2015.
- [30] D. R. Campagnari, E. Ebadati, H. Reinhardt, and P. Vastag, "Revised variational approach to QCD in Coulomb gauge," *Physical Review D: Particles, Fields, Gravitation and Cosmology*, vol. 94, no. 7, Article ID 074027, 2016.
- [31] H. Reinhardt and J. Heffner, "Effective potential of the confinement order parameter in the Hamiltonian approach," *Physical Review D: Particles, Fields, Gravitation and Cosmology*, vol. 88, no. 4, Article ID 045024, 2013.
- [32] H. Reinhardt, "Dielectric function of the QCD vacuum," *Physical Review Letters*, vol. 101, no. 6, 2008.
- [33] S. Mandelstam, "Vortices and quark confinement in non-Abelian gauge theories," *Physics Reports*, vol. 23, no. 3, pp. 245–249, 1976.
- [34] G. 't Hooft, "The topological mechanism for permanent quark confinement in a non-abelian gauge theory," *Physica Scripta*, vol. 25, no. 1, pp. 133–142, 1982.
- [35] G. Burgio, M. Quandt, and H. Reinhardt, "Coulomb-gauge gluon propagator and the Gribov formula," *Physical Review Letters*, vol. 102, no. 3, Article ID 032002, 2009.
- [36] D. R. Campagnari and H. Reinhardt, "Non-Gaussian wave functionals in Coulomb gauge Yang-Mills theory," *Physical Review D: Particles, Fields, Gravitation and Cosmology*, vol. 82, no. 10, Article ID 105021, 2010.
- [37] P. de Forcrand and J. E. Hetrick, "The continuum limit of the lattice Gribov problem, and a solution based on Hodge decomposition," *Nuclear Physics B (Proceedings Supplements)*, vol. 42, no. 1-3, pp. 861–866, 1995.
- [38] A. Sternbeck and M. Müller-Preussker, "Lattice evidence for the family of decoupling solutions of Landau gauge Yang-Mills theory," *Physics Letters B*, vol. 726, no. 1-3, pp. 396–403, 2013.
- [39] P. Cooper and D. Zwanziger, "Spectral decomposition of the ghost propagator and a necessary condition for confinement," *Physical Review D: Particles, Fields, Gravitation and Cosmology*, vol. 93, no. 10, Article ID 105024, 2016.
- [40] G. Burgio, M. Quandt, H. Reinhardt, and H. Vogt, "Gribov horizon and Gribov copies effect in lattice Coulomb gauge," *Physical Review D: Particles, Fields, Gravitation and Cosmology*, vol. 95, no. 1, Article ID 014503, 2017.
- [41] D. Zwanziger, "No confinement without Coulomb confinement," *Physical Review Letters*, vol. 90, 2003.
- [42] J. Greensite, Š. Olejnik, and D. Zwanziger, "Coulomb energy, remnant symmetry, and the phases of non-Abelian gauge theories," *Physical Review D: Particles, Fields, Gravitation and Cosmology*, vol. 69, no. 7, Article ID 074506, 2004.
- [43] A. Voigt, E.-M. Ilgenfritz, M. Müller-Preussker, and A. Sternbeck, "Effective Coulomb potential in SU(3) lattice yang-mills theory," *Physical Review D: Particles, Fields, Gravitation and Cosmology*, vol. 78, no. 1, Article ID 014501, 2008.
- [44] J. Greensite, *An Introduction to the Confinement Problem*, vol. 821 of *Lecture Notes in Physics*, Springer-Verlag, Berlin, Germany, 2011.
- [45] H. Reinhardt, "Topology of center vortices," *Nuclear Physics B*, vol. 628, no. 1-2, pp. 133–166, 2002.
- [46] P. De Forcrand and M. D'Elia, "Relevance of center vortices to QCD," *Physical Review Letters*, vol. 82, no. 23, pp. 4582–4585, 1999.
- [47] L. Del Debbio, M. Faber, J. Greensite, and S. Olejnik, "Detection of center vortices in the lattice Yang-Mills vacuum," *Physical Review D: Particles, Fields, Gravitation and Cosmology*, vol. 58, Article ID 094501, 1998.
- [48] K. Langfeld, H. Reinhardt, and O. Tennert, "Confinement and scaling of the vortex vacuum of SU(2) lattice gauge theory," *Physics Letters. B. Particle Physics, Nuclear Physics and Cosmology*, vol. 419, no. 1-4, pp. 317–321, 1998.
- [49] M. Pak and H. Reinhardt, "Quark sector of the QCD ground-state in Coulomb gauge," *Physical Review D: Particles, Fields, Gravitation and Cosmology*, vol. 88, no. 12, Article ID 125021, 2013.
- [50] P. Vastag, H. Reinhardt, and D. Campagnari, "Improved variational approach to QCD in Coulomb gauge," *Physical Review D: Particles, Fields, Gravitation and Cosmology*, vol. 93, no. 6, Article ID 065003, 2016.
- [51] J. R. Finger and J. E. Mandula, "Quark pair condensation and chiral symmetry breaking in QCD," *Nuclear Physics B*, vol. 199, no. 1, pp. 168–188, 1982.
- [52] S. L. Adler and A. C. Davis, "Chiral symmetry breaking in Coulomb gauge QCD," *Nuclear Physics B*, vol. 244, no. 2, pp. 469–491, 1984.
- [53] R. Alkofer and P. A. Amundsen, "Chiral symmetry breaking in an instantaneous approximation to Coulomb gauge QCD," *Nuclear Physics B*, vol. 306, no. 2, pp. 305–342, 1988.
- [54] H. Reinhardt, D. R. Campagnari, and A. P. Szczepaniak, "Variational approach to Yang-Mills theory at finite temperatures," *Physical Review D: Particles, Fields, Gravitation and Cosmology*, vol. 84, no. 4, Article ID 045006, 2011.
- [55] J. Heffner and H. Reinhardt, "Finite-temperature Yang-Mills theory in the Hamiltonian approach in Coulomb gauge from a compactified spatial dimension," *Physical Review D: Particles, Fields, Gravitation and Cosmology*, vol. 91, no. 8, Article ID 085022, 2015.
- [56] H. Reinhardt and P. Vastag, "Chiral and deconfinement phase transition in the Hamiltonian approach to QCD in Coulomb gauge," *Physical Review D: Particles, Fields, Gravitation and Cosmology*, vol. 94, no. 10, 2016.

- [57] B. Svetitsky, “Symmetry aspects of finite-temperature confinement transitions,” *Physics Reports*, vol. 132, no. 1, pp. 1–53, 1986.
- [58] J. Braun, H. Gies, and J. M. Pawłowski, “Quark confinement from colour confinement,” *Physics Letters B*, vol. 684, no. 4-5, pp. 262–267, 2010.
- [59] M. Florian and J. M. Pawłowski, *Confinement in Polyakov Gauge*, 2008.
- [60] M. Quandt and H. Reinhardt, “Covariant variational approach to Yang-Mills theory: effective potential of the Polyakov loop,” *Physical Review D: Particles, Fields, Gravitation and Cosmology*, vol. 94, no. 6, 065015, 17 pages, 2016.
- [61] N. Weiss, “Effective potential for the order parameter of gauge theories at finite temperature,” *Physical Review D: Particles, Fields, Gravitation and Cosmology*, vol. 24, no. 2, pp. 475–480, 1981.
- [62] H. Reinhardt and J. Heffner, “The effective potential of the confinement order parameter in the Hamiltonian approach,” *Physics Letters B*, vol. 718, no. 2, pp. 672–677, 2012.
- [63] B. Lucini, M. Teper, and U. Wenger, “The high temperature phase transition in SU(N) gauge theories,” *Journal of High Energy Physics*, vol. 2004, no. 01, pp. 061-061, 2004.
- [64] C. Gattringer, “Linking confinement to spectral properties of the Dirac operator,” *Physical Review Letters*, vol. 97, no. 3, Article ID 032003, 2006.
- [65] F. Synatschke, A. Wipf, and C. Wozar, “Spectral sums of the Dirac-Wilson operator and their relation to the Polyakov loop,” *Physical Review D: Particles, Fields, Gravitation and Cosmology*, vol. 75, no. 11, Article ID 114003, 2007.
- [66] E. Bilgici, F. Bruckmann, C. Gattringer, and C. Hagen, “Dual quark condensate and dressed Polyakov loops,” *Physical Review D: Particles, Fields, Gravitation and Cosmology*, vol. 77, no. 9, Article ID 094007, 2008.
- [67] B. Zhang, F. Bruckmann, Z. Fodor, C. Gattringer, and K. K. Szabó, “Dual condensate and QCD phase transition,” in *Proceedings of the 9th International Conference on Quark Confinement and the Hadron Spectrum, QCHS IX*, pp. 170–172, Spain, September 2011.
- [68] J. Braun, L. M. Haas, F. Marhauser, and J. M. Pawłowski, “Phase structure of two-flavor QCD at finite chemical potential,” *Physical Review Letters*, vol. 106, no. 2, Article ID 022002, 2011.
- [69] C. S. Fischer, A. Maas, and J. A. Müller, “Chiral and deconfinement transition from correlation functions: SU(2) vs. SU(3),” *The European Physical Journal C*, vol. 68, no. 1, pp. 165–181, 2010.
- [70] S. Borsányi, Z. Fodor, and C. Hoelbling, “Is there still any T_c mystery in lattice QCD? Results with physical masses in the continuum limit III,” *Journal of High Energy Physics*, vol. 2010, article 73, 2010.
- [71] A. Bazavov et al., “The chiral and deconfinement aspects of the QCD transition,” *Physical Review D: Particles, Fields, Gravitation and Cosmology*, vol. 85, Article ID 054503, 2012.

Research Article

A Renormalisation Group Approach to the Universality of Wigner's Semicircle Law for Random Matrices with Dependent Entries

Thomas Krajewski

Centre de Physique Théorique, Aix-Marseille Université, Marseille, France

Correspondence should be addressed to Thomas Krajewski; krajewsk@gmail.com

Received 15 June 2017; Revised 1 September 2017; Accepted 1 October 2017; Published 31 December 2017

Academic Editor: Ralf Hofmann

Copyright © 2017 Thomas Krajewski. This is an open access article distributed under the Creative Commons Attribution License, which permits unrestricted use, distribution, and reproduction in any medium, provided the original work is properly cited. The publication of this article was funded by SCOAP³.

We show that if the non-Gaussian part of the cumulants of a random matrix model obeys some scaling bounds in the size of the matrix, then Wigner's semicircle law holds. This result is derived using the replica technique and an analogue of the renormalisation group equation for the replica effective action.

1. Introduction

Random matrix theory (see the classical text [1]) first appeared in physics in Wigner's work on the level spacing in large nuclei. Since then, it has proven to have multiple applications to physics and other branches of science (see, e.g., [2]). Most of these applications rely on the universal behaviour of some of the observables for matrices of large size. A simple example is Wigner's semicircle law for the eigenvalue density that holds in the large N limit for matrices whose entries are independent and identically distributed.

Understanding the universal behaviour of eigenvalue distributions and correlations ranks among the major problems in random matrix theory. In this respect, the renormalisation group turns out to be a powerful technique. Introduced in the context of critical phenomena in statistical mechanics by K. Wilson to account for the universality of critical exponents, the latter has also been proven to be useful in understanding probability theory. For instance, it leads to an insightful proof of the central limit theorem (see the review by Jona-Lasinio [3] and references therein).

The renormalisation group has been used to derive the semicircle law for random matrices in the pioneering work of Brézin and Zee [4]. In the latter approach, the renormalisation group transformation consists in integrating over the last line and column of a matrix of size $N+1$ to reduce

it to a matrix of size N . This leads to a differential equation for the resolvent $G(z) = 1/N \langle \text{Tr}(z - M)^{-1} \rangle$ in the large N limit whose solution yields the semicircle law.

In this paper, we follow a different route: we first express the resolvent as an integral over replicas and introduce a differential equation for the replica effective action. This differential equation is a very simple analogue of Polchinski's exact renormalisation group equation [5]. It is used to derive inductive bounds on the various terms, ensuring that the semicircle law is obeyed provided the cumulants of the original matrix model fulfil some simple scaling bounds in the large N limit.

This paper is based on some work in collaboration with Krajewski et al. in which we extend Wigner's law to random matrices whose entries fail to be independent [6] to which we refer for further details. There have been other works on such an extension (see [7–9]).

2. What Are Random Matrices?

A random matrix is a probability law on a space of matrices, usually given by the joint probability density on its entries:

$$\rho(M) = \rho(M_{11}, M_{12}, \dots). \quad (1)$$

Thus, a random matrix of size N is defined as a collection of N^2 random variables. However, there is a much richer structure than this, relying notably on the spectral properties of the matrices.

Here, we restrict our attention to a single random matrix. Note that it is also possible to consider several random matrices, in which case the noncommutative nature of matrix multiplication plays a fundamental role, leading to the theory of noncommutative probabilities.

There are two important classes of probability laws on matrices:

- (i) Wigner ensemble: the entries are all independent variables:

$$\rho(M) = \prod_{i,j} \rho_{ij}(M_{ij}), \quad (2)$$

up to the Hermitian condition $\overline{M}_{ij} = M_{ji}$.

- (ii) Unitary ensemble: the probability law is invariant under unitary transformations:

$$\rho(UMU^\dagger) = \rho(M), \quad (3)$$

for any unitary matrix $U \in U(N)$.

The only probability laws that belong to both classes are the Gaussian ones:

$$\rho(M) \propto \exp - \frac{1}{2\sigma^2} \text{Tr}(M)^2, \quad (4)$$

up to a shift of M by a fixed scalar matrix.

The main objects of interest are the expectation values of observables, defined as

$$\langle \mathcal{O} \rangle = \int dM \rho(M) \mathcal{O}(M). \quad (5)$$

Among the observables, the spectral observables defined as symmetric functions of the eigenvalues of M play a crucial role in many applications. This is essentially due to their universal behaviour: in the large N limit, for some matrix ensembles and in particular regimes, the expectation values of specific spectral observables do not depend on the details of the probability law $\rho(M)$.

Universality is at the root of the numerous applications to physics and other sciences, since the results we obtain are largely model-independent. Among the applications to physics, let us quote the statistics of energy levels in heavy nuclei, disordered mesoscopic systems, quantum chaos, chiral Dirac operators, and so forth.

3. Wigner's Semicircle Law

In this paper, we focus on the eigenvalue density, defined as

$$\rho(\lambda) = \frac{1}{N} \left\langle \sum_{1 \leq i \leq N} \delta \left[\lambda - \lambda_i \left(\frac{M}{\sqrt{N}} \right) \right] \right\rangle. \quad (6)$$

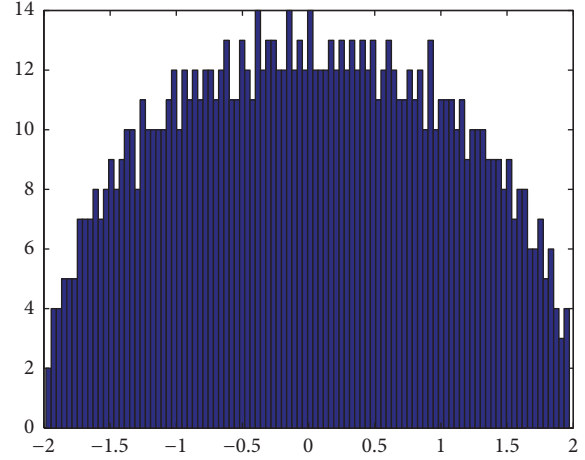


FIGURE 1: Spectrum of a large ($N = 1000$) Hermitian matrix with a Gaussian distribution ($\sigma = 1$).

In particular, a universal behaviour is expected in the large N limit for some ensembles.

For a Gaussian random Hermitian matrix $\rho(M) \propto \exp - (1/2\sigma^2) \text{Tr}(M^2)$, the eigenvalue density obeys Wigner's semicircle law:

$$\lim_{N \rightarrow \infty} \int_{\mathbb{R}} d\lambda \lambda^k \rho(\lambda) = \begin{cases} \frac{1}{2\pi\sigma^{k+2}} \int_{-2\sigma}^{2\sigma} d\lambda \lambda^k \sqrt{4\sigma^2 - \lambda^2}, & \text{if } k \text{ is even,} \\ 0, & \text{if } k \text{ is odd.} \end{cases} \quad (7)$$

Empirically, $\rho(\lambda)$ may be determined by plotting the histogram of eigenvalue of a matrix taken at random with a given probability law (see Figure 1).

The derivation of Wigner's semicircle in the large N limit is based on the resolvent (also known as the Green function):

$$G(z) = \lim_{N \rightarrow +\infty} \frac{1}{N} \left\langle \text{Tr} \left(z - \frac{M}{\sqrt{N}} \right)^{-1} \right\rangle = \frac{z}{2\sigma^2} \left(1 - \sqrt{1 - \frac{4\sigma^2}{z^2}} \right). \quad (8)$$

Then, the density of eigenvalues is recovered as

$$\rho(\lambda) = \frac{G(\lambda - i0^+) - G(\lambda + i0^+)}{2i\pi}, \quad (9)$$

where we have used the relation

$$\frac{1}{x \pm i0^+} = \text{p.v.} \frac{1}{x} \mp 2i\pi\delta(x). \quad (10)$$

In the large N limit, for the Gaussian model, the resolvent obeys the self-consistency equation (also known as the Schwinger-Dyson equation) (see, e.g., [10], Section VII.4):

$$G(z) = \sum_{k=0}^{\infty} \frac{\sigma^k G^k(z)}{z^{k+1}} = \frac{1}{z - \sigma G(z)}. \quad (11)$$

Its solution that behaves as $1/z$ for large z is

$$G(z) = \frac{z}{2\sigma^2} \left(1 - \sqrt{1 - \frac{4\sigma^2}{z^2}} \right). \quad (12)$$

Taking the cut of the square root on the negative real axis, we obtain Wigner's semicircle law (7) in the large N limit.

The semicircle law is not limited to the Gaussian case; it also holds for Wigner matrices in the large N limit. A random Hermitian $N \times N$ matrix is a Wigner matrix if

- (i) real and imaginary parts of upper diagonal elements are independent and identically distributed (i.i.d.) with mean 0 and variance σ ;
- (ii) diagonal elements are i.i.d. with finite mean and variance and independent of the off-diagonal ones.

Then, in the limit $N \rightarrow +\infty$, the eigenvalue distribution of M/\sqrt{N} is the semicircle law (7).

The original proof is of combinatorial nature and involves the expectation of the moments:

$$\begin{aligned} & \lim_{N \rightarrow +\infty} \frac{1}{N^{k/2+1}} \langle \text{Tr}(M^k) \rangle \\ &= \begin{cases} \frac{(2l)!}{(l!)^2 (l+1)}, & \text{for } k = 2l \text{ even,} \\ 0, & \text{for } k \text{ odd.} \end{cases} \end{aligned} \quad (13)$$

To derive this result, the idea is to first factorise ρ for a Wigner ensemble as

$$\rho(M) = \prod_i \rho'(M_{ii}) \prod_{i < j} \rho''(\text{Re } M_{ij}) \rho''(\text{Im } M_{ij}), \quad (14)$$

where ρ' is the common probability density of the real diagonal terms and ρ'' is the common probability density of the real and imaginary parts of the off-diagonal terms.

Then, we expand the trace and integrate over the independent real variables M_{ii} , $\text{Re } M_{ij}$, and $\text{Im } M_{ij}$. The power of N in the expectation of a given moment arises from the denominator $1/N^{k/2+1}$ and from the number of independent indices in the summations. In the large N limit, the only configurations that survive are counted by Catalan numbers: $C_l = (2l)!/(l!)^2(l+1)$. Since the latter also appear in the Taylor expansion,

$$\frac{z}{2\sigma^2} \left(1 - \sqrt{1 - \frac{4\sigma^2}{z^2}} \right) = \sum_{l \geq 0} \frac{(2l)!}{(l!)^2 (l+1)} \frac{\sigma^{2l}}{z^{2l+1}}, \quad (15)$$

we conclude that

$$\begin{aligned} G(z) &= \lim_{N \rightarrow +\infty} \frac{1}{N} \left\langle \text{Tr} \left(z - \frac{M}{\sqrt{N}} \right)^{-1} \right\rangle \\ &= \lim_{N \rightarrow +\infty} \sum_{k=0}^{\infty} \frac{1}{z^{k+1}} \frac{1}{N^{k/2+1}} \langle \text{Tr}(M^k) \rangle \\ &= \frac{z}{2\sigma^2} \left(1 - \sqrt{1 - \frac{4\sigma^2}{z^2}} \right). \end{aligned} \quad (16)$$

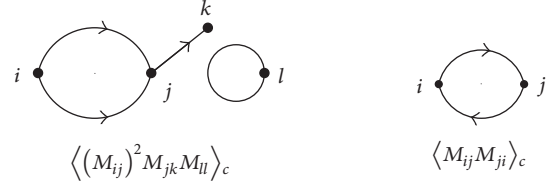


FIGURE 2: Examples of graph associated with cumulants.

This is the form of the resolvent which leads to Wigner's semicircle law. Here, we see universality at work: in the large N limit, the eigenvalue density is given by the semicircle law, whatever the probability densities ρ' and ρ'' are. However, this result relies on the independence of the matrix elements. In the next section, we will extend it to matrices whose entries are not necessary independent.

4. Wigner's Law beyond Wigner Ensembles

Let us introduce the cumulants, defined through their generating function:

$$\begin{aligned} & \langle M_{i_1 j_1} \cdots M_{i_l j_l} \rangle_c \\ &= \frac{\partial}{\partial J_{j_1 i_1}} \cdots \frac{\partial}{\partial J_{j_l i_l}} \log \langle \exp \text{Tr}(MJ) \rangle \Big|_{J=0}. \end{aligned} \quad (17)$$

In the physics terminology, these are the connected correlation functions. In particular, the Gaussian cumulants vanish beyond the quadratic term:

$$\begin{aligned} \rho(M) &\propto \exp - \frac{1}{2\sigma^2} \text{Tr}(M^2) \\ &\implies \begin{cases} \langle M_{ij} M_{kl} \rangle_c = \sigma^2 \delta_{il} \delta_{jk} \\ \text{vanish otherwise.} \end{cases} \end{aligned} \quad (18)$$

Therefore, cumulants of degree higher than 2 are a measure of the deviation from the Gaussian case.

Turning back to the general case, for each cumulant, we construct an oriented graph as follows (see Figure 2 for some examples):

- (i) Vertices are distinct matrix indices in the cumulant.
- (ii) There is an edge from i to j for every M_{ij} .

Since nonquadratic cumulants measure deviations from the Gaussian case, if the perturbation is small, it is reasonable to expect that the semicircle law is still obeyed.

To state this result, recall that an oriented graph is Eulerian if every vertex has an equal number of incoming and outgoing edges. Equivalently, it means that every connected component admits an Eulerian cycle, that is, an oriented cycle that passes through all edges, respecting the orientation. Furthermore, let us denote by $\nu(G)$, $e(G)$, and $c(G)$ the numbers of vertices, edges, and connected components of G , respectively.

Theorem 1 (Wigner's law for matrices with dependent entries). Let ρ_N be a probability law on the space of Hermitian $N \times N$ matrices M such that its cumulants can be decomposed as $C_G = C'_G + C''_G$, with C'_G being a Gaussian cumulant and C''_G being a perturbation such that, uniformly in the vertex indices $i_1, \dots, i_{v(G)}$ (i.e., all constants involved should not depend on these indices),

- (i) $\lim_{N \rightarrow \infty} N^{v(G)-c(G)-e(G)/2} C''_G(i_1, \dots, i_{v(G)}) = 0$ if G is Eulerian,
- (ii) $N^{v(G)-c(G)-e(G)/2} C''_G(i_1, \dots, i_{v(G)})$ is bounded if G is not Eulerian.

Then, the moments of the eigenvalue distribution of the matrix M/\sqrt{N} converge towards the moments of the semicircle law, with σ given by the Gaussian cumulant $\langle M_{ij} M_{kl} \rangle_c = \sigma^2 \delta_{il} \delta_{jk}$:

$$\begin{aligned} & \lim_{N \rightarrow \infty} \int_{\mathbb{R}} d\lambda \lambda^k \rho_N(\lambda) \\ &= \begin{cases} \frac{1}{2\pi\sigma^{k+2}} \int_{-2\sigma}^{2\sigma} d\lambda \lambda^k \sqrt{4\sigma^2 - \lambda^2} & \text{if } k \text{ is even,} \\ 0 & \text{if } k \text{ is odd.} \end{cases} \end{aligned} \quad (19)$$

For instance, for the graph

- (i) there is no graph with $v \geq 3$ (independence of off diagonal matrix elements);
- (ii) for $v = 1$ and $v = 2, e \geq 3$, bounds are satisfied because of $1/N^{e/2}$ and all moments are assumed to be finite;
- (iii) $C_{i \rightarrow j} (i, j) = \langle M_{ij} \rangle_c = \langle M_{ij} \rangle = 0$ (off diagonal elements have mean value 0);
- (iv) $C_{i \circ j \circ} (i, j) = \langle M_{ii} M_{jj} \rangle_c = \langle M_{ii} M_{jj} \rangle - \langle M_{ii} \rangle \langle M_{jj} \rangle = 0$ (independence of diagonal elements);
- (v) $C_{i \rightarrow j} (i, j) = \langle M_{ij} M_{jj} \rangle_c = \langle M_{ij} M_{jj} \rangle - \langle M_{ij} \rangle \langle M_{jj} \rangle = 0$ (independence of diagonal and off diagonal elements);
- (vi) $C_{i \circ j} (i, j) = \langle M_{ij} M_{ij} \rangle_c = \langle M_{ij} M_{ij} \rangle - \langle M_{ij} \rangle \langle M_{ij} \rangle = \langle (\text{Re} M_{ij})^2 - (\text{Im} M_{ij})^2 \rangle + 2i \langle \text{Re} M_{ij} \text{Im} M_{ij} \rangle = 0$ (independence of real and imaginary parts and equality of their distributions with mean value 0);
- (vii) $C_{i \circ j} = \sigma^2$ is the Gaussian cumulant leading to the semicircle law.

The case of unitarily invariant matrices is critical since the bounds are saturated (see [6]). This is consistent since we know that the semicircle law is not obeyed by unitary non-Gaussian ensembles [11].

It is possible to give a combinatorial proof of this result based on the relation between moments and cumulants:

$$\begin{aligned} & \langle M_{i_1 j_1} \cdots M_{i_k j_k} \rangle \\ &= \sum_{\substack{I_1, \dots, I_p \text{ partition of} \\ \{(i_1, j_1), \dots, (i_k, j_k)\}}} \left\langle \prod_{ij \in I_1} M_{ij} \right\rangle_c \cdots \left\langle \prod_{ij \in I_p} M_{ij} \right\rangle_c. \end{aligned} \quad (22)$$



which is not Eulerian, with $v = 3, e = 4$, and $c = 2$, the cumulant should obey

$$\frac{1}{N} \left| \left\langle (M_{ij})^2 M_{jk} M_{kl} \right\rangle_c \right| \leq K, \quad (20)$$

with K being a constant that does not depend on the indices i, j, k , and l . On the other hand, for the graph



which is Eulerian, with $v = 2, e = 4$, and $c = 1$, we impose

$$\lim_{N \rightarrow +\infty} \frac{1}{N} \left| \left\langle (M_{ij})^2 (M_{ji})^2 \right\rangle_c \right| = 0 \quad (21)$$

uniformly in i and j .

As an illustration, we recover the case of Wigner matrices (with finite moments). Indeed,

In the moment method, we have to estimate

$$\begin{aligned} & \frac{1}{N^{k/2+1}} \langle \text{Tr}(M^k) \rangle \\ &= \frac{1}{N^{k/2+1}} \sum_{1 \leq i_1, \dots, i_k \leq N} \langle M_{i_1 i_2} \cdots M_{i_k i_1} \rangle. \end{aligned} \quad (23)$$

Then, we express the moments in (23) in terms of cumulants using (22) and represent each cumulant as a graph. Because of the trace, one has to draw Eulerian cycles on the graphs after some vertex identifications. Then, the scaling bounds on the cumulants can be used to show that only Gaussian terms survive.

5. Proof Based on the Replica Effective Action

Let us give a renormalisation group proof of this result based on the replica effective action. The use of replicas in random matrix theory is a classical subject (see, e.g., [12] or [13]). To begin with, let us note that

$$\text{Tr} \left(z - \frac{M}{\sqrt{N}} \right)^{-1} = \frac{\partial}{\partial z} \log \det \left(z - \frac{M}{\sqrt{N}} \right). \quad (24)$$

It is convenient to express the logarithm using the replica method. First, observe that

$$\log(A) = \lim_{n \rightarrow 0} \frac{A^n - 1}{n}. \quad (25)$$

Then, we express the n th power of the determinant as a Gaussian integral over n replicas of a complex vector of size N (with a factor of π^{nN} included in the measure):

$$\frac{1}{\det^n(z - M)} = \int dX \exp -\text{Tr}(X^\dagger(z - M)X), \quad (26)$$

which fit into an $N \times n$ complex matrix $X = (X_{i,a})_{\substack{1 \leq i \leq N \\ 1 \leq a \leq n}}$.

The limit $n \rightarrow 0$ may be worrisome; its meaning is as follows. Because of $U(n)$ invariance, any perturbative result in powers of $1/z$ is a polynomial in n , from which we retain only the linear term. Of course, this may not hold beyond perturbation theory, where replica symmetry breaking can occur.

After averaging over M with the random matrix density $\rho(M)$, we obtain the following expression for the resolvent:

$$G(z) = -\frac{1}{N} \frac{\partial}{\partial z} \left[\int dX \exp \left\{ -\text{Tr}(X^\dagger X) + V_0(X) \right\} \right]_{\text{order 1 in } n}, \quad (27)$$

where the replica potential is

$$V_0(X) = \log \left\langle \exp \text{Tr} \left(X^\dagger \frac{M}{\sqrt{N}} X \right) \right\rangle. \quad (28)$$

Because of the logarithm, the potential involves the cumulants and can be expanded over graphs as

$$V_0(X) = \sum_{\substack{G \\ \text{oriented graph}}} \frac{1}{|\text{Aut}(G)| N^{e(G)/2}} \cdot \sum_{\substack{1 \leq i_1, \dots, i_{v(G)} \leq N \\ \text{all different}}} C_G(i_1, \dots, i_{v(G)}) \cdot \prod_{e \text{ edge}} (XX^\dagger)_{i_s(e) i_t(e)}, \quad (29)$$

where $s(e)$ is the source of edge e and $t(e)$ is its target.

Let us introduce a replica effective action, obtained by a partial integration:

$$V(t, X) = \log \int dY \exp \left\{ -\frac{\text{Tr}(Y^\dagger Y)}{t} + V_0(X + Y) \right\} - Nn \log t. \quad (30)$$

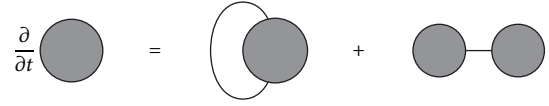


FIGURE 3: Graphical interpretation of the renormalisation group equation.

The parameter t ranges between 0 (where we have no integration, $V(t = 0, X) = V_0(X)$) and $t = 1/z$.

The effective potential obeys a semigroup property that follows from Gaussian convolution (see, e.g., [14], Section A10.1):

$$V(t + s, X) = \log \int dY \exp \left\{ -\frac{\text{Tr}(Y^\dagger Y)}{s} + V(t, X + Y) \right\} - Nn \log s. \quad (31)$$

For small $s = dt$, it translates into the following renormalisation group equation, which is a simple version of Polchinski's exact renormalisation group equation [5]:

$$\frac{\partial V(t, X)}{\partial t} = \sum_{i,a} \left(\frac{\partial^2 V(t, X)}{\partial X_{i,a} \partial \bar{X}_{i,a}} + \frac{\partial V(t, X)}{\partial X_{i,a}} \frac{\partial V(t, X)}{\partial \bar{X}_{i,a}} \right). \quad (32)$$

The first term on the RHS is referred to as the loop term, since it creates a new loop in the Feynman graph expansion of the effective action, while the second inserts a one-particle reducible line and is referred to as the tree term (see Figure 3).

Taking into account the boundary condition $V(t = 0, X) = V_0(X)$, it is convenient to write (32) in integral form:

$$V(t, X) = V_0(X) + \int_0^t ds \sum_{i,a} \left(\frac{\partial^2 V(s, X)}{\partial X_{i,a} \partial \bar{X}_{i,a}} + \frac{\partial V(s, X)}{\partial X_{i,a}} \frac{\partial V(s, X)}{\partial \bar{X}_{i,a}} \right). \quad (33)$$

This allows us to derive inductive bounds in powers of $t = 1/z$.

From a physical point of view, we evaluate the effective potential by a large succession of small partial integrations, with a total weight given by t . Let us stress that, in our context, this differential equation is merely a tool to control the t dependence of the effective action after integrating with a t -dependent propagator.

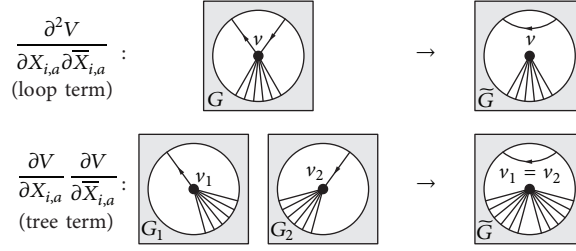


FIGURE 4: Action of the differential operators on the vertices of the effective action.

The effective potential also admits an expansion over graphs:

$$\begin{aligned}
 V(t, X) = & \sum_{\text{oriented graph } G} \frac{1}{|\text{Aut}(G)| N^{e(G)/2}} \\
 & \cdot \sum_{\substack{1 \leq i_1, \dots, i_{v(G)} \leq N \\ \text{all different}}} C_G(t; i_1, \dots, i_{v(G)}) \\
 & \cdot \prod_{e \text{ edge}} (XX^\dagger)_{i_{s(e)} i_{t(e)}}. \quad (34)
 \end{aligned}$$

This leads to a graphical interpretation of the action of the two differential operators in the renormalisation group equation (see Figure 4). Indeed, in the expansion (see (34)), an edge joining a vertex carrying label i to a vertex carrying j is equipped with a factor $\sum_a X_{i,a} \bar{X}_{j,a}$, with a being a replica index. Then, the differential operator $\partial/\partial X_{i,a}$ (resp., $\partial/\partial \bar{X}_{j,a}$) removes the outgoing (resp., incoming) half edge. Finally, the remaining half edges are reattached and the vertices identified to yield a new graph on the RHS of (33), with one less edge. These operations are performed on the same graph for the loop term and on distinct ones for the tree term.

Let us decompose the effective cumulants appearing in (34) into Gaussian ones and perturbations and expand both in a power series in $t = 1/z$:

$$C_G(t) = \sum_{k=0}^{\infty} t^k \left[\underbrace{C_G^{(k)}}_{\text{Gaussian}} + \underbrace{C_G^{(k)}}_{\text{perturbation}} \right]. \quad (35)$$

The Gaussian terms are those that are constructed using only the Gaussian term in the initial potential $V_0(X)$. Even if $V_0(X)$ is quartic in X , this does not hold for the Gaussian part of $V_t(X)$, which contains terms of all orders. The perturbation collects all the remaining terms; they contain at least one non-Gaussian perturbation from $V_0(X)$.

The renormalisation group equation (33) allows us to prove inductively on k that the perturbations $C_G^{(k)}$ obey the same scaling bound imposed on $C_G^{(0)} = C_G^{(0)}$ and that the purely Gaussian terms do not grow too fast.

$$\text{(i) } \lim_{N \rightarrow \infty} N^{v(G)-c(G)-e(G)/2} [C_G^{(k)}]_{\text{order } 0 \text{ in } n} = 0 \text{ if } G \text{ is Eulerian.}$$

$$\begin{aligned}
 \text{(ii) } & N^{v(G)-c(G)-e(G)/2} [C_G^{(k)}]_{\text{order } 0 \text{ in } n} \text{ is bounded if } G \text{ is not Eulerian.} \\
 \text{(iii) } & N^{v(G)-c(G)-e(G)/2} [C_G^{(k)}]_{\text{order } 0 \text{ in } n} \text{ is bounded for any } G.
 \end{aligned}$$

This involves a combinatorial discussion based on the graphical interpretation of Figure 4 which can be found in [6]. Let us simply mention that the terms that may violate the bounds are of higher order in n . Thus, they are harmless when taking the limit $n \rightarrow 0$ before the limit $N \rightarrow +\infty$.

Finally, using (27) and the renormalisation group equation (33), the resolvent can be expressed as

$$G(z) = \frac{1}{z} + \frac{1}{N^{3/2} z^2} \sum_{1 \leq i \leq N} \left[C_{i \bullet \circ} \left(\frac{1}{z}; i \right) \right]_{\text{order } 0 \text{ in } n}. \quad (36)$$

The scaling bounds for the non-Gaussian cumulants impose, perturbatively in $1/z$,

$$\lim_{N \rightarrow \infty} \frac{1}{\sqrt{N}} \left[C_{i \bullet \circ} \left(\frac{1}{z}; i \right) \right]_{\text{order } 0 \text{ in } n} = 0. \quad (37)$$

Therefore, only the Gaussian cumulants contribute and we recover Wigner's semicircle law.

6. Conclusion and Outlook

In this paper, we have argued that Wigner's semicircle law remains valid for matrices with dependent entries. The deviation from the independent case is measured by the joint cumulants of the entries, which are assumed to fulfil some scaling bound for large N . To establish this result, we have introduced an effective action for the replicas. This effective action obeys a renormalisation group equation that allowed us to prove perturbative bounds on the effective cumulants. As a consequence of these bounds, only the Gaussian terms contribute in the large N limit, thus establishing the validity of Wigner's semicircle law.

It may also be of interest to investigate the case of the sum of a random matrix M and a deterministic one A (see, e.g., [13], where such a model is discussed). In this case, the resolvent is expressed as

$$G(z) = -\frac{1}{N} \frac{\partial}{\partial z} \left[\int dX \exp \left\{ -\text{Tr} \left(X^\dagger (A + z) X \right) + V_0(X) \right\} \right]_{\text{order } 1 \text{ in } n} . \quad (38)$$

In our context, the deterministic matrix A induces a non-trivial kinetic for the replicas. In particular, if A is a discrete Laplacian, it yields a nontrivial renormalisation group flow that bears some similarities with the QFT renormalisation group. In this case, we expect to exploit the true power of the renormalisation group equation, with a discussion of fixed points and scaling dimensions.

Disclosure

This paper was presented at the 5th Winter Workshop on Non-Perturbative Quantum Field Theory, Sophia Antipolis, March 2017.

Conflicts of Interest

The author declares that there are no conflicts of interest regarding the publication of this paper.

Acknowledgments

The author wishes to thank the organisers of the workshop, Mario Gattobigio, Thierry Grandou, and Ralf Hoffmann, for their kind invitation, as well as Stan Brodsky for insightful remarks. The author is also grateful to his collaborators, Dinh Long Vu and Adrian Tanasa.

References

- [1] M. L. Mehta, *Random Matrices*, Academic Press, 2004.
- [2] G. Akemann, J. Baik, and Ph. Di Francesco, Eds., *Oxford Handbook of Random Matrix Theory*, Oxford Univ. Press, 2011.
- [3] G. Jona-Lasinio, “Renormalisation group and probability theory Phys,” *Physics Reports*, vol. 352, article 0009219, 439 pages, 2001, <https://arxiv.org/abs/cond-mat/0009219>.
- [4] E. Brézin and A. Zee, “Universality of the correlations between eigenvalues of large random matrices,” *Nuclear Physics B*, vol. 402, no. 3, pp. 613–627, 1993.
- [5] J. Polchinski, “Renormalization and effective lagrangians,” *Nuclear Physics B*, vol. 231, no. 2, pp. 269–295, 1984.
- [6] T. Krajewski, A. Tanasa, and D. L. Vu, “Wigner law for matrices with dependent entries: A perturbative approach,” *Journal of Physics A: Mathematical and Theoretical*, vol. 50, no. 16, 2017, <https://arxiv.org/abs/1609.01873>.
- [7] J. H. Schenker and H. Schulz-Baldes, “Semicircle law and freeness for random matrices with symmetries or correlations,” *Mathematical Research Letters*, vol. 12, no. 4, pp. 531–542, 2005.
- [8] K. Hofmann-Credner and M. Stolz, “Wigner theorems for random matrices with dependent entries: ensembles associated to symmetric spaces and sample covariance matrices,” *Electronic Communications in Probability*, vol. 13, pp. 401–414, 2008.
- [9] O. Friesen and M. Löwe, “The semicircle law for matrices with dependent entries”.

- [10] A. Zee, *Quantum Field Theory in a Nutshell*, Princeton University Press, Princeton, NJ, USA, 2nd edition, 2010.
- [11] E. Brezin, C. Itzykson, G. Parisi, and J. B. Zuber, “Planar diagrams,” *Communications in Mathematical Physics*, vol. 59, no. 1, pp. 35–51, 1978.
- [12] E. Kanzieper, “Replica Approach in Random Matrix Theory,” in *The Oxford Handbook of Random Matrix Theory*, Oxford Univ. Press, Oxford, UK, 2011.
- [13] A. Zee, “Law of addition in random matrix theory,” *Nuclear Physics B*, vol. 474, no. 3, pp. 726–744, 1996.
- [14] J. Zinn-Justin, “Quantum field theory and critical phenomena,” in *International Series of Monographs on Physics*, vol. 113, Oxford University Press, 2002.

Research Article

Relativistic Localizing Processes Bespeak an Inevitable Projective Geometry of Spacetime

Jacques L. Rubin

Université de Nice-Sophia Antipolis, Institut de Physique de Nice, UMR7010-UNS-CNRS, Site Sophia Antipolis, 1361 route des Lucioles, 06560 Valbonne, France

Correspondence should be addressed to Jacques L. Rubin; jacques.rubin@inphyni.cnrs.fr

Received 3 April 2017; Revised 15 June 2017; Accepted 3 July 2017; Published 25 October 2017

Academic Editor: Ralf Hofmann

Copyright © 2017 Jacques L. Rubin. This is an open access article distributed under the Creative Commons Attribution License, which permits unrestricted use, distribution, and reproduction in any medium, provided the original work is properly cited. The publication of this article was funded by SCOAP³.

Surprisingly, the issue of events localization in spacetime is poorly understood and *a fortiori* realized even in the context of Einstein's relativity. Accordingly, a comparison between observational data and theoretical expectations might then be strongly compromised. In the present paper, we give the principles of relativistic localizing systems so as to bypass this issue. Such systems will allow locating users endowed with receivers and, in addition, localizing any spacetime event. These localizing systems are made up of relativistic autolocating positioning subsystems supplemented by an extra satellite. They indicate that spacetime must be supplied everywhere with an unexpected local four-dimensional projective structure besides the well-known three-dimensional relativistic projective one. As a result, the spacetime manifold can be seen as a generalized Cartan space modeled on a four-dimensional real projective space, that is, a spacetime with both a local four-dimensional projective structure and a compatible (pseudo-)Riemannian structure. Localization protocols are presented in detail, while possible applications to astrophysics are also considered.

1. Introduction

The general principles of the *relativistic localizing systems* have been defined in a previous paper [1] with just a few details on the projective underlying structure provided by these localizing systems. The latter are based on the so-called *relativistic positioning systems* [2–9]. The protocols of relativistic positioning are a priori rather simple. For instance, in a four-dimensional spacetime, we can consider four emitting satellites and users with their respective (timelike) worldlines. The four emitters broadcast “emission coordinates” which are no more and no less than time stamps generated by onboard clocks and encoded within EM signals propagating in spacetime. Then, a so-called four-dimensional *emission grid* can be constructed from this relativistic positioning system and its system of emission coordinates. This grid can be eventually superposed to a *grid of reference* supplied by a “system of reference” (e.g., the well-known WGS84 system). And then, from this superposition, the positions of the users can be deduced in the given system of reference. More precisely, in relativistic positioning systems, the emitters broadcast not

only their own time stamps, but also the time stamps they receive from the others. This process of echoes undergone by the time stamps enables users to construct the four-dimensional emission grid because they can then deduce the spacetime positions of the four emitters. And then, because the positions of the four emitters can be known also in a given system of reference the users can deduce their own positions in this system of reference from their positions in the emission grid.

Here, we focus on the relativistic localizing systems which are systems incorporating relativistic positioning subsystems. We show how *causal axiomatics* [10–13] and particular projective structures (actually, compasses) homeomorphic to $P\mathbb{R}^1$ and $P\mathbb{R}^2$ attached all along the worldlines of the emitters of the localizing systems are sufficient to justify a four-dimensional projective structure of the spacetime; in addition to the well-known three-dimensional projective structure.

Beforehand, to proceed in the difficult and delicate description of the relativistic localizing systems, we first need to define as clearly as possible the terminology and the different conventions and notations.

2. Notations and Conventions

We consider a constellation of satellites called “*emitters*” which typically broadcast numerical values (called “*time stamps*”) generated, for instance, by embarked onboard clocks.

- (1) The “*main*” emitters are denoted by \mathcal{E} , $\overline{\mathcal{E}}$, $\tilde{\mathcal{E}}$, and $\hat{\mathcal{E}}$ with their respective worldlines \mathcal{W} , $\overline{\mathcal{W}}$, $\tilde{\mathcal{W}}$, and $\hat{\mathcal{W}}$. The “*ancillary*” emitter \mathcal{S} and the “*user*” \mathcal{U} have their worldlines denoted, respectively, by $\mathcal{W}^{\mathcal{S}}$ and \mathcal{V} .
- (2) The *main* emitters constitute the *relativistic positioning system*.
- (3) The *ancillary* emitter \mathcal{S} and the main emitters constitute the *relativistic localizing systems*.
- (4) The event to be localized is always denoted by the small capital letter e .
- (5) The user \mathcal{U} collects along its worldline all the data—in particular, the time stamps—from which the localization of the event e is deduced. Among these data, there are those for identifying physically the event e such as, for instance, its shape, its spectrum, and so forth, and which are obtained from apparatus making physical analyses embarked onboard each mean emitter.
- (6) Any explicit event will be marked by symbols like “ \bullet ,” “ \ast ,” “ \sim ,” “ \wedge ,” and so forth, or also by small capital letters like “ p ,” “ ℓ ,” and so forth. Non-marked or numbered events will refer to general or generic, unspecified events. For instance, E^\ast will be a specified event while E or E_2 will be generic, unspecified events.
- (7) The generic events E , \overline{E} , \tilde{E} , \hat{E} , S , and U belong, respectively, to the worldlines \mathcal{W} , $\overline{\mathcal{W}}$, $\tilde{\mathcal{W}}$, $\hat{\mathcal{W}}$, $\mathcal{W}^{\mathcal{S}}$, and \mathcal{V} .
- (8) The *time stamps* will be denoted by the Greek letters “ τ ,” “ $\overline{\tau}$,” “ $\tilde{\tau}$,” “ $\hat{\tau}$,” and “ τ^\ast .” The first four previous time stamps are “generated” and broadcast, respectively, by the main emitters \mathcal{E} , $\overline{\mathcal{E}}$, $\tilde{\mathcal{E}}$, and $\hat{\mathcal{E}}$, and the last one is “generated” and broadcast by the ancillary emitter \mathcal{S} . The four main emitters not only generate their own time stamps but transmit also the time stamps they receive. These main emitters constitute the various *autonomous autolocating* relativistic positioning systems from which the relativistic localizing systems presented further are constructed.
- (9) Two classes of *time stamps* are considered:
 - (i) The time stamps which are generated and then broadcast by the emitters at given events on their worldlines. Then, we agree to mark the corresponding time stamps like the given events. For instance, if an emitter generates and broadcasts a time stamp at the specified event \tilde{E}^\ast or at the generic event E_1 , then the respective time stamps will be denoted by $\tilde{\tau}^\ast$ or τ_1 .
 - (ii) The time stamps which are the *emission* (or *time*) coordinates of an event K —specified or

not—will be denoted by “ τ_K ,” “ $\overline{\tau}_K$,” “ $\tilde{\tau}_K$,” “ $\hat{\tau}_K$,” and “ τ_K^\ast .”

- (10) The ancillary emitter \mathcal{S} generates and broadcasts its own time stamp $\hat{\tau}$ and it broadcasts also its time (emission) coordinates provided by the relativistic positioning system. In other words, it is also a particular user of the relativistic positioning system like the user \mathcal{U} . Contrarily to the ancillary emitter, the user does not necessarily broadcast its emission coordinates.
- (11) Projective frames at events E will be denoted by \mathfrak{F}_E . There are sets of “canonical projective points $[\dots]_E$ ” which are the following:
 - (i) $\mathfrak{F}_E \equiv \{[0]_E, [1]_E, [\infty]_E\}$ for projective frames of the real projective line $P\mathbb{R}^1$, and
 - (ii) $\mathfrak{F}_E \equiv \{[0, 0]_E, [1, 1]_E, [0, \infty]_E, [\infty, 0]_E\}$ for projective frames of the 2-dimensional real projective space $P\mathbb{R}^2$.

The subscripts will be canceled out if there are no ambiguities on the referring event.

- (12) The celestial circles/spheres are denoted by \mathcal{C} , and then \mathcal{C}_K is the celestial circle/hemisphere at the event K . The celestial circles are invoked in the definition of the “echoing systems” of relativistic localizing systems in $(2 + 1)$ -dimensional spacetime presented in Section 4. Considering relativistic localizing systems and their corresponding echoing systems (Section 5) in $(3 + 1)$ -dimensional spacetime, then 2-dimensional projective spaces $P\mathbb{R}^2$ are also considered. But, contrarily to the relativistic localizing systems in $(2 + 1)$ -dimensional spacetime, the 2-dimensional real projective spaces $P\mathbb{R}^2$ cannot be immersed in spheres S^2 (or \mathbb{R}^2). Then, as well-known from the cell decomposition of $P\mathbb{R}^2 = \mathbb{R}^2 \cup P\mathbb{R}^1$, the Euclidean space \mathbb{R}^2 is identified in a standard way with a hemisphere of S^2 while $P\mathbb{R}^1$ is identified with half of the equatorial boundary (see, e.g., [14, p. 10–14] for details).
- (13) We denote by (see [15, Def. 3.1, p. R16] and [16])¹
 - (i) “ \prec ” the *causal* order,
 - (ii) “ \ll ” the *chronological* order, and
 - (iii) “ \rightarrow ” the *horismos* (or *horismotic* relation/order).
- (14) We call “*emission* (or *positioning*) grid \mathbb{R}_P^n ” the Euclidean space \mathbb{R}^n of positioning, and “*localization* (or *quadrometric/pentametric*) grid \mathbb{R}_L^m ” and “*anisotropic localization* (or *quadrometric/pentametric*) grid \mathbb{R}_{AL}^m ” two different Euclidean spaces $\mathbb{R}^{m-1} \times \mathbb{R}^\ast$ ascribed to two different, particular sets of time coordinates used for the localization.
- (15) The acronyms RPS and RLS mean, respectively, “*Relativistic Positioning System*” and “*Relativistic Localizing System*.”

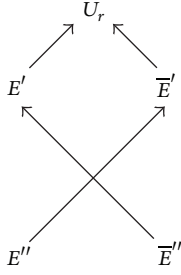


FIGURE 1: The causal structure of the RPS.

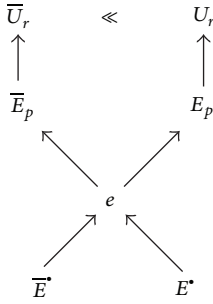


FIGURE 2: The causal structure of the RLS.

3. RLSs in (1 + 1)-Dimensional Spacetime

In this (1+1)-dimensional case, there are two main emitters \mathcal{E} and $\bar{\mathcal{E}}$ constituting the RPS, and with the ancillary emitter \mathcal{S} they constitute the RLS. We first give the causal structures of the RPS and the associated RLS. In Figures 1 and 2, and also, in all other subsequent figures representing a causal structure, the arrows represent always the horismotic relation between two events.

3.1. The Causal Structure of the RPS. We have the causal structure (see Figure 1 and Table 1) for the autolocating RPS from which the positioning of the user \mathcal{U} is realized.

Then, the position of the user at the event U_r in the emission grid \mathbb{R}_P^2 is $U_r \equiv (\tau', \bar{\tau}')$. Also, the user can know from the autolocating process the positions of the two emitters: $E' \equiv (\tau', \bar{\tau}'')$ and $\bar{E}' \equiv (\tau'', \bar{\tau}')$. Moreover, ephemerides are regularly uploaded onboard the main emitters which broadcast with their time stamps these ephemerides to the users. From these data, that is, ephemerides and positions of the main emitters, the users can deduce their own positions with respect to a given system of reference (e.g., the terrestrial frame of WGS84). This is the core and the important interest of the autolocating positioning systems to immediately furnish the positions of the users with respect to a given system of reference.

3.2. The Causal Structure of the RLS. In this very specific (1 + 1)-dimensional case, the localized event e is necessarily the intersection point of two null geodesics. The causal structure is shown in Figure 2 and Table 2.

TABLE 1: The events and their broadcast time stamps in the RPS.

Event	Broadcasts time stamp(s)	Received at
E''	τ''	\bar{E}'
\bar{E}''	$\bar{\tau}''$	E'
E'	$(\tau_{E'} = \tau', \bar{\tau}'')$	U_r
\bar{E}'	$(\tau'', \bar{\tau}' = \bar{\tau}_{\bar{E}'})$	U_r

TABLE 2: The events and their broadcast time stamps in the RLS.

Event	Broadcasts time stamp(s)	Received at
\bar{E}^*	$\bar{\tau}^*$	E_p
E^*	τ^*	\bar{E}_p
\bar{E}_p	$(\tau^*, \bar{\tau}_p = \bar{\tau}_{\bar{E}_p})$	U_r
E_p	$(\tau_{E_p} = \tau_p, \bar{\tau}^*)$	U_r

Then, the protocol of localization gives the following time coordinates for $e \equiv (\tau_e, \bar{\tau}_e)$ in the localization grid \mathbb{R}_L^2 : $\tau_e = \tau_{E'} = \tau^*$ and $\bar{\tau}_e = \bar{\tau}_{\bar{E}'} = \bar{\tau}^*$.

Remark 1. It matters to notice that the two events of reception U_r and \bar{U}_r are matched by the user on the basis of a crucial identification of the physical data transmitted by the two main emitters (see convention 5) which allow explicitly identifying the physical occurrence of an event e . And then, the whole different time stamps collected at these two events can be therefore considered by the user as those needed to make the localization of e .

3.3. Consistency between the Positioning and Localizing Protocols: Identification

Definition 2 (consistency). We say that the localizing and the positioning protocols or systems are “consistent” if and only if the time coordinates $(\tau_K, \bar{\tau}_K, \dots)$ ascribed to each event K belonging to an emitter’s worldline and provided by the localization (resp. positioning) system are the same as those provided by the positioning (resp., localization) system.

Remark 3. In this (1 + 1)-dimensional case, when we identify the time stamps τ_e and $\bar{\tau}_e$ with, respectively, $\tau_{E'}$ and $\bar{\tau}_{\bar{E}'}$, then the localization is equivalent to the positioning. This leads to the general Definition 5 below.

Remark 4. The consistency between the localizing and the positioning protocols is not an absolute necessity. We can obtain different time coordinates for the same event K belonging to an emitter’s worldline from the positioning system or the localizing one if we change the time stamps ascriptions in the protocols of localization presented further. Then, we can choose arbitrarily the emission grid or the grid of localization to position the event K , and, then, we can refer to the preferred grid for the time coordinates ascribed to any other event, positioned or localized. In other words, because the systems of localization include implicitly by construction derived positioning systems, the latter can differ from the initial ones. In this case, the consistency is not satisfied but

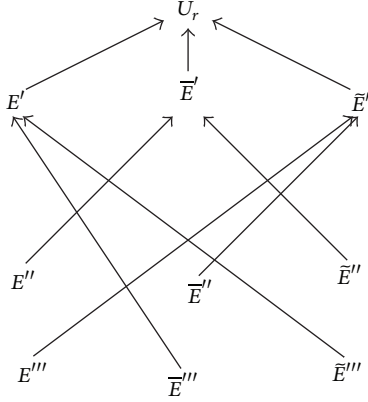


FIGURE 3: The causal structure of the RPS in a $(2 + 1)$ -dimensional spacetime.

we can still refer the time coordinates of any event with respect to the localization grids rather than to the emission grids. The only advantage of the consistency is that once the events are localized then the time coordinates can be ascribed indifferently to any of the two grids.

Definition 5. Let a localized event e and an event K on the worldlines of a *main* emitter or of the ancillary emitter be such that $e \rightarrow K$ or $K \rightarrow e$ or $e = K$. Then, we call “*identification*” in the emission (position) grid the ascription of an emission coordinate of e to an emission coordinate of K .

4. RLSs in $(2 + 1)$ -Dimensional Spacetime

In this case, there are three main emitters \mathcal{E} , $\bar{\mathcal{E}}$, and $\tilde{\mathcal{E}}$ constituting the autolocating RPS and, again, an ancillary emitter \mathcal{S} with which they constitute the RLS.

4.1. The Causal Structure of the RPS. This causal structure is described in Figure 3 and Table 3.

Then, the position in the emission grid \mathbb{R}_p^3 of the user at U_r is $(\tau', \bar{\tau}', \tilde{\tau}')$, and those of E' , \bar{E}' , and \tilde{E}' are, respectively, $(\tau', \bar{\tau}''', \tilde{\tau}''')$, $(\tau'', \bar{\tau}', \tilde{\tau}'')$, and $(\tau''', \bar{\tau}'', \tilde{\tau}')$.

Remark 6. It matters to notice that in autolocating RPSs the time stamp broadcast by each main emitter is also one of its emission coordinates, for example, $\tau_{E'} = \tau'$ for \mathcal{E} at E' in Table 1 and $\bar{\tau}' = \bar{\tau}_{\bar{E}'}$ for $\bar{\mathcal{E}}$ at \bar{E}' in Table 3. This property is common to any RPS whatever is the spacetime dimension.

4.2. The Description of the RLS and Its Causal Structures. The determination of the first emission coordinate τ_e for the event e to be localized is obtained from a first system of light “echoes” associated with the privileged emitter \mathcal{E} . And then, this system is linked to one event of reception $U_r \in \mathcal{V}$ where all the time stamps are collected by the user. We denote by $\mathcal{E}ch$ this system of light “echoes” on the worldline of the given, privileged emitter \mathcal{E} .

Also, one of the key ingredient in the echoing process presented below is the way any event K in the past null cone

TABLE 3: The events and their broadcast time stamps.

Event	Broadcasts time stamp(s)	Received at
E'''	τ'''	\bar{E}'
\bar{E}'''	$\bar{\tau}'''$	E'
\tilde{E}'''	$\tilde{\tau}'''$	E'
E''	τ''	\bar{E}'
\bar{E}''	$\bar{\tau}''$	\tilde{E}'
\tilde{E}''	$\tilde{\tau}''$	\bar{E}'
E'	$(\tau_{E'} = \tau', \bar{\tau}''', \tilde{\tau}''')$	U_r
\bar{E}'	$(\tau'', \bar{\tau}' = \bar{\tau}_{\bar{E}'}, \tilde{\tau}'')$	U_r
\tilde{E}'	$(\tau''', \bar{\tau}'', \tilde{\tau}_{\tilde{E}'} = \tilde{\tau}')$	U_r

of E_p is associated with a “bright” point on the celestial circle \mathcal{C}_{E_p} (see Figure 8). Because $K \rightarrow E_p$, we can only consider null “directions” k_{E_p} at the origin E_p and tangent at E_p to the null geodesic joining K to E_p . The abstract space whose element are these past null directions we call \mathcal{N}^- . This space can be represented by the intersection \mathcal{C}_{E_p} of the past null cone with a space-like surface passing through an event $N_p \in \mathcal{W}$ in the past vicinity of E_p , that is, $N_p \ll E_p$. Then, the exterior of this celestial circle represents space-like directions.

In physical terms, the significance of \mathcal{C}_{E_p} is the following. Light rays reaching the event E_p and detected by the “eye” of the satellite correspond to null lines through E_p whose past directions constitutes the field of vision of the “observing” satellite. This is \mathcal{N}^- and it is represented by the celestial circle \mathcal{C}_{E_p} which is an accurate geometrical representation of what the satellite actually “sees.” For, the satellite can be considered as permanently situated at the center of a unit circle (his circle of vision) onto which the satellite maps all it detects at any instant. Then, the mapping of the past null directions at E_p to the points of \mathcal{C}_{E_p} we can call the *sky mapping*.

Additionally, because (1) the circle S^1 is homeomorphic to the real projective line $P\mathbb{R}^1$ and (2) we need angle measurements to frame the points of \mathcal{C}_{E_p} associated with any event K in the past null cone of E_p to be furthermore localized, then a particular production process of projective frame for \mathcal{C}_{E_p} must be devised and incorporated in the echoing system definition now given below.

Definition 7 (the echoing system $\mathcal{E}ch$). The echoing system $\mathcal{E}ch$ associated with the *privileged* emitter \mathcal{E} is based on the following features (see Figure 4 and Table 4):

- (i) One *primary* event E_p with its celestial circle \mathcal{C}_{E_p} .
- (ii) Three *secondary* events \bar{E}^* , \tilde{E}^* , and \mathcal{S}^* , associated, respectively, with the canonical projective points $[0]_{E_p}$, $[\infty]_{E_p}$, and $[1]_{E_p}$ of the projective frame \mathfrak{F}_{E_p} defined on \mathcal{C}_{E_p} .
- (iii) Two *ternary* events: E^\diamond and E'' .
- (iv) A compass on \mathcal{C}_{E_p} with a moving origin *anchored* on the projective point $[1]_{E_p}$ of \mathcal{C}_{E_p} associated with \mathcal{S}^* .

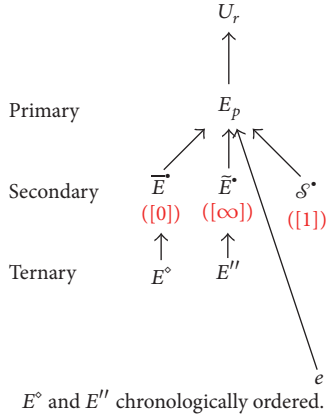

 FIGURE 4: The causal structure of $\mathcal{E}ch$ with the event e .

 TABLE 4: The events and their broadcast time stamps in the $\mathcal{E}ch$ system.

Event	Broadcasts time stamp	Received at
E^\diamond	τ^\diamond	\bar{E}
E''	τ''	\bar{E}'
\mathcal{S}^*	$\tau_{\mathcal{S}^*}$	E_p
\bar{E}	τ^\diamond	E_p
\bar{E}'	τ''	E_p

- (v) An event of reception $U_r \in \mathcal{V}$ at which all the data are collected and sent by the emitter \mathcal{E} .

The determination of the second (resp., third) emission coordinate $\bar{\tau}_e$ (resp., $\bar{\tau}'_e$) for the event e to be localized is obtained from a second (resp., third) system of “echoes” associated with the privileged emitter $\bar{\mathcal{E}}$ (resp., $\bar{\mathcal{E}}'$). It is also linked to one event of reception \bar{U}_e (resp., \bar{U}'_e) where all the time stamps are collected. We denote by $\bar{\mathcal{E}}ch$ (resp., $\bar{\mathcal{E}}'ch$) this second (resp., third) system of “echoes” on the worldline of the privileged emitter $\bar{\mathcal{E}}ch$ (resp., $\bar{\mathcal{E}}'ch$).

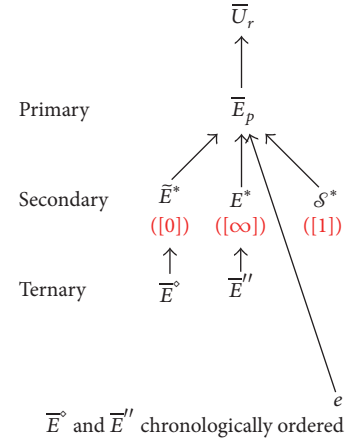
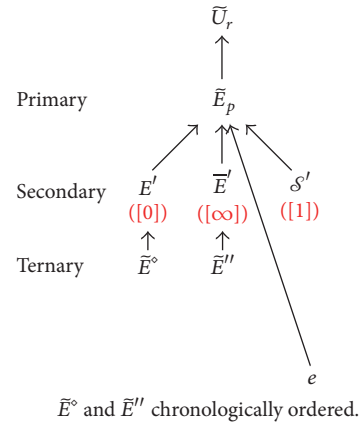
Then, we have the following.

Definition 8 (the echoing systems $\bar{\mathcal{E}}ch$ and $\bar{\mathcal{E}}'ch$). The definitions of the echoing systems $\bar{\mathcal{E}}ch$ and $\bar{\mathcal{E}}'ch$ are obtained when making the following substitutions of events and marks in the definition of $\mathcal{E}ch$:

- (i) For $\bar{\mathcal{E}}ch$: $(U, E, \bar{E}, \bar{E}) \rightarrow (\bar{U}, \bar{E}, \bar{E}, \bar{E})$ and $\bullet \rightarrow *$,
 (ii) For $\bar{\mathcal{E}}'ch$: $(U, E, \bar{E}, \bar{E}) \rightarrow (\bar{U}, \bar{E}, E, \bar{E})$ and $\bullet \rightarrow '.$

Then, we have the causal structure of the echoing system $\mathcal{E}ch$ (Figure 4 and Table 4); the other two causal structures for $\bar{\mathcal{E}}ch$ and $\bar{\mathcal{E}}'ch$ (Figures 5 and 6) are deduced from the causal structure of $\mathcal{E}ch$ by making the substitutions indicated in Definition 8. We indicate also the three structures with the event e (Figure 7).

Remark 9. Again (Remark 1), it matters to notice that the three events of reception U_r , \bar{U}_r , and \bar{U}'_r (Figure 7) are matched by the user on the basis of an identification of the


 FIGURE 5: The causal structure of $\bar{\mathcal{E}}ch$ with the event e .

 FIGURE 6: The causal structure of $\bar{\mathcal{E}}'ch$ with the event e .

physical data for e transmitted by the main emitters (see convention 5).

4.3. The Projective Frames and the Time Stamps Correspondences. The realization of the RLS is based on a sort of spacetime parallax, that is, a passage from angles “ α ” measured on celestial circles to spatiotemporal distances. And thus, because spatiotemporal distances are evaluated from time stamps “ τ ” in the present context, we need to make the translation of angles into time stamps. This involves onboard compasses embarked on each main emitter to find somehow the bearings. Then, this translation is neither more nor less than a change of projective frames.

To make this change of projective frames effective, we need to define the projective frames on the celestial circles attached to each main emitter. This can be done ascribing to specific “bright points” detected on the celestial circles both angles and time stamps. This ascription is then naturally achieved if these bright points are the main emitters themselves since they broadcast the time stamps. But, if we have three emitters for the RPS, then only two bright points can be detected on each celestial circle attached to each main emitter. And, we need three bright points to have a projective frame

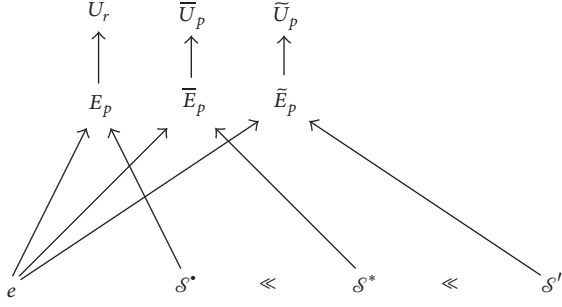


FIGURE 7: The causal structure for the three echoing systems \mathcal{E}^{ch} , $\bar{\mathcal{E}}^{\text{ch}}$, and $\tilde{\mathcal{E}}^{\text{ch}}$ with the event e . The chronological order between \mathcal{S}^* , $\bar{\mathcal{S}}^*$, and \mathcal{S}'^* belonging to $\mathcal{W}^{\mathcal{S}}$ can be different.

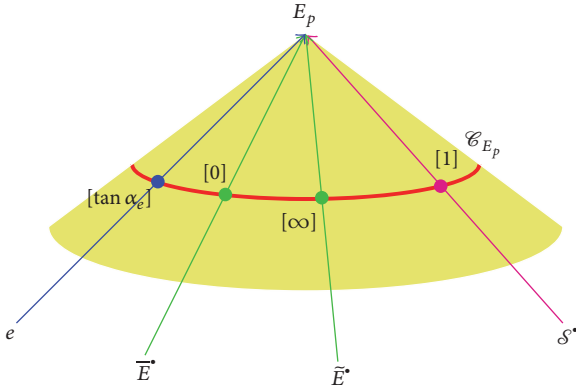


FIGURE 8: The past null cone and the celestial circle \mathcal{C}_{E_p} .

TABLE 5: The change of projective frame and the corresponding events.

Event	\mathfrak{F}_{E_p}	$\mathfrak{F}_{E_p}^{\tau}$
e	$[\tan \alpha_e]$	$[\tau_e]$
\bar{E}^*	$[0]$	$[\tau^\diamond]$
\bar{E}^*	$[\infty]$	$[\tau'']$
\mathcal{S}^*	$[1]$	$[\tau_{\mathcal{S}^*}]$

on the celestial circle homeomorphic to $P\mathbb{R}^1$, hence the need for the ancillary emitter \mathcal{S} . The change of projective frames is described in Table 5 and Figures 8 and 9. For instance, the main emitter $\bar{\mathcal{E}}$ broadcasts the time stamp τ^\diamond at the secondary event \bar{E}^* , and the former is then received by the emitter \mathcal{E} at the primary event E_p . Also, if $\bar{\mathcal{E}}$ is always associated by convention with the canonical projective point $[0]_{E_p}$ on the celestial circle of \mathcal{E} , then we deduce that τ^\diamond corresponds by a projective transformation to 0. And then, we proceed in the same way with the other two canonical projective points.

As a result, the relations between the angles and the time stamps are the following:

$$\tan \alpha_e = [\tau^\diamond : \tau'' | \tau_e : \tau_{\mathcal{S}^*}] = \frac{[\tau^\diamond : \tau'' | \tau_e]}{[\tau^\diamond : \tau'' | \tau_{\mathcal{S}^*}]} \quad (1a)$$

$$\equiv \mathfrak{M}(\tau_e),$$

$$\tan \bar{\alpha}_e = [\bar{\tau}^\diamond : \bar{\tau}'' | \bar{\tau}_e : \bar{\tau}_{\bar{\mathcal{S}}^*}] = \frac{[\bar{\tau}^\diamond : \bar{\tau}'' | \bar{\tau}_e]}{[\bar{\tau}^\diamond : \bar{\tau}'' | \bar{\tau}_{\bar{\mathcal{S}}^*}]} \quad (1b)$$

$$\equiv \bar{\mathfrak{M}}(\bar{\tau}_e),$$

$$\tan \tilde{\alpha}_e = [\tilde{\tau}^\diamond : \tilde{\tau}'' | \tilde{\tau}_e : \tilde{\tau}_{\tilde{\mathcal{S}}'^*}] = \frac{[\tilde{\tau}^\diamond : \tilde{\tau}'' | \tilde{\tau}_e]}{[\tilde{\tau}^\diamond : \tilde{\tau}'' | \tilde{\tau}_{\tilde{\mathcal{S}}'^*}]} \quad (1c)$$

$$\equiv \tilde{\mathfrak{M}}(\tilde{\tau}_e),$$

where $[a : b | c : d]$ is the cross-ratio of the four projective points a, b, c , and d :

$$[a : b | c : d] = \frac{[a : b | c]}{[a : b | d]} \quad (2)$$

$$\text{where } [a : b | c] = [a : b | c : \infty] = \left(\frac{a-c}{b-c} \right).$$

Conversely, the time coordinates for the event e are then obtained from the angles measurements and the following formulas:

$$\tau_e = \left(\frac{\tau^\diamond - \tau'' [\tau^\diamond : \tau'' | \tau_{\mathcal{S}^*}] \tan \alpha_e}{1 - [\tau^\diamond : \tau'' | \tau_{\mathcal{S}^*}] \tan \alpha_e} \right), \quad (3a)$$

$$\bar{\tau}_e = \left(\frac{\bar{\tau}^\diamond - \bar{\tau}'' [\bar{\tau}^\diamond : \bar{\tau}'' | \bar{\tau}_{\bar{\mathcal{S}}^*}] \tan \bar{\alpha}_e}{1 - [\bar{\tau}^\diamond : \bar{\tau}'' | \bar{\tau}_{\bar{\mathcal{S}}^*}] \tan \bar{\alpha}_e} \right), \quad (3b)$$

$$\tilde{\tau}_e = \left(\frac{\tilde{\tau}^\diamond - \tilde{\tau}'' [\tilde{\tau}^\diamond : \tilde{\tau}'' | \tilde{\tau}_{\tilde{\mathcal{S}}'^*}] \tan \tilde{\alpha}_e}{1 - [\tilde{\tau}^\diamond : \tilde{\tau}'' | \tilde{\tau}_{\tilde{\mathcal{S}}'^*}] \tan \tilde{\alpha}_e} \right). \quad (3c)$$

And thus, the event e is localized in the localization grid \mathbb{R}_L^3 . Then, we deduce the following lemma.

Lemma 10. *The map*

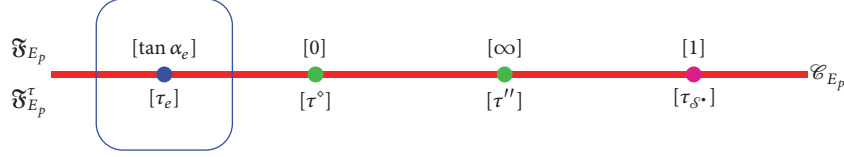
$$\mathbb{S} : (\tan \alpha_e, \tan \bar{\alpha}_e, \tan \tilde{\alpha}_e) \in \mathcal{F}^3 \longrightarrow (\tau_e, \bar{\tau}_e, \tilde{\tau}_e) \in \mathcal{T}^3, \quad (4)$$

where $\mathcal{F}^3 \equiv (P\mathbb{R}^1)^3$ is an automorphism.

Proof. This is obvious from the relations (1a)–(1c), because \mathfrak{M} , $\bar{\mathfrak{M}}$, and $\tilde{\mathfrak{M}}$ are bijective Möbius transformations. \square

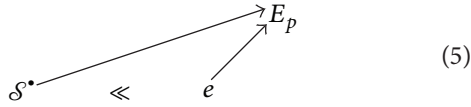
4.4. The Consistency between the Positioning and Localization Protocols

Theorem 11. *The localization and the positioning protocols or systems in a $(2 + 1)$ -dimensional spacetime are consistent.*

FIGURE 9: The projective line associated with the celestial circle \mathcal{C}_{E_p} .

Proof. The consistency must be satisfied if e is an element of the emitters' worldlines. Indeed, the localization protocol is consistent with the positioning protocol if the set of events on the emitters' worldlines from which the localization of any event e is possible are themselves localizable.

Case 1 ($e \in \mathcal{W}^{\mathcal{S}}$). We consider two cases: $e \ll \mathcal{S}^*$ and $\mathcal{S}^* \ll e$. The other cases with \mathcal{S}^* or S' instead of \mathcal{S}^* give the same results. Now, we start with the assumption $e \ll \mathcal{S}^*$ from which we deduce the following causal structure:



In particular, from $\mathcal{S}^* \ll e \rightarrow E_p$, we find² that $\mathcal{S}^* \ll e < E_p$, and then, with $\mathcal{S}^* \rightarrow E_p$, we obtain³ $\mathcal{S}^* \rightarrow e \rightarrow E_p$. But then², we have $\mathcal{S}^* \ll e$. With the assumption $e \ll \mathcal{S}^*$, we deduce also $e \ll \mathcal{S}^*$, and therefore $\mathcal{S}^* = e$. Hence, we consider that $\mathcal{S}^* = e$ and with the other two sets of events \mathcal{S}^* with \bar{E}_p or S' and \tilde{E}_p , we deduce finally that $e = \mathcal{S}^* = \mathcal{S}^* = S' \equiv S$. Therefore, we conclude that the time coordinates of e provided by the positioning system are $\tau_e = \tau_S$, $\bar{\tau}_e = \bar{\tau}_S$, and $\tilde{\tau}_e = \tilde{\tau}_S$.

Besides, from the projective frames, we have also

$$\tan \alpha_e = [\tau^\diamond : \tau'' \mid \tau_e : \tau_{\mathcal{S}^*}] = 1, \quad (6a)$$

$$\tan \bar{\alpha}_e = [\bar{\tau}^\diamond : \bar{\tau}'' \mid \bar{\tau}_e : \bar{\tau}_{\mathcal{S}^*}] = 1, \quad (6b)$$

$$\tan \tilde{\alpha}_e = [\tilde{\tau}^\diamond : \tilde{\tau}'' \mid \tilde{\tau}_e : \tilde{\tau}_{\mathcal{S}^*}] = 1. \quad (6c)$$

And therefore, we obtain

$$\begin{aligned} \tau_e &= \tau_{\mathcal{S}^*}, \\ \bar{\tau}_e &= \bar{\tau}_{\mathcal{S}^*}, \\ \tilde{\tau}_e &= \tilde{\tau}_{\mathcal{S}^*}, \end{aligned} \quad (7)$$

which are the coordinates of S .

In conclusion, the localization protocol is consistent with the positioning one.

Case 2 (e is a *primary* event: $e = E_p$ (primary) $\in \mathcal{W}$). In this case, we obtain the causal structure (Figure 10).

Then, from the three echoing causal structures $\mathcal{E}ch$, $\bar{\mathcal{E}}ch$, and $\tilde{\mathcal{E}}ch$, we have $e = E_p = E^* = E'$ where E^* is associated with the projective point $[\infty]_{\bar{E}_p}$ and E' is associated with the

projective point $[0]_{\tilde{E}_p}$. Consequently, we have $\tan \bar{\alpha}_e = \infty$ and $\tan \tilde{\alpha}_e = 0$. Also, we have $\bar{E} = \bar{E}''$ and $\tilde{E} = \tilde{E}^\diamond$ from which we deduce from the positioning system that their time coordinates are equal; that is, we have (one of the emission coordinates is equal to the broadcast one in the positioning protocol; see Remark 6)

$$\bar{\tau}_{\bar{E}} = \bar{\tau}^* = \bar{\tau}'' = \bar{\tau}_{\bar{E}''}, \quad (8)$$

$$\tilde{\tau}_{\tilde{E}} = \tilde{\tau}^* = \tilde{\tau}^\diamond = \tilde{\tau}_{\tilde{E}^\diamond}.$$

Besides, from the localization protocol, we have

$$\tan \alpha_e = [\tau^\diamond : \tau'' \mid \tau_e : \tau_{\mathcal{S}^*}] = ? \text{ (not defined)}, \quad (9a)$$

$$\tan \bar{\alpha}_e = [\bar{\tau}^\diamond : \bar{\tau}'' \mid \bar{\tau}_e : \bar{\tau}_{\mathcal{S}^*}] = \infty, \quad (9b)$$

$$\tan \tilde{\alpha}_e = [\tilde{\tau}^\diamond : \tilde{\tau}'' \mid \tilde{\tau}_e : \tilde{\tau}_{\mathcal{S}^*}] = 0. \quad (9c)$$

Hence, we deduce

$$\tau_e = ?,$$

$$\bar{\tau}_e = \bar{\tau}'' , \quad (10)$$

$$\tilde{\tau}_e = \tilde{\tau}^\diamond .$$

And from the positioning protocol, because E_p is a positioned point with emission coordinates $(\tau_{E_p}, \bar{\tau}^*, \tilde{\tau}^*)$, we have also

$$\bar{\tau}_e = \bar{\tau}_{E_p} = \bar{\tau}^*, \quad (11)$$

$$\tilde{\tau}_e = \tilde{\tau}_{E_p} = \tilde{\tau}^*,$$

and therefore, with (8), we deduce the consistency for two time stamps. Actually, τ_e is not obtained by localization but by *identification* (Definition 5). Indeed, we know that e is an element of \mathcal{W} and that $\tau_e = \tau_{E_p}$ is broadcast by the *identified* main emitter \mathcal{E} . This determination of τ_e is then similar to the emission coordinate ascription presented in the (1 + 1)-dimensional case for which localization is equivalent to positioning (Remark 3), hence the consistency.

Case 3 (e is a *secondary* event: $e = \bar{E}$ (secondary) $\in \bar{\mathcal{W}}$ or $e = \tilde{E}$ (secondary) $\in \tilde{\mathcal{W}}$). Then, the causal structure is the following whenever $e = \bar{E}$ (Figure 11):

- (i) $e = \bar{E}$ (secondary) $\in \bar{\mathcal{W}}$. Then, the localization protocol at E_p gives the formula $\tan \alpha_e = [\tau^\diamond : \tau'' \mid \tau_e :$

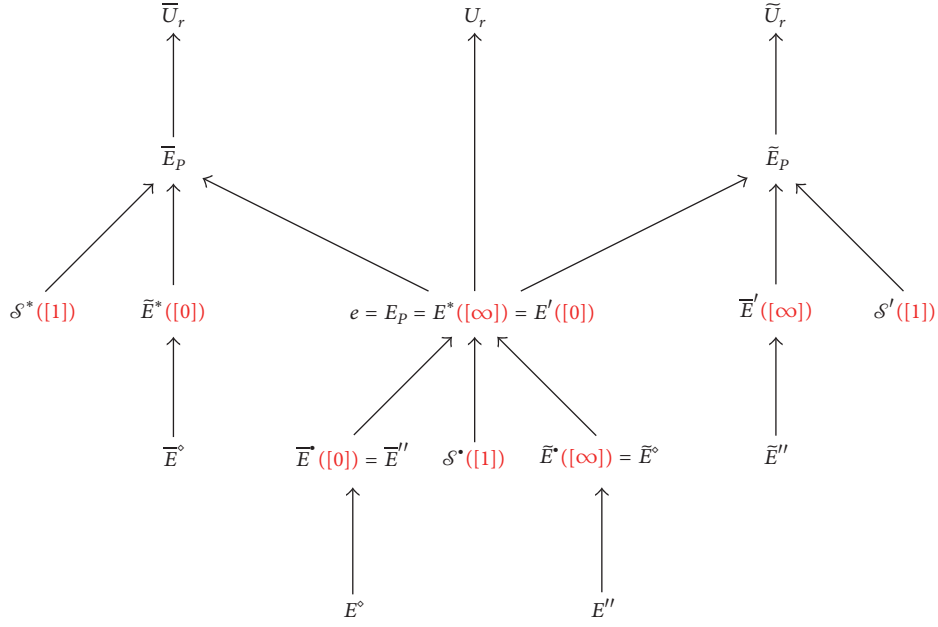


FIGURE 10: The causal structure for the three echoing protocols $\mathcal{E}\text{ch}$, $\bar{\mathcal{E}}\text{ch}$, and $\tilde{\mathcal{E}}\text{ch}$ whenever $e = E_p$.

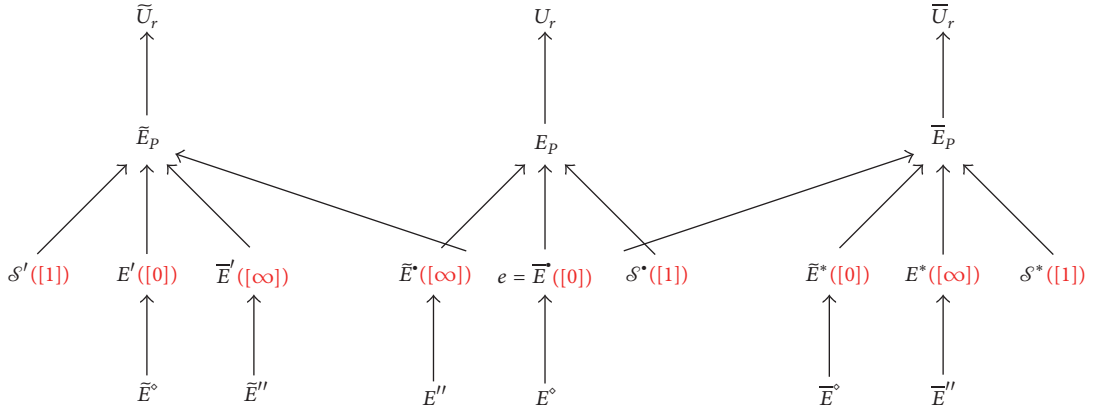


FIGURE 11: The causal structure for the three echoing protocols $\mathcal{E}\text{ch}$, $\bar{\mathcal{E}}\text{ch}$, and $\tilde{\mathcal{E}}\text{ch}$ whenever $e = \bar{E}^\diamond$.

$\tau_{S^*} = 0$ because \bar{E}^* is associated with the projective point $[0]_{E_p}$. Therefore, we have $\tau_e = \tau^\diamond$. But, from the positioning protocol, the emission coordinate $\tau_{\bar{E}^*}$ of \bar{E}^* relative to the main emitter \mathcal{E} is τ^\diamond broadcast at the ternary event E^\diamond . Hence, $\tau_{\bar{E}^*} = \tau^\diamond$ and we deduce the consistency of the localization protocol with the positioning protocol for one emission coordinate.

- (ii) $e = \bar{E}'$ (secondary) $\in \bar{\mathcal{W}}$. The reasoning is similar to the previous one. Then, we deduce the consistency for $\tilde{\tau}_e = \tilde{\tau}_{\bar{E}'} = \tilde{\tau}''$ because (1) \bar{E}_p is the primary event for \bar{E}' and \bar{E}'' is the ternary event for \bar{E}' , and (2) $[\tilde{\tau}^\diamond : \tilde{\tau}'' \mid \tilde{\tau}_e : \tilde{\tau}_{S'}] = \infty$ which involves $\tilde{\tau}_e = \tilde{\tau}''$.

Now, we consider two distinct causal structures of localization a and b such that $e = \bar{E}^{*a} = \bar{E}^{*b}$ from which we deduce the consistency for τ_e and $\tilde{\tau}_e$. Furthermore, as in Case 2, we deduce $\tilde{\tau}_e$ by *identification* (Definition 5) and we obtain $\tilde{\tau}_e = \tilde{\tau}_{\bar{E}^{*a}} = \tilde{\tau}_{\bar{E}^{*b}}$, hence the consistency.

Case 4 (e is a ternary event). For instance, we can set $e = E^\diamond$. But then, we have also $e = E^\diamond \rightarrow E_p$ on $\mathcal{W}^{\mathcal{E}}$ which is impossible since we have only the chronological order on the emitters' worldlines. \square

Remark 12. From this theorem, we can then notice that RLSs are based on *autolocalization* protocols similarly to RPSs which are based on *autolocation* protocols. As a result, RLSs and RPSs are independent of any *system of reference*.

4.5. The Local Projective Structure

Definition 13. We call

- (i) *Emission grid* the Euclidean space $\mathbb{R}_P^3 \equiv \mathbb{R}^3$ of the positioned events $e_P = (\tau_e, \bar{\tau}_e, \tilde{\tau}_e)$;
- (ii) *Localization* (or *quadrometric*) *grid* the Euclidean space $\mathbb{R}_L^4 \equiv \mathbb{R}^3 \times \mathbb{R}^*$ of the localized events $e_L = (\tau_e, \bar{\tau}_e, \tilde{\tau}_e, \dot{\tau}_e)$, where $\dot{\tau}_e$ is provided by the ancillary emitter \mathcal{S} by *identification* from the horismotic relation $S^L \rightarrow e_P$ ($S^L \in \mathcal{W}^{\mathcal{S}}$) or the “message function” [11] $f_{\mathcal{S}}^- : \mathbb{R}_P^3 \rightarrow \mathcal{W}^{\mathcal{S}}$; that is, the time stamp $\dot{\tau}^L$ broadcast by \mathcal{S} at S^L is such that $\dot{\tau}^L \equiv \dot{\tau}_e$;
- (iii) *Anisotropic localization* (or *quadrometric*) *grid* the Euclidean space $\mathbb{R}_{AL}^4 \equiv \mathbb{R}^3 \times \mathbb{R}^*$ of events $e_{AL} = (\dot{\tau}_e \tau_e, \dot{\tau}_e \bar{\tau}_e, \dot{\tau}_e \tilde{\tau}_e, \dot{\tau}_e)$.

Definition 14. We denote by $I : \mathbb{R}_L^4 \rightarrow \mathbb{R}_{AL}^4$ the bijective map such that $I(e_L) = e_{AL}$. And we denote by $\pi : \mathbb{R}_{AL}^4 \rightarrow \mathbb{R}_P^3$ the submersion such that $\pi(e_{AL}) = e_P$.

Remark 15. In these definitions, the time coordinate $\dot{\tau}_e$ must be nonvanishing. If this condition is not satisfied we can, nevertheless, always consider that the ancillary emitter \mathcal{S} generates a time number $\dot{\rho}$ and broadcasts $e^{\dot{\rho}} \equiv \dot{\tau}$. This can be realized from a real-time computer with $\dot{\rho}$ as the generated input and $e^{\dot{\rho}}$ as the broadcast output. Obviously, we can assume the same for the main emitters.

Let g be an element of $GL(4, \mathbb{R})$ such that $g \cdot e_{AL} = e'_{AL}$. And thus, $GL(4, \mathbb{R})$ acts linearly on \mathbb{R}_{AL}^4 . Then, the action of $GL(4, \mathbb{R})$ on \mathbb{R}_L^4 and \mathbb{R}_P^3 is nonlinear and locally transitive and it defines homographies (i.e., conformal transformations):

$$e'_P = \left(\frac{A \cdot e_P + b}{c \cdot e_P + \mu} \right), \quad (12a)$$

$$g \equiv \begin{pmatrix} A & b \\ c & \mu \end{pmatrix}, \quad (12b)$$

$$\dot{\tau}'_e = \dot{\tau}_e (c \cdot e_P + \mu),$$

where $\mu \in \mathbb{R}$, $(b, c) \in (\mathbb{R}^3)^2$, and $A \in M_{3 \times 3}(\mathbb{R})$. Let us notice that $\dot{\tau}_e$ does not intervene in (12a). Moreover, we deduce that $PGL(4, \mathbb{R})$ acts locally transitively on \mathbb{R}_P^3 . Therefore, we obtain the following.

Theorem 16. *The (2 + 1)-dimensional spacetime manifold has a local 3-dimensional projective structure inherited from its causal structure.*

Proof. Let x, t , and s_i ($i = 1, 2, 3$) in \mathbb{R}_{AL}^4 be such that

$$x \equiv e_{AL} = (x^3 = \dot{\tau}_e \tau_e, x^2 = \dot{\tau}_e \bar{\tau}_e, x^1 = \dot{\tau}_e \tilde{\tau}_e, x^0 = \dot{\tau}_e),$$

$$t \equiv (t^3 = t^0 \tan \alpha_e, t^2 = t^0 \tan \bar{\alpha}_e, t^1 = t^0 \tan \tilde{\alpha}_e, t^0),$$

$$(t^0 \neq 0),$$

$$s_1 \equiv (s_1^3 = s_1^0 \tau_{\mathcal{S}^*}, s_1^2 = s_1^0 \bar{\tau}^\diamond, s_1^1 = s_1^0 \tilde{\tau}''', s_1^0 = \tau_{\mathcal{S}^*} \tau^\diamond \tau'''),$$

$$(s_1^0 \neq 0),$$

$$s_2 \equiv (s_2^3 = s_2^0 \bar{\tau}_{\mathcal{S}^*}, s_2^2 = s_2^0 \bar{\tau}^\diamond, s_2^1 = s_2^0 \tilde{\tau}''', s_2^0 = \bar{\tau}_{\mathcal{S}^*} \bar{\tau}^\diamond \tilde{\tau}'''),$$

$$(s_2^0 \neq 0),$$

$$s_3 \equiv (s_3^3 = s_3^0 \tilde{\tau}_{\mathcal{S}'}, s_3^2 = s_3^0 \tilde{\tau}^\diamond, s_3^1 = s_3^0 \tilde{\tau}''', s_3^0 = \tilde{\tau}_{\mathcal{S}'} \tilde{\tau}^\diamond \tilde{\tau}'''),$$

$$(s_3^0 \neq 0). \quad (13)$$

Then, the relations (1a)–(1c) can be put in the forms $(\alpha, \beta, \mu, \nu = 0, 1, 2, 3; \text{no summation on } i = 1, 2, 3)$

$$K^i_{\alpha, \beta, \mu, \nu} s_i^\alpha s_i^\beta x^\mu t^\nu = 0, \quad (14)$$

$$K^0_{\alpha, \beta, \mu, \nu} s_i^\alpha s_i^\beta x^\mu t^\nu \neq 0,$$

where the coefficients of the tensors K^i take only the values 0 or ± 1 and the only nonvanishing coefficient of K^0 is $K^0_{0,0,0,0}$. Then, it is easy to show that for all g_x and g_t in $GL(4, \mathbb{R})$ there exists $g \in GL(4, \mathbb{R})$ such that

$$K^i (g \cdot s_i, g \cdot s_i, g_x \cdot x, g_t \cdot t) = 0, \quad (15)$$

$$K^0 (g \cdot s_i, g \cdot s_i, g_x \cdot x, g_t \cdot t) \neq 0.$$

In particular, if $g \equiv \text{Id}$ and if the s_i are fixed, then the set of localized events $x \equiv e_{AL} \in \mathbb{R}_{AL}^4$ is an orbit of $GL(4, \mathbb{R})$ and the set of corresponding events $e_P = \pi(e_{AL})$ is an orbit of the projective group $PGL(4, \mathbb{R})$.

And then, because the relations (14) are homogeneous polynomials, we deduce that \mathbb{R}_{AL}^4 has a projective structure as expected. \square

Remark 17. The map \mathbb{S} defined locally by $\mathfrak{M}^{-1} \times \overline{\mathfrak{M}}^{-1} \times \overline{\mathfrak{M}}^{-1}$ on \mathbb{R}_P^3 is the so-called “soldering map⁴” \mathbb{S} of Ehresmann defined on $P\mathbb{R}^3 = \mathbb{R}_P^3 \cup P\mathbb{R}^2$ to the spacetime manifold \mathcal{M} :

$$\begin{array}{ccc} P\mathbb{R}^3 \times P\mathbb{R}^3 & \longrightarrow & P\mathbb{R}^3 \\ \downarrow & \searrow & \downarrow \\ \mathcal{M} \cong P\mathbb{R}^3 & & \mathcal{M} \cong P\mathbb{R}^3 \end{array} \quad \mathbb{S} \equiv \mathfrak{M}^{-1} \times \overline{\mathfrak{M}}^{-1} \times \overline{\mathfrak{M}}^{-1} \quad (16)$$

loc. loc.

And the set of homogeneous equations $K^i(s_i, s_i, t, x) = 0$ when the s_i are fixed defines leaves in the trivial bundle $P\mathbb{R}^3 \times P\mathbb{R}^3$. After reduction of the bundle $\mathbb{R}^4 \times \mathbb{R}^4 \rightarrow \mathcal{M}$ to this projective bundle, the *projective Cartan connection* in the sense of Ehresmann [17] is defined as the differential $dK \equiv dK^1 \times dK^2 \times dK^3$ with respect to the vertical variables $\nu \simeq (\tan \alpha_e, \tan \bar{\alpha}_e, \tan \tilde{\alpha}_e)$ and the horizontal variables e_P ; and thus, the tangent spaces of these horizontal leaves are the *annihilators/contact elements* of dK .

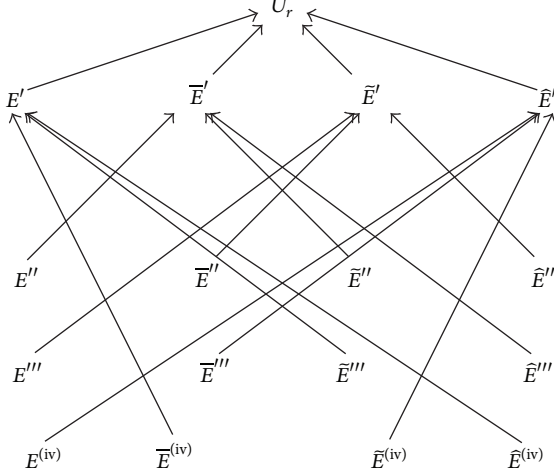


FIGURE 12: The causal structure of the RPS in a $(3 + 1)$ -dimensional spacetime.

Remark 18. Also, as a result, the spacetime manifold can be considered as a “generalized Cartan space” which is endowed with both (1) a “projective Cartan connection” (of dimension 4) providing a local projective structure, and (2) a compatible (pseudo-)Riemannian structure viewed for instance as a horizontal section in the four-dimensional anisotropic grid.

Also, we can eventually define a Ehresmann connection providing a horizontal/vertical splitting in the tangent space of the principal bundle of projective frames of the spacetime manifold. And then, once this Ehresmann connection is given, we can define from this splitting a projective Cartan connection⁵ which can be viewed as the infinitesimal changes of the projective frames with respect to themselves.

5. RLSs in $(3 + 1)$ -Dimensional Spacetime

We need similarly four main emitters \mathcal{E} , $\bar{\mathcal{E}}$, $\tilde{\mathcal{E}}$, and $\hat{\mathcal{E}}$ providing a RPS and, again, one ancillary emitter \mathcal{S} emitting its time coordinates and its own time stamp $\hat{\tau}$ from a clock to get a RLS.

5.1. The Causal Structure of the RPS. The protocol becomes more and more complex to implement. Indeed, sixteen time stamps are needed to provide to the users their positions in a given system of reference. These positions are obtained from the knowledge the users acquire of their own positions and those of the main emitters both in the emission grid and in the system of reference; and this is due to the ephemerides that the emitters upload to the users and the autolocating process. The causal structure of the RPS is shown in Figure 12 and Table 6.

The position in the emission grid \mathbb{R}_p^4 of the user at U_r is $(\tau', \bar{\tau}', \tilde{\tau}', \hat{\tau}')$.

5.2. The Description of the RLS. As in the $(2 + 1)$ -dimensional case, we need a system of light echoes associated with each privileged emitter, each linked to an event of reception on the user’s worldline. Again, we denote by $\mathcal{E}ch$ the system of

TABLE 6: The events E' , \bar{E}' , \tilde{E}' , and \hat{E}' and their broadcast time stamps received at U_r .

Event	Broadcasts time stamps
E'	$(\tau' = \tau_{E'}, \bar{\tau}^{(iv)}, \tilde{\tau}''', \hat{\tau}^{(iv)})$
\bar{E}'	$(\tau'', \bar{\tau}' = \bar{\tau}_{\bar{E}'}, \tilde{\tau}'', \hat{\tau}''')$
\tilde{E}'	$(\tau''', \bar{\tau}'', \tilde{\tau}' = \tilde{\tau}_{\tilde{E}'}, \hat{\tau}'')$
\hat{E}'	$(\tau^{(iv)}, \bar{\tau}''', \tilde{\tau}^{(iv)}, \hat{\tau}' = \hat{\tau}_{\hat{E}'})$

light echoes for the privileged emitter \mathcal{E} with E_p as primary event. But now, contrarily to the $(2 + 1)$ -dimensional case, we must consider celestial spheres rather than celestial circles. And then, we have again sky mappings from the past null cones directions at the primary events to the “bright” points on the associated celestial spheres. Nevertheless, we have only homeomorphisms between hemispheres with half of their boundaries and $P\mathbb{R}^2$. Thus, a problem occurs a priori in this $(3 + 1)$ -dimensional case because we have two disjoint hemispheres for each celestial sphere. And then, consecutive problems appear for the choice and the realization of these hemispheres in the localizing protocol. However, we show in the sequel this problem vanishes completely when considering the full set of echoing systems and the particular hemispheres implementation we present for the emitters. We need, first, the following definition for the determination of the first emission coordinate τ_e .

Definition 19 (the echoing system $\mathcal{E}ch$). The echoing system $\mathcal{E}ch$ associated with the privileged emitter \mathcal{E} is based on the following features (see Figure 15):

- (i) One primary event E_p with its celestial sphere \mathcal{C}_{E_p} .
- (ii) Four secondary events \bar{E}^\bullet , \tilde{E}^\bullet , and \hat{E}^\bullet with the ancillary event \mathcal{S}^\bullet , associated, respectively, with the canonical projective points $[\infty, 0]_{E_p}$, $[0, \infty]_{E_p}$, $[0, 0]_{E_p}$, and $[1, 1]_{E_p}$ of the projective frame \mathfrak{F}_{E_p} defining one specific hemisphere of the celestial sphere \mathcal{C}_{E_p} (Figure 15).
- (iii) One ternary event E^\sharp for \bar{E}^\bullet , two ternary events E^\diamond and \bar{E}_\diamond for \tilde{E}^\bullet , two ternary events E'' and \bar{E}_n for \hat{E}^\bullet , and none for \mathcal{S}^\bullet ,
- (iv) Two compasses on the specific hemisphere of \mathcal{C}_{E_p} defined above with a moving origin anchored on the projective point $[1, 1]_{E_p}$ associated with \mathcal{S}^\bullet .
- (v) One event of reception $U_r \in \mathcal{V}$ at which all the data are collected and sent by the emitter \mathcal{E} .

Then, we have the following hierarchy of events in the four different echoing systems $\mathcal{E}ch$, $\bar{\mathcal{E}}ch$, $\tilde{\mathcal{E}}ch$, and $\hat{\mathcal{E}}ch$:

- (i) Four primary events E_p , \bar{E}_p , \tilde{E}_p , and \hat{E}_p , each with three secondary events and one ancillary event (Table 7).
- (ii) Four horismotic relations $E_p \rightarrow U_r$, $\bar{E}_p \rightarrow \bar{U}_r$, $\tilde{E}_p \rightarrow \tilde{U}_r$, and $\hat{E}_p \rightarrow \hat{U}_r$, where the chronologically ordered

TABLE 7: The four primary events and their secondary/ancillary events with their corresponding projective points on the celestial hemispheres \mathcal{C}_{E_p} , $\mathcal{C}_{\bar{E}_p}$, $\mathcal{C}_{\tilde{E}_p}$, and $\mathcal{C}_{\hat{E}_p}$ homeomorphic to $P\mathbb{R}^2$.

Echoing system	Primary event	$[\infty, 0]$	$[0, \infty]$	$[0, 0]$	$[1, 1]$
$\mathcal{E}ch$	$E_p \in \mathcal{W}$	\bar{E}°	\bar{E}^\star	\bar{E}^\star	\mathcal{S}^\star
$\bar{\mathcal{E}}ch$	$\bar{E}_p \in \bar{\mathcal{W}}$	\bar{E}^\dagger	\bar{E}^\dagger	E^\dagger	\mathcal{S}^\dagger
$\tilde{\mathcal{E}}ch$	$\tilde{E}_p \in \tilde{\mathcal{W}}$	\tilde{E}^\star	E^\star	\bar{E}^\star	\mathcal{S}^\star
$\hat{\mathcal{E}}ch$	$\hat{E}_p \in \hat{\mathcal{W}}$	E'	\bar{E}'	\bar{E}'	\mathcal{S}'

events of reception U_r , \bar{U}_r , \tilde{U}_r , and \hat{U}_r belong to the user worldline \mathcal{V} .

- (iii) One or two (*normal* and *shifted*) ternary events by secondary event except for the ancillary event:

$$\mathcal{E}ch: \bar{E}^\circ : E^\dagger, \bar{E}^\star : E^\circ, \bar{E}_\diamond, \bar{E}^\star : E'', \bar{E}_\parallel, \quad (17a)$$

$$\bar{\mathcal{E}}ch: \bar{E}^\dagger : \bar{E}^\dagger, \bar{E}^\dagger : \bar{E}^\diamond, \bar{E}_\diamond, E^\dagger : \bar{E}'', \bar{E}_\parallel, \quad (17b)$$

$$\tilde{\mathcal{E}}ch: \tilde{E}^\star : \tilde{E}^\dagger, E^\star : \tilde{E}^\diamond, \tilde{E}_\diamond, \bar{E}^\star : \tilde{E}'', \tilde{E}_\parallel, \quad (17c)$$

$$\hat{\mathcal{E}}ch: E' : \hat{E}^\dagger, \bar{E}' : \hat{E}^\diamond, E_\diamond, \bar{E}' : \hat{E}'', E_\parallel. \quad (17d)$$

- (iv) Two events associated with the projective points $[\infty, 0]$ and $[0, \infty]$ define the equatorial circle dividing the celestial sphere $S^2 \simeq P\mathbb{R}^2 \# P\mathbb{R}^2$ in two celestial hemispheres \mathcal{C} which are identified to a unique projective space $P\mathbb{R}^2$. In other words, the directions of propagation of the light rays detected as bright points on the hemispheres are not considered. This could be a problem a priori. Actually, this difficulty is completely canceled out from the operating principles of RLSs as we will see in the sequel.

- (v) Two compasses on each celestial hemisphere \mathcal{C}_{E_p} , $\mathcal{C}_{\bar{E}_p}$, $\mathcal{C}_{\tilde{E}_p}$, and $\mathcal{C}_{\hat{E}_p}$ with a common moving origin for angle measurements *anchored* on the projective point $[1, 1]$.

- (vi) We recall that \mathcal{S} broadcasts as a particular user its own emission coordinates $(\tau_S, \bar{\tau}_S, \tilde{\tau}_S, \hat{\tau}_S)$ obtained from the positioning system for all $S \in \mathcal{W}^{\mathcal{S}}$. It broadcasts also all along $\mathcal{W}^{\mathcal{S}}$ its own time coordinate denoted again by $\hat{\tau}$.

5.3. The Causal Structure of the RLS. We represent (Figures 13 and 14 and Tables 8 and 9) only the causal structure for the echoing system $\mathcal{E}ch$; the other echoing systems $\bar{\mathcal{E}}ch$, $\tilde{\mathcal{E}}ch$, and $\hat{\mathcal{E}}ch$ can be easily obtained from the symbolic substitutions deduced from Table 7 and (17a)–(17d).

5.4. The Projective Frame, the Time Stamps Correspondence, and the Consistency. We consider the projective frame at the primary event E_p and the time stamps correspondence associated with the change of projective frame on \mathcal{C}_{E_p} (Table 10 and Figure 15). Obviously, the other correspondences and

changes of projective frames can be deduced in the same way for the three other primary events. Then, we obtain four corresponding pairs of time coordinates for e in the four celestial hemispheres (Table 11).

Then, the change of projective frame on the celestial hemisphere gives the following relation:

$$\begin{pmatrix} a & d & g \\ b & e & h \\ c & f & k \end{pmatrix} \begin{pmatrix} 1 & 0 & 0 & 1 & \rho \tan \alpha_e \\ 0 & 1 & 0 & 1 & \rho \tan \beta_e \\ 0 & 0 & 1 & 1 & \rho \end{pmatrix} = \begin{pmatrix} u\tau^\dagger & v\tau^\diamond & w\tau'' & (u+v+w)\tau_{\mathcal{S}^\circ} & r\hat{\tau}_e^\star \\ u\bar{\tau}^\star & v\bar{\tau}_\diamond & w\bar{\tau}_\parallel & (u+v+w)\bar{\tau}_{\mathcal{S}^\circ} & r\bar{\tau}_e^\star \\ u & v & w & (u+v+w) & r \end{pmatrix}, \quad (18)$$

where $\rho uvwr(u+v+w) \neq 0$, and where the determinant of the square matrix on the l.h.s. of this equality must be nonvanishing. Then, we deduce that

$$\begin{pmatrix} u\tau^\dagger & v\tau^\diamond & w\tau'' \\ u\bar{\tau}^\star & v\bar{\tau}_\diamond & w\bar{\tau}_\parallel \\ u & v & w \end{pmatrix} \begin{pmatrix} 1 & \rho \tan \alpha_e \\ 1 & \rho \tan \beta_e \\ 1 & \rho \end{pmatrix} = r(u+v+w) \begin{pmatrix} \tau_{\mathcal{S}^\circ} & \hat{\tau}_e^\star \\ \bar{\tau}_{\mathcal{S}^\circ} & \bar{\tau}_e^\star \\ 1 & 1 \end{pmatrix}, \quad (19)$$

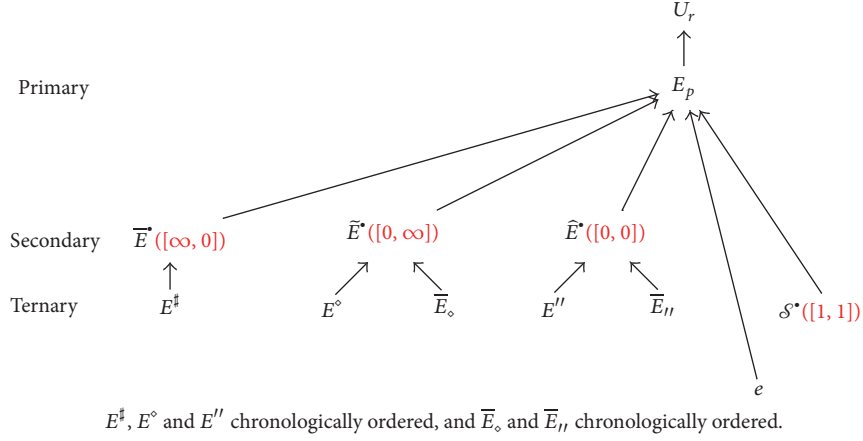
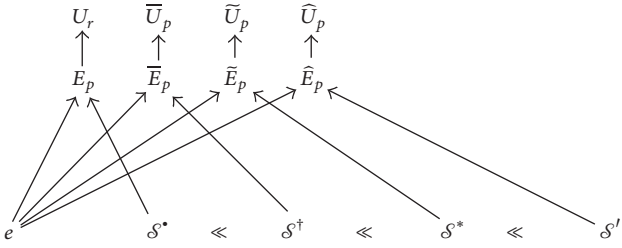
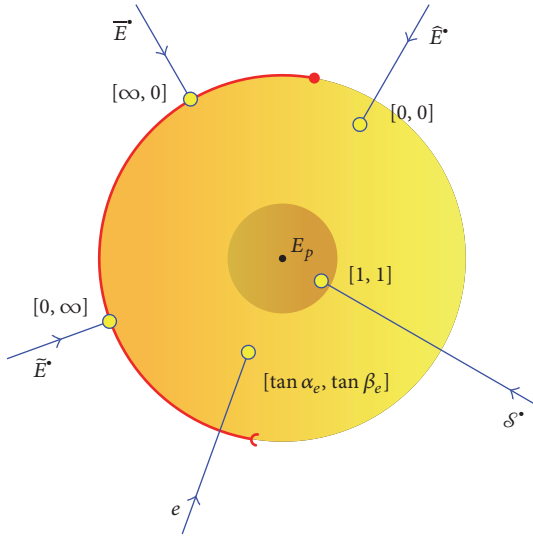
and we can take in addition $u+v+w=r=1$.

Obviously, we obtain from the three other echoing systems three other similar systems of equations for the other six unknown time coordinates given in Table 11 for e .

Now, besides, we have necessarily the relations:

$$\begin{aligned} \tau_e^\star &= \tau_e', \\ \bar{\tau}_e^\star &= \bar{\tau}_e^\dagger, \\ \tilde{\tau}_e^\star &= \tilde{\tau}_e^\dagger, \\ \hat{\tau}_e^\star &= \hat{\tau}_e'. \end{aligned} \quad (20)$$

Indeed, if one of these four precedent equalities is not satisfied, then it means that if the event e , the worldlines of the main emitters, and the ancillary one are fixed, then, at least one time stamp among the eight can vary. And then, one of

FIGURE 13: The echoing system $\mathcal{E}ch$.FIGURE 14: The causal structure for the four echoing systems $\mathcal{E}ch, \bar{\mathcal{E}}ch, \hat{\mathcal{E}}ch$, and $\tilde{\mathcal{E}}ch$ with the event e . The chronological order between $\mathcal{S}^{\circ}, \mathcal{S}^{\dagger}, \mathcal{S}^{\circ},$ and \mathcal{S}^{\dagger} belonging to $\mathcal{W}^{\mathcal{S}}$ can be different.FIGURE 15: The projective disk on the celestial hemisphere \mathcal{E}_{E_p} centered at E_p and the four canonical projective points and the corresponding projective point for e .

the eight angles on the four celestial hemispheres necessarily can vary as well. But then, it would mean that the position of the event e seen on the celestial hemispheres of the four main emitters can vary arbitrarily whenever e is fixed. In other

TABLE 8: The secondary/ancillary events and their broadcast time stamps in the $\mathcal{E}ch$ system.

Event	Broadcasts time stamps	Received at
\bar{E}^{\dagger}	$(\tau^{\dagger}, \bar{\tau}^{\circ} = \bar{\tau}_{\bar{E}^{\dagger}})$	E_p
\bar{E}°	$(\tau^{\diamond}, \bar{\tau}_{\diamond})$	E_p
\hat{E}°	$(\tau'', \bar{\tau}_{\parallel})$	E_p
\mathcal{S}°	$(\tau_{\mathcal{S}^{\circ}}, \bar{\tau}_{\mathcal{S}^{\circ}})$	E_p

TABLE 9: The ternary events and their broadcast time stamps in the $\mathcal{E}ch$ system.

Event	Broadcasts time stamps	Received at
E^{\dagger}	τ^{\dagger}	\bar{E}^{\dagger}
E^{\diamond}	τ^{\diamond}	\bar{E}°
\bar{E}_{\diamond}	$\bar{\tau}_{\diamond}$	\bar{E}°
E''	τ''	\hat{E}°
\bar{E}_{\parallel}	$\bar{\tau}_{\parallel}$	\hat{E}°

words, e might have more than one corresponding “bright” point on each celestial hemisphere; and, in particular, because we have continuous functions, then it might correspond to e , in particular, a connected “bright” line on one of the four celestial hemispheres. This would involve necessarily the existence of more than one and only one horismotic relation “ \rightarrow .” This situation can be encountered in the case of the existence of conjugate points for light-like geodesics for instance in Riemannian manifolds. Then, considering only one horismos, the relations (20) must be satisfied.

Then, we obtain the following.

Lemma 20. *Let $\mathcal{T}^4 \equiv (P\mathbb{R}^1)^4$ be the 4-torus. Then, the RLS provides a map*

$$\mathfrak{M}_4 : (\tan \alpha_e, \tan \bar{\alpha}_e, \tan \tilde{\alpha}_e, \tan \hat{\alpha}_e) \in \mathcal{T}^4 \longrightarrow (\tau_e, \bar{\tau}_e, \tilde{\tau}_e, \hat{\tau}_e) \in \mathcal{T}^4 \quad (21)$$

which is an automorphism.

TABLE 10: The change of projective frame and the corresponding events.

Event	\mathfrak{F}_{E_p}	$\mathfrak{F}_{E_p}^\tau$
e	$[\tan \alpha_e, \tan \beta_e]$	$[\tau_e^*, \bar{\tau}_e^*]$
\vec{E}	$[\infty, 0]$	$[\tau_e^\dagger, \bar{\tau}_e^\dagger]$
\vec{E}^*	$[0, \infty]$	$[\tau_e^\diamond, \bar{\tau}_e^\diamond]$
\vec{E}^\dagger	$[0, 0]$	$[\tau_e'', \bar{\tau}_e'']$
\mathcal{S}^*	$[1, 1]$	$[\tau_{\mathcal{S}^*}, \bar{\tau}_{\mathcal{S}^*}]$

TABLE 11: The pairs of time coordinates for e deduced in the four celestial hemispheres.

Celestial hemisphere	Time coordinates for e
\mathcal{C}_{E_p}	$(\tau_e^*, \bar{\tau}_e^*)$
$\mathcal{C}_{\vec{E}_p}$	$(\tau_e^\dagger, \bar{\tau}_e^\dagger)$
$\mathcal{C}_{\vec{E}_p}^*$	$(\tau_e^\diamond, \bar{\tau}_e^\diamond)$
$\mathcal{C}_{\vec{E}_p}^\dagger$	$(\tau_e'', \bar{\tau}_e'')$

Proof. This lemma can be easily proved simply by solving systems of equations like (19) but we indicate interesting intermediate homogeneous equations in the computations. From the relations (20) and the equations at each primary event such as (19) at E_p , we deduce that there are four linear relations between “ $\tan \alpha$ ” and “ $\tan \beta$.” And then, it can be shown that we obtain four Möbius relations linking the four $\tan \alpha$'s to the four time coordinates τ_e , $\bar{\tau}_e$, $\tilde{\tau}_e$, and $\hat{\tau}_e$ of e generalizing the situation encountered in the precedent (2 + 1)-dimensional case.

More precisely, considering the primary event E_p , we obtain (19). At the other primary event \vec{E}_p , we obtain the similar following relations ($\nu \neq 0$):

$$\begin{aligned} & \begin{pmatrix} p\tilde{\tau}^\# & q\tilde{\tau}^\diamond & m\tilde{\tau}'' \\ p\tilde{\tau}^* & q\tilde{\tau}^\diamond & m\tilde{\tau}'' \\ p & q & m \end{pmatrix} \begin{pmatrix} 1 & \nu \tan \tilde{\alpha}_e \\ 1 & \nu \tan \tilde{\beta}_e \\ 1 & \nu \end{pmatrix} \\ &= n(p+q+m) \begin{pmatrix} \tilde{\tau}_{\mathcal{S}^*} & \tilde{\tau}_e^* \\ \tilde{\tau}_{\mathcal{S}^*} & \tilde{\tau}_e^* \\ 1 & 1 \end{pmatrix}, \end{aligned} \quad (22)$$

where again we can impose the relations $n = p + q + m = 1$. Then, from now and throughout, we set

$$\begin{aligned} \tau_e &\equiv \tau_e^\bullet = \tau_e', \\ \bar{\tau}_e &\equiv \bar{\tau}_e^* = \bar{\tau}_e^\dagger, \\ \tilde{\tau}_e &\equiv \tilde{\tau}_e^* = \tilde{\tau}_e^\dagger, \\ \hat{\tau}_e &\equiv \hat{\tau}_e^* = \hat{\tau}_e'. \end{aligned} \quad (23)$$

And then, it can be shown that the relations (19) and (22), those depending explicitly on the time stamps, can be put in the following forms ($p, q = 1, \dots, 4$ and $\mu, \nu = 0, 1, \dots, 4$):

$$K_{pq\mu\nu} s^p S^q x^\mu t^\nu = 0, \quad (24a)$$

$$\bar{K}_{pq\mu\nu} \bar{s}^p \bar{S}^q x^\mu t^\nu = 0,$$

$$\tilde{K}_{pq\mu\nu} \tilde{s}^p \tilde{S}^q x^\mu t^\nu = 0, \quad (24b)$$

$$\hat{K}_{pq\mu\nu} \hat{s}^p \hat{S}^q x^\mu t^\nu = 0,$$

where

$$x \equiv (\dot{\tau}_e \tau_e, \dot{\tau}_e \bar{\tau}_e, \dot{\tau}_e \tilde{\tau}_e, \dot{\tau}_e \hat{\tau}_e, \dot{\tau}_e), \quad (25a)$$

$$t \equiv (\mu \tan \alpha, \mu \tan \beta, \mu \tan \tilde{\alpha}, \mu \tan \tilde{\beta}, \mu),$$

$$s \equiv (\tau^\#, \tau^\diamond, \tau'', s^0), \quad (25b)$$

$$\bar{s} \equiv (\bar{\tau}^*, \bar{\tau}_\diamond, \bar{\tau}_'', \bar{s}^0 = s^0),$$

$$\tilde{s} \equiv (\tilde{\tau}^\#, \tilde{\tau}^\diamond, \tilde{\tau}'', \tilde{s}^0), \quad (25c)$$

$$\hat{s} \equiv (\hat{\tau}^*, \hat{\tau}_\diamond, \hat{\tau}_'', \hat{s}^0 = \tilde{s}^0),$$

$$S \equiv \left(\begin{array}{c|c|c} \tau_{\mathcal{S}^*} & \tau^\diamond & \tau'' \\ \bar{\tau}_{\mathcal{S}^*} & \bar{\tau}_\diamond & \bar{\tau}_'' \\ 1 & 1 & 1 \end{array} \middle| \begin{array}{c|c|c} \tau^\# & \tau_{\mathcal{S}^*} & \tau'' \\ \bar{\tau}^* & \bar{\tau}_{\mathcal{S}^*} & \bar{\tau}_'' \\ 1 & 1 & 1 \end{array} \middle| \begin{array}{c|c|c} \tau^\# & \tau^\diamond & \tau_{\mathcal{S}^*} \\ \bar{\tau}^* & \bar{\tau}_\diamond & \bar{\tau}_{\mathcal{S}^*} \\ 1 & 1 & 1 \end{array} \right), \quad (26a)$$

$$\left(\begin{array}{c|c|c} \tau^\# & \tau^\diamond & \tau'' \\ \bar{\tau}^* & \bar{\tau}_\diamond & \bar{\tau}_'' \\ 1 & 1 & 1 \end{array} \right),$$

$$\tilde{S} \equiv \left(\begin{array}{c|c|c} \tilde{\tau}_{\mathcal{S}^*} & \tilde{\tau}^\diamond & \tilde{\tau}'' \\ \tilde{\tau}_{\mathcal{S}^*} & \tilde{\tau}_\diamond & \tilde{\tau}_'' \\ 1 & 1 & 1 \end{array} \middle| \begin{array}{c|c|c} \tilde{\tau}^\# & \tilde{\tau}_{\mathcal{S}^*} & \tilde{\tau}'' \\ \tilde{\tau}^* & \tilde{\tau}_{\mathcal{S}^*} & \tilde{\tau}_'' \\ 1 & 1 & 1 \end{array} \middle| \begin{array}{c|c|c} \tilde{\tau}^\# & \tilde{\tau}^\diamond & \tilde{\tau}_{\mathcal{S}^*} \\ \tilde{\tau}^* & \tilde{\tau}_\diamond & \tilde{\tau}_{\mathcal{S}^*} \\ 1 & 1 & 1 \end{array} \right), \quad (26b)$$

$$\left(\begin{array}{c|c|c} \tilde{\tau}^\# & \tilde{\tau}^\diamond & \tilde{\tau}'' \\ \tilde{\tau}^* & \tilde{\tau}_\diamond & \tilde{\tau}_'' \\ 1 & 1 & 1 \end{array} \right),$$

where s^0 and \tilde{s}^0 are nonvanishing arbitrary coefficients and $\mu \neq 0$. Hence, we have four homogeneous algebraic equations linking the vectors t and x . Obviously, we have also four other similar homogeneous equations for x and another $t' \approx (\tan \tilde{\alpha}, \tan \tilde{\beta}, \tan \tilde{\alpha}, \tan \tilde{\beta})$ deduced from the echoing systems at the other two primary events \vec{E}_p and \vec{E}_p^* :

$$K_{pq\mu\nu} s'^p \bar{S}^q x^\mu t'^\nu = 0, \quad (27a)$$

$$\bar{K}_{pq\mu\nu} \bar{s}'^p \bar{S}^q x^\mu t'^\nu = 0,$$

$$\tilde{K}_{pq\mu\nu} \tilde{s}'^p \tilde{S}^q x^\mu t'^\nu = 0, \quad (27b)$$

$$\hat{K}_{pq\mu\nu} \hat{s}'^p \hat{S}^q x^\mu t'^\nu = 0,$$

where $s'^0 = \bar{s}'^0$ and $\bar{s}'^0 = \tilde{s}'^0$ are nonvanishing arbitrary coefficients. And then, because x is determined completely from (24a)-(24b), (27a)-(27b) are linearly depending on (24a)-(24b) which involves that we have linear relations between the two sets of “angles” $t \simeq (\tan \alpha, \tan \beta, \tan \bar{\alpha}, \tan \bar{\beta})$ and $t' \simeq (\tan \bar{\alpha}, \tan \bar{\beta}, \tan \tilde{\alpha}, \tan \tilde{\beta})$. Hence, taking linear combinations of the systems of equations (27a)-(27b) and (24a)-(24b) and taking into account also the remaining equations in (19) and (22) not depending on the time stamps we can deduce a system of four homogeneous equations linking $y \equiv (\tan \alpha, \tan \bar{\alpha}, \tan \tilde{\alpha}, \tan \hat{\alpha}, 1)$ and $z \equiv (\tau_e, \bar{\tau}_e, \tilde{\tau}_e, \hat{\tau}_e, 1)$:

$$H_{\mu,\nu}^i y^\mu z^\nu = 0, \quad (i = 1, 2, 3, 4), \quad (28)$$

where s^0, \bar{s}^0, s'^0 , and \bar{s}'^0 do not intervene anymore. And (28) determines univocally x up to the time coordinate $\hat{\tau}_e$, that is, $(\tau_e, \bar{\tau}_e, \tilde{\tau}_e, \hat{\tau}_e)$. Moreover, (28) is another expression for Möbius transformations between each given angle and a linear combination of $(\tau_e, \bar{\tau}_e, \tilde{\tau}_e, \hat{\tau}_e)$, hence the result for an automorphism on the 4-torus. \square

Remark 21. We can notice from Lemma 20 that we obtain the time coordinates $(\tau_e, \bar{\tau}_e, \tilde{\tau}_e, \hat{\tau}_e)$ for e from only two echoing systems, for example, at E_p and \tilde{E}_p with the four “angles” $(\tan \alpha, \tan \beta, \tan \bar{\alpha}, \tan \bar{\beta})$, or from the four echoing systems at $E_p, \bar{E}_p, \tilde{E}_p,$ and \hat{E}_p with the four “angles” $(\tan \alpha, \tan \bar{\alpha}, \tan \tilde{\alpha}, \tan \hat{\alpha})$.

Theorem 22. *The localization and the positioning protocols or systems in a (3 + 1)-dimensional spacetime are consistent.*

Proof. The proof is obvious because (1) the RLS in the (3 + 1)-dimensional case has a causal structure which can be decomposed in four causal substructures each equivalent to the one given for the RLS in the (2 + 1)-dimensional case and (2) we need only the “angles” α to localize e in each of these subsystems of localization. \square

5.5. The Local Projective Structure

Definition 23. We call

- (i) *Emission grid* the Euclidean space $\mathbb{R}_P^4 \equiv \mathbb{R}^4$ of the positioned events $e_P = (\tau_e, \bar{\tau}_e, \tilde{\tau}_e, \hat{\tau}_e)$;
- (ii) *Localization (or pentametric) grid* the Euclidean space $\mathbb{R}_L^5 \equiv \mathbb{R}^4 \times \mathbb{R}^*$ of the localized events $e_L = (\tau_e, \bar{\tau}_e, \tilde{\tau}_e, \hat{\tau}_e, \hat{\tau}_e)$ where $\hat{\tau}_e$ is provided by the ancillary emitter \mathcal{S} by *identification* from the horismotic relation $S^L \rightarrow e_P$ ($S^L \in \mathcal{W}^{\mathcal{S}}$) or the “message function” [11] $f_{\mathcal{S}}^- : \mathbb{R}_P^4 \rightarrow \mathcal{W}^{\mathcal{S}}$; that is, the time stamp $\hat{\tau}^L$ broadcast by \mathcal{S} at S^L is such that $\hat{\tau}^L \equiv \hat{\tau}_e$;
- (iii) *Anisotropic localization (or pentametric) grid* the Euclidean space $\mathbb{R}_{AL}^5 \equiv \mathbb{R}^4 \times \mathbb{R}^*$ of events $e_{AL} = (\hat{\tau}_e \tau_e, \hat{\tau}_e \bar{\tau}_e, \hat{\tau}_e \tilde{\tau}_e, \hat{\tau}_e \hat{\tau}_e, \hat{\tau}_e)$.

Definition 24. We denote by $I : \mathbb{R}_L^5 \rightarrow \mathbb{R}_{AL}^5$ the bijective map such that $I(e_L) = e_{AL}$. And we denote by $\pi : \mathbb{R}_{AL}^5 \rightarrow \mathbb{R}_P^4$ the submersion such that $\pi(e_{AL}) = e_P$.

Let g be an element of $GL(5, \mathbb{R})$ such that $g \cdot e_{AL} = e'_P$. And thus, $GL(5, \mathbb{R})$ acts linearly on \mathbb{R}_{AL}^5 . Then, the action of $GL(5, \mathbb{R})$ on \mathbb{R}_L^5 and \mathbb{R}_P^4 defines homographies (i.e., conformal transformations):

$$e'_P = \begin{pmatrix} A \cdot e_P + b \\ c \cdot e_P + \mu \end{pmatrix}, \quad (29a)$$

$$g \equiv \begin{pmatrix} A & b \\ c & \mu \end{pmatrix}, \quad (29b)$$

where $\mu \in \mathbb{R}$, $(b, c) \in (\mathbb{R}^4)^2$, and $A \in M_{4 \times 4}(\mathbb{R})$. Therefore, we obtain the following.

Theorem 25. *The (3 + 1)-dimensional spacetime manifold has a local 4-dimensional projective structure inherited from its causal structure.*

Proof. The proof is similar with the proof of Theorem 16 but with the systems of homogeneous equations (24a)-(24b) or (27a)-(27b) or (28) instead of the system (14). \square

Remark 26. The map \mathbb{S} defined locally by \mathfrak{M}_4 on \mathbb{R}_P^4 is the so-called “soldering map” \mathbb{S} of Ehresmann defined on $P\mathbb{R}^4 = \mathbb{R}_P^4 \cup P\mathbb{R}^3$ to the spacetime manifold \mathcal{M} :

$$\begin{array}{ccc} P\mathbb{R}^4 \times P\mathbb{R}^4 & \xrightarrow{\quad} & P\mathbb{R}^4 \\ \downarrow & \searrow \mathbb{S} \simeq \mathfrak{M}_4 & \\ \mathcal{M} \simeq_{loc} P\mathbb{R}^4 & & \end{array} \quad (30)$$

And the set of homogeneous equations (24a)-(24b) or (27a)-(27b) or (28) defines leaves in the trivial bundle $P\mathbb{R}^4 \times P\mathbb{R}^4$. After reduction of the bundle $\mathbb{R}^5 \times \mathbb{R}^5 \rightarrow \mathcal{M}$ to this projective bundle, the *projective Cartan connection* in the sense of Ehresmann [17] is defined as the differential $dH \equiv dH^1 \times dH^2 \times dH^3 \times dH^4$ with respect to the vertical variables $v \simeq (\tan \alpha, \tan \bar{\alpha}, \tan \tilde{\alpha}, \tan \hat{\alpha})$ and the horizontal variables e_P ; and thus, the tangent spaces of these horizontal leaves are the *annihilators/contact elements* of dH .

Remark 27. As in the (2 + 1)-dimensional case (see Remark 18), the spacetime manifold can be considered as a “generalized Cartan space” which is endowed with both (1) a “projective Cartan connection” (of dimension 5) providing a local projective structure and (2) a compatible (pseudo-) Riemannian structure viewed for instance as a horizontal section in the five-dimensional anisotropic grid.

6. Conclusion

The previous results are obtained on manifolds of dimension less than or equal to four and satisfying only causal axiomatics. This involves only the following assumptions:

- (i) A finite speed of light from the existence of the horismotic relation “ \rightarrow ,”
- (ii) Isotropy (compasses) because the conformal invariance is a common consequence of all the causal axiomatics (Malament’s Theorem [13], Woodhouse’s axiomatics [11], King-Hawking-McCarty’s axiomatics [12], e.g.; see also [10]).
- (iii) Homogeneity is void of meaning in causal axiomatics.

And then, we deduced that

- (i) the spacetime manifold has a *local* projective structure in addition to the *global* (pseudo-)Riemannian structure.
- (ii) The spacetime manifold is a “*generalized Cartan space*” with a “*projective Cartan connection*” (see Remarks 18 and 27). A forthcoming publication is planned to clarify these aspects.
- (iii) The space and time coordinates are locally transformed by homographies. Indeed, the time stamps $(\tau^\alpha) = (\tau_e, \bar{\tau}_e, \tilde{\tau}_e, \hat{\tau}_e)$ ($\alpha = 1, \dots, 4$) are the “emission coordinates.” Then, they define a null coframe $(d\tau^\alpha)$ also called “null GPS coordinates” which are *linearly* related to timelike (GPS) coordinates [5] such as the usual space and time coordinates $(u^\alpha) \equiv (x, y, z, t)$. Therefore, we obtain transformations similar to the transformations (29a) for the space and time coordinates:

$$u^\alpha = \left(\frac{U_\beta^\alpha u'^\beta + v^\alpha}{w_\mu u'^\mu + \rho} \right), \quad \alpha, \beta, \mu = 1, \dots, 4. \quad (31)$$

Besides, applying by inquisitiveness these projective aspects in astrophysics, we consider a modification of the Newton’s law of gravitation by a homography:

$$\vec{F}(\vec{r}_0) \equiv -G \frac{m_0 m}{r_0^2} (\alpha + \beta t + \mu r_0)^2 \hat{r}_0, \quad \hat{r}_0 = \frac{\vec{r}_0}{r_0}, \quad (32)$$

where we consider that \vec{F} , the time t , and the radial distance r_0 between the punctual masses m_0 and m are *evaluated with respect to a frame attached to m* , and α , β , and μ are constants.

This modification differs from those investigated in MOND theories which satisfy the so-called Milgrom’s law [18]. Also, contrarily to MOND theories, the present modification of Newton’s law preserves the action/reaction principle. This modification is based on the notion of *projective tensor* differing from the usual notion of *Euclidean tensor*.

We can quote É. Cartan on this notion of *Euclidean tensor* [19, Section 23, p. 22]. The latter can be considered as a set of numbers (u^1, u^2, \dots, u^r) brought into coincidence with another set of numbers $(u'^1, u'^2, \dots, u'^r)$ by a

linear transformation S_o corresponding to a *rotation* R_o in a given “underlying” Euclidean space \mathbb{R}^k . Then, the linear transformation S_o corresponds to another transformation R_o preserving the origin o of \mathbb{R}^k . Thus, we obtain tensors at this origin.

Now, a *projective tensor* can be considered as a set of numbers (v^1, v^2, \dots, v^r) brought into coincidence with another set of numbers $(v'^1, v'^2, \dots, v'^r)$ by a *linear* transformation S_o corresponding to an *homography* H_o preserving the origin o (H_o is then a *central collineation* of center o) of a given “underlying” Euclidean space \mathbb{R}^k . In other words, the equivariance is defined for Euclidean tensors with respect to linear groups of transformations whereas the equivariance for projective tensors is defined with respect to the group of central collineations which is a subgroup of the projective group.

Also, if we have tensor fields, that is, tensors at different origins p elements of a manifold (as space of parameters), then, there correspond fields (or families) of transformations S_p on this manifold associated with fields of rotations $R_{o,p}$ (Euclidean tensor fields) or fields of central collineations $H_{o,p}$ (projective tensor fields) associated with the origin o of the underlying Euclidean space \mathbb{R}^k . Then, the tensor fields are equivariant if and only if the equivariance is satisfied at any point p . We recognize in this description the structure of a tensor bundle of rank k of which the transition morphisms (functions) are the rotation or the collineation fields, the transformation fields S_p are defined from the local trivializations of the bundle, and the origin o is an element of the fiber. Moreover, the equivariance of tensor fields is obviously the so-called left-invariance with respect to right actions of structural groups.

Then, we consider, first, the (non-modified) force of gravitation \vec{F} as a Euclidean vector field with a spherical symmetry with respect to the point p_0 where the mass m_0 is located. The mass m is at the point p and, as indicated previously, \vec{F} and \vec{r}_0 are evaluated with respect to a Euclidean frame attached to p . Then, clearly, rotating this frame does not change r_0 and it rotates in the same way the vector \hat{r}_0 .

Second, if \vec{F} is modified to be a projective vector field with a spherical symmetry with respect to p_0 , we must proceed as follows. In this projective framework, the central collineation fields $H_{o,p}$ are defined such that at each p they are particular changes of projective frames \mathfrak{F}_p . More precisely, we recall that the projective frames of a projective space of dimension four are defined by six vectors in a vector space of dimension five of which five are linearly independent. Then, projective transformations, that is, homographies, are the linear, injective transformations in this five-dimensional vector space which is also called the space of *homogeneous* coordinates. Then, central collineations are those projective transformations preserving, up to a multiplicative factor, a particular, given five-dimensional vector, that is, the origin o of the five-dimensional fiber. In general, this vector is chosen among the vectors of a given projective frame. Moreover, p can be kept invariant with respect to central collineations which constitute a subgroup of the group of projective

transformations. Indeed, these central collineations can also be viewed as local changes of *inhomogeneous* coordinates centered at p , that is, p is the origin of the local system of coordinates. Hence, if (x, y, z, t) are space and time coordinates centered at p such that $p \equiv (0, 0, 0, 0) = (x_p, y_p, z_p, t_p)$, then the changes of coordinates we must consider are given by the homographies (31) where $v^\alpha = 0$ ($\alpha = 1, \dots, 4$); that is, we have central collineations $H_{p,o} : (u'^\alpha) \equiv (x', y', z', t') \rightarrow (u^\alpha) \equiv (x, y, z, t)$ such that

$$u^\alpha = \frac{U_\beta^\alpha u'^\beta}{(q + ht' + \vec{k} \cdot \vec{r}')} \quad (33)$$

where $\vec{r}' \equiv (u'^i) \equiv (x', y', z')$ ($i, j, \dots = 1, 2, 3$), (U_β^α) is a matrix field, q and h are scalar fields, and \vec{k} is a vector field all of them depending on p .

In particular, if the time and space splitting of the Newtonian physics is maintained in this change of coordinates, then we must have $U_4^i = U_i^4 = 0$. And then, we deduce in particular that

$$\begin{aligned} r &= \lambda \frac{r'}{(q + ht' + \vec{k} \cdot \vec{r}')}, \\ t &= \mu \frac{t'}{(q + ht' + \vec{k} \cdot \vec{r}')}, \end{aligned} \quad (34)$$

where $\lambda = \det(U_j^i)$ and $\mu = U_4^4$. Also, from (33), considering that (1) \vec{F} is a projective five-vector with two vanishing components, that is, $\vec{F} \equiv (F^1, F^2, F^3, 0, 0)$, and (2) the central collineations are represented (or, are originated from) by the linear transformations $U \equiv (U_b^a)$ ($a, b = 1, \dots, 5$) such that $U_5^a = 0$, $U_i^5 = k^i$ ($i = 1, \dots, 3$), $U_4^5 = h$, and $U_5^5 = q$, then we obtain in particular $F^i \equiv \sum_{j=1}^3 U_j^i F'^j$.

Then, it is easy to see that (32) becomes equivariant with respect to these changes of coordinates if and only if we set the necessary but, nevertheless, sufficient condition that the vector field \vec{k} satisfies the relation $\vec{k} \equiv \sigma \vec{r}'_0 / r'_0$, where σ is a scalar field depending on p and \vec{r}'_0 is the vector from p to p_0 in the new system of coordinates. Indeed, with this condition, we obtain the new Newtonian force:

$$\vec{F}' \left(\frac{\vec{r}'}{r'_0} \right) \equiv -G \frac{m_0 m}{r_0'^2} (\alpha' + \beta' t' + \mu' r'_0)^2 \vec{r}'_0, \quad \vec{r}'_0 = \frac{\vec{r}'_0}{r'_0}. \quad (35)$$

More precisely, the equivariance is obtained as soon as \vec{r}' is equal to \vec{r}'_0 , that is, when we move along the line joining p and p_0 , and then, \vec{F} is an equivariant, projective vector field along this line onto which only the Newton's law is experimentally evaluated. Also, we obtain the field of transformations S_p as expected and a justification of the modification (32) of the Newton's law of gravitation.

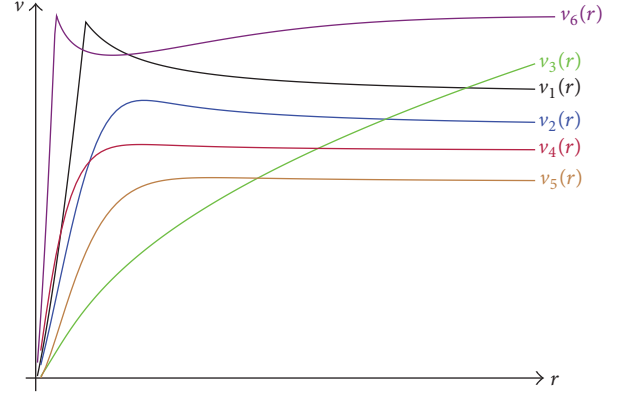


FIGURE 16

Furthermore, \vec{F} is then only equivariant with respect to a subgroup of the central collineations because we must set $\vec{k} \equiv \sigma \vec{r}'_0$. This is the result of (1) the central symmetry of \vec{F} and (2) the Newtonian physics framework with the time and space splitting. Also, it can be noticed that in this Newtonian context, the terms such as $\beta t + \mu r_0$ in the expression of \vec{F} may sound like a Minkowski inner product and could be the expression of a retarded Newtonian force as there exist retarded fields in electromagnetism.

In addition, we assume that the centripetal acceleration is a projective object and that it is modified in the same way as the Newton's law of gravitation: $v^2/r_0 \rightarrow (\alpha + \beta t + \mu r_0)v^2/r_0$.

Then, if we modify the Newton's law of gravitation with a homography as indicated above preserving the mass distribution $\rho(r)$ to see the relative change between $\rho(r)$ and the radius r , then we can deduce the following rotational velocity field:

$$\begin{aligned} v(r) &\equiv \left((1 + at + br) \frac{M(r)}{r} \right)^{1/2} \\ &\text{where } M(r) \equiv \int_0^r u^k \rho(u) du. \end{aligned} \quad (36)$$

Then, whenever $t = 1$ and for different mass distributions ρ , we obtain the following qualitative curves if we consider $k = 2$ for spherical distributions of mass in (36) (Figure 16 and Table 12).

Then, we see that the curves have a resemblance to the observed data. This suggests more exhaustive studies of the relations between galactic mass densities and rotational velocity fields according to relations (36) with varying exponent k . Moreover, the modified force \vec{F} in (32) depends on the time t which could be related to a notion of cosmological expansion, a relation which could be also studied in future works.

Finally, a last question arises from these projective aspects: what could be the *vanishing points* in such spacetime manifolds modeled locally by four-dimensional projective spaces? These vanishing points are at infinity in a projective space of dimension 3, and then, they appear to be points of congruence of timelike worldlines not necessarily crossing in

TABLE 12

Rotational velocity	Mass distribution	a	b
v_1	$\rho_1(r) = \begin{cases} 3 & \text{if } r \leq 1 \\ 0 & \text{if } r \geq 1 \end{cases}$	-0.7	0.5
v_2	$\rho_2(r) = e^{-r^2}$ (Gaussian)	-0.7	0.5
v_3	$\rho_3(r) = \frac{1}{1+2r^2}$ (Lorentzian)	-0.7	0.5
v_4	$\rho_4(r) = e^{-r}$ (Exponential)	-0.7	0.5
v_5	$\rho_5(r) = re^{-r}$	-0.7	0.5
v_6	$\rho_6(r) = 10000\rho_1(10r) + \rho_5(r)$	-0.7	5

the four-dimensional spacetime. Hence, could this produce a sort of Big-Bang effect?

Conflicts of Interest

The author declares that there are no conflicts of interest regarding the publication of this article.

Acknowledgments

The author would like to thank Professor Ralf Hofmann from *Karlsruhe Institute of Technology* (Karlsruhe, Germany) and Doctor Thierry Grandou from *Institut de Physique de Nice* (Valbonne, France) for their invitation to participate at the “5th Winter Workshop on Non-Perturbative Quantum Field Theory” which was held at Sophia Antipolis (22–24 March 2017, France) to present the principles of relativistic localizing systems.

Endnotes

1. Roughly speaking, let x and y be two events in space-time. Then, (1) $x < y$ means that y is in the future null cone of x or in its interior, (2) $x \ll y$ means that y is in the interior of the future null cone of x , and (3) $x \rightarrow y$ means that x and y are joined by a null geodesic starting from x to y . The relation of order \rightarrow is *reflexive* and it is also called the *horismotic* relation (see, e.g., [15, p. R9]).
2. In [16]: (i) Condition (V): $x \ll y \Rightarrow x < y$. (ii) Condition (VII): $x \rightarrow y \Leftrightarrow x < y$ and $x \ll y$.
3. Lemma 1-1 [16]: Let x , y , and z be points in a causal space. If $x < y < z$ and $x \rightarrow z$ then $x \rightarrow y \rightarrow z$.
4. The ancillary emitter \mathcal{S} can also be considered as the “soldering” emitter.
5. We can notice that projective Cartan connections differ from Ehresmann connections which are projector fields (in principal bundles) but projective Cartan connections are not; the word “projective” does not refer to a projection in a vector space but to the projective geometry/frames. Also, these two connections differ from the notion of Cartan connection in the sense of Ehresmann which is associated with the definition of the soldering map.

References

- [1] J. L. Rubin, “Relativistic pentametric coordinates from relativistic localizing systems and the projective geometry of the spacetime manifold,” *Electronic Journal of Theoretical Physics*, vol. 12, no. 32, pp. 83–112, 2015.
- [2] B. Coll, “Elements for a theory of relativistic coordinate systems: formal and physical aspects,” in *Proceedings of the XXIII Spanish Relativity Meeting (EREs '00)*, J.-F. Pascual-Sánchez, L. Flora, A. S. Miguel, and F. Vicente, Eds., pp. 53–65, World Scientific Publishing Company, Incorporated, Valladolid, Spain, September 2000.
- [3] T. B. Bahder, “Navigation in curved space-time,” *American Journal of Physics*, vol. 69, no. 3, pp. 315–321, 2001.
- [4] M. Blagojević, J. Garecki, F. W. Hehl, and Y. N. Obukhov, “Real null coframes in general relativity and GPS type coordinates,” *Physical Review*, vol. 65, no. 4, Article ID 044018, 2002.
- [5] C. Rovelli, “GPS observables in general relativity,” *Physical Review*, vol. 65, no. 4, Article ID 044017, 2002.
- [6] B. Coll, A principal positioning system for the Earth, in *Journées 2002 – systèmes de référence spatio-temporels. Astrometry from ground and from space*, (N. Capitaine and M. Stavinschi, eds.), vol. 14, pp. 34–38, 2003.
- [7] B. Coll, J. J. Ferrando, and J. A. Morales, “Two-dimensional approach to relativistic positioning systems,” *Physical Review D*, vol. 73, no. 8, Article ID 084017, 2006.
- [8] B. Coll, “Relativistic positioning systems,” *AIP Conference Proceedings*, vol. 841, no. 1, pp. 277–284, 2006.
- [9] B. Coll, “Relativistic positioning systems,” in *Proceedings of the Workshop on Relativistic Positioning Systems and their Scientific Applications*, ESA Advanced Concepts Team and the University of Ljubljana, Ljubljana, Slovenia, September 2012.
- [10] J. Ehlers, F. A. E. Pirani, and A. Schild, “The geometry of free fall and light propagation,” in *General Relativity, Papers in Honour of J. L. Synge*, L. O’Raifeartaigh, Ed., pp. 63–84, Clarendon Press, Oxford, UK, 1972.
- [11] N. M. Woodhouse, “The differentiable and causal structures of space-time,” *Journal of Mathematical Physics*, vol. 14, pp. 493–501, 1973.
- [12] S. W. Hawking, A. R. King, and P. J. McCarthy, “A new topology for curved space-time which incorporates the causal, differential, and conformal structures,” *Journal of Mathematical Physics*, vol. 17, no. 2, pp. 174–181, 1976.
- [13] D. B. Malament, “The class of continuous timelike curves determines the topology of spacetime,” *Journal of Mathematical Physics*, vol. 18, no. 7, pp. 1399–1404, 1977.

- [14] H. Seifert and W. Threlfall, *Seifert and Threlfall: A Textbook of Topology*, vol. 89 of *Pure and Applied Mathematics*, Academic Press, London, UK, 1980.
- [15] A. García-Parrado and J. M. Senovilla, “Causal structures and causal boundaries,” *Classical and Quantum Gravity*, vol. 22, no. 9, pp. R1–R84, 2005.
- [16] E. H. Kronheimer and R. Penrose, “On the structure of causal spaces,” *Mathematical Proceedings of the Cambridge Philosophical Society*, vol. 63, no. 2, pp. 481–501, 1967.
- [17] C. Ehresmann, Les connexions infinitésimales dans un espace fibré différentiable. Centre Belge Rech. Math., Colloque de Topologie, Bruxelles, 5th to 8th june 1950, 29–55, 1951.
- [18] B. Famaey and S. S. McGaugh, “Modified Newtonian dynamics (MOND): observational phenomenology and relativistic extensions,” *Living Reviews in Relativity*, vol. 15, no. 1, article 10, 2012.
- [19] É. Cartan, *The Theory of Spinors*, Dover Publications, New York, NY, USA, 1981.

Research Article

Cosmic Microwave Background as a Thermal Gas of SU(2) Photons: Implications for the High- z Cosmological Model and the Value of H_0

Steffen Hahn¹ and Ralf Hofmann²

¹Karlsruhe Institute of Technology (KIT), Karlsruhe, Germany

²Institut für Theoretische Physik, Universität Heidelberg, Philosophenweg 16, 69120 Heidelberg, Germany

Correspondence should be addressed to Steffen Hahn; steffen.t.hahn@gmail.com

Received 9 May 2017; Revised 20 June 2017; Accepted 16 July 2017; Published 16 October 2017

Academic Editor: Edward Sarkisyan-Grinbaum

Copyright © 2017 Steffen Hahn and Ralf Hofmann. This is an open access article distributed under the Creative Commons Attribution License, which permits unrestricted use, distribution, and reproduction in any medium, provided the original work is properly cited. The publication of this article was funded by SCOAP³.

Presently, we are facing a 3σ tension in the most basic cosmological parameter, the Hubble constant H_0 . This tension arises when fitting the Lambda-cold-dark-matter model (Λ CDM) to the high-precision temperature-temperature (TT) power spectrum of the Cosmic Microwave Background (CMB) and to local cosmological observations. We propose a resolution of this problem by postulating that the thermal photon gas of the CMB obeys an SU(2) rather than U(1) gauge principle, suggesting a high- z cosmological model which is void of dark-matter. Observationally, we rely on precise low-frequency intensity measurements in the CMB spectrum and on a recent model independent (low- z) extraction of the relation between the comoving sound horizon r_s at the end of the baryon drag epoch and H_0 ($r_s H_0 = \text{const}$). We point out that the commonly employed condition for baryon-velocity freeze-out is imprecise, judged by a careful inspection of the formal solution to the associated Euler equation. As a consequence, the above-mentioned 3σ tension actually transforms into a 5σ discrepancy. To make contact with successful low- z Λ CDM cosmology we propose an interpolation based on percolated/depercolated vortices of a Planck-scale axion condensate. For a first consistency test of such an all- z model we compute the angular scale of the sound horizon at photon decoupling.

1. Introduction

Since the pioneering work by Yang and Mills [1] on the definition of a local four-dimensional, classical, and minimal field theory, which is based on the nonabelian gauge group SU(2), much progress has been made in elucidating the role of topologically stabilized and (anti)-self-dual field configurations in building the nonperturbative ground state and influencing the properties of its excitations [2–8]. In particular, the deconfining phase is subject to a highly accurate thermal ground state estimate [9, 10], being composed of so-called Harrington-Shepard (anti)calorons [11]. This (cosmologically relevant) ground state invokes both an adjoint Higgs mechanism [12–15], rendering two out of three directions of the SU(2) algebra massive (free thermal quasiparticles), and a U(1)_A chiral anomaly [2, 3, 5, 6], giving mass to the Goldstone mode induced by the associated dynamical

breaking of this global symmetry. Radiative corrections to thermodynamical quantities, evaluated on the level of free thermal (quasi)particles, are minute and well under control [9, 10]. Note that this is in contrast to the large effects of radiative corrections attributed to the effective QCD action at zero temperature in [16, 17] which are exploited as potential inducers of vacuum energy in the cosmological context in [18–22]. However, it was argued in [23, 24] that QCD condensates, which contribute to the trace anomaly of the energy-momentum tensor (as implied by the effective action), do not act cosmologically.

Postulating that thermal photon gases obey an SU(2) rather than a U(1) gauge principle, the SU(2) Yang-Mills scale can be inferred from low-(radio)frequency spectral intensity measurements, for example [25], of the Cosmic Microwave Background (CMB) [26], prompting the name SU(2)_{CMB}. Below we will use the name SU(2)_{CMB} synonymously for the

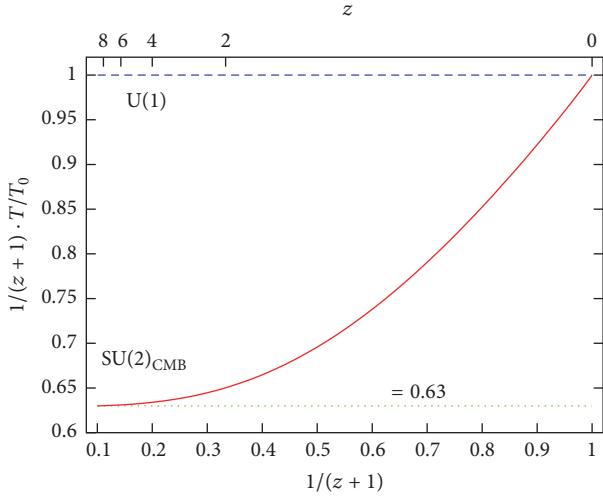


FIGURE 1: The T - z scaling relation $T/(T_0(z+1))$ in $SU(2)_{\text{CMB}}$ (solid). Note the emergence of $T/T_0 = 0.63(z+1)$ for $z \geq 9$ (dotted). The conventional U(1) theory for thermal photon gases associates with the dashed line. Data taken from [27] after slight and inessential correction.

implied cosmological model. To investigate the consequences of this postulate towards the equation of state radiative corrections are entirely negligible [9]. When subjecting local energy conservation in a Friedmann-Lemaître-Robertson-Walker (FLRW) universe to this equation of state the numerical temperature (T)-redshift (z) relation ($T(z)$) of the CMB follows; see Figure 1 [27, 28], where a comparison with the conventional U(1) photon gas is shown. The curvature of $T/(T_0(z+1))$ ($T_0 = 2.725$ K denoting today's CMB temperature) at low z is due to the influence of the SU(2) Yang-Mills mass scale on the equation of state. In [28] an argument is given why recent observational “extractions” of $T(z)$, which claim no deviations from the conventional behavior $T(z) = T_0(z+1)$, are circular. One has $T/T_0 = 0.63(z+1)$ at high z and therefore a lower slope compared to the conventional case. In an approximation, where recombination at z_* is subjected to thermodynamics, the decoupling condition is $\Gamma_{\text{Th}}(T_*) = H(z_*)$ where Γ_{Th} denotes the Thomson photon-electron scattering rate at the decoupling temperature $T_* \sim 3000$ K. We have $(\Omega_{0,b} + \Omega_{0,\text{DM}})/\Omega_{0,b} \sim 6.5 \equiv R_{m,1}$ where $\Omega_{0,b}$ and $\Omega_{0,\text{DM}}$ denote the respective ratios of today's energy densities in baryons and cold dark matter to the critical density. Since $z_{*,\text{SU}(2)_{\text{CMB}}}/z_{*,\Lambda\text{CDM}} \sim 1/0.63$ this roughly matches $(1/0.63)^3 \sim 4 \equiv R_{m,2}$. If a strong matter domination can be assumed during recombination then $R_{m,1}$ should be equal to $R_{m,2}$ but, due to matter-radiation equality occurring at $z \sim 1080$ in $SU(2)_{\text{CMB}}$, this assumption is not quite met, explaining the mild discrepancy between $R_{m,1}$ and $R_{m,2}$. Still, we take this rough argument and the desired minimality of the cosmological model as motivations to omit cold dark matter in the high- z cosmological model which operates down to recombination and well beyond it.

Concerning the number of massless neutrinos N_ν , a conservative input is used: $N_\nu = 3$ [29]. This high- z model, composed of $SU(2)_{\text{CMB}}$, baryonic matter, and massless

neutrinos ($N_\nu = 3$), is sufficient to predict the sound horizon r_s at the end of the baryon drag epoch which, in turn, can be confronted with the r_s - H_0 relation, recently extracted from local cosmological observations [30], to determine the value of H_0 . The value of r_s , as computed in a high- z model, rather sensitively depends on the definition of redshift z_{drag} for baryon-velocity (v_b) freeze-out. Usually, z_{drag} is identified with the maximum position of the so-called drag visibility function D_{drag} [31, 32]. However, inspecting the solution v_b of the corresponding Euler equation, given as a functional of D_{drag} , one concludes that this definition applies only in the limit of zero peak width. Realistic results for the ionization fraction χ_e , obtained by numerical integration of the according Boltzmann hierarchy (`recfast` [33]), imply that the width of this peak extends over several hundred units of redshift in both cases ΛCDM and $SU(2)_{\text{CMB}}$. As a consequence, a more precise definition of z_{drag} is in order which associates with the left flank of D_{drag} . Therefore, we will in the following refer to this corrected redshift for the freeze-out of v_b as $z_{\text{lf,drag}}$. Our value $r_s(z_{\text{lf,drag}}) \sim 1660$, after intersection with the r_s - H_0 relation of [30], determines the value of H_0 in good agreement with the value obtained in [34]. Also, we would like to point out that, as a consequence of the corrected baryon-velocity freeze-out condition, the value of H_0 in ΛCDM , obtained by this method, is now at a 5σ discrepancy with the value published in [34].

To be able to compute the CMB power spectra, our consistent high- z $SU(2)_{\text{CMB}}$ cosmological model of (3) needs to be connected to the observationally well cross-checked ΛCDM low- z parametrization of the universe's composition. To facilitate such an interpolation, a candidate real scalar field φ representing the dark sector is the so-called Planck-scale axion (PSA) condensate [35–37] which rests on chiral symmetry breaking within the Planckian epoch and the axial anomaly invoked by deconfining thermal ground states of Yang-Mills theories. Notice that the only Yang-Mills theory exhibiting the deconfining phase from today to well beyond recombination is $SU(2)_{\text{CMB}}$. A model, where φ undergoes coherent and damped oscillations at late times such as to effectively represent ΛCDM , is falsified by the redshift z_q , where the universe's expansion starts to accelerate, being too high. This prompts the idea that interpolation between $SU(2)_{\text{CMB}}$ at high z and ΛCDM at low z is achieved by the U(1) topologically stabilized solitonic configurations (vortices) of the PSA condensate occurring in percolated form (due to a Berezinskii-Kosterlitz-Thouless phase transition following their very creation during a nonthermal phase transition at very high z) down to intermediate z where a depercolation transition partially liberates them to effectively represent a pressureless vortex gas. Whether or not the cores of depercolated PSA vortices properly serve as dark-matter halos in spiral galaxies to explain the observed flattening of rotation curves and the lensing signatures of bullet galaxies is an open question. Likewise, it is not yet guaranteed that this new cosmological model, which exhibits radiation domination and baryon freeze-out prior to photon decoupling, explains the observed angular power spectra of the CMB.

TABLE 1: Cosmological parameter values employed in the computations and their sources, taken from [28].

Parameter	Value	Source
H_0 (SU(2) _{CMB})	$(73.24 \pm 1.74) \text{ km s}^{-1} \text{ Mpc}^{-1}$	[34]
H_0 (Λ CDM)	$(67.31 \pm 0.96) \text{ km s}^{-1} \text{ Mpc}^{-1}$	TT + low P , [38]
T_0	2.725 K	[39]
$\Omega_{\gamma,0} h^2$	2.46796×10^{-5}	Based on $T_0 = 2.725 \text{ K}$
$\Omega_{b,0} h^2$	0.02222 ± 0.99923	TT + low P [38]
$\Omega_{\text{CDM},0} h^2$	0.1197 ± 0.0022	TT + low P , [38]
η_{10}	6.08232 ± 0.06296	Based on $\Omega_{\gamma,0} h^2$, TT + low P [38]
Y_p	0.252 ± 0.041	TT, [38]
N_{eff}	3.15 ± 0.23	Abstract, [38]

This work is organized as follows. In Section 2 we explain our high- z cosmological model SU(2)_{CMB}, introduced in [28], and compare it with the conventional Λ CDM cosmology. The modification of decoupling conditions due to finite widths visibility functions is discussed in Section 3. Based on this, we perform the computation of r_s and confront it with the r_s - H_0 relation of [30] to determine the value of H_0 . Subsequently, in Section 5 we investigate whether coherent and damped oscillations of the PSA field can realistically represent Λ CDM at low z , with a negative result. According to [28] we are thus led to propose an interpolation between high- z SU(2)_{CMB} and low- z Λ CDM in terms of percolated PSA vortices which, at some intermediate redshift z_p , partially undergo a depercolation transition. Such a model is demonstrated to be consistent with the extremely well observed angular scale of the sound horizon at photon decoupling [38]. Finally, we summarize our results and provide an outlook on how the new model can be tested further by confrontation with the power spectra of various CMB angular correlation functions.

2. Definition of Cosmological Model SU(2)_{CMB}

In a flat FLRW universe, a cosmological model is given in terms of the z -dependence of the Hubble parameter

$$H(z) = H_0 \sqrt{\sum_i \Omega_i(z)}, \quad (1)$$

where H_0 is today's cosmological expansion rate and $\Omega_i(z) = f_i(z)\Omega_{i,0}$. Here $\Omega_{i,0}$ is the fraction of the energy density $\rho_{i,0}$ of fluid i to the critical density $\rho_{c,0}$ today. The function $f_i(z)$ is determined by energy conservation subject to fluid i 's equation of state. From now on we work in supernatural units ($c = \hbar = k_B = 1$) where Newton's constant G has units of inverse mass squared. Table 1 lists the parameter values used subsequently.

2.1. The Conventional Λ CDM Model. In the conventional high- z Λ CDM model $H(z)$ is given as

$$H(z) = H_0 \left[(\Omega_{b,0} + \Omega_{\text{CDM},0})(z+1)^3 + \left(1 + \frac{7}{8} \left(\frac{4}{11} \right)^{4/3} N_{\text{eff}} \right) \Omega_{\gamma,0} (z+1)^4 \right]^{1/2}. \quad (2)$$

Here nonrelativistic matter decomposes into baryonic (b) and cold dark matter (CDM). The radiation component contains photons with two polarizations, two relativistic vector modes with three polarizations each, and N_{eff} flavours of massless neutrinos with two polarizations each. $\Omega_{\gamma,0}$ is today's fraction of photonic energy density to critical energy density (for details see [38]).

2.2. Modifications of Λ CDM towards SU(2)_{CMB}. In high- z SU(2)_{CMB} the Hubble parameter is given as

$$H(z) = H_0 \left[\Omega_{b,0} (z+1)^3 + 4 \cdot (0.63)^4 \left(1 + \frac{7}{32} \left(\frac{16}{23} \right)^{4/3} N_\nu \right) \Omega_{\gamma,0} (z+1)^4 \right]^{1/2}. \quad (3)$$

In this case, only baryonic matter is present. We reiterate that both models, (2) and (3), need to be supplemented by a dark sector to yield successful low- z Λ CDM cosmology; see (32). The radiation sector is modified due to a different number of relativistic degrees of freedom and due to the SU(2)_{CMB} high- z temperature-redshift relation $T(z)$; for details see [27, 28].

3. The End of Recombination

The comoving sound horizon r_s at redshift z is defined as

$$r_s(z) = \int_z^\infty dz' \frac{c_s(z')}{H(z')}, \quad (4)$$

whereby c_s denotes the sound velocity in the primordial baryon-electron-photon plasma, given as

$$c_s \equiv \frac{1}{\sqrt{3(1+R)}}. \quad (5)$$

The function $R(z)$ is determined by 3/4 of the ratio of energy densities in baryons and photons. In Λ CDM we have

$$R(z) \equiv 111.019 \frac{\eta_{10}}{z+1}, \quad (6)$$

whereas in SU(2)_{CMB} one obtains

$$R(z) \equiv 111.019 \frac{\eta_{10}}{(0.63)^4 (z+1)}. \quad (7)$$

The values of η_{10} can be read off Table 1.

3.1. Conventional Freeze-Out. The final stages of recombination can be characterized in a twofold way. One considers either (i) photon temperature freeze-out, which is relevant for the peak structure in the temperature-temperature (TT) angular power spectrum of the CMB or (ii) baryon-velocity freeze-out, which is detectable in the matter correlation function (galaxy counts). Concerning case (i), the conventional criterion, which fixes the redshift z_* , reads

$$\tau(z_*) = \sigma_T \int_0^{z_*} dz \frac{\chi_e(z) n_e^b(z)}{(z+1)H(z)} = 1, \quad (8)$$

where σ_T denotes the total cross section for Thomson scattering, χ_e is the ionization fraction (calculated with `recfast`), and n_e^b refers to the density of free electrons just before hydrogen recombination, given as

$$n_e^b(z) = 410.48 \cdot 10^{-10} \eta_{10} (1 - Y_p) (z+1)^3 \text{ cm}^{-3}. \quad (9)$$

Here Y_p denotes the helium mass fraction in baryons (see Table 1). Concerning case (ii), the conventional criterion is defined as

$$\tau_{\text{drag}}(z) = \sigma_T \int_0^z dz' \frac{\chi_e(z') n_e^b(z')}{(z'+1)H(z')R(z')} = 1. \quad (10)$$

3.2. Corrected Freeze-Out. We now show that conditions (8) and (10) are imprecise due to the finite widths of the respective visibility functions. To see this, we have to analyze the formal solution of the Boltzmann hierarchy for the temperature perturbation and of the Euler equation for v_b [31, 32, 40]. Since the argument is similar for both cases we focus on the latter only. The Euler equation reads

$$\dot{v}_b = \frac{\dot{z}}{z+1} v_b + k\Psi + \dot{\tau}_{\text{drag}} (\Theta_1 - v_b), \quad (11)$$

where k is the comoving wave number (omitted as a subscript in the following), Θ_1 denotes the (relative) dipole of the temperature anisotropy [41], and Ψ represents the Newtonian gravitational potential. The overdot demands differentiation with respect to conformal time. Transforming the conformal time to a redshift dependence, the solution of (11) is

$$\begin{aligned} \frac{v_b(z)}{z+1} &= \lim_{Z \rightarrow \infty} \int_z^Z dz' \\ &\cdot \frac{e^{-\tau_{\text{drag}}(z',z)}}{H(z')(z'+1)} (\dot{\tau}_{\text{drag}}(z') \Theta_1(z') + k\Psi(z')) \\ &\sim \lim_{Z \rightarrow \infty} \int_z^Z dz' D_{\text{drag}}(z',z) \Theta_1(z'). \end{aligned} \quad (12)$$

Here τ_{drag} is defined as

$$\tau_{\text{drag}}(z',z) \equiv \int_z^{z'} dz'' \frac{\dot{\tau}_{\text{drag}}(z'')}{H(z'')}, \quad (13)$$

and the visibility function $D_{\text{drag}}(z',z)$ is represented by

$$D_{\text{drag}}(z',z) \equiv \frac{e^{-\tau_{\text{drag}}(z',z)} \dot{\tau}_{\text{drag}}(z')}{H(z')(z'+1)}. \quad (14)$$

In order to study freeze-out the function Θ_1 in (12) is considered slowly varying. Therefore, the variability of the integral solely depends on D_{drag} within its peak region. In both cases ΛCDM and $\text{SU}(2)_{\text{CMB}}$ function D_{drag} exhibits a broad peak in dependence of z' whose shape and maxima do not depend on z ; see Figure 2. Note that (10) describes the maxima $z'_{\text{max,drag}}$ of $D_{\text{drag}}(z',z)$. However, due to the finite width the integral in (12) is not saturated at $z = z_{\text{max,drag}}$ but rather ceases to vary for $z < z_{\text{lf,drag}}$ where lf denotes the maxima of the z' derivative of D_{drag} . Therefore, $z_{\text{lf,drag}}$ defines the freeze-out point more realistically than $z_{\text{max,drag}}$. According to Figure 2's caption the values of $z_{\text{drag}}, z_{\text{lf,drag}}$ deviate substantially. Namely,

$$\begin{aligned} z_{\text{drag}} &= 1813, \\ z_{\text{max,drag}} &= 1789, \\ z_{\text{lf,drag}} &= 1659 \\ &\quad (\text{SU}(2)_{\text{CMB}}), \\ z_{\text{drag}} &= 1059, \\ z_{\text{max,drag}} &= 1046, \\ z_{\text{lf,drag}} &= 973 \\ &\quad (\Lambda\text{CDM}). \end{aligned} \quad (15)$$

An analogous discussion applies to photon temperature freeze-out with the following results (see [28]):

$$\begin{aligned} z_* &= 1694, \\ z_{\text{max,*}} &= 1694, \\ z_{\text{lf,*}} &= 1555 \\ &\quad (\text{SU}(2)_{\text{CMB}}), \\ z_* &= 1090, \\ z_{\text{max,*}} &= 1072, \\ z_{\text{lf,*}} &= 988 \\ &\quad (\Lambda\text{CDM}). \end{aligned} \quad (16)$$

4. The Value of H_0

Subjecting the freeze-out redshifts of (15) to (4) under consideration of (2) and (3) yields

$$\begin{aligned} r_s(z_{\text{drag}}) &= (129.22 \pm 0.52) \text{ Mpc} \quad (\text{SU}(2)_{\text{CMB}}), \\ r_s(z_{\text{lf,drag}}) &= (137.19 \pm 0.45) \text{ Mpc} \quad (\text{SU}(2)_{\text{CMB}}), \end{aligned}$$

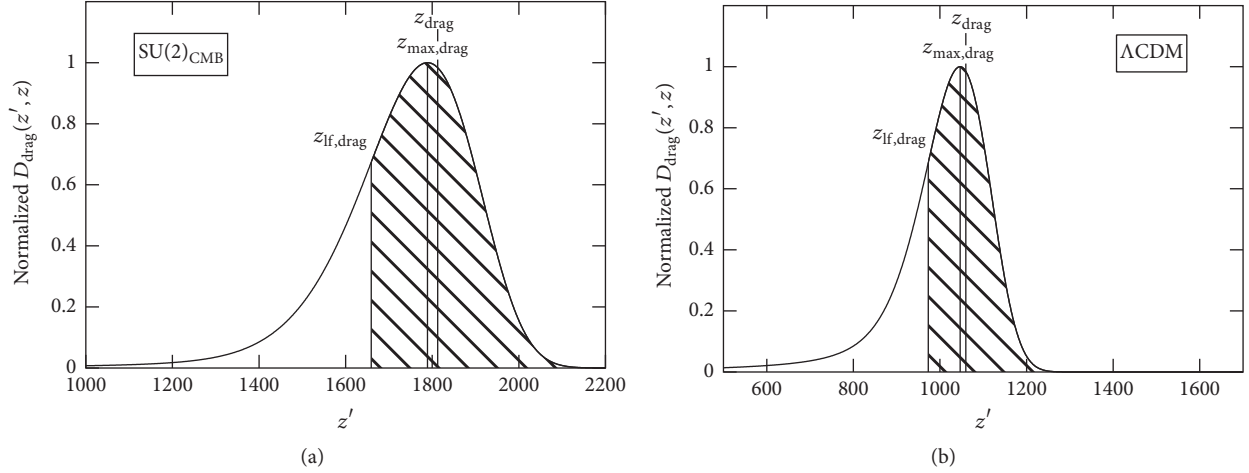


FIGURE 2: Normalised function $D_{\text{drag}}(z', z)$, defined in (14), if $z \leq z_{\text{max,drag}}$ for $SU(2)_{\text{CMB}}$ (a) and ΛCDM (b). Redshift $z_{\text{if,drag}}$ is defined as the position of the maximum of dD_{drag}/dz' (position of left flank of D_{drag}) whereas $z_{\text{max,drag}}$ denotes the position of the maximum of D_{drag} . The value of z_{drag} , defined in (10), essentially coincides with $z_{\text{max,drag}}$: $z_{\text{drag}} = 1813 \sim z_{\text{max,drag}} = 1789$ for $SU(2)_{\text{CMB}}$ and $z_{\text{drag}} = 1059 \sim z_{\text{max,drag}} = 1046$ for ΛCDM . This should be contrasted with $z_{\text{if,drag}} = 1659$ for $SU(2)_{\text{CMB}}$ and $z_{\text{if,drag}} = 973$ for ΛCDM . The hatched area under the curve determines the freeze-out value of $v_b/(z+1)$.

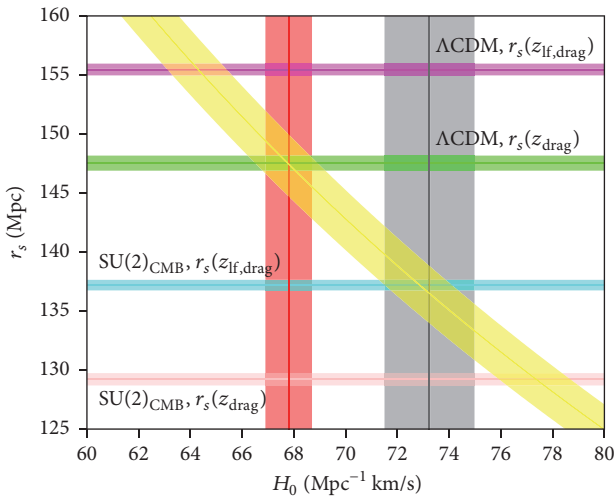


FIGURE 3: The $r_s(z_{\text{if,drag}})$ - H_0 relation (curved band) of [30] in confrontation with the high- z predictions of $r_s(z_{\text{if,drag}})$ and $r_s(z_{\text{drag}})$ in ΛCDM and $SU(2)_{\text{CMB}}$ (horizontal bands) of (17). Vertical bands indicate the values of H_0 extracted in [38] (low) and in [34] (high). Note that there is a $\sim 3\sigma$ tension. However, a $\sim 7\sigma$ discrepancy exists between the H_0 values of $(64.3 \pm 1.1) \text{ km s}^{-1} \text{ Mpc}^{-1}$ and $(72.9 \pm 1.2) \text{ km s}^{-1} \text{ Mpc}^{-1}$ associated with the intersections of $r_s(z_{\text{if,drag}})$ in ΛCDM and in $SU(2)_{\text{CMB}}$, respectively, with the $r_s(z_{\text{if,drag}})$ - H_0 relation. Taking $H_0 = (73.24 \pm 1.7) \text{ km s}^{-1} \text{ Mpc}^{-1}$ from [34] the discrepancy between this value and $(64.3 \pm 1.1) \text{ km s}^{-1} \text{ Mpc}^{-1}$ is about 5σ .

$$\begin{aligned} r_s(z_{\text{drag}}) &= (147.33 \pm 0.49) \text{ Mpc} \quad (\Lambda\text{CDM}), \\ r_s(z_{\text{if,drag}}) &= (154.57 \pm 3.33) \text{ Mpc} \quad (\Lambda\text{CDM}). \end{aligned} \quad (17)$$

In Figure 3, these (H_0 independent) values of the sound horizon are confronted with the r_s - H_0 relation of [30]. Note

the good agreement between the values of H_0 implied by $r_s(z_{\text{if,drag}})$ in $SU(2)_{\text{CMB}}$ and the extraction performed in [34]. On the other hand, $r_s(z_{\text{drag}})$ reproduces the value of H_0 published in [38] which exhibits a 3σ tension compared to [34]. However, according to Figure 3, the more realistic freeze-out value $z_{\text{if,drag}}$ in ΛCDM entails

$$H_0 = (64.5 \pm 1) \text{ km s}^{-1} \text{ Mpc}^{-1}. \quad (18)$$

Thus, in ΛCDM there actually is a 5σ discrepancy between the value of H_0 quoted in [34] and obtained by confrontation of r_s with the r_s - H_0 relation of [30].

5. Planck-Scale-Axion Field and Interpolation of High- z with Low- z Cosmology

Here we would like to analyze cosmological models which link low- z ΛCDM with high- z $SU(2)_{\text{CMB}}$. We assume a dark sector which originates from a real, minimally coupled scalar field, a pseudo Nambu-Goldstone mode of dynamical chiral symmetry occurring at the Planck scale [35, 36], whose potential is due to the chiral $U(1)_A$ anomaly invoked by (anti)calorons of the deconfining, thermal ground state of Yang-Mills theories [1–3, 6, 42–44]. This prompts the name Planck-scale axion (PSA). The only Yang-Mills theory, which is deconfining well above recombination, is $SU(2)_{\text{CMB}}$ because otherwise there would not be just one species of photons.

The radiatively protected potential for the axion condensate φ , arising due to the thermal ground state of $SU(2)_{\text{CMB}}$ [43, 44], reads as follows:

$$V(\varphi) = (\kappa \Lambda_{\text{CMB}})^4 \cdot \left(1 - \cos \frac{\varphi}{m_P}\right), \quad (19)$$

where $\Lambda_{\text{CMB}} \sim 10^{-4}$ eV, κ is a dimensionless factor of order unity, and the reduced Planck mass reads

$$m_p \equiv \frac{1.22 \times 10^{19}}{\sqrt{8\pi}} \text{ GeV} = (8\pi G)^{-1/2}. \quad (20)$$

With a canonical kinetic term for φ the according equation of motion is

$$\ddot{\varphi} + 3H\dot{\varphi} + \frac{d}{d\varphi}V(\varphi) = 0, \quad (21)$$

where an overdot signals the derivative with respect to cosmological time.

In a first attempt at a ΛCDM - $\text{SU}(2)_{\text{CMB}}$ interpolation we assume spatially homogeneous φ -field dynamics subject to ΛCDM constraints at low z . It turns out, however, that such a model predicts a value of z_q , defined as the zero of the deacceleration parameter

$$q(z) \equiv \frac{z+1}{2\widehat{H}^2} (\widehat{H}^2)' - 1, \quad (22)$$

of about $z_q \sim 3$ which is much higher than the realistic value ~ 0.7 obtained in ΛCDM . Therefore, as a second proposal we abolish the energy density arising from *spatially homogeneous* configurations of the field φ . Rather, we conceive the dark-matter sector in ΛCDM as a piece of energy density due to depercolated topological solitons (vortices) of the field φ which percolate instantaneously into a dark-energy like piece at some redshift z_p such that $z_{\text{re}} \ll z_p \ll z_{\text{lf,drag}}$. The origin of such a vortex percolate, with hierarchically ordered core sizes, could be due to Hagedorn transitions of Yang-Mills theories in the early universe which are accompanied by Berezinskii-Kosterlitz-Thouless transitions in the axionic sector. Today's value of Ω_Λ would then be interpreted in terms of not-yet depercolated vortices. Indeed, in such an interpolation between ΛCDM and $\text{SU}(2)_{\text{CMB}}$ a value of $z_p \sim 155$ can be fitted to the angular size of the sound horizon at photon decoupling. At $z_{\text{lf,drag}}$ the extra contribution to dark-energy amounts to $\sim 0.65\%$ of the baryonic energy density which is consistent with $\text{SU}(2)_{\text{CMB}}$.

5.1. Spatially Homogeneous, Coherent Oscillations. Here we discuss a cosmological model where the interpolation between ΛCDM and $\text{SU}(2)_{\text{CMB}}$ is attempted by a spatially homogeneous PSA field undergoing damped and coherent oscillations at late times. This models a pressureless component (cold dark matter) and component with negative pressure (dark-energy). Notice that these two components represent fluids that are not separately conserved.

The Hubble equation reads

$$H^2 = \frac{8\pi G}{3} \left(\frac{1}{2}\dot{\varphi}^2 + V(\varphi) + \rho_b + \rho_r \right) \equiv \frac{8\pi G}{3} \rho_c. \quad (23)$$

Here ρ_r denotes radiation-like energy density including $\text{SU}(2)_{\text{CMB}}$ (for $z \leq 9$ radiation energy density is severely suppressed in the cosmological model; for $z > 9$ the thermal ground state and the masses of the vector modes of

$\text{SU}(2)_{\text{CMB}}$ can be neglected) and three flavours of massless neutrinos; ρ_b is the energy density of baryons, in addition to the energy density $(1/2)\dot{\varphi}^2 + V(\varphi)$ associated with the spatially homogeneous PSA field φ which evolves temporally. Eqs. (21) and (23) can be cast into fully dimensionless equations by rescaling with powers of m_p in the following way:

$$\begin{aligned} V &= m_p^4 \widehat{V}, \\ \rho_i &= m_p^4 \widehat{\rho}_i \quad (i = b, r), \\ \varphi &= m_p \widehat{\varphi}, \\ H &= m_p \widehat{H}. \end{aligned} \quad (24)$$

In general, dimensionless quantities (after rescaling with the appropriate power of m_p) are indicated by the hat-symbol. After rescaling and in dependence of z (21) and (23) transmute into

$$\begin{aligned} \widehat{\varphi}'' \left[(z+1) \widehat{H} \right]^2 \\ + \widehat{\varphi}' \left[\frac{1}{2} (z+1)^2 (\widehat{H}^2)' - 2(z+1) \widehat{H}^2 \right] + \frac{d\widehat{V}}{d\widehat{\varphi}} = 0, \end{aligned} \quad (25)$$

$$\widehat{H}^2 = \frac{1}{3} \frac{\widehat{V} + \widehat{\rho}_{b,0} (z+1)^3 + \widehat{\rho}_r}{1 - (1/6)(z+1)^2 \widehat{\varphi}'^2}, \quad (26)$$

where a prime demands z -differentiation. In (26) we approximate $\widehat{\rho}_r$ as

$$\widehat{\rho}_r = \widehat{\rho}_{r,0} \begin{cases} 0 & (z < 9) \\ 4(0.63)^3 \left(1 + \frac{7}{32} \left(\frac{16}{23} \right)^{4/3} 3 \right) (z+1)^4 & (z \geq 9). \end{cases} \quad (27)$$

With the initial conditions

$$\begin{aligned} \widehat{\varphi}(z = z_i) &= \widehat{\varphi}_i, \\ \widehat{\varphi}'(z = z_i) &= 0 \end{aligned} \quad (28)$$

for sufficiently large z_i (no roll; in practice one safely can choose $z_i \sim 50$) the solution to (25) subject to (26) is unique. To fix the values of κ in (19) and $\widehat{\varphi}_i$ in (28) we demand

$$\rho_{c,0} = \frac{3H_0^2}{8\pi G} = 3m_p^4 \widehat{H}_0^2 \quad (29)$$

and that Ω_Λ coincides with typical fit value $\Omega_\Lambda \sim 0.7$ obtained in ΛCDM cosmology [38]:

$$\Omega_\Lambda = \frac{m_p^4}{\rho_{c,0}} \lim_{z \rightarrow 0} \left(\widehat{V} - \frac{1}{2} \left((z+1) \widehat{H} \widehat{\varphi}' \right)^2 \right) \sim 0.7. \quad (30)$$

Figure 4 shows the deacceleration parameter $q(z)$ for the model defined by (25), (26), (29), and (30). Obviously, this model is falsified by a much too high value of the zero z_q of $q(z)$.

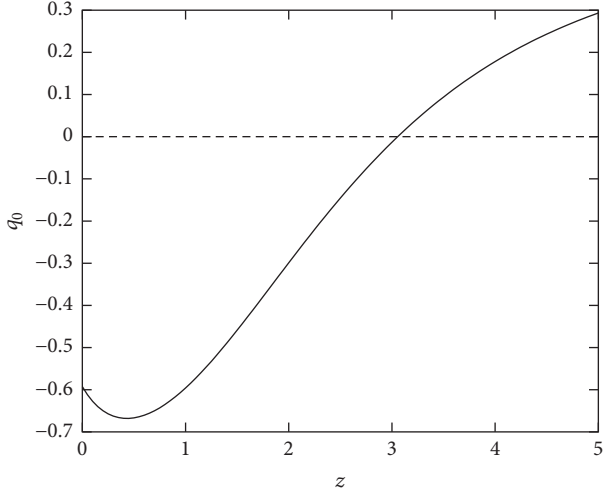


FIGURE 4: The deacceleration parameter $q(z)$ of (22) for the model defined by (25), (26), (29), and (30). Notice that the value of the zero z_q of $q(z)$ is $z_q \sim 3$. This is much higher than the realistic value $z_q \sim 0.7$ obtained in Λ CDM.

5.2. Percolated and Unpercolated Vortices. Here the basic idea invokes the fact that a PSA field φ , due to nonthermal phase transitions of the Hagedorn type (e.g., there should be an $SU(2)_e$ Yang-Mills theory of scale $\Lambda_e \gg \Lambda_{SU(2)_{\text{CMB}}}$ going confining at $T \sim \Lambda_e$) is subject to $U(1)_A$ winding and in this way creation of a density of percolated topological solitons (vortex percolate) with a hierarchical ordering of core sizes. Percolation could be understood as a Berezinskii-Kosterlitz-Thouless phase transition [45, 46]. Effectively, this percolate represents homogeneous, constant energy density. As the universe expands the vortex percolate is increasingly stretched, and at around some critical redshift $z_p \ll z_{\text{lf,drag}}$ it releases a part of its solitons characterized by some specific core size. The ensuing vortex gas acts cosmologically like pressureless matter. Vortices of larger core sizes remain trapped in the percolate. For this scenario to be a consistent interpolation of $SU(2)_{\text{CMB}}$ and Λ CDM we need to assure that $z_p \gg z_{\text{re}} \sim 6$ [47, 48].

With the definition of (27) the cosmological model to be considered thus reads

$$\widehat{H}^2 = \frac{1}{3} (\widehat{\rho}_b + \widehat{\rho}_{\text{DS}} + \widehat{\rho}_r), \quad (31)$$

where $\widehat{\rho}_{\text{DS}}$ is the dark sector energy density, defined as

$$\widehat{\rho}_{\text{DS}} = \widehat{\rho}_\Lambda + \widehat{\rho}_{\text{CDM},0} \cdot \begin{cases} (z+1)^3 & (z < z_p) \\ (z_p+1)^3 & (z \geq z_p) \end{cases}, \quad (32)$$

where $\widehat{\rho}_\Lambda$ and $\widehat{\rho}_{\text{CDM},0}$ are today's values of the dark-energy and cold-dark-matter densities associated with (30) and the value quoted in Table 1, respectively.

In order to fix the value of z_p we confront the model of (31) and (32) with the observed angular scale θ_* of the

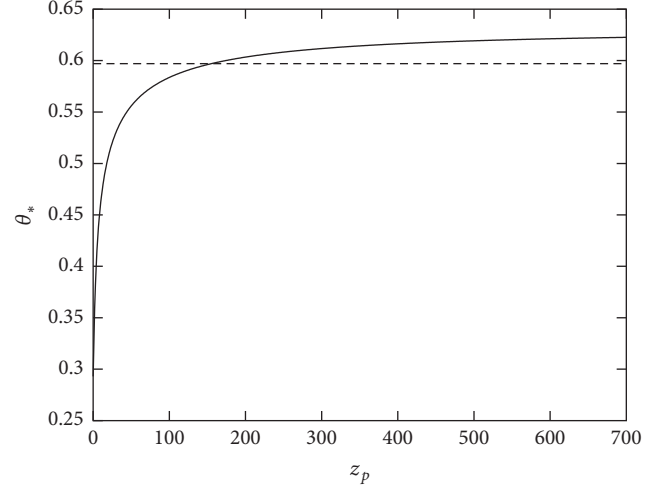


FIGURE 5: Function $\theta_*(z_p)$ for $\Omega_\Lambda = 0.7$, $\Omega_{\text{DM},0} = 0.26$, $\Omega_{b,0} = 0.04$, $\Omega_{\nu,0} = 4.6 \times 10^{-5}$, and $H_0 = 73.24 \text{ km s}^{-1} \text{ Mpc}^{-1}$ for the high- z $SU(2)_{\text{CMB}}$ and low- z Λ CDM interpolating cosmological model considered. Also indicated is the value $\theta_* = 0.597^\circ$ (dashed line), fitted to the CMB TT power spectrum.

sound horizon at CMB photon decoupling, occurring at $z_{\text{lf},*}$. Theoretically, θ_* is given as

$$\theta_* = \frac{r_s(z_{\text{lf},*})}{\int_0^{z_{\text{lf},*}} (dz/H(z))}. \quad (33)$$

To match $\theta_* = 0.597^\circ$, as extracted in [38] from the TT power spectrum, we require $z_p = 155.4$; see Figure 5. This yields a percentage of vacuum energy at CMB photon decoupling of about

$$\frac{\Omega_{\text{DM},0}}{\Omega_{b,0}} \left(\frac{z_p + 1}{z_{\text{lf},*} + 1} \right)^3 \sim 0.65\%. \quad (34)$$

The omission of vacuum energy in our $SU(2)_{\text{CMB}}$ high- z cosmological model of (3) thus is justified for the interpolating model defined in (31) and (32).

6. Summary and Outlook

In the present work we have analyzed, based on a modified temperature-redshift relation for the CMB which, in turn, derives from the postulate that thermal photon gases are subject to an $SU(2)$ rather than a $U(1)$ gauge principle, a high- z cosmological model which is void of dark-matter and considers three species of massless neutrinos. Such a model predicts (after a reconsideration of baryon-velocity freeze-out) a value of the sound horizon r_s which, together with a model independent extraction of the r_s - H_0 relation from cosmologically local observations in [30], yields good agreement with the value of H_0 determined by low- z observations in [34]. The same r_s - H_0 relation predicts a low value of H_0 in standard Λ CDM cosmology which is at a 5σ discrepancy with the value given in [34].

Motivated by the above results, an interpolation between Λ CDM at low z and our new high- z model is called for. In a first attempt, we have investigated whether coherent and damped oscillations of a Planck-scale axion condensate can realistically accomplish this, with a negative result. With [28] we were thus led to propose an interpolation in terms of percolated PSA vortices which, at some intermediate z_p , partially undergo a depercolation transition. We have demonstrated this model to be consistent with the angular scale of the sound horizon at photon decoupling.

The new model needs to be tested against the various CMB angular spectra. Our hope is that radiative corrections in SU(2) Yang-Mills thermodynamics, which play out at low z , are capable of explaining the large-angle anomalies of the CMB [49].

Conflicts of Interest

The authors declare that they have no conflicts of interest.

References

- [1] C. N. Yang and R. L. Mills, "Conservation of isotopic spin and isotopic gauge invariance," *Physical Review*, vol. 96, no. 1, pp. 191–195, 1954.
- [2] S. L. Adler and W. A. Bardeen, "Absence of higher-order corrections in the anomalous axial-vector divergence equation," *Physical Review*, vol. 182, no. 5, pp. 1517–1536, 1969.
- [3] J. S. Bell and R. Jackiw, "A PCAC puzzle: $\pi^0 \rightarrow \gamma\gamma$ in the σ -model," *Il Nuovo Cimento A*, vol. 60, no. 1, pp. 47–61, 1969.
- [4] T. Banks and A. Casher, "Chiral symmetry breaking in confining theories," *Nuclear Physics, Section B*, vol. 169, no. 1-2, pp. 103–125, 1980.
- [5] G. 't Hooft, "How instantons solve the U(1) problem," *Physics Reports*, vol. 142, no. 6, pp. 357–387, 1986.
- [6] K. Fujikawa, "Path integral for gauge theories with fermions," *Physical Review D*, vol. 21, no. 10, pp. 2848–2858, 1980, Erratum to: *Physical Review D*, vol. 22, p. 1499, 1980.
- [7] D. Dyakonov and V. Yu. Petrov, "Instanton-based vacuum from the Feynman variational principle," *Nuclear Physics B*, vol. 245, pp. 259–292, 1984.
- [8] T. Schäfer and E. V. Shuryak, "Instantons in QCD," *Reviews of Modern Physics*, vol. 70, no. 2, pp. 323–425, 1998.
- [9] R. Hofmann, *The Thermodynamics of Quantum Yang-Mills Theory: Theory and Applications*, World Scientific, 2nd edition, 2016.
- [10] I. Bischer, T. Grandou, and R. Hofmann, "Massive loops in thermal SU(2) Yang-Mills theory: radiative corrections to the pressure beyond two loops," *International Journal of Modern Physics A*, vol. 32, no. 19-20, Article ID 1750118, 2017.
- [11] B. J. Harrington and H. K. Shepard, "Periodic Euclidean solutions and the finite-temperature Yang-Mills gas," *Physical Review D*, vol. 17, no. 8, pp. 2122–2125, 1978.
- [12] P. W. Anderson, "Plasmons, gauge invariance, and mass," *Physical Review*, vol. 130, no. 1, pp. 439–442, 1963.
- [13] P. W. Higgs, "Broken symmetries and the masses of gauge bosons," *Physical Review Letters*, vol. 13, pp. 508–509, 1964.
- [14] G. S. Guralnik, C. R. Hagen, and T. W. B. Kibble, "Global conservation laws and massless particles," *Physical Review Letters*, vol. 13, no. 20, pp. 585–587, 1964.
- [15] F. Englert and R. Brout, "Broken symmetry and the mass of gauge vector mesons," *Physical Review Letters*, vol. 13, pp. 321–323, 1964.
- [16] H. Pagels and E. Tomboulis, "Vacuum of the quantum Yang-Mills theory and magnetostatics," *Nuclear Physics B*, vol. 143, no. 3, pp. 485–502, 1978.
- [17] S. G. Matinyan and G. K. Savvidy, "Vacuum polarization induced by the intense gauge field," *Nuclear Physics, Section B*, vol. 134, no. 3, pp. 539–545, 1978.
- [18] Y. Zhang, "Inflation with quantum Yang-Mills condensate," *Physics Letters B*, vol. 340, no. 1-2, pp. 18–22, 1994.
- [19] R. Pasechnik, V. Beylin, and G. Vereshkov, "Dark energy from graviton-mediated interactions in the QCD vacuum," *Journal of Cosmology and Astroparticle Physics*, vol. 2013, no. 6, article 011, 2013.
- [20] R. Pasechnik, V. Beylin, and G. Vereshkov, "Possible compensation of the QCD vacuum contribution to the dark energy," *Physical Review D*, vol. 88, no. 2, Article ID 023509, 2013.
- [21] R. Pasechnik, G. Prokhorov, and O. Teryaev, "Mirror QCD and cosmological constant," *Universe*, vol. 3, no. 2, article 43, 2017.
- [22] P. Donà, A. Marcianò, Y. Zhang, and C. Antolini, "Yang-Mills condensate as dark energy: a nonperturbative approach," *Physical Review D*, vol. 93, no. 4, Article ID 043012, 13 pages, 2016.
- [23] A. Casher and L. Susskind, "Chiral magnetism (or magnetohydrochironics)," *Physical Review D*, vol. 9, no. 2, pp. 436–460, 1974.
- [24] S. J. Brodsky and R. Shrock, "Condensates in quantum chromodynamics and the cosmological constant," *Proceedings of the National Academy of Sciences of the United States of America*, vol. 108, no. 1, pp. 45–50, 2011.
- [25] D. J. Fixsen, A. Kogut, S. Levin et al., "Arcade 2 measurement of the absolute sky brightness at 3–90 GHz," *The Astrophysical Journal*, vol. 734, p. 5, 2011.
- [26] R. Hofmann, "Low-frequency line temperatures of the CMB," *Annalen der Physik*, vol. 18, no. 9, pp. 634–639, 2009.
- [27] R. Hofmann, "Relic photon temperature versus redshift and the cosmic neutrino background," *Annalen der Physik*, vol. 527, no. 3-4, pp. 254–264, 2015.
- [28] S. Hahn and R. Hofmann, "SU(2)CMB at high redshifts and the value of H_0 ," *Monthly Notices of the Royal Astronomical Society*, vol. 469, no. 1, pp. 1233–1245, 2017.
- [29] C. Patrignani, K. Agashe, G. Aielli et al., "Review of particle physics," *Chinese Physics C*, vol. 40, no. 10, Article ID 100001, 2016.
- [30] J.-L. Bernal, L. Verde, and A. G. Riess, "The trouble with H_0 ," *Journal of Cosmology and Astroparticle Physics*, vol. 10, article 019, 2016.
- [31] W. Hu and N. Sugiyama, "Anisotropies in the cosmic microwave background: an analytic approach," *The Astrophysical Journal*, vol. 444, p. 489, 1995.
- [32] W. Hu and N. Sugiyama, "Small-scale cosmological perturbations: an analytic approach," *The Astrophysical Journal*, vol. 471, no. 2, pp. 542–570, 1996.
- [33] <http://www.astro.ubc.ca/people/scott/recfast.html>.
- [34] A. G. Riess, L. M. Macri, S. L. Hoffmann et al., "A 2.4% determination of the local value of the hubble constant," *The Astrophysical Journal*, vol. 826, no. 1, article 56, 2016.
- [35] J. A. Frieman, C. T. Hill, A. Stebbins, and I. Waga, "Cosmology with ultralight pseudo nambu-goldstone bosons," *Physical Review Letters*, vol. 75, no. 11, pp. 2077–2080, 1995.

- [36] F. Giacosa and R. Hofmann, “A Planck-scale axion and SU(2) Yang-Mills dynamics: Present acceleration and the fate of the photon,” *European Physical Journal C*, vol. 50, no. 3, pp. 635–646, 2007.
- [37] F. Giacosa, R. Hofmann, and M. Neubert, “A model for the very early Universe,” *Journal of High Energy Physics*, vol. 2008, no. 2, article 077, 2008.
- [38] P. A. R. Ade, N. Aghanim, M. Arnaud et al., “Planck 2015 results,” *Astronomy & Astrophysics*, vol. 594, article A13, 63 pages, 2016.
- [39] D. J. Fixsen, E. S. Cheng, J. M. Gales et al., “The cosmic microwave background spectrum from the full COBE FIRAS data set,” *The Astrophysical Journal*, vol. 473, p. 576, 1996.
- [40] J. R. Bond and G. Efstathiou, “Cosmic background radiation anisotropies in universes dominated by nonbaryonic dark matter,” *The Astrophysical Journal*, vol. 285, p. L45, 1984.
- [41] P. J. E. Peebles and D. T. Wilkinson, “Comment on the anisotropy of the primeval fireball,” *Physical Review*, vol. 174, no. 5, p. 2168, 1968.
- [42] K. Fujikawa, “Path-integral measure for gauge-invariant fermion theories,” *Physical Review Letters*, vol. 42, no. 18, pp. 1195–1198, 1979.
- [43] R. D. Peccei and H. R. Quinn, “Constraints imposed by CP conservation in the presence of pseudoparticles,” *Physical Review D*, vol. 16, no. 6, pp. 1791–1797, 1977.
- [44] R. D. Peccei and H. R. Quinn, “CP conservation in the presence of pseudoparticles,” *Physical Review Letters*, vol. 38, no. 25, pp. 1440–1443, 1977.
- [45] V. L. Berezinskii, “Destruction of long-range order in one-dimensional and two-dimensional systems possessing a continuous symmetry group. II. Quantum systems,” *Soviet Physics—JETP*, vol. 34, no. 3, p. 610, 1972.
- [46] J. M. Kosterlitz and D. J. Thouless, “Ordering, metastability and phase transitions in two-dimensional systems,” *Journal of Physics C: Solid State Physics*, vol. 6, no. 7, pp. 1181–1203, 1973.
- [47] J. E. Gunn and B. A. Peterson, “On the density of neutral hydrogen in intergalactic space,” *The Astrophysical Journal*, vol. 142, p. 1633, 1965.
- [48] R. H. Becker, X. Fan, R. L. White et al., “Evidence for reionization at $z \sim 6$: detection of a Gunn-Peterson trough in a $z = 6.28$ quasar,” *The Astronomical Journal*, vol. 122, p. 2850, 2001.
- [49] R. Hofmann, “The fate of statistical isotropy,” *Nature Physics*, vol. 9, pp. 686–689, 2013.

Research Article

Massive Fluctuations in Deconfining SU(2) Yang-Mills Thermodynamics

Ingolf Bischer

Institut für Theoretische Physik, Universität Heidelberg, Philosophenweg 16, 69120 Heidelberg, Germany

Correspondence should be addressed to Ingolf Bischer; bischer@thphys.uni-heidelberg.de

Received 3 April 2017; Revised 17 July 2017; Accepted 10 August 2017; Published 27 September 2017

Academic Editor: Sally Seidel

Copyright © 2017 Ingolf Bischer. This is an open access article distributed under the Creative Commons Attribution License, which permits unrestricted use, distribution, and reproduction in any medium, provided the original work is properly cited. The publication of this article was funded by SCOAP³.

We review how vertex constraints inherited from the thermal ground state strongly reduce the integration support of loop four-momenta associated with massive quasiparticles in bubble diagrams constituting corrections to the free thermal quasiparticle pressure. In spite of the observed increasingly suppressing effect when increasing 2-particle-irreducible (2PI) loop order, a quantitative analysis enables us to disprove the conjecture voiced in hep-th/0609033 that the loop expansion would terminate at a finite order. This reveals the necessity to investigate exact expressions of (at least some) higher-loop order diagrams. Explicit calculation shows that although the behaviour of the 2PI three-loop contribution at low temperatures displays hierarchical suppression compared to lower loop orders, its high-temperature expression instead dominates all lower orders. However, an all-loop-order resummation of a class of 2PI bubble diagrams is shown to yield an analytic continuation of the low-temperature hierarchy to all temperatures in the deconfining phase.

1. Introduction

There is a variety of topologically nontrivial solutions to classical equations of motion in SU(2) gauge theory on a flat Euclidean spacetime manifold. That the trivial vacuum may not be the relevant one at nonzero temperature becomes apparent in the problems of the standard perturbative approach, in particular in the infrared problem already pointed out by Linde in 1980 [1]. Divergences in the soft-magnetic sector, as encountered in small-coupling expansions at high temperature [2–8], motivated by asymptotic freedom [9–11], invalidate the perturbative expansion starting at some finite order [12] and hint at relevant substructures that are missed. Indeed, lattice-based studies relate topological configurations to fundamental properties of Yang-Mills theory [13–15]. An approach to finding a thermal ground state estimate that includes gauge field configurations of nontrivial topology reveals that Harrington-Shepard (anti)calorons [16] of topological charge $|k| = 1$ are the constituents of this ground state with spatially densely packed centers and overlapping peripheries. Their contribution is manifest in the nontriviality of the spatial and

scale-parameter average (spatial coarse-graining) of the two-point field-strength correlator in association with the magnetic field of an (anti)caloron [17]. Lattice gauge theory qualitatively reproduces certain aspects of this correlation in infrared sensitive thermodynamical quantities such as the pressure, provided that the *differential* method is used which appeals to the nonperturbative beta function [18, 19]. However, this function needs to be approximated. On the other hand, the *integral* method [20], which does not rely on the beta function but introduces an integration constant, yields results that are largely disparate, the reason being the choice of integration constant (no negative pressure) and finite-volume artifacts [21].

In this work, we give an overview of recent proceedings in the treatment of radiative corrections to the pressure of this thermal ground state beyond two-loop order. These corrections are obtained by a loop expansion of the three effective gauge fields (quasiparticles) obtained after coarse-graining over the ground state constituent configurations, two of which become massive by an adjoint Higgs mechanism. We find that resummation of infinitely many diagrams

is necessary to obtain a finite result which after resummation is well-controlled in the case of the diagrams treated here. A much more detailed and technical presentation of our results can be found in [22].

This work is structured as follows. In Section 2, we present a nonexhaustive way of using constraints in the massive sector to reduce the number of possible loop-momentum configurations in bubble diagrams in a purely combinatorical way. In Section 3, we state the contributions of all bubble diagrams in the massive sector up to three loops and conclude why resummation is necessary. This resummation of a particular family of diagrams is finally demonstrated in Section 4 and followed by a summary and conclusions in Section 5.

2. Sign Constraints in Massive Bubble Diagrams

In this section, we explain the origin and structure of sign constraints on massive quasiparticle loop momenta mediated by four-vertices. We state the results of an efficient book-keeping explained in [22] in terms of the ratio of the number of nonexcluded sign configurations and the number of a priori possible sign configurations. To close the section, an explanation of why nonvanishing diagrams exist at any finite loop order is given.

The full set of Feynman rules for the quasiparticles populating the thermal ground state in the deconfining phase is listed in [17]. Here, we restrict the discussion to 2PI diagrams, by which we mean bubble diagrams that do not become 1PI contributions to a polarisation tensor upon cutting any single line, including only the two massive fields (corresponding to two $su(2)$ algebra directions that are broken by the thermal ground state and obtain a mass by an adjoint Higgs mechanism). This implies that only four-vertices may appear. The first important fact for what follows is that those massive fields propagate strictly on-shell

$$p^2 = m^2 = 4e^2 |\phi|^2, \quad (1)$$

where p is any four-momentum, m is the mass, e is the effective gauge coupling, and $|\phi|$ is the gauge invariant modulus of the inert, adjoint scalar field associated with densely packed (anti)caloron centers in the thermal ground state [17, 23] which sets the scale of maximal resolution. The second important fact is that the scattering channels at four-vertices are restricted not to resolve higher energies than this scale. By this we mean that each four-vertex hosts a superposition of channels corresponding to the three Mandelstam variables s , t , and u constrained by $|s|, |t|, |u| \leq |\phi|^2$. By virtue of the on-shellness, each constraint on a Mandelstam variable implies a restriction of the energy-signs of the respective loop momenta according to [24]

$$\begin{aligned} |(p+q)^2| \leq |\phi|^2 &\implies \\ \text{sgn}(p_0) &= -\text{sgn}(q_0), \\ |(p-q)^2| \leq |\phi|^2 &\implies \\ \text{sgn}(p_0) &= \text{sgn}(q_0). \end{aligned} \quad (2)$$

TABLE 1: Ratio R of allowed versus a priori possible energy-sign and scattering-channel combinations for 2PI bubble diagrams up to six loops. S denotes a diagram's symmetry factor.

Loop number	Diagram number	R	S^{-1}	$R \cdot S$
3	1	0.1667	48	0.00347222
4	1	0.0463	48	0.00096451
5	1	0.0139	128	0.00010851
5	2	0.0123	32	0.00038580
6	1	0.0044	320	0.00001366
6	2	0.0036	32	0.00011253
6	3	0.0033	16	0.00020898
6	4	0.0033	120	0.00002572

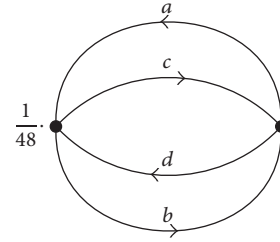


FIGURE 1: The only 2PI three-loop diagram (symmetry factor $1/48$, $R = 1/6$).

Hence, for all scattering channel combinations in a diagram, one can exclude several sign configurations. We define the ratio R of a diagram by the sum (over channel combinations) of the numbers of nonexcluded sign configurations divided by the number of a priori possible sign configurations times the number of channel combinations ($2^{2n} \cdot 3^n$, where n denotes the number of vertices). In Figure 1 through Figure 5 we give all 2PI diagrams up to six-loop order and their respective values of R . All results are listed in Table 1.

In agreement with a simple counting argument given in [25], we observe a monotonic decrease of R with increasing loop order. However, none of the diagrams become completely excluded. Indeed, one can show that diagrams with nonexcluded sign configurations (i.e., diagrams with $R > 0$) exist at any finite loop order [22]. This is most transparent in the class of diagrams of highest symmetry, namely, Figure 1, and the diagrams symmetric under the n -th dihedral group, Figures 2, 3(a), and 4. In this class, there is a vertex channel combination such that only the two momenta connecting the same two vertices appear as pairs in a constraint, for example, for the diagram in Figure 4 the configuration

$$\begin{aligned} |(p_1 - p_6)^2| &= |(p_2 - p_7)^2| = |(p_3 - p_8)^2| \\ &= |(p_4 - p_9)^2| = |(p_5 - p_{10})^2| \leq |\phi|^2, \end{aligned} \quad (3)$$

where the equalities stem from momentum conservation at each vertex. One independent constraint, however, is not sufficient to exclude all sign configurations and it follows that

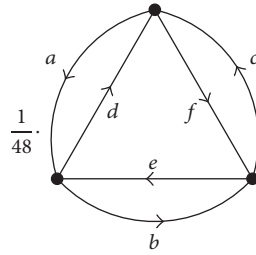


FIGURE 2: The only 2PI four-loop diagram (symmetry factor $1/48$, $R = 5/108 = 0.0463$).

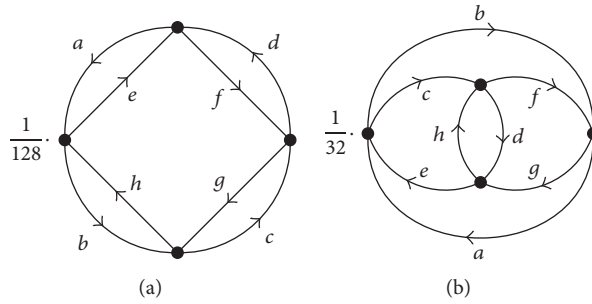


FIGURE 3: The first and second 2PI five-loop diagram (symmetry factors $1/128$ (first) and $1/32$ (second), $R = 1/72 = 0.0139$ (first) and $R = 1/81 = 0.0123$ (second)).

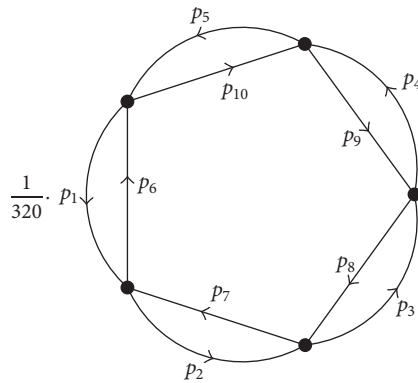
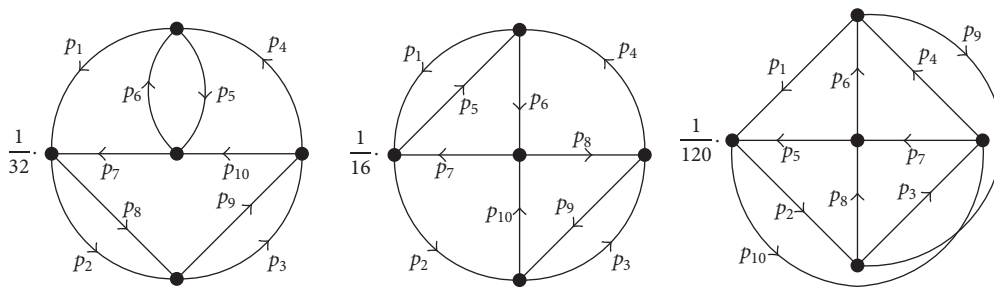


FIGURE 4: The first and most symmetric 2PI six-loop diagram (symmetry factor $1/320$, $R = 17/3888 = 0.0044$).



(a) The second and third 2PI six-loop diagrams (symmetry factors $1/32$ and $1/16$, $R = 7/1944 = 0.0036$ and $R = 13/3888 = 0.0033$)

(b) The fourth 2PI six-loop diagram (symmetry factor $1/120$, $R = 1/324 = 0.0031$). This is the only nonplanar diagram up to six-loop order

FIGURE 5

$R > 0$. In the cases of lower-symmetry diagrams in Figures 3(b) and 5 there are fewer nonexcluded configurations compared to Figures 3(a) and 4, respectively, so indeed symmetry appears to be associated with the ratio R .

Despite this drawback, the actual order of magnitude of the higher-loop order diagrams is not at all obvious from these sign considerations. Thus it is necessary to consider full expressions of the loop integrals to make definite statements about the convergence properties of the loop expansion. In the next section, we hence discuss the results of explicit calculations up to three-loop order which display hierarchical ordering at low temperatures but a dominating three-loop contribution at high temperatures.

3. The Massive Sector up to Three Loops

3.1. One-Loop Pressure. In general, the expansion of the deconfining pressure in SU(2) Yang-Mills thermodynamics reads

$$P = P_{\text{gs}} + P_{1\text{-loop}} + \Delta P, \quad (4)$$

where $P_{\text{gs}} = -4\pi\Lambda^3 T$ denotes the negative contribution from the ground state estimate, $P_{1\text{-loop}}$ represents the pressure exerted by noninteracting thermal quasiparticles (one-loop), and ΔP summarises all radiative corrections as expanded in ascending loop orders. Here, Λ denotes the Yang-Mills scale. Unlike in standard perturbation theory, the radiative corrections do not represent an asymptotic (power) series in the coupling constant. As hinted in Section 2, the usefulness of loop ordering in this case stems from the increasing number of constraints on loop integrations with increasing loop order. Loosely speaking, the quantity which serves as a (nonlocal) expansion parameter is the highly constrained volume of loop momenta over the unconstrained volume. The expectation consistent with previous calculations [26, 27] is that fixed-order contributions to ΔP decrease strongly enough with increasing loop order and number of constraints so as to render the expansion convergent in the standard mathematical sense. As we discuss below, however, this is not the case at high temperatures, where resummation techniques have to be applied in order to extend the convergent low-temperature behaviour. On the level of free quasiparticles, the trace anomaly of the energy-momentum tensor, which rises linearly in T , is invoked by both P_{gs} and the massive contribution of $P_{1\text{-loop}}$ [28].

Restricting ourselves to the massive sector only, the one-loop pressure reads [17]

$$P(\lambda)|_{1\text{-loop}} = -\Lambda^4 \frac{12\lambda^4}{(2\pi)^6} \bar{P}(2a), \quad (5)$$

where

$$\bar{P}(y) = \int_0^\infty dx x^2 \log \left[1 - e^{-\sqrt{x^2+y^2}} \right], \quad (6)$$

$\lambda \equiv 2\pi T/\Lambda$, and $a \equiv m/2T$. The one-loop pressure rapidly saturates into the T^4 behaviour of the Stefan-Boltzmann limit. Notice that, even at high temperatures, where this limit is

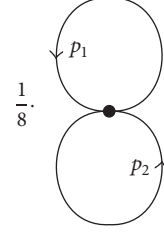


FIGURE 6: The two-loop diagram for the pressure in the massive sector of deconfining SU(2) Yang-Mills thermodynamics (symmetry factor 1/8).

approached in a power-like way, the number of independent polarisations is six rather than four due to the thermal ground state minutely breaking the original gauge symmetry. This means that including the massless gauge mode one arrives at eight rather than six polarisations as generally utilised in perturbative and phenomenological “bag model” [29] calculations, the two additional degrees of freedom originating from the scalar magnetic monopole and its antimonopole [17]. The thermal ground state contribution P_{gs} would be modelled by a temperature-dependent bag pressure.

3.2. Two-Loop Correction. The pressure contribution associated with the two-loop diagram in Figure 6 reads [26, 27]

$$\begin{aligned} \Delta P|_{2\text{-loop}} &= \frac{-2e^2 T^4}{\lambda^6} \int dr_1 dr_2 d\cos\theta \\ &\cdot \frac{r_1^2 r_2^2}{\sqrt{r_1^2 + m^2} \sqrt{r_2^2 + m^2}} \times \left[14 - 2 \frac{k^4}{m^4} \right] \\ &\cdot n_B \left(2\pi \sqrt{\frac{r_1^2 + m^2}{\lambda^3}} \right) \\ &\cdot n_B \left(2\pi \sqrt{\frac{r_2^2 + m^2}{\lambda^3}} \right), \end{aligned} \quad (7)$$

where

$$k^2 \equiv p_1 p_2 = -\sqrt{r_1^2 + m^2} \sqrt{r_2^2 + m^2} - r_1 r_2 \cos\theta \quad (8)$$

is defined as the Lorentz-invariant product of the dimensionless (we normalise physical four-momentum components P^μ by $|\phi|$ to arrive at dimensionless components p^μ). Likewise, the physical mass is made dimensionless: $m = 2e$) loop four-momenta p_1 and p_2 , $r_1 = |\mathbf{p}_1|$ and $r_2 = |\mathbf{p}_2|$ denote the moduli of their spatial parts, $n_B(x) = (\exp(x) - 1)^{-1}$ refers to the Bose-Einstein distribution function, and the integration is subject to the constraint

$$\left| 2m^2 - 2\sqrt{r_1^2 + m^2} \sqrt{r_2^2 + m^2} - 2r_1 r_2 \cos\theta \right| \leq 1. \quad (9)$$

In Figure 7(a), the temperature dependence of the numerical integrations in (7) and (5) is shown in terms of their ratio.

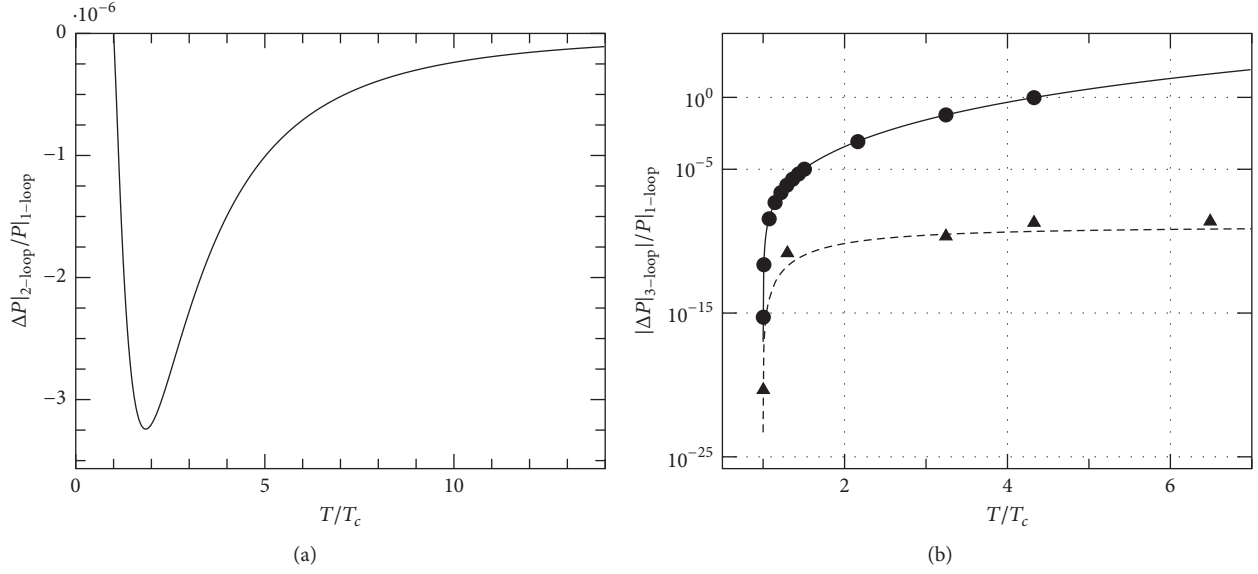


FIGURE 7: The two-loop pressure contribution (a) and moduli of the three-loop pressure corrections (b), $1/3\Delta P|_{3\text{-loop,ss}}$ (solid) and $2/3\Delta P|_{3\text{-loop,st}}$ (dashed), divided by the massive sector one-loop pressure $P|_{1\text{-loop}}$. In (b), the continuous curves represent the analytical high- T expressions from [22], while the dots and triangles are the respective ss and st Monte Carlo (MC) results.

3.3. Three-Loop Correction. The pressure contribution associated with the diagram in Figure 1 has been calculated in [22]. After relabelling $(a, b, c, d \rightarrow p_1, p_3, p_2, p_4)$ and in terms of dimensionless momenta, it reads

$$\begin{aligned} \Delta P|_{3\text{-loop}} &= i \frac{\Lambda^4}{48\lambda^2} e^4 \frac{1}{(2\pi)^6} \sum_{\text{signs}} \int d\theta_1 d\varphi_1 dr_1 dr_2 d\theta_3 \\ &\cdot \sum_{\{r_3\}} r_1^2 r_2^2 r_3^2 \sin \theta_1 \sin \theta_3 \times P(p_i) \\ &\cdot \frac{n'_B(r_1) n'_B(r_2) n'_B(r_3) n'_B(r_4)}{8 |P_1^0 P_2^0 P_3^0 P_4^0|}. \end{aligned} \quad (10)$$

The first sum in (10) runs over allowed sign combinations for p_i^0 , $i = 1, \dots, 4$. All four-momenta $p_i \equiv (p_i^0, \mathbf{p}_i)$ are on-shell, $|p_i^0| \equiv \sqrt{\mathbf{p}_i^2 + m^2}$, and are parametrised as

$$\begin{aligned} p_4 &\equiv p_2 + p_3 - p_1, \\ \mathbf{p}_2 &\equiv \begin{pmatrix} 0 \\ 0 \\ r_2 \end{pmatrix}, \\ \mathbf{p}_3 &\equiv r_3 \begin{pmatrix} 0 \\ \sin \theta_3 \\ \cos \theta_3 \end{pmatrix}, \\ \mathbf{p}_1 &\equiv r_1 \begin{pmatrix} \sin \theta_1 \cos \varphi_1 \\ \sin \theta_1 \sin \varphi_1 \\ \cos \theta_1 \end{pmatrix}. \end{aligned} \quad (11)$$

In the equivalent cases ss, tt, uu (diagonal), the integration is constrained by

$$|(p_1 + p_4)^2| = |(p_2 + p_3)^2| \leq 1. \quad (12)$$

Summing over these cases, the resulting contribution to $\Delta P|_{3\text{-loop}}$ is denoted by $1/3\Delta P|_{3\text{-loop,ss}}$. On the other hand, for the equivalent cases st, su, tu, ts, us, ut (off-diagonal) the constraints on the integration read

$$\begin{aligned} |(p_1 + p_4)^2| &= |(p_2 + p_3)^2| \leq 1, \\ |(p_1 - p_2)^2| &= |(p_3 - p_4)^2| \leq 1. \end{aligned} \quad (13)$$

The sum of these cases amounts to $2/3\Delta P|_{3\text{-loop,st}}$, such that

$$\Delta P|_{3\text{-loop}} = \frac{1}{3} \Delta P|_{3\text{-loop,ss}} + \frac{2}{3} \Delta P|_{3\text{-loop,st}}. \quad (14)$$

The second sum in (10) runs over all solutions in r_3 of

$$\begin{aligned} &\text{sgn}(p_2^0) \sqrt{r_2^2 + m^2} + \text{sgn}(p_3^0) \sqrt{r_3^2 + m^2} - \sqrt{r_1^2 + m^2} \\ &= - [r_1^2 + r_2^2 + r_3^2 - 2r_1 r_2 \cos \theta_1 \\ &- 2r_1 r_3 (\sin \varphi_1 \sin \theta_1 \sin \theta_3 + \cos \theta_1 \cos \theta_3) \\ &+ 2r_2 r_3 \cos \theta_3 + m^2]^{1/2}. \end{aligned} \quad (15)$$

The polynomial $P(\{p_i\})$ reads

$$\begin{aligned}
P(\{p_i\}) = & 144 - 12 \frac{1}{m^4} \{ (p_1 p_2)^2 + (p_1 p_3)^2 + (p_1 p_4)^2 \\
& + (p_2 p_3)^2 + (p_2 p_4)^2 + (p_3 p_4)^2 \} + 36 \\
& \cdot \frac{1}{m^6} \{ (p_1 p_2)(p_1 p_3)(p_2 p_3) \\
& + (p_1 p_2)(p_1 p_4)(p_2 p_4) + (p_1 p_3)(p_1 p_4)(p_3 p_4) \\
& + (p_2 p_3)(p_2 p_4)(p_3 p_4) \} + 12 \\
& \cdot \frac{1}{m^8} \{ (p_1 p_2)^2 (p_3 p_4)^2 + (p_1 p_3)^2 (p_2 p_4)^2 \\
& + (p_1 p_4)^2 (p_2 p_3)^2 - (p_1 p_2)(p_1 p_3)(p_2 p_4)(p_3 p_4) \\
& - (p_1 p_2)(p_1 p_4)(p_2 p_3)(p_3 p_4) \\
& - (p_1 p_3)(p_1 p_4)(p_2 p_3)(p_2 p_4) \},
\end{aligned} \tag{16}$$

and the Bose-Einstein distribution shorthand notation is

$$n'_B(r) \equiv n_B \left(\frac{2\pi \sqrt{r^2 + m^2}}{\lambda^{3/2}} \right). \tag{17}$$

This complicated expression can be evaluated by Monte Carlo methods for low temperatures (close to the critical temperature $\lambda_c = 13.87$) due to the Bose suppression of large spatial momenta r_1 and r_2 . However, the high-temperature limit is inaccessible in this way, since the maxima of the product of the Bose functions $n'_B(r_i)$ and polynomials in r_i get shifted to large r_i like $\lambda^{3/2}$. Analysing the properties of the constraints, it is possible to obtain analytic high-temperature expressions for both diagonal and off-diagonal contribution whose leading powers in λ read [22]

$$\begin{aligned}
\frac{1}{3} \Delta P|_{3\text{-loop},ss} \approx & i\Lambda^4 \frac{1}{3375} \frac{1}{(2\pi)^{15}} \frac{1}{m^4} \left(1 + \frac{1}{4m^2} \right) \\
& \cdot (\pi^4 - 90\zeta(5))^2 \lambda^{13} \equiv i c_{13} \Lambda^4 \lambda^{13},
\end{aligned} \tag{18}$$

where $\zeta(x)$ denotes Riemann's zeta function and the numerical value of the coefficient is $c_{13} = 5.2968 \cdot 10^{-20}$ and

$$\begin{aligned}
\frac{2}{3} \Delta P|_{3\text{-loop},st} \approx & i\Lambda^4 e^4 \frac{C}{(2\pi)^4} \frac{1}{12m^4} \lambda^4 \\
\approx & i\Lambda^4 \lambda^4 \cdot 2.2011 \cdot 10^{-12},
\end{aligned} \tag{19}$$

where

$$\begin{aligned}
C \equiv & \frac{1}{2304} \frac{1}{(2\pi)^5} \\
& \cdot \sqrt{\frac{4}{m^2} + \frac{1}{m^4}} \left(132 + \frac{72}{64} \frac{1}{m^4} + \frac{3}{1024} \frac{1}{m^8} \right).
\end{aligned} \tag{20}$$

The numerical values are obtained using the high-temperature plateau value of the mass and coupling $m = 2e = 2\sqrt{8}\pi$.

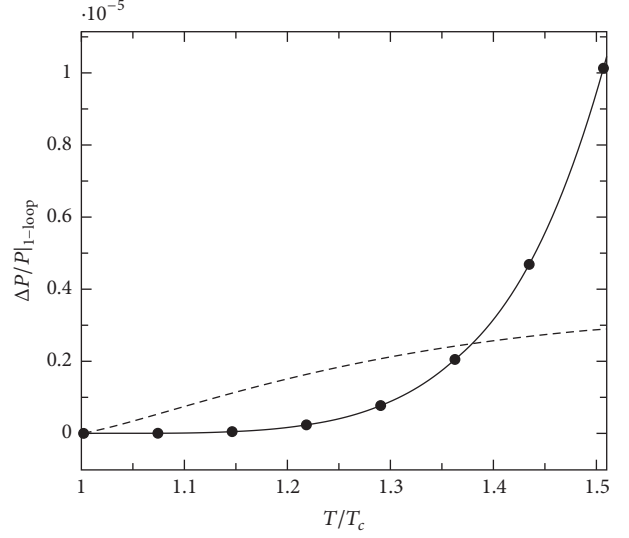


FIGURE 8: Monte Carlo results of $\Delta P|_{3\text{-loop}}/P|_{1\text{-loop}}$ close to λ_c (dots). The solid line is a smooth interpolation of the latter while the dashed line represents $|\Delta P|_{2\text{-loop}}/P|_{1\text{-loop}}$.

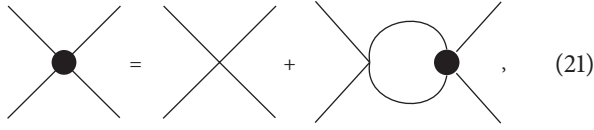
In Figure 7, we compare the results of the two-loop and three-loop expressions $\Delta P|_{2\text{-loop}}$ and $\Delta P|_{3\text{-loop}} = 1/3\Delta P|_{3\text{-loop},ss} + 2/3\Delta P|_{3\text{-loop},st}$ divided by the one-loop expression $P|_{1\text{-loop}}$. We emphasise the excellent matching of the Monte Carlo results at low temperatures with the high-temperature approximations, displaying a consistent transition into the power laws (18) and (19). Firstly we note that in the 3-loop case the off-diagonal contribution $2/3\Delta P|_{3\text{-loop},st}$ is subleading to the diagonal contribution $1/3\Delta P|_{3\text{-loop},ss}$. This allows us to neglect the former in the following discussions, while we stress that the power of an additional independent vertex constraint is impressively demonstrated by a reduction of the power law from λ^{13} to λ^4 .

Comparing $|\Delta P|_{2\text{-loop}}$ and $|\Delta P|_{3\text{-loop}}$ with $P|_{1\text{-loop}}$, apparently the high-temperature behaviour of $|\Delta P|_{3\text{-loop}}$ is dramatically exceeding the lower orders. However, as shown in Figure 8, at low temperatures a hierarchical ordering $|\Delta P|_{3\text{-loop}} \ll |\Delta P|_{2\text{-loop}}$ is in fact observed. This leads us to the following conclusion: A fixed-order loop expansion is inappropriate at high temperatures. Instead, one needs to consider a resummation of diagrams with large contributions like the three-loop diagram which should then analytically continue the controlled low-temperature situation. This is demonstrated in the next section and amounts to the resummation of the family of dihedrally symmetric diagrams introduced in Section 2. We will comment on the imaginary nature of some contributions after this resummation procedure.

4. Resummation of the Highest-Symmetry Diagrams

In order to make sense of the high-temperature behaviour of the three-loop diagram, we consider a truncated version of

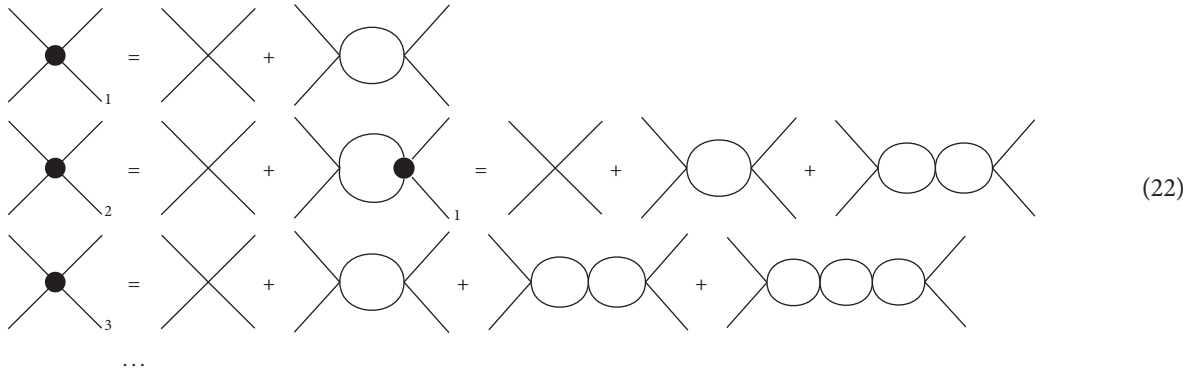
the Dyson-Schwinger (DS) equation of the four-vertex which reads



$$\text{dotted vertex} = \text{undotted vertex} + \text{loop correction}, \quad (21)$$

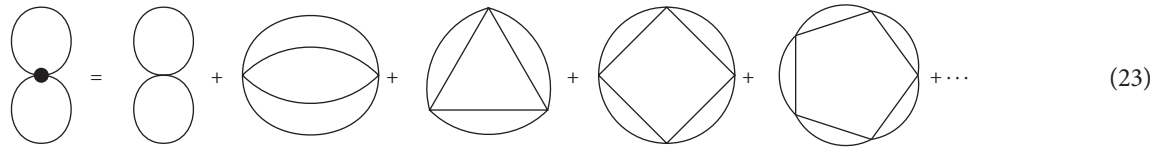
where undotted vertices are tree-level vertices, dotted vertices are (fully) resummed vertices, and loop lines correspond to

(fully) resummed propagators. For a nonvanishing result of the tree-level vertex (in the absence of massless fields), it is required that two external lines carry an algebra index of the first broken direction and the other two lines carry an index of the second broken direction. We assume in the following that this tensorial structure also holds for the resummed vertex. This amounts to a scalar form factor $f(\lambda, i), i = s, t, u$, multiplying the tree-level expression. Resummation of the propagators amounts to only mild deviations from the tree-level expressions [25]. This justifies using the latter for further argumentation. Then (21) has the interpretation of iteratively summing the following infinite number of diagrams



$$\dots \quad (22)$$

When closing legs into two (extra) loops, this becomes the resummation of the class of dihedrally symmetric bubble diagrams:

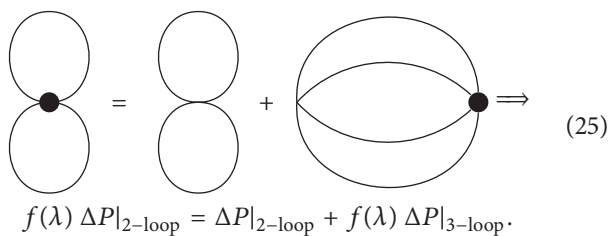


$$\dots \quad (23)$$

In the high-temperature limit the Mandelstam variables are constrained like

$$|s|, |t|, |u| \leq |\phi|^2 = \frac{\Lambda^3}{2\pi T} \propto \frac{1}{T} \rightarrow 0. \quad (24)$$

Hence, for $\lambda \gg \lambda_c$ it is then sufficient to consider $f(\lambda, 0) \equiv f(\lambda)$ which is independent of the loop integrations and can be factored out in the DS equation; namely,



$$f(\lambda) \Delta P|_{2\text{-loop}} = \Delta P|_{2\text{-loop}} + f(\lambda) \Delta P|_{3\text{-loop}}. \quad (25)$$

Solving for $f(\lambda)$ yields

$$f(\lambda) = \frac{\Delta P|_{2\text{-loop}}}{\Delta P|_{2\text{-loop}} - \Delta P|_{3\text{-loop}}} \approx -0.94 \cdot 10^{15} i \lambda^{-11.6}, \quad (26)$$

where in the final step we worked to leading order in λ and used for $\Delta P|_{2\text{-loop}}$ a fit to numerical data between $\lambda = 200 = 14.42\lambda_c$ and $\lambda = 1000 = 72.10\lambda_c$ which yields $\Delta P|_{2\text{-loop}} = -5 \cdot 10^{-5} \Lambda^4 \lambda^{1.4}$ and for $\Delta P|_{3\text{-loop}}$ we used the power law of (18). The fact that $\Delta P|_{2\text{-loop}}$ is real while $\Delta P|_{3\text{-loop}}$ is imaginary ensures that $f(\lambda)$ is free of singularities. Using this result to calculate the two-loop and three-loop contributions with resummed vertices now yields the well-bounded results

$$\begin{aligned} f^2(\lambda) \Delta P|_{3\text{-loop}} &= -4.7 \cdot 10^{10} i \Lambda^4 \lambda^{-10.2}, \\ f(\lambda) \Delta P|_{2\text{-loop}} &= 4.7 \cdot 10^{10} i \Lambda^4 \lambda^{-10.2} \end{aligned} \quad (27)$$

to leading order in λ , implying that these leading orders exactly cancel. Subleading order contributions are thus safely bounded and contain imaginary contributions. We interpret the small imaginary contributions as nonthermal modifications of the thermodynamically self-consistent one-loop pressure. Their origin may be inhomogeneities in the thermal ground state and thus the packing voids between densely packed (anti)caloron centers. A rather reassuring observation is that if one postulates that the fractional form of $f(\lambda)$ in (26) persists down to low temperatures, this would imply that $f(\lambda) \approx 1$ close to λ_c which would be consistent with the hierarchy displayed already at the nonresummed level as illustrated in Figure 8.

5. Summary and Conclusions

We aimed in this work to provide an insight into how radiative corrections beyond two-loop order to the thermal ground state of SU(2) Yang-Mills theory can be organised. The vertex constraints arising from the thermal ground state have been demonstrated to be insufficient to reduce the loop expansion to a finite number of diagrams. Moreover, explicit calculation of the 2PI three-loop diagram in the massive sector showed that these constraints are also not strong enough to extend the hierarchy in loop orders observed at low temperatures up to high temperatures. Resummation of corresponding classes of diagrams, however, has been demonstrated to be a promising resolution to this problem, yielding well-bounded corrections at all temperatures. The arising small nonthermal (imaginary) corrections to the pressure have been interpreted as a result of inhomogeneities in the thermal ground state constituted of densely packed centers of Harrington-Shepard (anti)calorons. At this stage it is not yet clear if further 2PI bubble diagrams in the massive sector are sufficiently constrained prior to resummation, due to lower symmetry and hence likely lower number of possibly equivalent constraints (Section 2), or if more resummation procedures are necessary and possible to control the expansion. For an exhaustive understanding of the radiative corrections, the massless and mixed sectors will also have to be treated in a similar manner.

The subject of how to organise the computation of radiative corrections in deconfining Yang-Mills thermodynamics thus is a broad one. Being of immediate urgency, it would be important to analyse diagrams symmetric under the n th dihedral group (Section 2) that are generated by one massless and one massive propagator per bubble.

Conflicts of Interest

The author declares that there are no conflicts of interest regarding the publication of this paper. This includes the funding mentioned in Acknowledgments.

Acknowledgments

The author thanks his collaborators Thierry Grandou and Ralf Hofmann for their contributions to the related paper [22]. Furthermore he thanks ITP of Heidelberg University for

the funding of a two-week stay at INLN (Nice) in September 2016 during which, among other projects, this work was pursued and both ITP Heidelberg and INPHYNI (Nice) for funding his participation at the 5th Winter Workshop on Non-Perturbative QFT (2017) at INPHYNI, where these results were presented.

References

- [1] A. Linde, "Infrared problem in the thermodynamics of the Yang-Mills gas," *Physics Letters B*, vol. 96, no. 3-4, pp. 289–292, 1980.
- [2] E. V. Shuryak, *Soviet Physics, Journal of Experimental and Theoretical Physics*, vol. 47, p. 212, 1978.
- [3] E. Braaten and R. D. Pisarski, "Resummation and gauge invariance of the gluon damping rate in hot QCD," *Physical Review Letters*, vol. 64, no. 12, pp. 1338–1341, 1990.
- [4] E. Braaten and R. Pisarski, *Nuclear Physics B*, vol. 337, p. 569, 1990.
- [5] J. Frenkel and J. C. Taylor, "High-temperature limit of thermal QCD," *Nuclear Physics B*, vol. 334, no. 1, pp. 199–216, 1990.
- [6] P. Arnold and C. Zhai, "Three-loop free energy for pure gauge QCD," *Physical Review D*, vol. 50, no. 12, pp. 7603–7623, 1994.
- [7] C. Zhai and B. Kastening, "Free energy of hot gauge theories with fermions through," *Physical Review D*, vol. 52, no. 12, pp. 7232–7246, 1995.
- [8] E. Braaten and A. Nieto, "Free energy of QCD at high temperature," *Physical Review D*, vol. 53, no. 6, pp. 3421–3437, 1996.
- [9] D. J. Gross and F. Wilczek, "Ultraviolet behavior of non-Abelian gauge theories," *Physical Review Letters*, vol. 30, no. 26, pp. 1343–1346, 1973.
- [10] H. D. Politzer, "Reliable perturbative results for strong interactions?" *Physical Review Letters*, vol. 30, no. 26, article 1346, 1973.
- [11] I. B. Khriplovich, *Soviet Journal of Nuclear Physics*, vol. 10, Article ID 235242, pp. 235–242, 1969.
- [12] K. Kajantie, M. Laine, K. Rummukainen, and Y. Schröder, "Pressure of hot QCD up to," *Physical Review D*, vol. 67, no. 10, 2003.
- [13] J. Gattnar, C. Gatttringer, K. Langfeld et al., "Center vortices and Dirac eigenmodes in SU(2) lattice gauge theory," *Nuclear Physics B*, vol. 716, no. 1-2, pp. 105–127, 2005.
- [14] R. Höllwieser, M. Faber, J. Greensite, U. M. Heller, and Š. Olejník, "Center vortices and the Dirac spectrum," *Physical Review D*, vol. 78, no. 5, 2008.
- [15] P. Gerhold, E.-M. Ilgenfritz, and M. Müller-Preussker, *Nuclear Physics B*, vol. 760, Article ID 0607315, pp. 1–37, 2007.
- [16] B. J. Harrington and H. K. Shepard, "Periodic Euclidean solutions and the finite-temperature Yang-Mills gas," *Physical Review D*, vol. 17, no. 8, pp. 2122–2125, 1978.
- [17] R. Hofmann, *The thermodynamics of quantum Yang-Mills theory*, World Scientific Publishing Co. Pte. Ltd., Hackensack, NJ, Second edition, 2016.
- [18] Y. Deng, "Proc. Lattice 1988 (Battavia)," p. 334, 1988.
- [19] F. R. Brown et al., *Physical Review Letters*, vol. 61, 1988.
- [20] J. Engels, F. Karsch, and T. Scheideler, *Nuclear Physics B*, 564, p. 302, 1999.
- [21] R. Hofmann, "Nonperturbative approach to Yang-Mills thermodynamics," *International Journal of Modern Physics A. Particles and Fields. Gravitation. Cosmology*, vol. 20, no. 18, pp. 4123–4216, 2005.

- [22] I. Bischer, T. Grandou, and R. Hofmann, “Massive loops in thermal SU(2) Yang–Mills theory: Radiative corrections to the pressure beyond two loops,” *International Journal of Modern Physics A. Particles and Fields. Gravitation. Cosmology*, vol. 32, no. 19-20, 1750118, 39 pages, 2017.
- [23] R. Hofmann, *Entropy*, vol. 18, no. 19, 2016.
- [24] N. Krasowski and R. Hofmann, “One-loop photon–photon scattering in a thermal, deconfining SU(2) Yang–Mills plasma,” *Annals of Physics*, vol. 347, pp. 287–308, 2014.
- [25] R. Hofmann, *Brazilian Journal of Physics*, vol. 42, Article ID 110119, pp. 110–119, 2006.
- [26] U. Herbst, R. Hofmann, and J. Rohrer, *Acta Physica Polonica B*, vol. 36, pp. 881–904, 2004.
- [27] M. Schwarz, R. Hofmann, and F. Giacosa, *International Journal of Modern Physics A*, pp. 1213–1238, 2007.
- [28] F. Giacosa and R. Hofmann, “Linear growth of the trace anomaly in Yang-Mills thermodynamics,” *Physical Review D*, vol. 76, no. 8, 2007.
- [29] H. Satz, *Nuclear Physics A*, 862-863, 2011, arXiv:1101.3937.

Review Article

Asymptotic Behaviour of the QED Perturbation Series

Idrish Huet,¹ Michel Rausch de Traubenberg,² and Christian Schubert³

¹Facultad de Ciencias en Física y Matemáticas, Universidad Autónoma de Chiapas, Ciudad Universitaria, 29050 Tuxtla Gutiérrez, CHIS, Mexico

²IPHC-DRS, Uds, IN2P3, 23 rue du Loess, 67037 Strasbourg Cedex, France

³Instituto de Física y Matemáticas, Universidad Michoacana de San Nicolás de Hidalgo, Edificio C-3, Apdo. Postal 2-82, 58040 Morelia, MICH, Mexico

Correspondence should be addressed to Christian Schubert; schubert@ifm.umich.mx

Received 23 April 2017; Accepted 12 July 2017; Published 19 September 2017

Academic Editor: Ralf Hofmann

Copyright © 2017 Idrish Huet et al. This is an open access article distributed under the Creative Commons Attribution License, which permits unrestricted use, distribution, and reproduction in any medium, provided the original work is properly cited. The publication of this article was funded by SCOAP³.

I will summarize the present state of a long-term effort to obtain information on the large-order asymptotic behaviour of the QED perturbation series through the effective action. Starting with the constant-field case, I will discuss the Euler-Heisenberg Lagrangian in various dimensions and up to the three-loop level. This Lagrangian holds the information on the N-photon amplitudes in the low-energy limit, and combining it with Spinor helicity methods explicit all-N results can be obtained at the one-loop and, for the “all +” amplitudes, also at the two-loop level. For the imaginary part of the Euler-Heisenberg Lagrangian, an all-loop formula has been conjectured independently by Affleck, Alvarez, and Manton for Scalar QED and by Lebedev and Ritus for Spinor QED. This formula can be related through a Borel dispersion relation to the leading large-N behaviour of the N-photon amplitudes. It is analytic in the fine structure constant, which is puzzling and suggests a diagrammatic investigation of the large-N limit in perturbation theory. Preliminary results of such a study for the 1 + 1 dimensional case throw doubt on the validity of the conjecture.

1. Motivation

In 1952 Dyson [1] shocked the high energy physics community by declaring that, quite generally, the QED perturbation series cannot converge. Writing the series as

$$F(e^2) = c_0 + c_2 e^2 + c_4 e^4 + \dots, \quad (1)$$

Dyson argues, “suppose, if possible, that the series converges for some positive value of e^2 ; this implies that $F(e^2)$ is an analytic function of e at $e = 0$. Then for sufficiently small values of e , $F(-e^2)$ will also be a well-behaved analytic function with a convergent power-series expansion.”

He then argues that, on physical grounds, this cannot be the case, since for $e^2 < 0$ the QED vacuum will be unstable due to a runaway production of e^+e^- pairs which coalesce into like-charge graphs.

Shortly later Hurst [2] already provided a mathematical proof of this fact for scalar $\lambda\phi^3$ theory. The proof is essentially based on the following three elements.

(1) The use of the inequality

$$\prod_{i=1}^F \left(\frac{1}{p_i^2 + \kappa^2} \right) \geq \frac{F^F}{\left(\sum_{i=1}^F p_i^2 + F\kappa^2 \right)^F} \quad (2)$$

to establish lower bounds for arbitrary Feynman diagrams (in the Euclidean).

(2) Proof that the number of distinct Feynman diagrams at n th loop order grows like $(n/2)!n!$.

(3) Absence of sign cancellations between graphs.

In 1994, ‘t Hooft [3] found another very general, but very different, argument against convergence of the perturbation series based on renormalon chains. Thus today it is believed that the perturbation series in nontrivial quantum field theories generically is asymptotical rather than convergent, so that summation methods must be used. Of those by far the most important one is Borel summation, since it is ideally suited to the typical factorial growth of perturbation

theory coefficients. Let me remind you that, for a factorially divergent series

$$F(g) \sim \sum_{n=0}^{\infty} c_n g^{n+1}, \quad (3)$$

one defines the Borel transform as

$$B(t) \equiv \sum_{n=0}^{\infty} c_n \frac{t^n}{n!}. \quad (4)$$

If $B(t)$ has no singularities on the positive real axis and does not increase too rapidly at infinity, one can also define the Borel integral

$$\tilde{F}(g) \equiv \int_0^{\infty} dt e^{-t/g} B(t). \quad (5)$$

\tilde{F} is the Borel sum of the original series F . F is asymptotic to \tilde{F} by construction, although the true physical quantity represented by the series F might still differ from \tilde{F} by nonperturbative terms. The Borel transform remains a useful concept even when it leads to singularities, since those usually contain information on the large-order structure of the theory. In many cases they can be traced either to instantons, renormalons, or Euclidean bounces.

Until recently, there was a dearth of nontrivial examples for field theory models where sufficient information would be available to decide the question of Borel summability in a definite manner. Fortunately, this has changed through the advent of supersymmetry; in recent years Borel summability (or Borel nonsummability) has been rigorously demonstrated in a number of supersymmetric models [4].

Even when Borel summability does not apply, Borel analysis can still be very useful through the use of Borel dispersion relations. This goes as follows. Assume that a function $F(g)$ has an asymptotic series expansion

$$F(g) \sim \sum_{n=0}^{\infty} c_n g^n, \quad (6)$$

where the expansion coefficients c_n have the leading-order large n behaviour

$$c_n \sim \rho^n \Gamma(\mu n + \nu) \quad (7)$$

with some real constants $\rho > 0$, $\mu > 0$, and ν . It is easy to see that such a series is not Borel-summable, since the Borel integral (5) can never converge (e.g., in the textbook case $\mu = \nu = 1$ it has a pole at $t = 1/\rho$). Nevertheless, applying a dispersion relation to this integral one can show that the leading contribution to its imaginary part for small g is given by

$$\text{Im } F(g) \sim \frac{\pi}{\mu} \left(\frac{1}{\rho g} \right)^{\nu/\mu} \exp \left[- \left(\frac{1}{\rho g} \right)^{1/\mu} \right]. \quad (8)$$

Coming back to the case of QED, given the arguments by Dyson and 't Hooft it is certainly safe to exclude a nonzero

convergence radius of the full QED perturbation series. However, despite the immense work that has gone into low-order perturbative QED computations, presently still little is known about the precise large-order behaviour of the coefficients. Contrary to the case of scalar field theories mentioned above, straightforward estimates based on lower bounds for individual diagrams cannot be used in gauge theory, since here Feynman diagrams come with different signs, and gauge invariance is known to lead to cancellations between them. And these cancellations are particularly extensive in the abelian case, where there are no obstructing color factors. Thus QED in this respect is more difficult than QCD, which is made worse by the absence of (space-time) instantons in QED, which in the nonabelian case can provide some large-order information. In 1977 Cvitanovic [5] suggested, based on an analysis of the calculation of the three-loop anomalous magnetic momentum $g - 2$ which he had done with Cvitanovic and Kinoshita [6], that these cancellations should be taken into account by counting the number of classes of gauge-invariant diagrams, rather than the number of individual diagrams. He also conjectured that, for the case of $g - 2$, they reduce the coefficients of the perturbation series sufficiently to make it convergent in the quenched approximation. This conjecture, though nowadays forgotten, is actually still standing, since neither Dyson's nor 't Hooft's arguments work in the absence of fermionic bubbles.

Here I will summarize the state of a long-term effort [7–15] to get information on the large-order behaviour of the QED perturbation series using the Euler-Heisenberg Lagrangian and its higher-loop radiative corrections.

2. The 1-Loop Euler-Heisenberg Lagrangian

The Euler-Heisenberg Lagrangian (“EHL”) is the one-loop QED effective Lagrangian for a constant external field. Heisenberg and Euler [16] obtained for it in 1936 the following well-known proper-time representation:

$$\mathcal{L}_{\text{spin}}^{(1)}(F) = -\frac{1}{8\pi^2} \int_0^{\infty} \frac{dT}{T^3} e^{-m^2 T} \cdot \left[\frac{(eaT)(ebT)}{\tanh(eaT)\tan(ebT)} - \frac{e^2}{3} (a^2 - b^2) T^2 - 1 \right]. \quad (9)$$

Here a, b are the two invariants of the Maxwell field, related to \mathbf{E}, \mathbf{B} by

$$a^2 - b^2 = B^2 - E^2, \quad ab = \mathbf{E} \cdot \mathbf{B}. \quad (10)$$

The analogous result for Scalar QED was obtained by Weisskopf [17] but will be called “Scalar Euler-Heisenberg Lagrangian” in the following:

$$\mathcal{L}_{\text{scal}}^{(1)}(F) = \frac{1}{16\pi^2} \int_0^{\infty} \frac{dT}{T^3} e^{-m^2 T} \left[\frac{(eaT)(ebT)}{\sinh(eaT)\sin(ebT)} + \frac{e^2}{6} (a^2 - b^2) T^2 - 1 \right]. \quad (11)$$

The Euler-Heisenberg Lagrangian (“EHL”) holds information on the one-loop N -photon amplitudes, but only in the

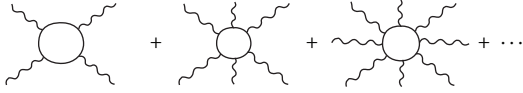


FIGURE 1: Sum of diagrams equivalent to the one-loop EHL.

low-energy limit (since a constant field can emit only zero-energy photons).

Thus diagrammatically $\mathcal{L}^{(1)}(F)$ is equivalent to the sum of the Feynman graphs shown in Figure 1, where all photon energies are small compared to the electron mass, $\omega_i \ll m$.

In [10] it was shown how to carry out explicitly the construction of these limiting low-energy amplitudes starting from the weak-field expansion of the EHL:

$$\mathcal{L}(F) = \sum_{k,l} c_{kl} a^{2k} b^{2l}. \quad (12)$$

It turned out that if one fixes the number of photons, their momenta k_1, \dots, k_N , and a helicity assignment for each photon, then in this limit the full dependence on the momenta and polarization vectors is carried by a unique invariant. Thus the magnitude of the amplitude can be specified by a single number, which will be essential for our whole approach.

Except for the purely magnetic case, the EHL has also an imaginary part related to vacuum pair creation by the electric field component (to be called ‘‘Sauter-Schwinger pair creation’’ in the following) [18, 19]. In the purely electric case one finds, from the poles in the T -integration, the following decomposition due to Schwinger [19]:

$$\text{Im } \mathcal{L}^{(1)}(E) = \frac{m^4}{8\pi^3} \beta^2 \sum_{k=1}^{\infty} \frac{1}{k^2} \exp\left[-\frac{\pi k}{\beta}\right], \quad (13)$$

$$\text{Im } \mathcal{L}_{\text{scal}}^{(1)}(E) = -\frac{m^4}{16\pi^3} \beta^2 \sum_{k=1}^{\infty} \frac{(-1)^k}{k^2} \exp\left[-\frac{\pi k}{\beta}\right].$$

($\beta = eE/m^2$). In the following we will focus on the weak-field limit $\beta \ll 1$ where only the first of these ‘‘Schwinger-exponentials’’ is relevant.

The nonperturbative dependence of the Schwinger-exponentials on the field supports the interpretation of field-induced pair creation as a vacuum tunneling effect, as proposed by Sauter as early as 1931 [18].

As usual in quantum field theory, the real and imaginary parts of the EHL are related by a dispersion relation. For the N -photon amplitudes at full momentum, this would be a standard dispersion relation performed diagram-by-diagram, relating the diagrams of Figure 1 to the ‘‘cut diagrams’’ shown in Figure 2, involving on-shell electrons.

However, in the zero-energy limit the cut diagrams all vanish, since a finite number of zero-energy photons cannot create a pair on-shell. Thus what counts here is only the asymptotic behaviour for a large number of photons, and instead of an ordinary dispersion relation we have to use a *Borel dispersion relation*. This works in the following way [7].


 FIGURE 2: Cut diagrams giving the imaginary part of the N -photon amplitudes.

Consider the purely magnetic EHL. Expanding it out in powers of the field yields

$$\begin{aligned} \mathcal{L}^{(1)}(B) &= -\frac{1}{8\pi^2} \int_0^{\infty} \frac{dT}{T^3} e^{-m^2 T} \left[\frac{eBT}{\tanh(eBT)} - \frac{1}{3} (eBT)^2 - 1 \right] \quad (14) \\ &= \frac{2m^4}{\pi^2} \sum_{n=2}^{\infty} c_n^{(1)} g^n \end{aligned}$$

with an effective expansion parameter $g = (eB/m^2)^2$, and coefficients $c_n^{(1)}$ that can be written in terms of the Bernoulli numbers B_n :

$$c_n^{(1)} = -\frac{2^{2n-4} B_{2n}}{(2n)(2n-1)(2n-2)}. \quad (15)$$

Here $c_n^{(1)}$ holds information on the $N = 2n$ photon amplitudes. The asymptotic behaviour of the coefficients can be easily studied using well-known properties of the Bernoulli numbers. One finds

$$c_n^{(1)} \stackrel{n \rightarrow \infty}{\sim} (-1)^n \frac{1}{8} \frac{\Gamma(2n-2)}{\pi^{2n}} \left(1 + \frac{1}{2^{2n}} + \frac{1}{3^{2n}} + \dots \right). \quad (16)$$

Thanks to the factor $(-1)^n$, the individual terms on the right hand side of (16) all give convergent Borel integrals. This is one (rather roundabout) way of seeing that the purely magnetic EHL has no imaginary part and does not give rise to pair creation.

The analogous expansion for the purely electric field case is almost the same:

$$\begin{aligned} \mathcal{L}^{(1)}(E) &= -\frac{1}{8\pi^2} \int_0^{\infty} \frac{dT}{T^3} e^{-m^2 T} \left[\frac{eET}{\tan(eET)} + \frac{1}{3} (eET)^2 - 1 \right] \quad (17) \\ &= \frac{2m^4}{\pi^2} \sum_{n=2}^{\infty} (-1)^n c_n^{(1)} g^n, \end{aligned}$$

where now $g = (eE/m^2)^2$, but with the same $c_n^{(1)}$. However, the additional factor $(-1)^n$ makes the series nonalternating, which is crucial, because now the termwise use of expansion (16) leads to divergent Borel integrals. These divergent integrals do, however, all possess well-defined imaginary parts, by a (now ordinary) dispersion relation. One finds

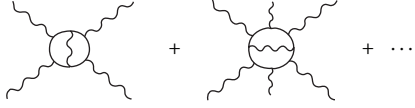


FIGURE 3: Feynman diagrams contributing to the 2-loop EHL.



FIGURE 4: Feynman diagrams contributing to 2-loop Schwinger pair creation.

QED S -matrix by representing the scalar particles in terms of relativistic particle path integrals, and coupling them through photons in all possible ways. Upon restriction to the purely photonic part of the S -matrix (no external scalars) and to the “quenched” contribution (only one virtual scalar), this “worldline representation” can be stated very compactly in terms of the (quenched) effective action $\Gamma[A]$:

$$\begin{aligned} \Gamma_{\text{scalar}}[A] &= \int d^4x \mathcal{L}_{\text{scalar}}[A] \\ &= \int_0^\infty \frac{dT}{T} e^{-m^2 T} \int_{x(T)=x(0)} \mathcal{D}x(\tau) e^{-S[x(\tau)]}. \end{aligned} \quad (24)$$

Here T denotes the proper-time of the scalar particle in the loop, m its mass, and $\int_{x(T)=x(0)} \mathcal{D}x(\tau)$ a path integral over all closed loops in space-time with fixed periodicity in the proper-time. The worldline action $S[x(\tau)]$ has three parts:

$$S = S_0 + S_{\text{ext}} + S_{\text{int}}. \quad (25)$$

They are given by

$$\begin{aligned} S_0 &= \int_0^T d\tau \frac{\dot{x}^2}{4} \quad (\text{free propagation}), \\ S_{\text{ext}} &= ie \int_0^T \dot{x}^\mu A_\mu(x(\tau)) \quad (\text{external photons}), \\ S_{\text{int}} &= -\frac{e^2}{8\pi^2} \int_0^T d\tau_1 \int_0^T d\tau_2 \frac{\dot{x}(\tau_1) \cdot \dot{x}(\tau_2)}{(x(\tau_1) - x(\tau_2))^2} \\ &\quad (\text{internal photons}). \end{aligned} \quad (26)$$

The kinetic term S_0 describes the free propagation of the scalar, S_{ext} describes its interaction with the external field, and S_{int} generates the corrections due to internal photon exchanges in the loop. Expanding out the two interaction exponentials leads back to Feynman diagrams, however with the important difference that no particular ordering of the photon legs along the loop needs to be fixed. Thus the term S_{ext} alone upon expansion yields the diagrams of Figure 1 (where each leg now stands for an interaction with the arbitrary field $A(x)$).

The “worldline instanton” of Affleck et al. [26] is an extremal trajectory of the worldline path integral for a

stationary phase approximation. For the case of a constant electric field in the z direction this extremal action trajectory is given by a circle in the (Euclidean) t - z plane:

$$x_{\text{instanton}}(\tau) = \frac{m}{eE} \left(0, 0, \cos\left(\frac{2\pi\tau}{T}\right), \sin\left(\frac{2\pi\tau}{T}\right) \right). \quad (27)$$

It can be shown that in the weak-field (= large mass) limit the imaginary (although not the real) part of the effective Lagrangian can be well-approximated by replacing the path integral with this single trajectory:

$$\text{Im } \mathcal{L}_{\text{scalar}}^{(\text{quenched})}(E) \sim e^{-S[x_{\text{instanton}}]}. \quad (28)$$

This is easily evaluated to be

$$(S_0 + S_{\text{ext}})[x_{\text{instanton}}] = \pi \frac{m^2}{eE}, \quad (29)$$

$$S_{\text{int}}[x_{\text{instanton}}] = -\alpha\pi.$$

Thus the contribution of $S_0 + S_{\text{ext}}$ just reproduces the leading (one-loop) Schwinger-exponential of (13) and the one of S_{int} the $e^{\alpha\pi}$ factor.

Thus Affleck et al. arrive, with very little effort, at the same exponentiation for Scalar QED that Lebedev and Ritus find in Spinor QED:

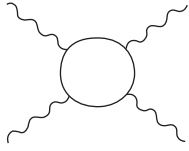
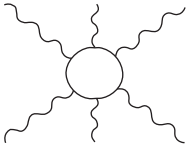
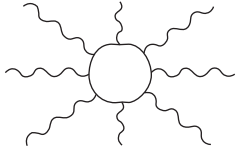
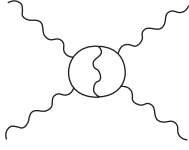
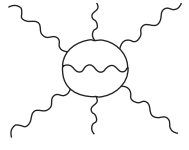
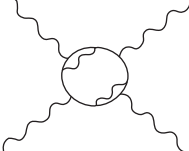
$$\begin{aligned} \text{Im } \mathcal{L}_{\text{scal}}^{(\text{all-loop})}(E) &= \sum_{l=1}^{\infty} \text{Im } \mathcal{L}_{\text{scal}}^{(l)}(E) \\ &\stackrel{\beta \rightarrow 0}{\sim} -\frac{m^4 \beta^2}{16\pi^3} \exp\left[-\frac{\pi}{\beta} + \alpha\pi\right] \\ &= \text{Im } \mathcal{L}_{\text{scal}}^{(1)}(E) e^{\alpha\pi}. \end{aligned} \quad (30)$$

Their argument assumes the field to be weak, but there is no restriction on the strength of the coupling α . We note the following:

- (i) Formula (30), if true, constitutes a rare case of an all-loop summation of an infinite series of graphs of arbitrary loop order. Those graphs are shown in Table 1.
- (ii) According to [26], the contribution of all non-quenched diagrams gets suppressed in the weak-field limit.
- (iii) Perhaps, most surprisingly, the scalar mass appearing in (30) is already *the physically renormalized one*, implying that the worldline instanton approach automatically takes all mass renormalization counterdiagrams into account. This is remarkable considering that the determination of the physical mass parameter for the EHL becomes a rather nontrivial issue already at two loops [20, 22, 23].

Thus, according to Affleck et al. a true all-loop summation has produced the factor $e^{\alpha\pi}$, which is not only unreasonably simple but also perfectly analytical in the fine structure constant α !. According to what has been said above, this

TABLE 1: Feynman diagrams contributing to the AAM formula.

Number of loops	Number of external legs			
	4	6	8	...
1				...
2		
3		...	⋮	⋮
⋮	⋮	⋮	⋮	⋮

would seem to point towards extensive cancellations between Feynman diagrams. However, neither [26] nor [24] made this point, perhaps because the Schwinger pair creation rate is a rather peculiar quantity. Thus our next goal will be to transfer the exponential factor from the imaginary to the real part of the EHL, by a Borel dispersion relation, and from there to the low-energy photon S-matrix through the same procedure as at one-loop:

$$\text{Im } \mathcal{L} \xrightarrow{\text{disp. rel.}} \text{Re } \mathcal{L} \longrightarrow \Gamma [k_1, \varepsilon_1; \dots; k_N, \varepsilon_N]. \quad (31)$$

First we need to see whether our one-loop Borel dispersion relation can be extended to the multiloop level. For this it will be useful to consider the simplest possible nonzero constant-field background, which is the self-dual one.

5. The Self-Dual Case

As we mentioned above, the two-loop correction to the EHL for a purely electric or purely magnetic field are known only in terms of intractable integrals, and only the first few coefficients have been calculated so far. However, this case is not the simplest one that one can consider; mathematically much better behaved is the one of a (Euclidean) constant self-dual field, defined by $F_{\mu\nu} = (1/2)\varepsilon_{\mu\nu\alpha\beta}F^{\alpha\beta}$. The field strength tensor can be written as

$$F = \begin{pmatrix} 0 & f & 0 & 0 \\ -f & 0 & 0 & 0 \\ 0 & 0 & 0 & f \\ 0 & 0 & -f & 0 \end{pmatrix}. \quad (32)$$

At the one-loop level, the self-dual (“SD”) EHLs for Scalar and Spinor QED are special cases of (9) and (11). Anticipating the result of the two-loop calculation below, it will be useful

here to eliminate the proper-time integral and perform a change of variables from f to $\kappa \equiv m^2/2ef$. This leads to [8]

$$\begin{aligned} \mathcal{L}_{\text{scal}}^{(1)(\text{SD})}(\kappa) &= \frac{m^4}{(4\pi)^2} \frac{1}{\kappa^2} \left[-\frac{1}{12} \ln(\kappa) + \zeta'(-1) + \Xi(\kappa) \right], \end{aligned} \quad (33)$$

where the function $\Xi(x)$ is defined as follows:

$$\begin{aligned} \Xi(x) \equiv \int_0^x dy \ln \Gamma(y) - x \ln \Gamma(x) + \frac{x^2}{2} \ln(x) - \frac{x^2}{4} \\ - \frac{x}{2}. \end{aligned} \quad (34)$$

The Spinor EHL in this SD case after renormalization differs from the scalar one only by a trivial global factor of -2 (the reason for the independence of spin is that the Dirac equation in such a background possesses a hidden supersymmetry [28]).

Remarkably, for the SD case it is possible to do all integrals in closed form not only at one loop but even at two loops, in both Scalar and Spinor QED. The results can be written compactly in terms of the digamma function $\psi(x) \equiv \Gamma'(x)/\Gamma(x)$ [8]:

$$\begin{aligned} \mathcal{L}^{(2)}(f) &= -2\alpha \frac{m^4}{(4\pi)^3} \frac{1}{\kappa^2} \left[3\xi^2(\kappa) - \xi'(\kappa) \right], \\ \mathcal{L}_{\text{scal}}^{(2)}(f) &= \alpha \frac{m^4}{(4\pi)^3} \frac{1}{\kappa^2} \left[\frac{3}{2}\xi^2(\kappa) - \xi'(\kappa) \right]. \end{aligned} \quad (35)$$

Here $\kappa \equiv m^2/2ef$ and

$$\xi(x) \equiv -x \left(\psi(x) - \ln(x) + \frac{1}{2x} \right) \quad (36)$$

(note that $\xi(x) = \Xi'(x)$). Using the well-known expansion of the digamma function at $x = \infty$ in terms of the Bernoulli numbers

$$\psi(x) \sim \ln x - \frac{1}{2x} - \sum_{k=1}^{\infty} \frac{B_{2k}}{2kx^{2k}} \quad (37)$$

one finds the following closed-form expressions for the one- and two-loop weak-field expansion coefficients $c_n^{(1,2)(SD)}$ (we write them down for the Spinor case):

$$\begin{aligned} c_n^{(1)(SD)} &= -\frac{B_{2n}}{2n(2n-2)}, \\ c_n^{(2)(SD)} &= \frac{1}{(2\pi)^2} \left\{ \frac{2n-3}{2n-2} B_{2n-2} + 3 \sum_{k=1}^{n-1} \frac{B_{2k}}{2k} \frac{B_{2n-2k}}{(2n-2k)} \right\}. \end{aligned} \quad (38)$$

Further, in this self-dual case there is also an analogue of the distinction between a purely magnetic and a purely electric field. For real f the SD EHL turns out to have a weak-field expansion with alternating coefficients, so that it is Borel-summable, and there is no imaginary part. Thus we call this case “magnetic-like.” Taking imaginary f removes the alternating sign and creates a pole in the Borel integral, which implies an imaginary part for the EHL. Thus we call this case “electric-like.” This imaginary part of the self-dual EHL with complex f is obtained from (35) simply by using the analytic continuation of the digamma function and thus also known in closed form.

Studying the self-dual case turned out to be useful in three ways:

- (i) For this case we could verify that the Borel dispersion relation (8) can be used to construct the imaginary part of the EHL from the weak-field expansion even at the two-loop level. That is, the asymptotic three-parameter matching (7) works, and (more nontrivially) the Borel summation procedure does not miss any nonperturbative terms (see [29] for a case where such a thing actually occurred, even at one-loop).
- (ii) The AAM exponentiation formula (30) can be generalized to the SD case unchanged, by a simple modification of the worldline instanton to a double circle,

$$\begin{aligned} x_{\text{instanton}}(\tau) &= \frac{m}{\sqrt{2}eE} \left(\cos\left(\frac{2\pi\tau}{T}\right), \sin\left(\frac{2\pi\tau}{T}\right), \right. \\ &\quad \left. \cos\left(\frac{2\pi\tau}{T}\right), \sin\left(\frac{2\pi\tau}{T}\right) \right). \end{aligned} \quad (39)$$

And the initial step of exponentiation (21) is easy to verify explicitly from (33) and (35). This holds independently of spin.

- (iii) The effective action for a self-dual field is unphysical, since such a field cannot be real in Minkowski space. Nevertheless, it still carries information on the physical photon amplitudes; the self-duality condition

corresponds precisely to a projection on the “all +” (or “all -”) photon amplitudes [30, 31]. Thanks to the closed-form expressions (35), even at the two-loop level we are still able to write down a closed-form all- N expression for this particular polarization choice:

$$\begin{aligned} \Gamma^{(1)}[k_1, \varepsilon_1^+; \dots; k_N, \varepsilon_N^+] &= -2 \frac{(2e)^N}{(4\pi)^2 m^{2N-4}} c_{N/2}^{(1)(SD)} \chi_N, \\ \Gamma^{(2)}[k_1, \varepsilon_1^+; \dots; k_N, \varepsilon_N^+] &= -2\alpha\pi \frac{(2e)^N}{(4\pi)^2 m^{2N-4}} c_{N/2}^{(2)(SD)} \chi_N. \end{aligned} \quad (40)$$

As was mentioned above, here all the dependence on momenta and polarization is absorbed by a unique (independent of loop order) invariant χ_N . Using Spinor helicity techniques, this invariant can be constructed explicitly for all N [10].

6. Synthesis: A Conjecture for the Photon S Matrix

We are now ready to state a conjecture for the N -photon amplitudes at arbitrary loop level l [11]. Consider the l -loop correction to the purely electric EHL, and define its weak-field expansion coefficients by

$$\mathcal{L}^{(l)}(E) = \sum_{n=2}^{\infty} c^{(l)}(n) \left(\frac{eE}{m^2} \right)^{2n} \quad (41)$$

(note the change of convention with respect to (14)). Assuming that the AAM formula (30) holds and that the Borel dispersion relation (8) works at each loop order, we can conclude that the leading asymptotic factorial growth rate must be the same at each loop order, namely, $\sim \Gamma(2n-2)$:

$$c^{(l)}(n) \stackrel{n \rightarrow \infty}{\sim} c_{\infty}^{(l)} \pi^{-2n} \Gamma(2n-2). \quad (42)$$

And here $c_{\infty}^{(l)}$ relates to the leading Schwinger-exponential at l loops:

$$\text{Im } \mathcal{L}^{(l)}(E) \stackrel{\beta \rightarrow 0}{\sim} c_{\infty}^{(l)} e^{-\pi m^2 / eE}. \quad (43)$$

At two loops, the numerical calculations of [7] confirm this, but only if physical mass renormalization is used! For generic mass renormalization one finds instead a leading factorial behaviour of $\Gamma(2n)$, and it is only through a cancellation of this leading order term between the unrenormalized EHL and its mass renormalization counterterm that this leading factorial behaviour gets reduced to the same $\Gamma(2n-2)$ behaviour as at one loop. At the l -loop level, it is still not difficult to establish the leading factorial growth of the weak-field expansion coefficients before renormalization, which is

$$c^{(l)}(n) \stackrel{n \rightarrow \infty}{\sim} \Gamma(2n+2l-4). \quad (44)$$

Thus at higher-loop orders the correctness of the AAM conjecture requires increasingly extensive cancellations in

the mass renormalization process to cut the leading factorial growth all the way down to $\Gamma(2n - 2)$.

Now let us consider the ratio of the l -loop to the one-loop coefficients. Combining (42) and (43) with the AAM conjecture (30), we find at any fixed loop order

$$\lim_{n \rightarrow \infty} \frac{c^{(l)}(n)}{c^{(1)}(n)} = \frac{c_{\infty}^{(l)}}{c_{\infty}^{(1)}} \stackrel{\text{AAM}}{=} \frac{1}{(l-1)!} (\alpha\pi)^{l-1}. \quad (45)$$

At this stage, let us switch to the self-dual case. This is not essential for our argumentation, but we prefer it for two reasons: first, more is known explicitly about the SD EHL; second, as mentioned above the SD EHL directly translates into one particular helicity component of the N -photon amplitude, the one with all helicities equal (“all +” or “all –”).

Using our above rule for the conversion of the self-dual weak-field expansion coefficients into the “all +” photon amplitudes, which is independent of the loop order, we get the following statement for the “all +” amplitudes in the limit of large photon number $N = 2n$:

$$\begin{aligned} \lim_{N \rightarrow \infty} \frac{\Gamma^{(l)}[k_1, \varepsilon_1^+; \dots; k_N, \varepsilon_N^+]}{\Gamma^{(1)}[k_1, \varepsilon_1^+; \dots; k_N, \varepsilon_N^+]} &= \lim_{N \rightarrow \infty} \frac{\chi_N c^{(l)}(N/2)}{\chi_N c^{(1)}(N/2)} \\ &= \frac{1}{(l-1)!} (\alpha\pi)^{l-1}. \end{aligned} \quad (46)$$

Summing this relation over l we get

$$\lim_{N \rightarrow \infty} \frac{\Gamma^{(\text{total})}[k_1, \varepsilon_1^+; \dots; k_N, \varepsilon_N^+]}{\Gamma^{(1)}[k_1, \varepsilon_1^+; \dots; k_N, \varepsilon_N^+]} = e^{\alpha\pi}. \quad (47)$$

Assuming sufficient uniformity in l of the convergence for $N \rightarrow \infty$, one could now conclude that the amplitude must be analytic in α for some sufficiently large N . But analyticity of the complete amplitude can certainly be safely excluded by renormalons and other arguments. Therefore uniformity must fail, and it is easy to see how this comes about diagrammatically. In Figure 5 we show the diagrams contributing to the EHL up to four loops, not showing the external legs.

In the worldline instanton based derivation of the AAM conjecture (30), only quenched diagrams contribute to the weak-field limit of the imaginary part of the electric EHL; thus this must also be true for the leading asymptotic terms in the large N expansion of the weak-field expansion coefficients; nonquenched diagrams must get suppressed for $N \rightarrow \infty$. However, the number of such diagrams is strongly growing with the loop order, so that the process of the suppression of the nonquenched contributions by increasing N should slow down with increasing l . This provides a good reason for uniformity to fail for the whole amplitude, but there is no obvious reason to expect such a nonuniformity if one stays inside the class of quenched diagrams from the beginning. This led Dunne and one of the authors in 2006 [11] to conjecture that *perturbation theory converges for the QED photon amplitudes in the one-electron-loop approximation*. If true, this would imply enormous cancellations between Feynman diagrams, presumably due to gauge invariance.

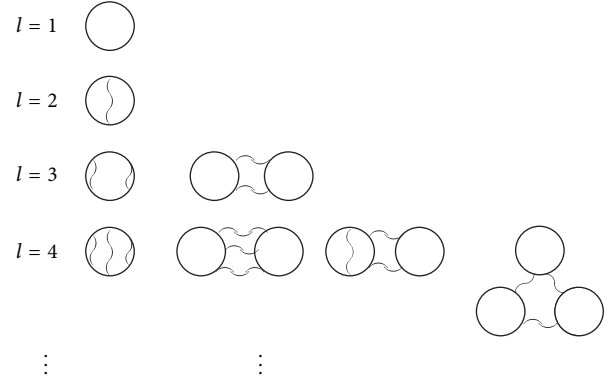


FIGURE 5: Diagrams contributing to the EHL up to four loops (external legs not shown).

Only afterwards we learned that, as mentioned in the beginning, Cvitanovic [5] had conjectured the analogous statement for the electron $g - 2$ factor,

7. Three Predictions for the Three-Loop EHL

To either disprove or further corroborate this conjecture, a calculation of the EHL at the three-loop level is called for. We would like to see the following three things happen:

- (1) We should see the next term of the exponentiation:

$$\lim_{n \rightarrow \infty} \frac{c^{(3)}(n)}{c^{(1)}(n)} = \frac{1}{2} (\alpha\pi)^2. \quad (48)$$

- (2) At three loops there is already a nonquenched contribution, and it should be suppressed in the large N limit.
- (3) The convergence of $c^{(3)}(n)/c^{(1)}(n)$ should not be slower than the one of $c^{(2)}(n)/c^{(1)}(n)$ when only quenched diagrams are taken.

However, a calculation of the three-loop EHL in $D = 4$ seems presently technically out of reach.

8. QED in 1 + 1 Dimensions

The proper-time representation of the one-loop EHL is essentially independent of dimension. In 2008 Krasnansky [32] studied the Scalar EHL in various dimensions also at two loops and found, in particular, the rather surprising fact that the Scalar EHL in 1 + 1 dimensions even at two loops has a structure almost identical to the one of the self-dual Scalar EHLs in 3 + 1 dimensions. Let us contrast the two cases: above we wrote down the self-dual field strength tensor for $D = 4$:

$$F = \begin{pmatrix} 0 & f & 0 & 0 \\ -f & 0 & 0 & 0 \\ 0 & 0 & 0 & f \\ 0 & 0 & -f & 0 \end{pmatrix}. \quad (49)$$

We also gave the Scalar EHL for this background:

$$\begin{aligned} \mathcal{L}_{\text{scal}}^{(2)(4D)}(\kappa) &= \alpha \frac{m^4}{(4\pi)^3} \frac{1}{\kappa^2} \left[\frac{3}{2} \xi^2 - \xi' \right], \\ \xi(\kappa) &= -\kappa \left(\psi(\kappa) - \ln(\kappa) + \frac{1}{2\kappa} \right). \end{aligned} \quad (50)$$

In 2D the field strength tensor is $F = \begin{pmatrix} 0 & f \\ -f & 0 \end{pmatrix}$, and the two-loop Scalar QED EHL comes out as [32]

$$\begin{aligned} \mathcal{L}_{\text{scal}}^{(2)(2D)}(\kappa) &= -\frac{e^2}{32\pi^2} \left[\xi_{2D}^2 - 4\kappa \xi'_{2D} \right], \\ \xi_{2D} &= -\left(\psi\left(\kappa + \frac{1}{2}\right) - \ln(\kappa) \right). \end{aligned} \quad (51)$$

Since higher-loop calculations are somewhat easier in two dimensions, this suggests using the 2D case as a toy model for studying the AAM conjecture. An effort along these lines was started in [13], however switching from Scalar to Spinor QED. Here we derived an analogue of the AAM conjecture in 2D, also using the worldline instanton approach, and established the correspondences between the 4D and 2D cases shown in Box 1.

There are two essential differences. First, in 2D the fine structure constant $\tilde{\alpha}$ is not dimensionless. Thus the exponent of the AAM formula (rhs of third line) here involves also a factor of κ^2 , which in the formula for the asymptotic behaviour of the weak-field expansion coefficients (rhs of fourth line) leads to a shift in the argument between the l -loop and the one-loop coefficients. Thus in 2D the leading asymptotic growth of the coefficients increases with increasing loop order, as it does in the 4D case *before* mass renormalization, and correspondingly it can be shown that the contributions to the EHL from mass renormalization are asymptotically subleading and thus irrelevant for our purposes (although the fermion propagator in 2D does not have UV divergences, mass renormalization is still a quite nontrivial issue; see [33] and refs. therein). Presumably this relates to the fact that QED in 2D is confining.

In any case, all three of our three-loop predictions above have an analogue in the 2D case. In [13] we also obtained the following formulas for the one- and two-loop EHLs in 2D Spinor QED:

$$\begin{aligned} \mathcal{L}^{(1)}(\kappa) &= -\frac{m^2}{4\pi} \frac{1}{\kappa} \left[\ln \Gamma(\kappa) - \kappa (\ln \kappa - 1) + \frac{1}{2} \ln \left(\frac{\kappa}{2\pi} \right) \right], \end{aligned} \quad (52)$$

$$\begin{aligned} \mathcal{L}^{(2)}(f) &= \frac{m^2}{4\pi} \frac{\tilde{\alpha}}{4} \left[\tilde{\psi}(\kappa) + \kappa \tilde{\psi}'(\kappa) + \ln(\lambda_0 m^2) + \gamma + 2 \right], \end{aligned}$$

where we have now abbreviated

$$\tilde{\psi}(x) \equiv \psi(x) - \ln x + \frac{1}{2x}. \quad (53)$$

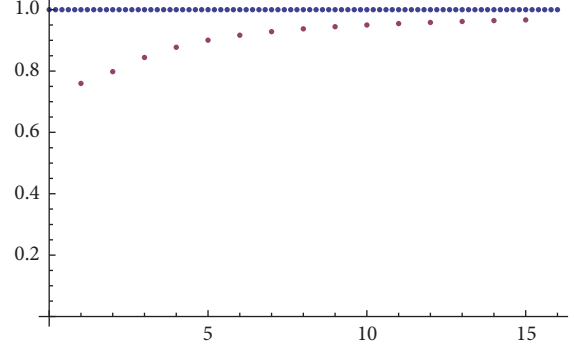


FIGURE 6: Convergence of $c_{2D}^{(2)}(n)/c_{2D}^{(1)}(n+1)$ to the AAM prediction (normalized such that the limit is unity).

Comparing with the Scalar QED result (51), we see that the Spinor QED one is significantly simpler, as it involves the digamma function only linearly. This is another surprise, since in 4D the Scalar and Spinor EHLs do not show structural differences.

Remarkably, the two-loop EHL can (up to an irrelevant constant) even be written in terms of derivatives of the one-loop EHL:

$$\mathcal{L}^{(2)}(f) = -\frac{\tilde{\alpha}}{4} \left(m^2 \frac{\partial}{\partial m^2} \right)^2 \mathcal{L}^{(1)}(f). \quad (54)$$

From (52) we find for the one- and two-loop weak-field expansion coefficients

$$\begin{aligned} c_{2D}^{(1)}(n) &= (-1)^{n+1} \frac{B_{2n}}{4n(2n-1)}, \\ c_{2D}^{(2)}(n) &= (-1)^{n+1} \frac{\tilde{\alpha}}{8} \frac{2n-1}{2n} B_{2n}. \end{aligned} \quad (55)$$

From this we can, using properties of the Bernoulli numbers, easily show that

$$\lim_{n \rightarrow \infty} \frac{c_{2D}^{(2)}(n)}{c_{2D}^{(1)}(n+1)} = \tilde{\alpha} \pi^2. \quad (56)$$

This verifies the 2D AAM-like formula of Box 1 at the linearized level.

In Figure 6 we show the convergence to the asymptotic limit, which is rather rapid.

Even in the 2D case, the calculation of the three-loop EHL turned out to be a formidable task, and it is only very recently that we were able to obtain it in a form suitable for computing a sufficient number of the weak-field expansion coefficients [14, 15].

At three loops, we have the three Feynman diagrams shown in Figure 7.

Here the solid lines denote the electron propagator in the constant field. A and B are quenched; C is nonquenched.

$$\begin{aligned}
& 4D \text{ QED} \longleftrightarrow 2D \text{ QED} \\
& \alpha = \frac{e^2}{4\pi} \longleftrightarrow \tilde{\alpha} = \frac{2e^2}{\pi m^2} \\
& \text{Im } \Gamma^{D=4} \sim e^{-m^2 \pi / eE + \alpha \pi} \longleftrightarrow \text{Im } \Gamma^{D=2} \sim e^{-m^2 \pi / eE + \tilde{\alpha} \pi^2 \kappa^2} \\
& \lim_{n \rightarrow \infty} \frac{c_{4D}^{(l)}(n)}{c_{4D}^{(1)}(n)} = \frac{(\alpha \pi)^{l-1}}{(l-1)!} \longleftrightarrow \lim_{n \rightarrow \infty} \frac{c_{2D}^{(l)}(n)}{c_{2D}^{(1)}(n+l-1)} = \frac{(\tilde{\alpha} \pi^2)^{l-1}}{(l-1)!} \\
& \text{Mass renormalization essential} \longleftrightarrow \text{Mass renormalization irrelevant}
\end{aligned}$$

Box 1: Correspondences between the 4D and 2D cases.

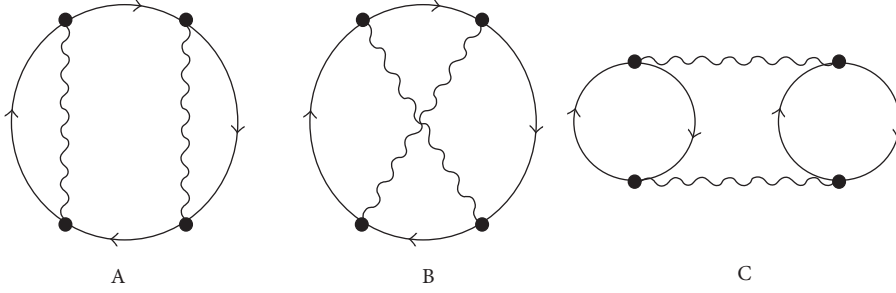


FIGURE 7: Three-loop Feynman diagrams.

The last one is by far the easiest one, and it is straightforward to obtain for it the following compact integral representation:

$$\begin{aligned}
\mathcal{L}^{3C}(f) &= \frac{e^3}{16\pi^3 f} \int_0^\infty dz dz' d\tilde{z} dz'' \\
& \cdot \frac{\sinh z \sinh z' \sinh \tilde{z} \sinh z''}{[\sinh(z+z') \sinh(\tilde{z}+z'')]^2} \\
& \cdot \frac{e^{-2\kappa(z+z'+\tilde{z}+z'')}}{\sinh z \sinh z' \sinh(\tilde{z}+z'') + \sinh \tilde{z} \sinh z'' \sinh(z+z')}.
\end{aligned} \quad (57)$$

This representation turned out to be quite adequate for a numerical calculation of the first 9 weak-field expansion coefficients $c_C^{(3)}(n)$ of diagram C. In Figure 8 we use these nine coefficients to show that this unquenched contribution is indeed asymptotically subleading.

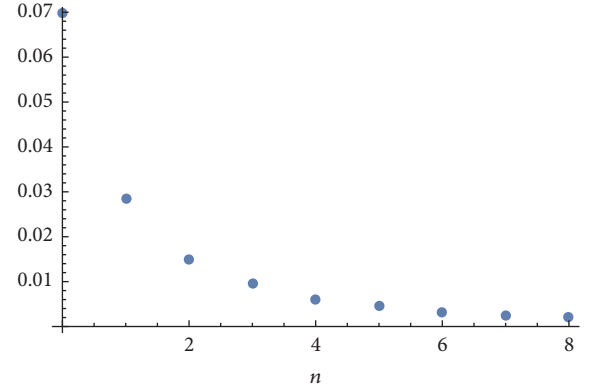
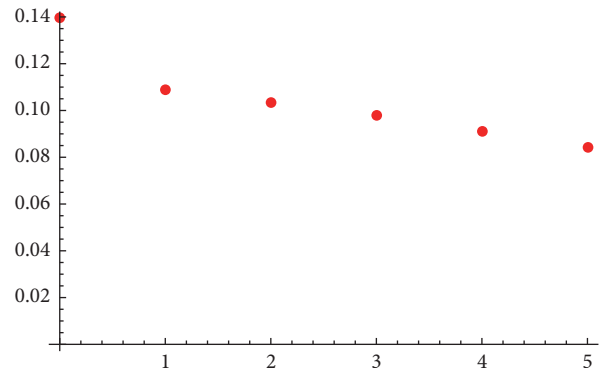
This settles point 2 of our wish list above!

Diagrams A and B are much more difficult, but the use of the “traceless gauge” choice $\lambda = 2$ led to simplifications and in particular to manifesting IR finiteness term by term. We managed to compute the first coefficient analytically

$$c_{A+B}^3(0) = \left(-\frac{3}{2} + \frac{7}{4}\zeta(3)\right) \frac{\tilde{\alpha}^2}{64} \quad (58)$$

and five more coefficients numerically. Using these to plot the ratio $(c_{A+B}^{(3)}(n)/c_{2D}^{(1)}(n+2))/((\tilde{\alpha}\pi^2)^2/2)$ we get Figure 9.

Thus we are falling even below the asymptotic prediction!

FIGURE 8: The ratio $(c_C^{(3)}(n)/c_{2D}^{(1)}(n+2))/((\tilde{\alpha}\pi^2)^2/2)$ for $n = 0, \dots, 8$.FIGURE 9: The ratio $(c_{A+B}^{(3)}(n)/c_{2D}^{(1)}(n+2))/((\tilde{\alpha}\pi^2)^2/2)$ for $n = 0, \dots, 5$.

9. Conclusions and Outlook

Let us summarize:

- (i) We have presented here first results of a calculation of the three-loop 2D EHL. This is the first calculation of a three-loop effective Lagrangian in QED.
- (ii) Although so far we have been able to compute only six coefficients of the weak-field expansion (we should be able to obtain a few more) it seems already very likely that the analogue of the AAM conjecture fails in 2D QED. This would throw also serious doubts on the validity of the 4D AAM conjecture.
- (iii) However, since the coefficient ratios fall below, rather than above, the asymptotic prediction, *the riddle of the unreasonable smallness of loop corrections remains*. Presumably the worldline instanton approach captures some valid information on large-scale cancellations between Feynman diagrams but needs refinement beyond two loops.
- (iv) We have also made an effort to make the point that the QED photon amplitudes in the limit of low energy and large number of photons are very natural objects for a study of the asymptotic properties of the QED perturbation series.
- (v) It should also have become clear that physical mass renormalization is essential for asymptotic estimates in QED! Unless mass renormalization is done physically, QED perturbation theory will break down already at the two-loop level, because the two-loop contribution to any helicity component of the N -photon amplitude will, at least in the low-energy limit, dominate over the one-loop one for sufficiently large N . This implies, in particular, that approaches to the study of the large-order behaviour of the QED perturbation series that are indifferent to the issue of physical mass renormalization ought to be viewed with caution.
- (vi) As an aside, it would be interesting to study also the QCD N -gluon amplitudes for large N from the point of view of mass renormalization.

Conflicts of Interest

The authors declare that there are no conflicts of interest regarding the publication of this paper.

References

- [1] F. J. Dyson, "Divergence of perturbation theory in quantum electrodynamics," *Physical Review*, vol. 85, no. 4, pp. 631-632, 1952.
- [2] C. A. Hurst, "An example of a divergent perturbation expansion in field theory," vol. 48, pp. 625-639, 1952.
- [3] G. 't Hooft, "Can we make sense out of 'quantum chromodynamics?'" in *The Whys of Subnuclear Physics*, A. Zichichi, Ed., Plenum, New York, NY, USA, 1978, Reprinted in: G. 't Hooft, *Under the Spell of The Gauge Principle*, World Scientific, Singapore, 1994.
- [4] J. G. Russo, "A note on perturbation series in supersymmetric gauge theories," *Journal of High Energy Physics*, vol. 2012, p. 38, 2012.
- [5] P. Cvitanovic, "Asymptotic estimates and gauge invariance," *Nuclear Physics B*, vol. 127, pp. 176-188, 1977.
- [6] P. Cvitanovic and T. Kinoshita, "Sixth-order magnetic moment of the electron," *Physical Review D*, vol. 10, article 4007, 1974.
- [7] G. V. Dunne and C. Schubert, "Two-loop Euler-Heisenberg QED pair-production rate," *Nuclear Physics B*, vol. 564, Article ID 9907190, p. 591, 2000.
- [8] G. V. Dunne and C. Schubert, "Two-loop self-dual Euler-Heisenberg Lagrangians (I): real part and helicity amplitudes," *Journal of High Energy Physics*, vol. 2002, article 0208, p. 53, 2002.
- [9] G. V. Dunne and C. Schubert, "Two-loop self-dual Euler-Heisenberg Lagrangians (II): imaginary part and Borel analysis," *Journal of High Energy Physics*, vol. 2002, article 0206, 2002.
- [10] L. C. Martin, C. Schubert, and V. M. Villanueva Sandoval, "On the low-energy limit of the QED N -photon amplitudes," *Nuclear Physics B*, vol. 668, no. 1-2, Article ID 0301022, pp. 334-335, 2003.
- [11] G. V. Dunne and C. Schubert, "Multiloop information from the QED effective Lagrangian," *Journal of Physics. Conference Series*, vol. 37, pp. 59-72, 2006.
- [12] G. V. Dunne, A. Huet, D. Rivera, and C. Schubert, "Closed-form weak-field expansion of two-loop Euler-Heisenberg lagrangians," *Journal of High Energy Physics*, vol. 2006, 2006.
- [13] I. Huet, D. G. C. McKeon, and C. Schubert, "Euler-Heisenberg lagrangians and asymptotic analysis in 1+1 QED. Part I: two-loop," *Journal of High Energy Physics*, vol. 2010, article 1012, p. 36, 2010.
- [14] I. Huet, M. R. De Trautenberg, and C. Schubert, "The Euler-Heisenberg Lagrangian beyond one loop," in *Proceedings of the Eleventh Conference on Quantum Field Theory under The Influence of External Conditions (QFEXT '11)*, vol. 14, pp. 383-393, 2012.
- [15] I. Huet, M. Rausch de Trautenberg, and C. Schubert, "Three-loop Euler-Heisenberg Lagrangian in 1+1 QED," In preparation.
- [16] W. Heisenberg and H. Euler, "Folgerungen aus der Diracschen theorie des positrons," *Zeitschrift für Physik*, vol. 98, no. 11-12, pp. 714-732, 1936.
- [17] V. Weisskopf, *Kong. Dans. Vid. Selsk. Math-fys. Medd. XIV No. 6 (1936)*, Quantum Electrodynamics, Dover, New York, NY, USA, 1958.
- [18] F. Sauter, "Über das Verhalten eines Elektrons im homogenen elektrischen Feld nach der relativistischen Theorie Diracs," *Zeitschrift für Physik*, vol. 69, no. 11-12, pp. 742-764, 1931.
- [19] J. Schwinger, "On gauge invariance and vacuum polarization," *Physical Review*, vol. 82, pp. 664-679, 1951.
- [20] V. I. Ritus, "Lagrangian of an intense electromagnetic field and quantum electrodynamics at short distances," *Journal of Experimental and Theoretical Physics*, vol. 69, p. 1517, 1975, [Sov. Phys. JETP 42 (1975) 774].
- [21] V. I. Ritus, "On the relation between the quantum electrodynamics of an intense field and the quantum electrodynamics at small distances," *Zh.Eksp.Teor.Fiz*, vol. 73, pp. 807-821, 1977 (Russian).
- [22] W. Dittrich and M. Reuter, *Effective Lagrangians in Quantum Electrodynamics*, Springer, Berlin, Germany, 1985.

- [23] M. Reuter, M. G. Schmidt, and C. Schubert, "Constant external fields in gauge theory and the spin 0,1,2,1 path integrals," *Annals of Physics*, vol. 259, no. 2, pp. 313–365, 1997.
- [24] S. L. Lebedev and V. I. Ritus, "Virial representation of the imaginary part of the lagrange function of the electromagnetic field," *Zh.Eksp.Teor.Fiz*, vol. 86, pp. 408–421, 1984.
- [25] V. I. Ritus, "Method of eigenfunctions and mass operator in quantum electrodynamics of a constant field," *Zh.Eksp.Teor.Fiz*, vol. 75, pp. 1560–1583, 1978.
- [26] I. K. Affleck, O. Alvarez, and N. S. Manton, "Pair production at strong coupling in weak external fields," *Nuclear Physics, Section B*, vol. 197, no. 3, pp. 509–519, 1982.
- [27] R. P. Feynman, "Mathematical formulation of the quantum theory of electromagnetic interaction," *Physical Review A*, vol. 80, p. 440, 1950.
- [28] A. D'Adda and P. Di Vecchia, "Supersymmetry and instantons," *Physics Letters B*, vol. 73, no. 2, pp. 162–166, 1978.
- [29] A. Das and G. V. Dunne, "Large-order perturbation theory and de Sitter/anti de Sitter effective actions," *Physical Review. D. Third Series*, vol. 74, no. 4, 044029, 9 pages, 2006.
- [30] M. J. Duff and C. J. Isham, "Self-duality, helicity, and supersymmetry: The scattering of light by light," *Physics Letters B*, vol. 86, no. 2, pp. 157–160, 1979.
- [31] M. J. Duff and C. J. Isham, "Self-duality, helicity and coherent states in nonabelian gauge theories," *Nuclear Physics. B*, vol. 162, no. 2, pp. 271–284, 1980.
- [32] M. Krasnansky, "Two-loop vacuum diagrams in background field and the Heisenberg-Euler effective action," *International Journal of Modern Physics A. Particles and Fields. Gravitation. Cosmology*, vol. 23, no. 32, pp. 5201–5215, 2008.
- [33] A. Das, J. Frenkel, C. Schubert, and B. Phys. Lett, "Infrared divergences, mass shell singularities and gauge dependence of the dynamical fermion mass," *Physics Letters B*, vol. 720, no. 4-5, pp. 414–418, 2013.

Research Article

Supersymmetry across the Hadronic Spectrum

Hans Günter Dosch

Institut für Theoretische Physik der Universität Heidelberg, Heidelberg, Germany

Correspondence should be addressed to Hans Günter Dosch; h.g.dosch@gmail.com

Received 16 May 2017; Accepted 20 June 2017

Academic Editor: Thierry Grandou

Copyright © 2017 Hans Günter Dosch. This is an open access article distributed under the Creative Commons Attribution License, which permits unrestricted use, distribution, and reproduction in any medium, provided the original work is properly cited. The publication of this article was funded by SCOAP³.

Semiclassical light-front bound-state equations for hadrons are presented and compared with experiment. The essential dynamical feature is the holographic approach; that is, the hadronic equations in four-dimensional Minkowski space are derived as holograms of classical equations in a 5-dimensional anti-de Sitter space. The form of the equations is constrained by the imposed superconformal algebra, which fixes the form of the light-front potential. If conformal symmetry is strongly broken by heavy quark masses, the combination of supersymmetry and the classical action in the 5-dimensional space still fixes the form of the potential. By heavy quark symmetry, the strength of the potential is related to the heavy quark mass. The contribution is based on several recent papers in collaboration with Stan Brodsky and Guy de Téramond.

1. Introduction

Semiclassical approximations play an essential role in quantum field theories. Think of atomic or molecular physics: in spite of all refinement of renormalized QED, the semiclassical Dirac and Schrödinger equations not only are of enormous practical advantage but also are essential in order to exhibit structural properties.

The search for semiclassical approximations even in strongly interacting quantum field theories received a significant advance through the Maldacena conjecture [1], which postulates the correspondence of a superconformal gauge quantum field theory in 4 dimensions with a classical gravitational theory in a 5-dimensional anti-de Sitter space (AdS₅). Here a light-front Hamiltonian for meson and boson wave functions is presented, which is based on the holographic AdS/CFT correspondence and receives essential dynamical constraints from an implemented superconformal algebra.

The kinematical frame is based on the light-front (LF) quantization at fixed LF time $x_+ = x^0 + x^3$; I refer for the essential features and the importance of this frame to the contribution of Stan Brodsky in the same volume. In the two constituent sectors, an essential variable is the boost invariant transverse separation $\zeta = \sqrt{x_1 x_2} |\vec{b}_{\perp,2} - \vec{b}_{\perp,1}|$, where x_i and $\vec{b}_{\perp,i}$, $i = 1, 2$, are the longitudinal

momentum fractions and the transverse coordinates of the two constituents, respectively.

Since in the holographic correspondence there is only one variable to describe the internal structure of hadrons, namely, the coordinate of the 5th dimension, hadrons with more than two constituents have to be treated as clusters. In that case, one introduces the effective longitudinal momentum fraction $x_a^{\text{eff}} = \sum_{i=1}^{N_a} x_i$, where N_a is the number of constituents in the cluster a , and correspondingly one introduces an effective transverse coordinate $\vec{b}_{\perp,a}^{\text{eff}} = (\sum_{i=1}^{N_a} x_i \vec{b}_{\perp,i}) / x_a^{\text{eff}}$. The effective boost invariant separation is then $\zeta = \sqrt{x_a^{\text{eff}} x_b^{\text{eff}}} |\vec{b}_{\perp,b}^{\text{eff}} - \vec{b}_{\perp,a}^{\text{eff}}|$. There is no theoretical limit for the number of the constituents in the cluster.

In the conformal limit (massless quarks), the LF Hamiltonian in the two-particle sector does not contain the longitudinal variable x_i or x_i^{eff} explicitly:

$$H = -\frac{d^2}{d\zeta^2} + \frac{4L^2 - 1}{4\zeta^2} + U(\zeta); \quad (1)$$

here, L is the LF angular momentum. In this approach, the squared hadron masses are the eigenvalues of the LF Hamiltonian.

In order to get some insight into the LF potential $U(\zeta)$, which is in principle determined by the QCD Lagrangian, we turn to the dynamical scheme of AdS₅/CFT correspondence.

AdS₅ is a maximally symmetric 5-dimensional space with the metric

$$(ds)^2 = \frac{R^2}{z^2} \left((dx^0)^2 - (dx^1)^2 - (dx^2)^2 - (dx^3)^2 - (dz)^2 \right), \quad (2)$$

where the coordinate of the 5th dimension z is the holographic variable.

From the AdS₅ action, one derives the field equations of AdS, which are interpreted as bound-state wave equations. As noticed and exploited first by Brodsky and de Téramond [2], the structure of the field equations from the AdS₅ action is equal to the structure of the LF Hamilton, if one identifies the holographic variable z with the boost invariant separation ζ . From unperturbed AdS, one obtains a vanishing LF potential. This is no wonder: the space AdS₅ has maximal symmetry that in turn leads to a conformal symmetry in the holographically corresponding 4-dimensional quantum field theory and no scale can appear.

In order to introduce interaction, one has to break the maximal symmetry. This is done by introducing a dilaton term $e^{\varphi(z)}$ into the AdS action. Due to the occurrence of covariant derivatives in the AdS Lagrangian, the derivation of the Euler-Lagrange equations is rather tedious, but finally one obtains for a meson wave function [3] $\Phi_{\mu_1 \dots \mu_J} = \epsilon_{\mu_1 \dots \mu_J}^J \phi_{J,L}(\zeta)$ the bound-state equation:

$$\left(-\frac{d^2}{d\zeta^2} + \frac{4L^2 - 1}{4\zeta^2} + U(\zeta) \right) \phi_J(\zeta) = M^2 \phi_J(\zeta) \quad (3)$$

$$\text{with } U(\zeta) = \frac{1}{2} \varphi''(\zeta) + \frac{1}{4} \varphi'(\zeta)^2 + \frac{2J-3}{2\zeta} \varphi'(\zeta);$$

here, $\epsilon_{\mu_1 \dots \mu_J}^J$ is the polarization tensor of a meson with total angular momentum J ; the LF angular momentum L is related to the AdS mass by $(mR)^2 = -(2-J)^2 + L^2$; the holographic variable z is identified with the LF separation ζ .

For Baryons, a dilaton factor $e^{\varphi(\zeta)}$ does not lead to an interaction and there one has to introduce an additional Yukawa term $\bar{u}V(\zeta)u$ in the 5-dimensional fermionic AdS action. The wave function is split into a positive-chirality and a negative-chirality component:

$$u_{\mu_1 \dots \mu_{J-1/2}}(p) = \frac{1 + \gamma_5}{2} u_{\dots}(p) \psi_{B^+}(\zeta) + \frac{1 - \gamma_5}{2} u_{\dots}(p) \psi_{B^-}(\zeta) \quad (4)$$

and one obtains the wave equations [3] with the potential $U_{\pm} = V^2 \pm V' + ((1+2L)/\zeta)V$:

$$\left(-\frac{d^2}{d\zeta^2} + \frac{4(L+1)^2 - 1}{4\zeta^2} + U_{-}(\zeta) \right) \psi_{B^-}(\zeta) = M^2 \psi_{B^-}(\zeta), \quad (5)$$

$$\left(-\frac{d^2}{d\zeta^2} + \frac{4L^2 - 1}{4\zeta^2} + U_{+}(\zeta) \right) \psi_{B^+}(\zeta) = M^2 \psi_{B^+}(\zeta). \quad (6)$$

For phenomenological reasons one has chosen ad hoc [4–8]

$$e^{\varphi(\zeta)} = e^{\lambda_M z^2}, \quad V(\zeta) = \lambda_B z; \quad (7)$$

which leads to the potential for

$$\text{mesons: } U(\zeta) = \lambda_M^2 \zeta^2 + 2\lambda_M (J-1), \quad (8)$$

$$\text{baryons: } U_{\pm}(\zeta) = \lambda_B^2 \zeta^2 + 2L\lambda_F + \lambda_F \left(\frac{1}{2} \pm \frac{1}{2} \right). \quad (9)$$

These potentials lead to linear Regge trajectories and a massless pion. For the Delta trajectory, however, one has to choose formally half-integer twist (i.e., to add 1/2 to the angular momentum L) in order to get agreement with the data.

2. Constraints Given by the Superconformal Graded Algebra

Although one obtains in that way a satisfactory description of several essential features of hadron spectroscopy, there are some points that are not so satisfactory. First, and this is the most important shortcoming, the special choice of maximal symmetry breaking given in (7) is completely arbitrary and has no theoretical foundation. Second, the symmetry breaking for mesons and baryons is completely unrelated, and finally the remarkable fact that the Regge slopes of mesons and baryons are very similar, which implies that $\lambda_M \approx \lambda_B$ in (7), is in this context completely fortuitous.

In the search for further dynamical constraints, we go back to the original Maldacena correspondence [1] of a classical 5-dimensional theory and a 4-dimensional quantum field theory. There the latter is heavily constrained by symmetries: it is superconformal; that is, it obeys supersymmetry and conformal symmetry. Since our goal is to find a semiclassical approximation to QCD, it is not too far-fetched to investigate *superconformal* quantum mechanics (QM).

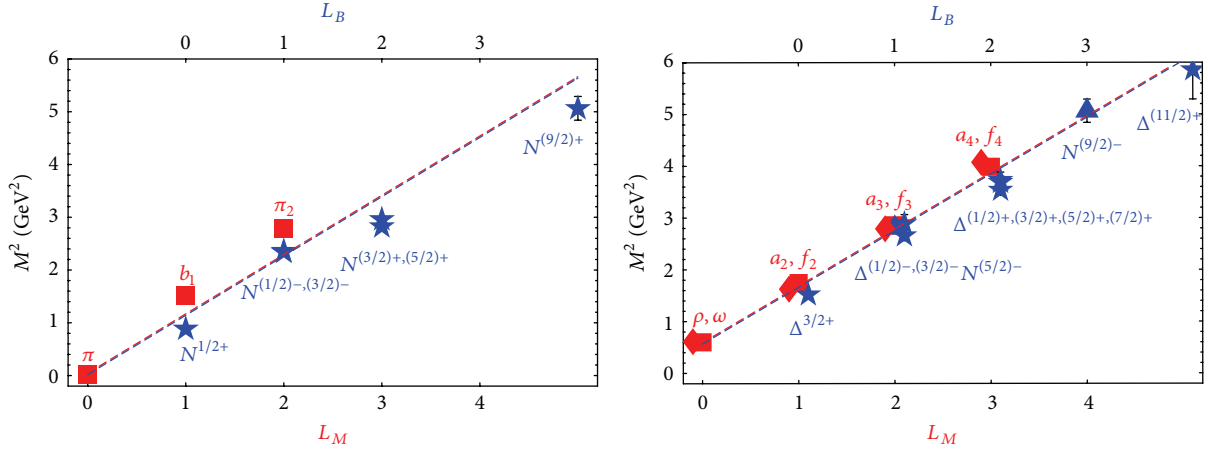
Supersymmetric QM is very simple [9]. It is built on a graded algebra consisting of two fermionic operators (supercharges), Q and Q^\dagger , and a bosonic operator (the Hamiltonian), H , with the anticommutation and commutation relations:

$$\{Q, Q^\dagger\} = H, \quad \{Q, Q\} = \{Q^\dagger, Q^\dagger\} = 0; \quad (10)$$

$$[Q, H] = [Q^\dagger, H] = 0.$$

A matrix realization in a Hilbert space with two components is

$$Q = \begin{pmatrix} 0 & q \\ 0 & 0 \end{pmatrix}, \quad Q^\dagger = \begin{pmatrix} 0 & 0 \\ q^\dagger & 0 \end{pmatrix}, \quad (11)$$

FIGURE 1: The $\pi - N$ trajectory and the $\rho - \Delta$ trajectory from [10].

$$q = -\frac{d}{dx} + \frac{f}{x} + V(x), \quad (12)$$

$$q^\dagger = \frac{d}{dx} + \frac{f}{x} + V(x),$$

where f is a dimensionless constant and V is the arbitrary superpotential.

If the superpotential $V = 0$, then there is no scale present and also conformal symmetry holds: one can extend the supersymmetric (graded) algebra 9 to a superconformal one by introducing the additional supercharges S and S^\dagger , which can be viewed as a square root of the special conformal transformation K , since $\{S, S^\dagger\} = K$; for more details, see [10, 11]. In matrix notation, one can write

$$S = \begin{pmatrix} 0 & x \\ 0 & 0 \end{pmatrix}, \quad (13)$$

$$S^\dagger = \begin{pmatrix} 0 & 0 \\ x & 0 \end{pmatrix}.$$

Following the procedure introduced by de Alfaro et al. [12] for the conformal algebra and extended by and Fubini and Rabinovici [13] to the superconformal algebra, one can construct a new Hamiltonian G inside the superconformal algebra:

$$G = \{R_\lambda, R_\lambda^\dagger\} \quad \text{with } R_\lambda = Q + \lambda S, \quad R_\lambda^\dagger = Q^\dagger + \lambda S^\dagger. \quad (14)$$

In this generalization of the Hamiltonian, a scale λ appears naturally, since the supercharges S and Q have different physical dimensions.

The new Hamiltonian is diagonal with

$$G_{11} = -\frac{d^2}{dx^2} + \frac{4(f+1/2)^2 - 1}{4x^2} + \lambda^2 x^2 + 2\lambda \left(f - \frac{1}{2}\right), \quad (15)$$

$$G_{22} = -\frac{d^2}{dx^2} + \frac{4(f-1/2)^2}{4x^2} + \lambda^2 x^2 + 2\lambda \left(f + \frac{1}{2}\right). \quad (16)$$

By construction, the eigenvalues of the two operators are identical and the operator R_λ^\dagger transforms an eigenstate of G_{11} with eigenvalue $E \neq 0$ into an eigenfunction of G_{22} .

If we identify $f = L + 1/2$ and $x = \zeta$, it turns out that the potentials occurring in the new Hamiltonian in (15) and (16) are exactly the potentials following from the ad hoc introduced Yukawa term in (7) in the fermion action. Furthermore, the operator G_{11} is the Hamiltonian of a meson with $L = J = f + 1/2$ (see (8)). And G_{22} is the Hamiltonian of the baryon component ψ_{B^+} with $L = f - 1/2$ (see (9)). That is, the meson eigenfunction of G_{11} with LF $L_M = f + 1/2$ has the same eigenvalue as a baryon with $L_B = f - 1/2$, eigenfunction of G_{22} . The supercharge R_λ^\dagger transforms the meson wave function into a wave function of the mass-degenerate baryon. A meson with $L_M = f + 1/2$ is superpartner of baryon with $L_B = f - 1/2$; mesons with $L_M = 0$ (π , e.g.) have no superpartner, since the supercharge R_λ^\dagger annihilates its wave function.

3. Spin Effects

In the superconformal quantum mechanical approach, no internal quark spin effects are foreseen, in contrast to the AdS₅ approach for mesons. The meson Hamiltonian derived in the frame of the superconformal QM, G_{11} , differs from the one derived from AdS by the constant λs , where s is the total quark spin of the meson. Supersymmetry demands the occurrence of the same term also for baryons; that is, we arrive at the following expression for the supersymmetric Hamiltonian for mesons and baryons:

$$G = \{R_\lambda, R_\lambda^\dagger\} + \lambda s \mathbf{I}, \quad (17)$$

where for π and its SUSY partner, namely, the nucleon, we have $s = 0$, and for ρ and its SUSY partner Δ , we have $s = 1$. Generally, for baryons, s is the lowest possible internal spin of the cluster. The results for the $\pi - N$ and the $\rho - \Delta$ trajectories are displayed in Figure 1; they show especially for Δ and ρ the nearly perfectly realized symmetry.

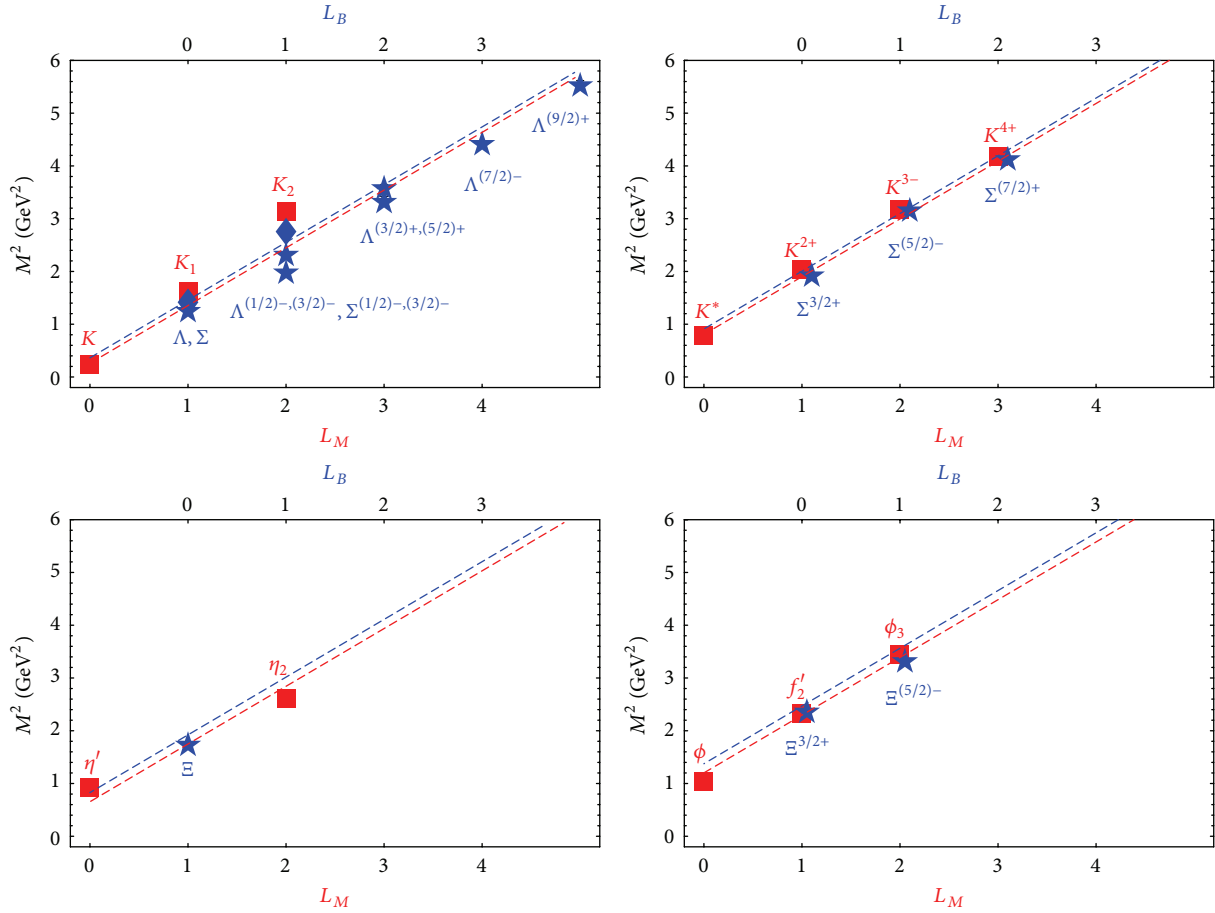


FIGURE 2: The K , Λ , K^* , Σ^* , η' , Ξ , and ϕ , Ξ^* trajectories, from [14].

4. Completing the Supersymmetric Multiplet

The supersymmetric quadruplet containing the meson and the baryon is not yet complete, since the partner of negative chirality component of the baryon, ψ_{B-} , is missing. We can complete the supersymmetric multiplet by applying the fermion operator R_λ^\dagger to that negative-chirality component baryon wave function and thus obtain a bosonic state. This operator, which transforms the meson wave function in the positive-chirality baryon wave function, can be interpreted as transforming a quark into an antiquark cluster in the colour representation $\{3\}$. Therefore the operator R_λ^\dagger applied to the negative-chirality component of a baryon will give a wave function $\phi_T = R_\lambda^\dagger \psi_{B-}$, which can be interpreted as that of a tetraquark consisting of a diquark cluster and an antiquark cluster. The SUSY quadruplet can be arranged in a 2×2 matrix in the following way: $\begin{pmatrix} \phi_M^{(L_B+1)} & \psi_{B-}^{(L_B+1)} \\ \psi_{B+}^{(L_B)} & \phi_T^{(L_B)} \end{pmatrix}$.

Candidates for complete supermultiplets with fitting quantum numbers $I(J^P)$ are

$b_1(1235)1(1^+)$ and $N_{+,-}(940)(1/2)(1/2^+)$ and as tetraquark $f_0(980)0(0^+)$,

$a_2(1320)1(2^+)$ and $\Delta_{+,-}(1230)(3/2)(3/2^+)$ and as tetraquark $a_1(1260)1(1^+)$.

A special feature of tetraquarks is that states consisting of a spin-singlet and a spin-triplet cluster are degenerate in G parity.

5. Beyond the Chiral Limit

It is reasonable to assume that small quark masses do not affect superconformal dynamics; that is, the LF potentials remain unchanged and only the invariant mass is affected; that is, the chiral expression $\sum_i (k_{\perp i}^2/x_i)$ has to be replaced by $\sum_i ((k_{\perp i}^2 + m_i^2)/x_i)$. To first approximation, this gives an additive term to the squared hadron mass [14–16] for mesons $M_M^2 = 4\lambda(n + L_M) + 2\lambda s + \Delta M_2^2(m_1, m_2)$ and for baryons: $M_B^2 = 4\lambda(n + L_B + 1) + 2\lambda s + \Delta M_3^2(m_1, m_2, m_3)$, where $\Delta M^2[m_1, \dots, m_n] = (\lambda^2/F)(dF/d\lambda)$ with $F[\lambda] = \int_0^1 \dots \int dx_1 \dots dx_n e^{-(1/\lambda)(\sum_i (m_i^2/x_i))} \delta(\sum_i x_i - 1)$.

From π and K mass, the light quark masses are determined to $m_q = 0.046$ GeV and $m_s = 0.357$ GeV; the resulting spectra are shown in Figure 2.

6. Strong Breaking of Conformal Symmetry by Heavy Quark Masses

In heavy-light hadrons, where one constituent is heavy and the other is light, we have still ultrarelativistic kinematics,

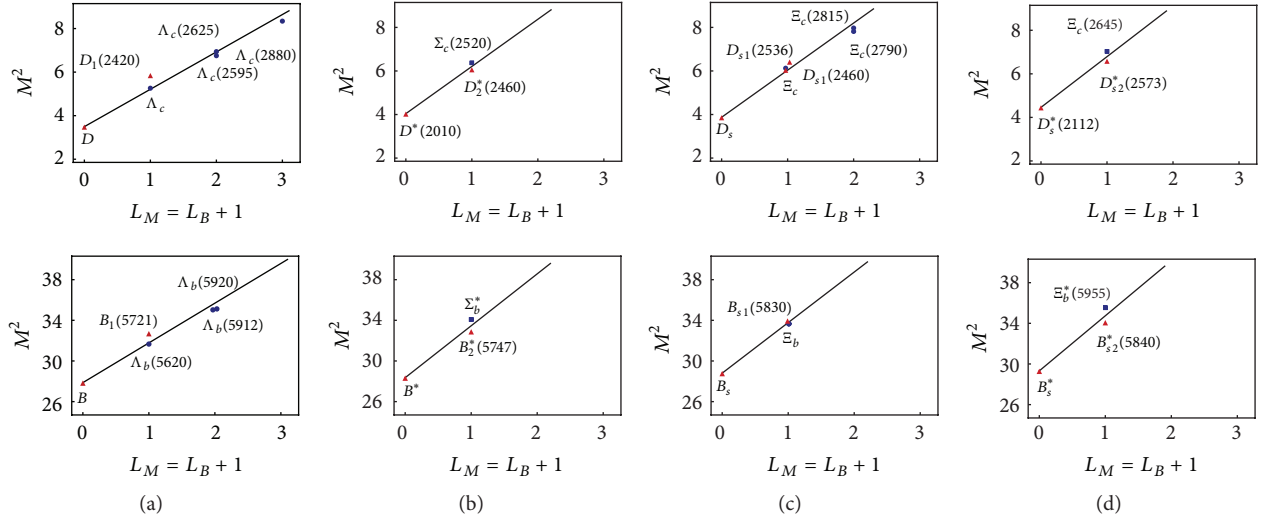


FIGURE 3: Trajectories for heavy-light hadrons with strongly broken conformal symmetry, from [14].

but conformal symmetry is strongly broken. Supersymmetry, however, can still survive and can give, together with AdS/CFT breaking, crucial dynamical constraints.

Let us go back to the SUSY algebra in (11) and (12). From $H = \{Q, Q^\dagger\}$, we can express the mesonic LF potential in terms of $V(x)$. For a meson with $J_M = L_M = L + 1$, we obtain

$$U_{\text{Susy}}(\zeta) = V^2 + \frac{2L+1}{\zeta}V - V'. \quad (18)$$

With a dilaton term $e^{\varphi(\zeta)}$, we obtain, from the AdS/CFT action for the same meson,

$$U_{\text{dil}}(\zeta) = \frac{1}{4}(\varphi')^2 + \frac{2L_M - 3}{2\zeta}\varphi' + \frac{1}{2}\varphi''. \quad (19)$$

It has been shown in [14] that the two expressions are only compatible if

$$\begin{aligned} \varphi(\zeta) &= \frac{1}{2}\lambda A\zeta^2 + B, \\ V(\zeta) &= \frac{1}{2}\lambda A\zeta. \end{aligned} \quad (20)$$

Thus, the combination of SUSY with AdS constraints implies that the LF potential even for strongly broken conformal invariance is harmonic; the strength, however, is not determined. The resulting hadronic spectrum is for mesons $M^2 = 4\lambda_Q(n+L) + \mu_2^2$ and for baryons $M^2 = 4\lambda_Q(n+L+1) + \mu_3^2$.

In Figure 3, the heavy-light hadrons together with linear trajectories are displayed. In all cases where several recurrences are observed, the data are within the expected accuracy compatible with the predicted harmonic potential. The approximate masses of many states, which are still to be observed, can be predicted in that way [14]. The average values for the scale parameters for hadrons, which contain one c -quark or b -quark, are $\sqrt{\lambda_c} = 0.71 \pm 0.04 \text{ GeV}$ and $\sqrt{\lambda_b} = 1.06 \pm 0.1 \text{ GeV}$.

7. Constraints from Heavy Quark Symmetry

If the mass of the heavy quark M_Q goes to ∞ , it decouples and heavy quark symmetry (HQS) holds [17]. This has as a consequence that the decay constant of the heavy-light pseudoscalar meson, f_M , scales in that limit with the inverse square root of the meson mass [17, 18]:

$$\sqrt{M_M} f_M \rightarrow C. \quad (21)$$

With mass dependence of the wave functions modified according to the modification of the invariant mass discussed above, we can include the mass dependence into the wave function:

$$\psi_{n,L}^{(m)} = \frac{1}{N_m} e^{-(1/2\lambda)\sum_{i=1}^n (m_i^2/x_i)} \psi_{n,L}^{(0)}, \quad (22)$$

where $\psi_{n,L}^{(0)}$ is the wave function in the case of massless quarks.

From this wave function, one derives the decay constant:

$$\begin{aligned} f_M &= \frac{1}{\sqrt{\int_0^1 dx e^{-m_Q^2/\lambda(1-x)}}} \\ &\cdot \sqrt{\frac{\lambda}{\pi}} \int_0^1 dx e^{-m_Q^2/2\lambda(1-x)} \sqrt{x(1-x)}. \end{aligned} \quad (23)$$

Performing an integration by steepest descent, one obtains

$$f_M = \sqrt{\frac{6}{\pi e}} \left(1 + \operatorname{erf}\left(\frac{1}{2}\right)\right) \frac{\lambda^{3/2}}{m_Q^2}. \quad (24)$$

Taking into account the fact that, in the limit of $m_Q \rightarrow \infty$, the heavy quark mass and the meson mass become equal, comparison of this equation with (21) yields that $\lambda_Q \sim M_M$. Thus, HQS demands that, for heavy quark masses, the scale parameter λ increase. It relates λ_b with λ_c even in a quantitative way, as can be seen from Figure 4.

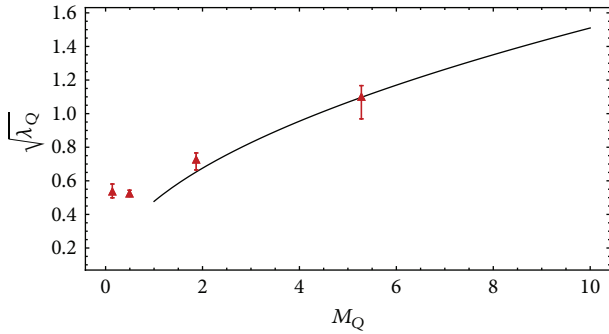


FIGURE 4: The scale parameter $\sqrt{\lambda}$ for different pseudoscalar mesons versus the meson mass. The solid line is the functional dependence $\sqrt{\lambda} \sim \sqrt{M_M}$ as predicted by HQS.

8. Conclusions

We were motivated by the Maldacena conjecture, which relates a classical gravitational theory in AdS_5 to a superconformal colour gauge QFT with infinitely many colours. Our approach, which aimed at a semiclassical approximation, led to superconformal quantum mechanics on the light front. The form of the light-front potential is determined by the superconformal algebra. This model describes essential features of light hadron spectra: linear trajectories in orbital and radial excitations and a massless pion. The observed similarity of meson and baryon spectra is a consequence of the supersymmetry between the wave functions. We also predict tetraquarks with definite masses and quantum numbers.

The supersymmetry seems to survive even in the case where conformal symmetry is strongly broken by heavy quark masses. Here, the supersymmetry, together with the embedding into AdS_5 , implies a harmonic potential $\lambda\zeta^2$ also for heavy-light hadrons, but the scale parameter $\sqrt{\lambda}$ increases with heavy quark mass, in quantitative accordance with heavy quark symmetry.

Our model does not contain colour degrees of freedom, but the fact that all states have zero width is well compatible with the $N_C \rightarrow \infty$ limit of QCD; the accuracy, which is generally about 10%, is also compatible with the application of this limit to an $N_C = 3$ theory. The model can also be applied beyond spectroscopy [8, 19], but in this case additional assumptions and input are necessary.

Conflicts of Interest

The author declares that there are no conflicts of interest regarding the publication of this paper.

References

[1] J. Maldacena, “The large N limit of superconformal field theories and supergravity,” in *Proceedings of the Second Meeting on Trends in Theoretical Physics*, pp. 51–63, Buenos Aires, Argentina.

- [2] S. J. Brodsky and G. F. de Téramond, “Light-front hadron dynamics and AdS/CFT correspondence,” *Physics Letters B*, vol. 582, no. 3–4, pp. 211–221, 2004.
- [3] G. F. de Téramond, H. G. Dosch, and S. J. Brodsky, “Kinematical and dynamical aspects of higher-spin bound-state equations in holographic QCD,” *Physical Review D*, vol. 87, no. 7, 2013.
- [4] A. Karch, E. Katz, D. T. Son, and M. A. Stephanov, “Linear confinement and AdS/QCD,” *Physical Review D*, vol. 74, no. 1, Article ID 015005, 2006.
- [5] S. J. Brodsky and G. F. de Téramond, “Hadronic spectra and light-front wavefunctions in holographic QCD,” Tech. Rep. SLAC-PUB-11716, 2006.
- [6] I. Kirsch, “Spectroscopy of fermionic operators in AdS/CFT,” *Journal of High Energy Physics*, vol. 2006, no. 09, pp. 052–052, 2006.
- [7] Z. Abidin and C. E. Carlson, “Gravitational form factors of vector mesons in an AdS/QCD model,” *Physical Review D*, vol. 77, no. 9, 2008.
- [8] S. J. Brodsky, G. F. de Téramond, H. . Dosch, and J. Erlich, “Light-front holographic QCD and emerging confinement,” *Physics Reports. A Review Section of Physics Letters*, vol. 584, pp. 1–105, 2015.
- [9] E. Witten, “Dynamical breaking of supersymmetry,” *Nuclear Physics B*, vol. 188, no. 3, pp. 513–554, 1981.
- [10] H. G. Dosch, G. F. de Téramond, and S. J. Brodsky, “Superconformal baryon-meson symmetry and light-front holographic QCD,” *Physical Review D*, vol. 91, no. 8, 2015.
- [11] G. F. de Téramond, H. G. Dosch, and S. J. Brodsky, “Baryon spectrum from superconformal quantum mechanics and its light-front holographic embedding,” *Physical Review D*, vol. 91, no. 4, 2015.
- [12] V. de Alfaro, S. Fubini, and G. Furlan, “Conformal invariance in quantum mechanics,” *Il Nuovo Cimento A*, vol. 34, no. 4, pp. 569–612, 1976.
- [13] S. Fubini and E. Rabinovici, “Superconformal quantum mechanics,” *Nuclear Physics. B. Theoretical, Phenomenological, and Experimental High Energy Physics. Quantum Field Theory and Statistical Systems*, vol. 245, no. 1, pp. 17–44, 1984.
- [14] H. G. Dosch, G. F. de Téramond, and S. J. Brodsky, “Supersymmetry across the light and heavy-light hadronic spectrum. II,” *Physical Review D*, vol. 95, no. 3, 2017.
- [15] H. G. Dosch, G. F. de Téramond, and S. J. Brodsky, “Supersymmetry across the light and heavy-light hadronic spectrum,” *Physical Review D*, vol. 92, no. 7, 2015.
- [16] S. J. Brodsky, G. F. de Téramond, H. G. Dosch, and C. Lorcé, “Universal effective hadron dynamics from superconformal algebra,” *Physics Letters B*, vol. 759, pp. 171–177, 2016.
- [17] N. Isgur and M. B. Wise, “Spectroscopy with heavy-quark symmetry,” *Physical Review Letters*, vol. 66, no. 9, pp. 1130–1133, 1991.
- [18] E. Shuryak, “Hadrons containing a heavy quark and QCD sum rules,” *Nuclear Physics B*, vol. 198, no. 1, pp. 83–101, 1982.
- [19] R. S. Fufian, G. F. de Téramond, S. J. Brodsky, A. Deur, and H. G. Dosch, “Analysis of nucleon electromagnetic form factors from light-front holographic QCD: The spacelike region,” *Physical Review D*, vol. 95, no. 1, 2017.

Research Article

Exact Computations in Topological Abelian Chern-Simons and BF Theories

Philippe Mathieu

LAPTh, Université de Savoie, CNRS, Chemin de Bellevue, BP 110, 74941 Annecy-le-Vieux Cedex, France

Correspondence should be addressed to Philippe Mathieu; philippe.mathieu@lapth.cnrs.fr

Received 15 May 2017; Accepted 18 June 2017; Published 30 August 2017

Academic Editor: Ralf Hofmann

Copyright © 2017 Philippe Mathieu. This is an open access article distributed under the Creative Commons Attribution License, which permits unrestricted use, distribution, and reproduction in any medium, provided the original work is properly cited. The publication of this article was funded by SCOAP³.

We introduce Deligne cohomology that classifies $U(1)$ fibre bundles over 3 manifolds endowed with connections. We show how the structure of Deligne cohomology classes provides a way to perform exact (nonperturbative) computations in $U(1)$ Chern-Simons theory (BF theory, resp.) at the level of functional integrals. The partition functions (and observables) of these theories are strongly related to topological invariants well known to the mathematicians.

1. Introduction

Consider the following actions:

$$\begin{aligned} S_{\text{CS}_N}[A] &= 2\pi N \int_{\mathbb{R}^3} A \wedge dA = 2\pi N \int_{\mathbb{R}^3} A \wedge F, \\ S_{\text{BF}_N}[A, B] &= 2\pi N \int_{\mathbb{R}^3} B \wedge dA = 2\pi N \int_{\mathbb{R}^3} B \wedge F, \end{aligned} \quad (1)$$

where A and B are $U(1)$ connections. Here, the coupling constant N is any real number.

The gauge transformation $A \rightarrow A + d\Lambda$, where Λ is a function that leaves the actions (1) invariant. Since in the quantum context we consider the complex exponential of the action, the invariance required is less restrictive. Indeed, we can consider an invariance of S up to an integer:

$$S \rightarrow S + 2\pi n, \quad n \in \mathbb{Z} \implies e^{iS} \rightarrow e^{iS} \quad (2)$$

which implies that N is quantized. Studying the gauge invariance properties of the holonomies, which are the observables of Chern-Simons and BF theories, it turns out that the most general gauge transformation is $A \rightarrow A + \omega_{\mathbb{Z}}$, where $\omega_{\mathbb{Z}}$ is a closed 1-form with integral periods. On a contractible open set this transformation reduces to the classical one since, by Poincaré Lemma, there exists Λ such that $\omega_{\mathbb{Z}} = d\Lambda$.

In particular, this is the case when the theory is defined in \mathbb{R}^3 which is a contractible space. However, this generalized gauge transformation enables defining a theory on any closed (i.e., compact without boundary) 3-manifold M . The classical gauge transformation appears thus to be a particular case of the quantum one.

In this paper we will consider the equivalence classes according to this quantum gauge transformation. These classes classify $U(1)$ fibre bundles over M endowed with connections and their collection is the so-called first Deligne cohomology group of M . We will show that this structure enables performing exact computations in the framework of $U(1)$ Chern-Simons and BF theories.

2. Deligne Cohomology

The most general statement we can start from is a collection of local gauge fields A_{α} in open sets U_{α} that cover the manifold M we are considering. We suppose these open sets and their intersections to be contractible, so that we can in particular use the Poincaré Lemma inside. To define a global field, we need to explain how A_{α} and A_{β} stick together in the intersection $U_{\alpha} \cap U_{\beta}$. This, by definition, is done thanks to a gauge transformation:

$$A_{\beta} = A_{\alpha} + d\Lambda_{\alpha\beta} \quad \text{in } U_{\alpha\beta} = U_{\alpha} \cap U_{\beta}. \quad (3)$$

The antisymmetry of this relation in α and β implies that $d(\Lambda_{\alpha\beta} + \Lambda_{\beta\gamma} + \Lambda_{\gamma\alpha}) = 0$, making $\Lambda_{\alpha\beta} + \Lambda_{\beta\gamma} + \Lambda_{\gamma\alpha}$ a constant in $U_\alpha \cap U_\beta \cap U_\gamma$, that is an integer (since (4) is nothing but the cocycle condition for a $U(1)$ fibre bundle):

$$\Lambda_{\alpha\beta} + \Lambda_{\beta\gamma} + \Lambda_{\gamma\alpha} = n_{\alpha\beta\gamma} \in \mathbb{Z} \quad (4)$$

$$\text{in } U_{\alpha\beta\gamma} = U_\alpha \cap U_\beta \cap U_\gamma.$$

The symmetry in α , β , and γ of this last relation implies that

$$n_{\alpha\beta\gamma} - n_{\alpha\beta\delta} + n_{\alpha\gamma\delta} - n_{\beta\gamma\delta} = 0. \quad (5)$$

Thus, the generalization of our gauge potential on any closed 3-manifold M imposes considering a collection $(A_\alpha, \Lambda_{\alpha\beta}, n_{\alpha\beta\gamma})$ constituted of a family of potentials A_α defined in open sets U_α , a family of functions $\Lambda_{\alpha\beta}$ defined in the double intersections $U_{\alpha\beta}$, and a family of integers defined in the triple intersections $U_{\alpha\beta\gamma}$ (all those open sets and intersections being contractible). Elements of those collections are related by

$$A_\beta = A_\alpha + d\Lambda_{\alpha\beta} \quad \text{in } U_{\alpha\beta}.$$

$$\Lambda_{\alpha\beta} + \Lambda_{\beta\gamma} + \Lambda_{\gamma\alpha} = n_{\alpha\beta\gamma} \in \mathbb{Z} \quad \text{in } U_{\alpha\beta\gamma} \quad (6)$$

$$n_{\alpha\beta\gamma} - n_{\alpha\beta\delta} + n_{\alpha\gamma\delta} - n_{\beta\gamma\delta} = 0$$

These statements define a Deligne cocycle.

We need now to describe how this collection transforms when we perform a gauge transformation of the A_α :

$$A_\alpha \longrightarrow A_\alpha + dq_\alpha \quad \text{in } U_\alpha, \quad (7)$$

where $\Omega^1/\Omega^1_{\mathbb{Z}}$ is the quotient of the 1 form by the closed 1 form with integral periods and $H^2(\mathbb{Z})$ is the space of cohomology classes of the manifold. This is an abelian group, which can thus be decomposed as a direct sum of a free part $F^2 = \mathbb{Z}^{b^2}$ and a torsion part $T^2 = \mathbb{Z}_{p_1} \oplus \dots \oplus \mathbb{Z}_{p_n}$. This exact sequence shows that the space of Deligne cohomology classes can be

$$0 \longrightarrow \frac{\Omega^1}{\Omega^1_{\mathbb{Z}}} = \left(\frac{\Omega^1}{\Omega^1_0} \right) \times \left(\frac{\Omega^1_0}{\Omega^1_{\mathbb{Z}}} \right) \longrightarrow H_D^{[1]}(\mathbb{Z}) \longrightarrow H^2(\mathbb{Z}) = F^2 \oplus T^2 \longrightarrow 0, \quad (11)$$

where the family of q_α is a family of functions defined in the U_α . This implies that $\Lambda_{\alpha\beta}$ have to transform according to

$$\Lambda_{\alpha\beta} \longrightarrow \Lambda_{\alpha\beta} + q_\alpha - q_\beta - m_{\alpha\beta} \quad \text{in } U_{\alpha\beta}, \quad (8)$$

where the family $m_{\alpha\beta}$ consists in integers, mainly because $n_{\alpha\beta\gamma}$ do. Finally, $n_{\alpha\beta\gamma}$ transform thus according to

$$n_{\alpha\beta\gamma} \longrightarrow n_{\alpha\beta\gamma} - m_{\beta\gamma} + m_{\alpha\gamma} - m_{\alpha\beta} \quad \text{in } U_{\alpha\beta\gamma}. \quad (9)$$

Hence, the collection $(q_\alpha, m_{\alpha\beta})$ where q_α are functions defined in the U_α and $m_{\alpha\beta}$ are integers defined in the intersections $U_{\alpha\beta}$ together with the set of rules

$$A_\alpha \longrightarrow A_\alpha + dq_\alpha \quad \text{in } U_\alpha$$

$$\Lambda_{\alpha\beta} \longrightarrow \Lambda_{\alpha\beta} + q_\alpha - q_\beta - m_{\alpha\beta} \quad \text{in } U_{\alpha\beta} \quad (10)$$

$$n_{\alpha\beta\gamma} \longrightarrow n_{\alpha\beta\gamma} - m_{\beta\gamma} + m_{\alpha\gamma} - m_{\alpha\beta} \quad \text{in } U_{\alpha\beta\gamma}$$

generalizes the idea of gauge transformation. These rules define the addition of a Deligne coboundary to a Deligne cocycle. The quotient set of Deligne cocycles by Deligne coboundaries is the first Deligne cohomology group $H_D^{[1]}$.

3. Structure of the Space of Deligne Cohomology Classes

$H_D^{[1]}$ is naturally endowed with a structure of \mathbb{Z} -modulus. It can be described in particular through two exact sequences. The first one is

thought as a set of fibres over the discrete net constituted by $H^2(\mathbb{Z})$ and inside which we can move thanks to elements of $\Omega^1/\Omega^1_{\mathbb{Z}}$ (see Figure 1).

The second exact sequence that enables representing $H_D^{[1]}$ is

$$0 \longrightarrow H^1\left(\frac{\mathbb{R}}{\mathbb{Z}}\right) = \left(\frac{\Omega^1_0}{\Omega^1_{\mathbb{Z}}}\right) \times T^2 \longrightarrow H_D^{[1]}(\mathbb{Z}) \longrightarrow \Omega^2_{\mathbb{Z}} = \left(\frac{\Omega^1}{\Omega^1_0}\right) \times F^2 \longrightarrow 0, \quad (12)$$

where $H^1(\mathbb{R}/\mathbb{Z})$ is the first cohomology group \mathbb{R}/\mathbb{Z} -valued and $\Omega^2_{\mathbb{Z}}$ is the set of closed 2 forms with integral periods.

This exact sequence leads to the representation shown in Figure 2.

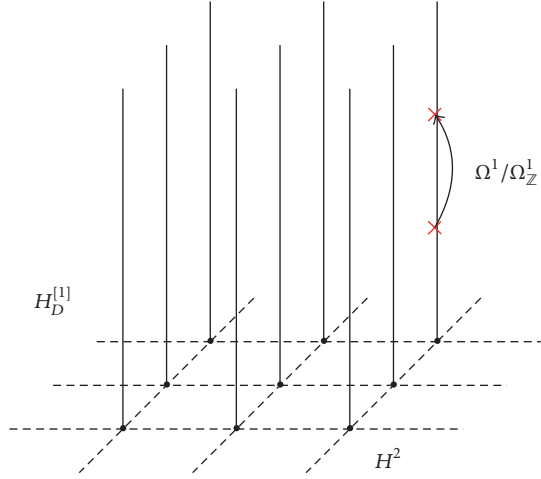


FIGURE 1

Those two exact sequences contain the same information.

$$\begin{array}{ccccccc}
 0 & \longrightarrow & \frac{\Omega^1}{\Omega_{\mathbb{Z}}^1} & \longrightarrow & H_D^{[1]} & \longrightarrow & H^2 \longrightarrow 0 \\
 & & \parallel & & \parallel & & \\
 & & \left(\frac{\Omega_0^1}{\Omega_{\mathbb{Z}}^1} \times \frac{\Omega^1}{\Omega_0^1} \right) & & T^2 \times F^2 & & \\
 & & \left(\frac{\Omega_0^1}{\Omega_{\mathbb{Z}}^1} \times T^2 \right) & & \left(\frac{\Omega^1}{\Omega_0^1} \times F^2 \right) & & \\
 & & \parallel & & \parallel & & \\
 0 & \longrightarrow & H^1 \left(\frac{\mathbb{R}}{\mathbb{Z}} \right) & \longrightarrow & H_D^{[1]} & \longrightarrow & \Omega_{\mathbb{Z}}^2 \longrightarrow 0
 \end{array} \quad (13)$$

4. Operations and Duality on Deligne Cohomology Classes

Given two Deligne cohomology classes A and B with respective representatives $(A_\alpha, \Lambda_{\alpha\beta}, n_{\alpha\beta\gamma})$ and $(B_\alpha, \Theta_{\alpha\beta}, m_{\alpha\beta\gamma})$, we define a Deligne cohomology class $A \star B$ with representative:

$$(A_\alpha \wedge dB_\alpha, \Lambda_{\alpha\beta} B_\beta, n_{\alpha\beta\gamma} B_\gamma, n_{\alpha\beta\gamma} \Theta_{\gamma\rho}, n_{\alpha\beta\gamma} m_{\gamma\rho\sigma}). \quad (14)$$

The integral of a Deligne cohomology class A with representative $(A_\alpha, \Lambda_{\alpha\beta}, n_{\alpha\beta\gamma})$ over a cycle z is defined by

$$\oint_z A \stackrel{=}{=} \sum_\alpha \int_{z_\alpha = U_\alpha \cap z} A_\alpha - \sum_{\alpha\beta} \int_{z_{\alpha\beta} = U_{\alpha\beta} \cap z} \Lambda_{\alpha\beta}, \quad (15)$$

where $\stackrel{=}{=}$ means that the equality is satisfied in \mathbb{R}/\mathbb{Z} , that is, up to an integer. This integral is nothing but a holonomy, that is, a typical observable of Chern-Simons and BF quantum field theories. This definition ensures gauge invariance in the sense described in the introduction.

We can define in the same way the integral over M of $A \star B$ which provides a generalization of Chern-Simons and BF abelian actions:

$$\begin{aligned}
 \int_M A \star B \stackrel{=}{=} & \sum_\alpha \int_{U_\alpha} A_\alpha \wedge dB_\alpha - \sum_{\alpha\beta} \int_{U_{\alpha\beta}} \Lambda_{\alpha\beta} B_\beta \\
 & + \sum_{\alpha\beta\gamma} \int_{U_{\alpha\beta\gamma}} n_{\alpha\beta\gamma} B_\gamma - \sum_{\alpha\beta\gamma\delta} \int_{U_{\alpha\beta\gamma\delta}} n_{\alpha\beta\gamma} \Theta_{\gamma\rho}.
 \end{aligned} \quad (16)$$

Let us point out that the first term is nothing but the local classical action, the other terms ensuring the gluing of local expressions up to an integer.

Note that

$$\begin{aligned}
 Z_1 \times H_D^{[1]} & \longrightarrow \frac{\mathbb{R}}{\mathbb{Z}} \\
 (z, A) & \longmapsto \oint_z A
 \end{aligned} \quad (17)$$

defines a bilinear pairing from the space Z_1 of 1 cycle and the space of Deligne cohomology classes (both considered as \mathbb{Z} -moduli) in \mathbb{R}/\mathbb{Z} as well as

$$\begin{aligned}
 H_D^{[1]} \times H_D^{[1]} & \longrightarrow \frac{\mathbb{R}}{\mathbb{Z}} \\
 (A, B) & \longmapsto \int_M A \star B.
 \end{aligned} \quad (18)$$

Starting from that remark and for later convenience, we will consider Pontrjagin dual $(X)^\# = \text{Hom}(X, \mathbb{R}/\mathbb{Z})$ of a group X . Considering Hom as a functor, we can show that the following sequences are exact:

$$\begin{aligned}
 0 & \longrightarrow (\Omega_{\mathbb{Z}}^2)^\# \longrightarrow (H_D^{[1]})^\# \longrightarrow \left(H^1 \left(\frac{\mathbb{R}}{\mathbb{Z}} \right) \right)^\# \longrightarrow 0, \\
 0 & \longrightarrow (H^2)^\# \longrightarrow (H_D^{[1]})^\# \longrightarrow \left(\frac{\Omega^1}{\Omega_{\mathbb{Z}}^1} \right)^\# \longrightarrow 0.
 \end{aligned} \quad (19)$$

Moreover, the information of the first two exact sequences is included in those two new ones.

$$\begin{array}{ccccccc}
 0 & \longrightarrow & \frac{\Omega^1}{\Omega_{\mathbb{Z}}^1} & \longrightarrow & H_D^{[1]} & \longrightarrow & H^2 \longrightarrow 0 \\
 & & \cap & & \cap & & \parallel \\
 0 & \longrightarrow & (\Omega_{\mathbb{Z}}^2)^\# & \longrightarrow & (H_D^{[1]})^\# & \longrightarrow & \left(H^1 \left(\frac{\mathbb{R}}{\mathbb{Z}} \right) \right)^\# \longrightarrow 0 \\
 & & & & & & \parallel \\
 0 & \longrightarrow & H^1 \left(\frac{\mathbb{R}}{\mathbb{Z}} \right) & \longrightarrow & H_D^{[1]} & \longrightarrow & \Omega_{\mathbb{Z}}^2 \longrightarrow 0 \\
 & & \parallel & & \cap & & \cap \\
 0 & \longrightarrow & (H^2)^\# & \longrightarrow & (H_D^{[1]})^\# & \longrightarrow & \left(\frac{\Omega^1}{\Omega_{\mathbb{Z}}^1} \right)^\# \longrightarrow 0
 \end{array} \quad (20)$$

The Pontrjagin dual is a generalization to distributional objects. Finally, we see that $Z_1 \subset (H_D^{[1]})^\#$ in the sense of (17).

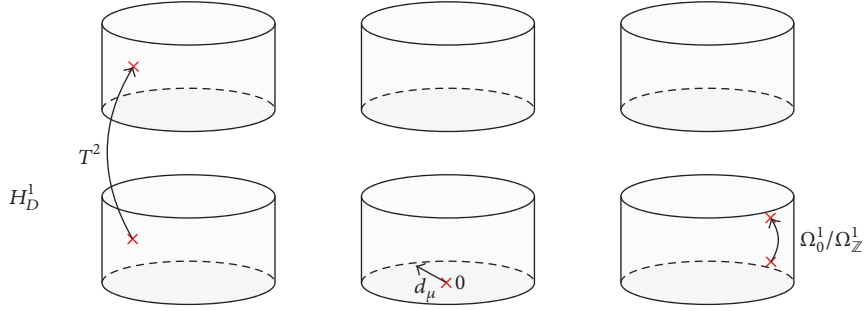


FIGURE 2

5. Decomposition of Deligne Cohomology Classes

The structure of Deligne cohomology classes is such that each class A can be decomposed as the sum of an origin indexed on the cohomology of M (basis of the discrete fibre bundle of Deligne cohomology classes) and a translation taken in $\Omega^1/\Omega_{\mathbb{Z}}^1$:

$$A = A_{\mathbf{a}}^0 + \omega, \quad \mathbf{a} \in H^2(\mathbb{Z}). \quad (21)$$

The result of functional integrals over the space of Deligne cohomology classes will not depend on the choice of the origins, but the complexity of the computations will. Thus, our goal is to find convenient origins with algebraic properties that will enable performing computations easily.

Concerning the translations, we can decompose (non-canonically) $\Omega^1/\Omega_{\mathbb{Z}}^1$ as

$$\frac{\Omega^1}{\Omega_{\mathbb{Z}}^1} \simeq \frac{\Omega^1}{\Omega_0^1} \times \frac{\Omega_0^1}{\Omega_{\mathbb{Z}}^1}, \quad (22)$$

where Ω_0^1 denotes the set of closed 1 form. Furthermore

$$\frac{\Omega_0^1}{\Omega_{\mathbb{Z}}^1} \simeq \left(\frac{\mathbb{R}}{\mathbb{Z}} \right)^{b_1}, \quad (23)$$

b_1 being the first Betti number. We will call *zero modes* the elements $\omega_0 \in \Omega_0^1/\Omega_{\mathbb{Z}}^1$. With this decomposition, we obtain

$$\forall \omega_0 \in \frac{\Omega_0^1}{\Omega_{\mathbb{Z}}^1}, \quad \forall \omega \in \frac{\Omega^1}{\Omega_{\mathbb{Z}}^1}, \quad \int_M \omega * \omega_0 \stackrel{\mathbb{Z}}{=} 0. \quad (24)$$

Let us consider generators z_a of the free part of the homology of M . Then, by Pontrjagin duality, we can associate to it a unique element $\eta_{z_a} \in (H_D^{[1]})^{\#}$. Thus, for a fibre over $\sum_a m^a z_a \in F_1 \simeq F^2$ we will consider as origin the element

$$A_{\mathbf{m}} = \sum_a m^a \eta_{z_a} \in (H_D^{[1]})^{\#}. \quad (25)$$

Note that

$$\int_M A_{\mathbf{m}} * A_{\mathbf{n}} \stackrel{\mathbb{Z}}{=} 0 \quad (26)$$

since it represents a linking number which is necessarily an integer. We impose as a convention the so-called *zero regularisation*:

$$\int_M A_{\mathbf{m}} * A_{\mathbf{m}} \stackrel{\mathbb{Z}}{=} 0 \quad (27)$$

which is ill-defined as self-linking. Finally, if we decompose $\omega_0 \in \Omega_0^1/\Omega_{\mathbb{Z}}^1$ as $\omega_0 = \sum_b \theta_b \rho^b$ with $\oint_{z_a} \rho^b = \delta_a^b$, then we obtain

$$\int_M A_{\mathbf{m}} * \omega_0 \stackrel{\mathbb{Z}}{=} \mathbf{m} \cdot \boldsymbol{\theta}. \quad (28)$$

Let us consider now a generator τ_a of the component \mathbb{Z}_{p_a} of the torsion part of the homology of M . This means that τ_a is the boundary of no surface, but $p_a \tau_a$ is. Consider now $\eta_{\tau_a} \in (H_D^{[1]})^{\#}$ defined by

$$\eta_{\tau_a} = \left(0, \frac{m_{\alpha\beta}}{p_a}, n_{\alpha\beta\gamma} \right), \quad (29)$$

where $p_a n_{\alpha\beta\gamma} = m_{\beta\gamma} - m_{\alpha\gamma} + m_{\alpha\beta}$. Thus, for a fibre over $\sum_a \kappa^a \tau_a \in T_1 \simeq T^2$ we will consider as origin the element

$$A_{\boldsymbol{\kappa}}^0 = \sum_a \kappa^a \eta_{\tau_a} \in (H_D^{[1]})^{\#}. \quad (30)$$

This choice has several advantages since we can show that

$$\int_M A_{\boldsymbol{\kappa}_1}^0 * A_{\boldsymbol{\kappa}_2}^0 \stackrel{\mathbb{Z}}{=} -Q(\boldsymbol{\kappa}_1, \boldsymbol{\kappa}_2), \quad (31)$$

where Q is the so-called linking form, which is a quadratic form over the torsion of the cohomology. Also

$$\int_M A_{\boldsymbol{\kappa}}^0 * A_{\mathbf{m}} \stackrel{\mathbb{Z}}{=} 0 \quad (32)$$

for any free origin $A_{\mathbf{m}}$ and

$$\int_M A_{\boldsymbol{\kappa}}^0 * \omega \stackrel{\mathbb{Z}}{=} 0 \quad (33)$$

for any translation ω .

6. $U(1)$ Chern-Simons and BF Theories

Chern-Simons abelian action is generalized as

$$S_{CS_N} [A] = 2\pi N \int_M A \star A. \quad (34)$$

Since $\int_M A \star A \in \mathbb{R}/\mathbb{Z}$, then N has to be quantized here:

$$N \in \mathbb{Z}. \quad (35)$$

The partition function is defined as

$$Z_{CS_N} = \frac{1}{\mathcal{N}_{CS_N}} \int_{(H_D^{[1]})^\#} e^{iS_{CS_N}[A]} \mathcal{D}A, \quad (36)$$

\mathcal{N}_{CS_N} being a normalization that has to cancel the intrinsic divergence of the functional integral. The functional measure we use is then

$$d\mu_{CS_N} [A] = \mathcal{D}A e^{iS_{CS_N}[A]}. \quad (37)$$

Assume that this measure verifies the so-called Cameron-Martin property; that is,

$$d\mu_{CS_N} [A + \omega] = d\mu_{CS_N} [A] e^{4i\pi N \int_M A \star \omega} e^{2i\pi N \int_M \omega \star \omega} \quad (38)$$

for a fixed connection A and a translation ω , then, for j_γ a translation in $(H_D^{[1]})^\#$ associated with a cycle γ :

$$d\mu_{CS_N} \left[A + m \frac{j_\gamma}{2N} \right] = d\mu_{CS_N} [A]. \quad (39)$$

Using the algebraic properties given before, we can compute exactly the Chern-Simons abelian partition function.

As a convention, for the normalization we choose

$$\mathcal{N}_{CS_N} = \int_{(\Omega^1/\Omega_2^1)^\#} e^{iS_{CS_N}[\omega]} \mathcal{D}\omega = \int_{(\Omega^1/\Omega_0^1)^\#} e^{iS_{CS_N}[\omega]} \mathcal{D}\omega \quad (40)$$

which corresponds to the trivial fibre of Deligne bundle for our theory defined over a manifold M . This trivial fibre is the (only) one that constitutes Deligne bundle if we consider a theory over S^3 . This choice enables establishing a link with Reshetikhin-Turaev abelian invariant (see [1]). Note that usually the normalization of Reshetikhin-Turaev invariant is chosen to be related to $S^1 \times S^2$. However if the normalization is done with respect to S^3 then one recovers in the abelian case the invariants obtained with convention (40).

This way, we find

$$Z_{CS_N} = \sum_{\tau_A \in T^2} e^{-2i\pi N Q(\tau_A, \tau_A)}. \quad (41)$$

Analogous considerations apply to BF abelian theory whose generalized action is

$$S_{BF_N} [A, B] = 2\pi N \int_M A \star B \quad (42)$$

(N being here also quantized) which leads to a partition function written as

$$Z_{BF_N} = \sum_{\tau_A \in T^2} \sum_{\tau_B \in T^2} e^{-2i\pi N Q(\tau_A, \tau_B)} = \prod_{i=1}^n \text{gcd}(p_i, N) p_i. \quad (43)$$

Computations of expectation values of observables can also be performed thanks to this method in both Chern-Simons and BF abelian theories (see [1, 2]).

7. Conclusion

Several correspondences in the nonabelian case, mainly $SU(2)$, have been established formally, that is, with manipulations of ill-defined quantities:

- (1) Chern-Simons partition function is related to Reshetikhin-Turaev topological invariant [3].
- (2) BF partition function is related to Turaev-Viro topological invariant [4].
- (3) The square modulus of Chern-Simons partition function is equal to the BF partition function [5].

This is summed up on the following diagram:

$$\begin{array}{ccc} |Z_{CS_N}|^2 & \overset{\text{Cattaneo}}{\dots\dots} & Z_{BF_N} \\ \text{Witten} & \vdots & \vdots \\ & & \text{Ponzano, Regge} \dots \end{array} \quad (44)$$

$$\begin{array}{ccc} |RT_N|^2 & = & TV_N \\ & \underset{\text{Turaev}}{} & \end{array}$$

the only result perfectly rigorously established being the one of Turaev, Reshetikhin, and Viro (see [6–8]).

In the abelian case, we saw that Deligne cohomology approach enables defining rigorously functional integration in the specific case of Chern-Simons and BF theories. Using this tool, we show that the previous diagram is no longer correct and has to be replaced by the following one:

$$\begin{array}{ccc} |Z_{CS_N}|^2 & \overset{\text{Thuillier \& M.}}{\neq} & Z_{BF_N} \\ \text{Guadagnini \& Thuillier} & \parallel & \parallel \\ & & \text{Thuillier \& M.} \end{array} \quad (45)$$

$$\begin{array}{ccc} |RT_N|^2 & \neq & TV_N, \end{array}$$

where the hypothesis of Turaev are not necessarily satisfied with abelian representations, leading to an inequality in general.

This shows that the abelian theories, contrary to what could be expected, are not a simple trivial subcase of the

nonabelian ones. However, we expect to find some traces of this abelian case in the nonabelian one, which is the aim of present works.

Conflicts of Interest

The author declares that there are no conflicts of interest regarding the publication of this paper.

References

- [1] P. Mathieu and F. Thuillier, “Abelian BF theory and Turaev-Viro invariant,” *Journal of Mathematical Physics*, vol. 57, no. 2, Article ID 022306, 31 pages, 2016.
- [2] P. Mathieu and F. Thuillier, “A reciprocity formula from abelian BF and Turaev-Viro theories,” *Nuclear Physics. B. Theoretical, Phenomenological, and Experimental High Energy Physics. Quantum Field Theory and Statistical Systems*, vol. 912, pp. 327–353, 2016.
- [3] E. Witten, “Quantum field theory and the Jones polynomial,” *Communications in Mathematical Physics*, vol. 121, no. 3, pp. 351–399, 1989.
- [4] G. Ponzano and T. Regge, “Semiclassical limit of Racah coefficients,” in *Spectroscopic and Group Theoretical Methods in Physics*, F. Bloch, Ed., pp. 1–58, North-Holland Publishing Company, Amsterdam, The Netherlands, 1968.
- [5] A. S. Cattaneo, P. Cotta-Ramusino, J. Fröhlich, and M. Martellini, “Topological BF theories in 3 and 4 dimensions,” *Journal of Mathematical Physics*, vol. 36, no. 11, pp. 6137–6160, 1995.
- [6] N. Y. Reshetikhin and V. G. Turaev, “Ribbon graphs and their invariants derived from quantum groups,” *Communications in Mathematical Physics*, vol. 127, no. 1, pp. 1–26, 1990.
- [7] V. G. Turaev and O. Y. Viro, “State sum invariants of 3-manifolds and quantum 6j-symbols,” *Topology. An International Journal of Mathematics*, vol. 31, no. 4, pp. 865–902, 1992.
- [8] V. G. Turaev, *Quantum Invariants of Knots and 3-Manifolds*, vol. 10 of *De Gruyter Studies in Mathematics*, Walter de Gruyter, Berlin, Germany, 2010.

Research Article

Charges and Electromagnetic Radiation as Topological Excitations

Manfried Faber

Atominstytut, Technische Universität Wien, Österreich, Austria

Correspondence should be addressed to Manfried Faber; faber@kph.tuwien.ac.at

Received 11 May 2017; Accepted 4 July 2017; Published 22 August 2017

Academic Editor: Ralf Hofmann

Copyright © 2017 Manfried Faber. This is an open access article distributed under the Creative Commons Attribution License, which permits unrestricted use, distribution, and reproduction in any medium, provided the original work is properly cited. The publication of this article was funded by SCOAP³.

We discuss a model with stable topological solitons in Minkowski space with only three degrees of freedom, the rotational angles of a spatial Dreibein. This model has four types of solitons differing in two topological quantum numbers which we identify with electric charge and spin. The vacuum has a two-dimensional degeneracy leading to two types of massless excitations, characterised by a topological quantum number which could have a physical equivalent in the photon number.

1. Introduction

In our mathematical description of nature we use two different concepts. Following Einstein we formulate gravity in a geometrical language, whereas particle physics uses the algebraic formulae of quantum field theory. To unify the two very successful theories most physicists try quantized gravity. I go here into the opposite direction and follow first steps in a geometrical formulation of particle physics. We should find out from experiments the direction which we should take in our investigations. Nature may give us some hints about the mechanisms. I get my first intuition from the sine-Gordon model and its experimental realisation with a pendulum model. The mathematics of the sine-Gordon model is nicely described in [1]. Here I want only to repeat the most interesting physical pictures of this model. It is a fully relativistic model in $1 + 1D$, where the velocity of light corresponds to the propagation velocity c of small amplitude waves. In the experimental realisation (see [1]), this velocity is of the order of 1 m/s . Besides waves, we find two types of particle-like excitations, kinks, and antikinks. They behave in many ways like particles. Their energy density is concentrated in a certain region in space with a total energy defining the mass. The three contributions to the energy, stress energy, potential energy, and kinetic energy have different dependencies on the velocity v of a moving kink. The potential energy is decreasing; stress energy and kinetic energy are increasing with v .

As expected for a relativistic model, the three contributions nicely sum up to a mass increasing with $\gamma = 1/\sqrt{1 - (v/c)^2}$. A moving kink is Lorentz contracted. In the mechanical model, we can easily imagine what nature does to decrease the size of the kink. To accelerate the pendula at the front of the kink the angle between them has to increase, leading to a smaller size of the kink. The pendulum model gives me some idea on how nature could work to realise the phenomena of special relativity. Even more impressive is the existence of two types of kinks, kinks and antikinks and their interaction. They behave like charged particles: kinks and kinks repel; kinks and antikinks attract each other. In soft collisions kinks behave similarly to billiard balls. In hard collisions the diameters of kinks shrink proportional to $1/\gamma$ and get point-like. Further, we can observe how kinks and antikinks annihilate. In the mechanical model the annihilation due to friction effects gives rise to the emission of waves. In the abstract theoretical model solitons and antisolitons get through each other with a small time delay. Mathematically we can separate the various kink configurations in homotopy classes differing in their winding number. This is condensed in the relation $\Pi_1(\mathbb{S}^1) = \mathbb{Z}$ of homotopy theory.

I get a second hint from a simple model teaching us about the nature of 4π -rotations. I saw it for the first time in Figure 41.6 on page 1149 of “Gravitation” by Misner et al. [2]. A ball is attached with several wires to the surrounding, for example,

with eight wires to the corners of a cube. Rotating the ball one or two times around some axis leads to a complete mess of the strings. But after a 4π -rotation one can disentangle the wires without moving the ball. We can learn from this model that a body which is connected to the surrounding returns only after a 4π -rotation to his original state. For a disconnected body this happens already after a 2π -rotation. This is mathematically formulated in the relation $\Pi_1(\mathbb{S}^3) = 1$. There is a continuous transition between 4π -rotations and no rotation. This ball model gives me a hint on how possibly nature realises particles with spin 1/2 just by connecting them with the surrounding.

Thirdly, I want to mention that, observing phenomena at and below the atomic scale, we always observe particles or clicks and never waves. Remember the double-slit experiment. In this interference experiment of electrons or photons, the wave-picture appears only after several hundreds or thousands of particles have been registered on the screen.

In the main part of this article, I describe a Lorentz covariant model which has stable topological excitations with properties of particles. In a certain sense, it is a generalisation of the sine-Gordon model to 3 + 1D. Several features of this model were already described in a few articles [3–8]. In this article, I will mainly concentrate on topological questions.

2. Definition of the Model

We are using a scalar $\text{SO}(3)$ -field in 3 + 1D Minkowski space. The only degrees of freedom of this model are therefore three rotational angles, for example, the three Euler angles, describing the rotations of a spatial Dreibein. Work with $\text{SU}(2)$ is simpler than using $\text{SO}(3)$ -matrices, that is, with 2×2 -matrices. Since $\text{SU}(2)$ is the double covering group of $\text{SO}(3)$ there is an essential difference between $\text{SU}(2)$ - and $\text{SO}(3)$ -fields. Every field configuration of an $\text{SO}(3)$ -field is twice realised by $\text{SU}(2)$ -fields. The two realisations differ by a transformation with the nontrivial center element, by a 2π -rotation. We have to remember this property using $\text{SU}(2)$ -matrices:

$$Q(x) = e^{-i\alpha(x)\vec{\sigma}\vec{n}(x)} = \cos \alpha(x) - i\vec{\sigma}\vec{n}(x) \sin \alpha(x), \quad (1)$$

at every site x in M_4 . The symbol Q we are using reminds us of quaternions, invented by Rodrigues [9] in the year 1840, to describe active rotations with the three imaginary quaternionic units $\mathbf{i}, \mathbf{j}, \mathbf{k}$. In (1), they are represented by Pauli matrices $\mathbf{i} := -i\sigma_1$, $\mathbf{j} := -i\sigma_2$, $\mathbf{k} := -i\sigma_3$. \vec{n} is a three-component unit vector and $\vec{\sigma}\vec{n} := \sum_{i=1}^3 \sigma_i n_i$ is the component of the Pauli matrices in direction of \vec{n} . Rotations are unit quaternions $Q = q_0 - i\vec{\sigma}\vec{q}$ with $q_0^2 + \vec{q}^2 = 1$. Their manifold is isomorphic to \mathbb{S}^3 .

The idea for the definition of the dynamical part of the Lagrangian is its identification with the square of the area density on \mathbb{S}^3 in appropriate units of an action density. We start defining tangential vectors:

$$\partial_\mu Q := -i\vec{\sigma}\vec{\Gamma}_\mu Q \quad \text{with} \quad \vec{\sigma}\vec{\Gamma}_\mu := \sum_{i=1}^3 \sigma_i \Gamma_{\mu i}, \quad (2)$$

(tangential one-forms) to \mathbb{S}^3 . We would like to emphasise that $\vec{A}_\mu = 2\vec{\Gamma}_\mu$ is a trivial connection but $\vec{\Gamma}_\mu$ is not. With the cross-product $\vec{R}_{\mu\nu} := \vec{\Gamma}_\mu \times \vec{\Gamma}_\nu$ we can get the square of the area density $\vec{R}_{\mu\nu}\vec{R}^{\mu\nu}$ and define the Lagrangian in appropriate SI-units with $\alpha_f := e_0^2/4\pi\epsilon_0\hbar c$:

$$\begin{aligned} \mathcal{L} &:= \mathcal{L}_{\text{dyn}} - \mathcal{H}_{\text{pot}} := -\frac{\alpha_f \hbar c}{4\pi} \left(\frac{1}{4} \vec{R}_{\mu\nu} \vec{R}^{\mu\nu} + \Lambda(q_0) \right) \\ \vec{R}_{\mu\nu} &:= \vec{\Gamma}_\mu \times \vec{\Gamma}_\nu, \\ \vec{\Gamma}_\mu &\stackrel{(2)}{=} \frac{i}{2} \text{Sp}(\vec{\sigma} \partial_\mu Q Q^\dagger). \end{aligned} \quad (3)$$

Up to a proportionality factor, the kinetic term \mathcal{L}_{dyn} of this model agrees with the Skyrme term in the Skyrme model [10]. To get stable solitons, Skyrme suggested to use a mass term for the vector field $\vec{\Gamma}_\mu$ leading to Skyrmons with short-range forces which are accepted as approximations for nucleons. We want to describe particles with long-range Coulombic forces and have therefore to avoid the Skyrme term. The Hobart-Derrick theorem [11, 12] allows as additional terms only terms without derivative, a potential term, which we chose as

$$\Lambda(q_0) = q_0^{2m}. \quad (4)$$

Therefore, we have a two-dimensional manifold of degenerate vacua; the equatorial sphere $\mathbb{S}_{\text{equ}}^2$ is defined by $q_0 = 0$. The choice of the potential term (4) has two immediate physical consequences. There are two Goldstone bosons which we can identify with the two photon degrees of freedom. Further, we get nontrivial field configurations of finite energy which can be classified by $\Pi_2(\mathbb{S}_{\text{equ}}^2) = \mathbb{Z}$, by the map of $\mathbb{S}_{\text{equ}}^2$ to the sphere \mathbb{S}_∞^2 at spatial infinity.

3. Stable Solitons of Finite Energy

Inserting the time-independent hedgehog ansatz

$$\begin{aligned} q_0 &= \cos \alpha(r), \\ \vec{q} &= \vec{n}(r) \sin \alpha(r), \\ \vec{n}(r) &= \frac{\vec{r}}{r}, \\ \alpha(r) &\in \left[0, \frac{\pi}{2} \right] \end{aligned} \quad (5)$$

into Lagrangian (3), we get the Euler-Lagrange equation:

$$\partial_\rho^2 \cos \alpha + \frac{(1 - \cos^2 \alpha) \cos \alpha}{\rho^2} - m\rho^2 \cos^{2m-1} \alpha = 0 \quad (6)$$

with $\rho = \frac{r}{r_0}$,

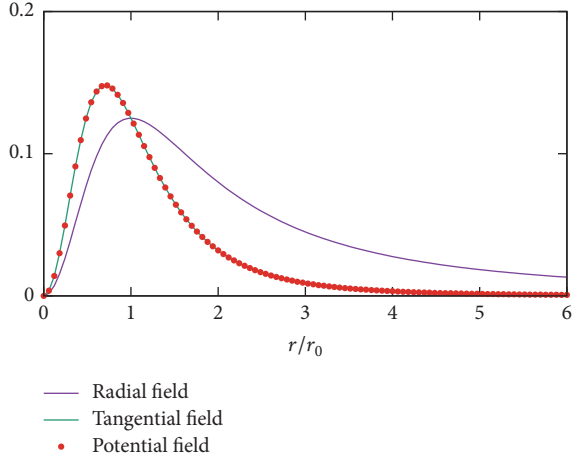


FIGURE 1: Contributions to the radial energy density according to (8) in units of $\alpha_f \hbar c / r_0$.

a nonlinear differential equation, which we can most easily solve for $m = 3$. It has the simple solution

$$\begin{aligned} \alpha(r) &= \arctan \rho, \\ \sin \alpha(r) &= \frac{\rho}{\sqrt{1 + \rho^2}}, \\ \cos \alpha(r) &= \frac{1}{\sqrt{1 + \rho^2}}. \end{aligned} \quad (7)$$

leading to the radial energy density:

$$h = \frac{\alpha_f \hbar c}{r_0} \left[\frac{\rho^2}{2(1 + \rho^2)^2} + \frac{\rho^2}{(1 + \rho^2)^3} + \frac{\rho^2}{(1 + \rho^2)^3} \right]. \quad (8)$$

The radial dependencies of its three contributions are shown in Figure 1. At large distances the radial energy density agrees with the Coulombic energy density of a point charge. As one can clearly see, the singularity at the origin that point-charges usually are suffering from is removed. The tangential and the potential energy density have equal shapes and decay faster. They lead to a deviation from the Coulomb interaction at distances in the order of r_0 and smaller. The total energy sums up to $E = (\alpha_f \hbar c / r_0)(\pi/4)$. Comparing this result with the rest energy of an electron we get a value for the scale r_0 of 2.21 fm.

The hedgehog configuration, defined in (5), is schematically depicted in the upper diagram of Figure 2. It maps \mathbb{R}^3 to half of \mathbb{S}^3 . This half-sphere is indicated in the lower diagram of Figure 2. By the electric field, the hedgehog is wired to the surrounding. If the center of the hedgehog is rotated by 4π , the tangled lines of constant \vec{n} -field can be disentangled without further rotation of the center, and the original configuration can get restored. This behaviour reminds us of the rotational property of spin-1/2 particles.

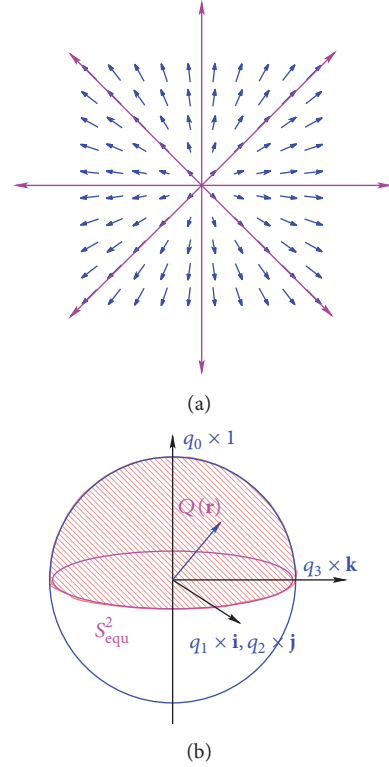


FIGURE 2: (a) Scheme of the hedgehog configuration (5). The small blue arrows show the imaginary part $\vec{q} = \vec{n}(\mathbf{r}) \sin \alpha(r)$ of the Q-field in an arbitrary plane through the origin. The long magenta lines indicate the electric field lines of a point charge, the lines of constant \vec{n} -field. (b) Half-sphere covered by the hedgehog configuration.

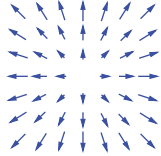
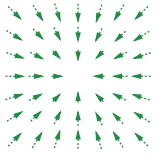
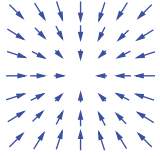
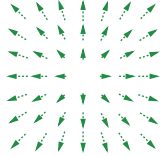
4. Topological Quantum Numbers

We can find a further relation to spin in the number of coverings of \mathbb{S}^3 , the topological charge \mathcal{Q} which we define in spherical coordinates r, ϑ, φ by

$$\mathcal{Q} := \frac{1}{2\pi^2} \int_0^\infty dr \int_0^\pi d\vartheta \int_0^{2\pi} d\varphi \vec{\Gamma}_r \cdot (\vec{\Gamma}_\vartheta \times \vec{\Gamma}_\varphi). \quad (9)$$

The configuration of (5) and Figure 2 results in $\mathcal{Q} = 1/2$. Continuous modifications of the soliton field do not change \mathcal{Q} and the homotopy class of the configuration. The homotopy class can be changed by parity transformations $\Pi_n : \vec{n} \mapsto -\vec{n}$ in the internal space and by transformations with the nontrivial center element $z = -1$. The four types of solitons which we get by these transformations are shown in Table 1. Q-values with $q_0 \geq 0$ are indicated by full blue arrows and with $q_0 \leq 0$ by dashed green arrows. Besides the topological charge, the four configurations differ in the direction of the rotational axis of the Q-field at infinity which we will relate in (16)–(18) with the electric charge Q_{el} . This field at large distances from the center determines the interaction with other solitons, attraction, or repulsion. The pairs of configurations with the same electric charge differ in the value $\pm 1/2$ of the topological charge, in the chirality. We can combine pairs of solitons with $\mathcal{Q} = \pm 1/2$ either to

TABLE 1: Soliton types differ by transformations with Π_n and z . The signs of \vec{n} and q_0 and the topological quantum numbers Q_{el} and \mathcal{Q} are quoted. The configurations are spherically symmetric.

Transf.	1	z	Π_n	$z\Pi_n$
\vec{n}	\vec{r}/r	$-\vec{r}/r$	$-\vec{r}/r$	\vec{r}/r
q_0	≥ 0	≤ 0	≥ 0	≤ 0
Q_{el}	-1	1	1	-1
\mathcal{Q}	1/2	1/2	-1/2	-1/2
Diagram				

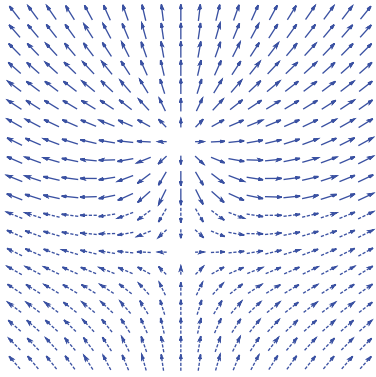


FIGURE 3: Dipole configuration with $S = 1$. The small blue arrows show the imaginary part $\vec{q} = \vec{n}(\mathbf{r}) \sin \alpha(r)$ of the Q -field in an arbitrary plane through the centers of both solitons. Full arrows correspond to $q_0 \leq 0$ and dashed arrows to $q_0 \geq 0$.

$\mathcal{Q} = 0$ or to $\mathcal{Q} = \pm 1$. Since $SU(2)$ is the spin group and due to the above described properties of the soliton configurations under 4π rotations we dare to identify the absolute value of the topological charge with the spin quantum number:

$$s = |\mathcal{Q}|. \quad (10)$$

We would like to remember that, within $SO(3)$, the two configurations which differ in the sign of \mathcal{Q} are identical.

Traversing the center of a soliton we follow a rotation of the local Dreibeins by $\pm 2\pi$. This may answer a question, posed by Tsung-Dao Lee in a talk given in Vienna in the 1980s: “why does the mass break chiral symmetry?”

Besides its group theoretical properties, spin is a contribution to the total angular momentum. We will investigate these angular momentum properties in a dipole configuration. Since a dipole is uncharged, the field at infinity is independent of the direction, it approaches, for example, $\lim_{r \rightarrow \infty} Q(\mathbf{r}) = -i\sigma_3$. The symmetry of the vacuum is broken. We can combine the first configuration in Table 1 with the second to total spin $S = 1$ or with the third to $S = 0$. The energy for $S = 0$ is slightly lower than that for $S = 1$, the configuration shown in Figure 3. During a rotation of the dipole, the vacuum has to remain unchanged; a rigid rotation is not possible. If the dipole axis is rotated, for example, by

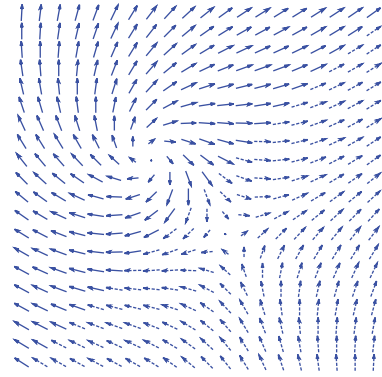


FIGURE 4: Configuration of Figure 3, after rotation by $\pi/4$.

$\pi/4$, as shown in Figure 4, the centers of the solitons have to rotate by the same angle. These rotations contribute to the total angular momentum.

Dipole configurations are not stable due to the attractive interaction between the charges. Their time evolution follows the general equations of motion [3]:

$$\partial_\mu \left[\vec{\Gamma}_\nu \times \vec{R}^{\mu\nu} \right] + \vec{q} \frac{d\Lambda}{dq_0} = 0 \quad (11)$$

derived from the Lagrangian (3). The energy-momentum tensor

$$\Theta^\mu{}_\nu = -\frac{\alpha_f \hbar c}{4\pi} \left\{ \left(\vec{\Gamma}_\nu \times \vec{\Gamma}_\sigma \right) \left(\vec{\Gamma}^\mu \times \vec{\Gamma}^\sigma \right) \right\} - \mathcal{L}(x) \delta^\mu{}_\nu \quad (12)$$

turns out to be symmetric. There is no special symmetrisation necessary as in Maxwell’s electrodynamics [13]. Since there are no external forces, the force density is vanishing:

$$f_\nu = \partial_\mu \Theta^\mu{}_\nu = 0. \quad (13)$$

To determine a static potential one has to fix the positions of the centers at a chosen distance d . For distances $d \gg r_0$ the Coulombic behaviour is nicely reproduced, as can be seen in the diploma theses [14–16]. For distances $d \lesssim r_0$ the interaction strength increases.

5. Electrodynamic Limit

One gets a pure Coulombic behaviour in the limit $r_0 \rightarrow 0$ where one arrives at the Wu and Yang description [17] of dual Dirac monopoles by two degrees of freedom which we can choose as a normalised three-dimensional vector field \vec{n} . In this limit, we get

$$\begin{aligned} Q(x) &= -i\vec{\sigma} \cdot \vec{n}(x), \\ \vec{\Gamma}_\mu(x) &\stackrel{(2)}{=} \vec{n}(x) \times \partial_\mu \vec{n}(x), \\ \vec{R}_{\mu\nu}(x) &\stackrel{(3)}{=} \partial_\mu \vec{n}(x) \times \partial_\nu \vec{n}(x). \end{aligned} \quad (14)$$

This is a description where the singularity of the Dirac string is removed, but the singularity of the Coulomb field is still present. The Lagrangian (3) reduces to (The same degrees of freedom but a different Lagrangian is used in the Fadeev-Niemi = Skyrme-Fadeev = Baby-Skyrme model [18–20]. The same Lagrangian was used in [21].)

$$\mathcal{L}_{\text{ED}} = -\frac{1}{4\mu_0} {}^*F_{\mu\nu}(x) {}^*F^{\mu\nu}(x) \quad (15)$$

with the dual field strength tensor

$$\begin{aligned} {}^*F_{\mu\nu}(x) &= -\frac{e_0}{4\pi\epsilon_0 c} \vec{R}_{\mu\nu} \cdot \vec{n} \\ &= -\frac{e_0}{4\pi\epsilon_0 c} \vec{n}(x) \cdot [\partial_\mu \vec{n}(x) \times \partial_\nu \vec{n}(x)]. \end{aligned} \quad (16)$$

In this limit hedgehogs are characterised by point-like singularities in space and closed world-lines of line-like singularities in space-time:

$$j^\mu = -e_0 c \sum_{i=1}^N \int d\tau_i \frac{dX^\mu(\tau_i)}{d\tau_i} \delta^4(x - X(\tau_i)) = (c\rho, \mathbf{j}). \quad (17)$$

Charges and fields are related by the inhomogeneous Maxwell equations:

$$\frac{1}{2\mu_0} \oint_{\partial V} dx^\mu dx^\nu {}^*F_{\mu\nu} = \frac{1}{6} \int_V dx^\mu dx^\nu dx^\rho \epsilon_{\mu\nu\rho\sigma} j^\sigma. \quad (18)$$

Already here we see an essential difference to Maxwell's theory. Charges are quantized; there are no other charges possible than integer multiples of the elementary charge e_0 . We get two further differences from the equations of motion:

$$\partial_\mu \vec{n} \cdot g^\mu = 0. \quad (19)$$

They allow for nonvanishing magnetic currents:

$$g^\mu = c\partial_\nu {}^*f^{\nu\mu} \iff \begin{cases} \rho_{\text{mag}} = \nabla \cdot \mathbf{B}, \\ \mathbf{g} = -\nabla \times \mathbf{E} - \partial_t \mathbf{B}. \end{cases} \quad (20)$$

The solutions of the homogeneous Maxwell equations fulfil the equations of motion (19). But there are further solutions possible which fulfil the relations:

$$\begin{aligned} \mathbf{B} \mathbf{g} &\stackrel{(19)}{=} 0, \\ c^2 \mathbf{B} \rho_{\text{mag}} &\stackrel{(19)}{=} \mathbf{g} \times \mathbf{E}, \end{aligned} \quad (21)$$

equivalent to the equations of motion (19). The presence of unquantized closed magnetic currents may be a discrepancy to experiments. But we could explain it with the observation, mentioned in the introduction, that in the experiment we only detect particles and never waves. We can speculate that such currents contribute to the recently intensively discussed dark matter. Further, we read from these equations that there are no solutions possible where \mathbf{E} and \mathbf{B} are parallel. This seems obviously also in contradiction to experiments, where it is rather simple to produce static parallel electric and magnetic fields. In this case it is more difficult to find an excuse. It could be that \mathbf{E} and \mathbf{B} are locally perpendicular and they appear to be parallel only in the average over space or time. This is the price to pay for restricting charges to integer multiples to the elementary charge and the fields to the two degrees of freedom of the \vec{n} -field.

6. Coulomb and Lorentz Forces

By the artificial splitting (16) of a single field $Q(x)$ in particles and their fields we reduce Θ^μ_ν to the symmetric energy-momentum tensor,

$$T^\mu_\nu(x) \stackrel{(12)}{=} -\frac{1}{\mu_0} {}^*F_{\nu\sigma}(x) {}^*F^{\mu\sigma}(x) - \mathcal{L}_{\text{ED}}(x) \delta^\mu_\nu, \quad (22)$$

and split the force density in two contributions

$$f_\nu = \partial_\mu \Theta^\mu_\nu = f_{\text{charges}}^\mu + \partial^\nu T^\mu_\nu \stackrel{(13)}{=} 0, \quad (23)$$

showing clearly the presence of Coulomb and Lorentz forces:

$$\begin{aligned} f_{\text{charges}}^0 &= \frac{1}{c} \mathbf{j} \cdot \mathbf{E}, \\ \mathbf{f}_{\text{charges}} &= \rho \mathbf{E} + \mathbf{j} \times \mathbf{B}. \end{aligned} \quad (24)$$

Here we would like to underline that the magnetic currents \mathbf{g} do not contribute to electromagnetic forces.

7. U(1) Gauge Invariance

A U(1) gauge invariance appears as a rotational invariance by $\omega(x)$ around the \vec{n} -axis. By a rotation in colour space with

$$\Omega(x) = e^{i\theta(x)\vec{e}_\phi(x)\vec{L}} e^{i\omega(x)\vec{n}\vec{L}}. \quad (25)$$

We can rotate the \vec{n} -field in 3-direction:

$$\vec{n} = \begin{pmatrix} \sin\theta \cos\phi \\ \sin\theta \sin\phi \\ \cos\theta \end{pmatrix} \longrightarrow \vec{n}' := \Omega \vec{n} = \begin{pmatrix} 0 \\ 0 \\ 1 \end{pmatrix} = \vec{e}_3. \quad (26)$$

Under this transformation the vector field $\vec{L} \vec{\Gamma}_\mu$ transforms to $\vec{L} \vec{\Gamma}'_\mu = \Omega(\Gamma_\mu - i\partial_\mu)\Omega^\dagger$ with

$$\vec{\Gamma}'_\mu = [(1 - \cos\theta)\partial_\mu\phi + \partial_\mu\omega] \vec{e}_3. \quad (27)$$

The curvature $\vec{R}_{\mu\nu}$ gets rotor form and turns out to be invariant against the rotations with $\omega(x)$:

$$\begin{aligned}\vec{R}_{\mu\nu} &= \partial_\mu \vec{\Gamma}'_\nu - \partial_\nu \vec{\Gamma}'_\mu \\ &= [-\partial_\mu \cos\theta \partial_\nu \phi + \partial_\nu \cos\theta \partial_\mu \phi] \vec{e}_3.\end{aligned}\quad (28)$$

The far field of a hedgehog soliton is the electric field strength of a classical electron and the vector field of a dual Dirac monopole:

$$\begin{aligned}\vec{E}'_r &= \frac{e_0}{4\pi\epsilon_0} \frac{\vec{e}_3}{r^2}, \\ \vec{\Gamma}'_\varphi(\vartheta) &= \frac{1 - \cos\vartheta}{r \sin\vartheta} \vec{e}_3\end{aligned}\quad (29)$$

with a Dirac string along the 3-direction.

8. Hopf Number

In Figure 2(a), we realised that the field lines of a point charge are lines of constant \vec{n} -field. We find also this relation for the dipole fields in Figures 3 and 4. Since in our model the vacuum has broken symmetry the field at infinity, “ ∞ ” is independent of the direction. Thus we get the isomorphism $\mathbb{R}^3 \cup \infty \sim \mathcal{S}^3$. Due to the topological relation $\pi_3(\mathcal{S}^2) = \mathbb{Z}$ there is an additional quantum number for the \vec{n} -field, the Hopf number, or Gauß linking number ν of fibres \mathcal{F} defined by $\vec{n}_{\mathcal{F}} = \text{const}$ and thus by certain values $\theta_{\mathcal{F}}$ and $\phi_{\mathcal{F}}$. This linking number is especially interesting in regions where we can neglect the influence of charges, in regions of pure \vec{n} -field, where the Lagrangian reduces to \mathcal{L}_{ED} of (16). According to the Hobart-Derrick theorem [11, 12] such configurations are unstable, if they move with a velocity slower than the speed of light c . Moving with c they have an action constant in time and can be used to describe electromagnetic waves. For simplicity we choose the z -axis in the direction of motion; then it is sufficient to describe these configurations in \mathbb{R}^3 given by the coordinates x , y , and $\zeta = z - ct$. The linking number ν is a topological invariant. Its natural physical equivalent is the number of photons n_ν in this configuration.

As an example of such a configuration in \mathbb{R}^3 with $\nu = 1$ we defined in the diploma thesis [22] a field by an area preserving map of \mathcal{S}^2 to a circle rotating with φ around the line $\rho = \rho_0 = 3$, $\zeta = 0$, defined in cylindrical coordinates ρ , φ , ζ by

$$\begin{aligned}\cos\theta &= \begin{cases} \frac{(\rho - \rho_0)^2 + \zeta^2}{2} - 1 \leq 1 \\ 1 \end{cases} \quad \text{else} \\ \phi &= \varphi + \arctan \frac{\zeta}{\rho - \rho_0}.\end{aligned}\quad (30)$$

For a given \vec{n} -field one can get the linking number in \mathbb{R}^3 by the famous formula of Carl Friedrich Gauß:

$$\nu = \frac{1}{4\pi} \oint_{\mathcal{E}_1} \oint_{\mathcal{E}_2} \frac{\mathbf{r}_1 - \mathbf{r}_2}{|\mathbf{r}_1 - \mathbf{r}_2|^3} \cdot (\mathbf{dr}_1 \times \mathbf{dr}_2), \quad (31)$$

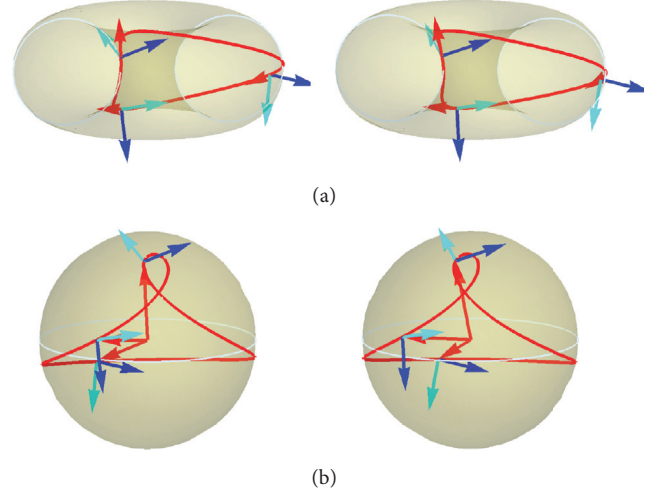


FIGURE 5: Stereographic view with parallel eyes at a fibre neighbourhood. (a) Fibre \mathcal{F} on a torus in \mathbb{R}^3 . Dreibins of red tangential vectors and blue and cyan tangential vectors are drawn at three positions. (b) Gauß map $\mathcal{C}_{\mathcal{F}}$ of \mathcal{F} with red radial vector $\vec{e}'_{\mathcal{F}}(s)$ and blue and cyan tangential vectors at the corresponding three positions.

by a double integral. We get from the observation of the neighbourhood of a single fibre \mathcal{F} another determination of ν , by a single integral. We parametrize the position along the fibre with some parameter s . We determine the tangential vector $\mathbf{e}_{\mathcal{F}}(s)$ to the fibre and a unit vector to some neighbouring fibre, for example, defined by the perpendicular component $\mathbf{e}_\theta(s) := (\nabla \cos\theta_{\mathcal{F}} / |\nabla \cos\theta_{\mathcal{F}}|)_{\perp}$ of the gradient $\nabla \cos\theta_{\mathcal{F}}(s)$. We get a local Dreibein with $\mathbf{e}_{\perp}(s) := \mathbf{e}_{\mathcal{F}}(s) \times \mathbf{e}_\theta(s)$. Then we determine the rotational velocity along the fibre by

$$\frac{d\omega}{ds} := \mathbf{e}_{\perp} \cdot \nabla_s \mathbf{e}_\theta = \mathbf{e}_{\mathcal{F}} \cdot (\mathbf{e}_\theta \times \nabla_s \mathbf{e}_\theta). \quad (32)$$

It turns out that the integrated rotational angle ω depends on the radius $R = \sqrt{(\rho - \rho_0)^2 + \zeta^2}$ of the torus surrounded by the fibre

$$\omega(R) := \oint_{\mathcal{F}} \frac{d\omega}{ds} ds \neq 2\pi n, \quad n \in \mathcal{N} \quad (33)$$

and is not an integer. Its dependence on R is depicted in Figure 6. This is understandable from the Gauß map $\mathbf{e}_{\mathcal{F}}(s) \mapsto \mathbf{e}'_{\mathcal{F}}(s)$ and $\mathbf{e}_\theta(s) \mapsto \mathbf{e}'_\theta(s)$ to the $\mathcal{S}^2_{\mathbb{G}}$ unit sphere; see Figure 5. $\mathbf{e}'_{\mathcal{F}}(s)$, plotted from the origin of $\mathcal{S}^2_{\mathbb{G}}$ by $\vec{e}'_{\mathcal{F}}(s) = \vec{e}_{\mathcal{F}}(s)$, draws a curve $\mathcal{C}_{\mathcal{F}}$ on $\mathcal{S}^2_{\mathbb{G}}$ (With bold symbols \mathbf{e} we indicate the vectors and with \vec{e} the set of its coordinates.). $\mathbf{e}'_\theta(s)$ and $\mathbf{e}'_{\perp}(s)$ are defined as vectors in the tangential space at $\mathbf{e}_{\mathcal{F}}(s)$ by the coordinate equalities $\vec{e}'_\theta(s) = \vec{e}_\theta(s)$ and $\vec{e}'_{\perp}(s) = \vec{e}_{\perp}(s)$. Their parallel transport along $\mathcal{C}_{\mathcal{F}}$ is nontrivial, except for $\mathcal{C}_{\mathcal{F}}$ that is a great circle. Deviations from a great circle lead to an additional contribution of the curved geometry on $\mathcal{S}^2_{\mathbb{G}}$ to the rotational angle. Indicating the position on $\mathcal{S}^2_{\mathbb{G}}$ in

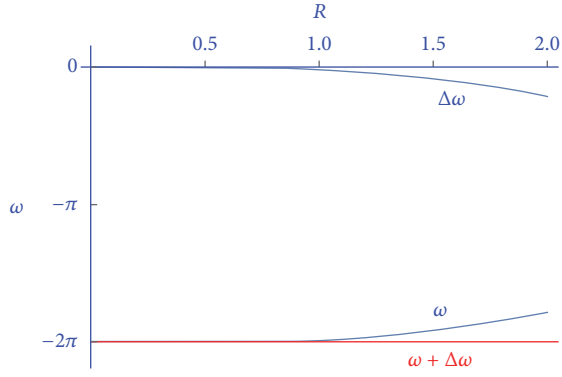


FIGURE 6: Contributions $\omega(R)$ and $\Delta\omega(R)$ to the determination of the rotational angle of the fibre neighbourhood.

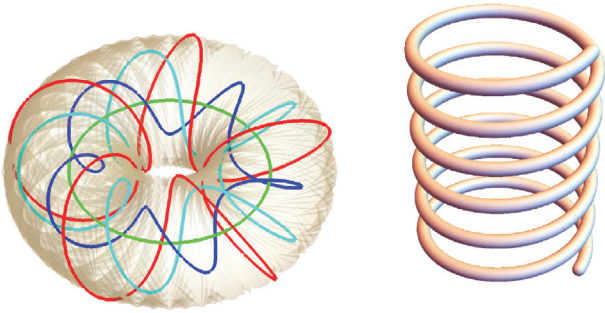


FIGURE 7: Configurations with higher linking numbers arranged with the shape of a torus or in spiral form.

spherical coordinates $\vec{e}'_{\mathcal{F}} = (\sin \alpha \cos \beta, \sin \alpha \sin \beta, \cos \alpha)$, we can derive, for the corresponding spherical coordinate bases \mathbf{e}_α and \mathbf{e}_β , the affine $U(1)$ connection:

$$\begin{aligned} C_\alpha &= 0, \\ C_\beta &= \frac{\cos \alpha}{\sin \alpha}, \\ \vec{C} &= C_\alpha \vec{e}_\alpha + C_\beta \vec{e}_\beta \end{aligned} \quad (34)$$

which is trivial for meridians and the equator of \mathcal{S}_G^2 . The additional contribution reads

$$\Delta\omega(R) := \oint ds \frac{d\vec{e}'_{\mathcal{F}}}{ds} \cdot \vec{C}. \quad (35)$$

The sum of both contributions gives then the expected value:

$$\omega(R) + \Delta\omega(R) = 2\pi\nu. \quad (36)$$

Both contributions of our example are shown in Figure 6; they give $\nu = -1$.

With the conjecture that the photon number of a configuration is given by the Gauß linking number ν of fibres, configurations with higher linking numbers ν correspond to states with several photons. In such configurations, see Figure 7; the linked fibres are spiraling several times. The

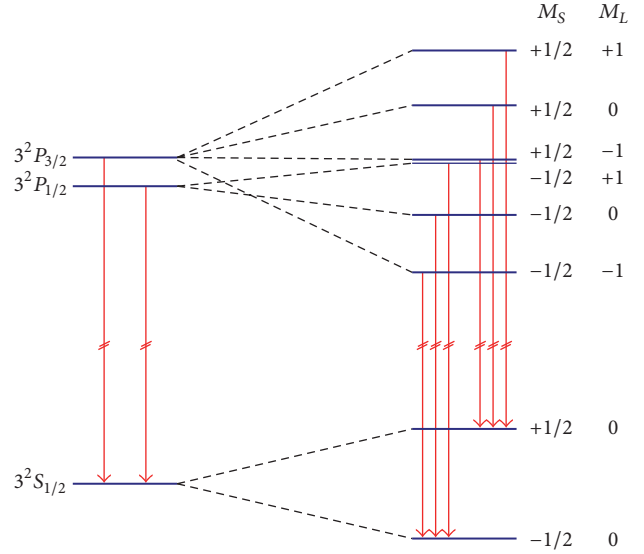


FIGURE 8: In a strong magnetic field the Na-D-line splits into three spectral lines with $\Delta M_L = 0, \pm 1$ and $\Delta M_S = 0$.

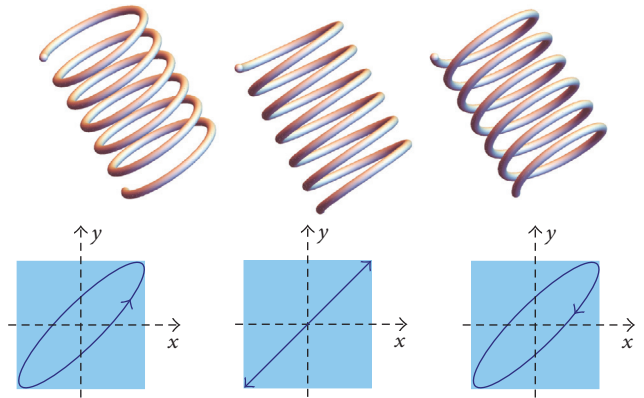


FIGURE 9: Different projections of rotations around a circle produce different polarisations.

spiral in the right diagram of Figure 7 reminds us of circular polarised waves.

It may be helpful to have a look at experiments. The Na-D-line in a strong magnetic field splits into three lines, the Lorentz triple (see Figure 8), according to $\Delta M_L = 0, \pm 1$. It is interesting to observe the three spectral lines parallel and perpendicular to the magnetic field, as depicted in Figure 10. The lines with $\Delta M_L = 0$, the “ π -components,” are linearly polarised with an azimuth dependency of the intensity $I(\vartheta) = \sin^2 \vartheta$. The $\Delta M_L = \pm 1$ -lines, the “ σ -components,” are circularly polarised with $I(\vartheta) = (1/2)(1 + \cos^2 \vartheta)$. If the circular polarised lines are observed in the direction perpendicular to the \mathbf{B} -field they appear linearly polarised. This reminds us of different projections of circular motion, of a spiral in the comoving $x, y, z - ct$ frame; see Figure 9.

Here a problem may appear. Rotations of a spiral do not change their chirality. After a rotation by π a right-handed

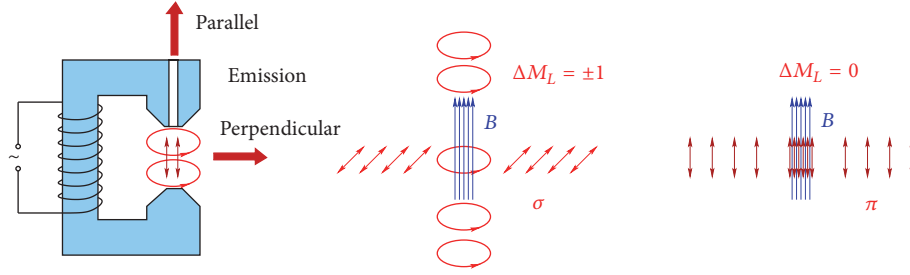


FIGURE 10: Scheme of observation of the Na-D-line in a strong magnetic field.

spiral remains right-handed as one can easily check with a right-handed thread of a screw. It is well-known that right polarised light can be easily transformed to linear polarised and to left polarised light by quarter-wave plates. These plates have perpendicular fast and slow axes.

This looks as a counterargument for the interpretation of the Hopf number as photon number. But it may also be an unknown feature of polarised light? Looking carefully at polarisation filters, one realises that filters exist for linear polarised light only! Right and left circular polarised light is detected by transforming it with quarter-wave plates, by interaction with matter, to linear polarisation.

9. Conclusion

The model described in this article is based on a field of $SO(3)$ -matrices in $3 + 1D$ Minkowski space-time. Therefore, the model has 3 degrees of freedom only, corresponding to the 3 Euler angles. These rotational matrices can be interpreted as describing the field of orientations of spatial Dreibeins at the points of space-time. In this sense, this simple model needs only the degrees of freedom of space and time to describe the various phenomena discussed in this article. To formulate the algebra of this model we are using the simpler representation of rotations by $SU(2)$ -matrices. As a consequence of this treatment we have to take into account the fact that for every $SO(3)$ -configuration there exist two $SU(2)$ -configurations representing the same field. Vector fields (potentials) and tensor fields (field strength) are derived from the basic soliton field $Q(x)$.

The Lagrangian (3) of the model contains two terms. The kinetic term is proportional to the square of the curvature $\vec{R}_{\mu\nu}$ or to the dual field strength. Such a term is well-known from electrodynamics and QCD. The potential term reminds us of the Higgs potential and the cosmological constant. According to the Hobart-Derrick theorem a quarter of the mass of solitons would contribute with its average to the cosmological constant. The transition from $Q = 1$ and $\Lambda = 1/r_0^4$ to $\Lambda = 0$ releases an energy density of $\alpha_f \hbar c / (4\pi r_0^4) = 4.8 \text{ keV/fm}^3 = 7.7 \cdot 10^{29} \text{ J/m}^3$ and could have contributed to inflation. Further, the potential term allows for a two-dimensional degeneracy of the vacuum states.

In this model, there appear particle-like excitations as topological solitons. Their mass is field energy only. The field configurations are characterised by three topological

quantum numbers which could find a physical realisation as electric charge, spin quantum number, and photon number. The topological structure does not allow two solitons to occupy the same space. This could be the topological origin of the Pauli principle. Charges appear as integer multiples of an elementary charge. No fractional charges are possible for stable excitations. Charges are characterised by regions where the spatial Dreibein rotates by 2π . Such regions interact via Coulomb and Lorentz forces. The electric force follows the $1/r^2$ behaviour at large distances and increases for high momentum transfers. The distinction between charges and their fields is unnecessary. Such a distinction can be introduced as an approximation and simplifies the comparison with our physical experience. Eigenangular momentum (spin) appears as a consequence of orbital motion. The degenerate vacuum allows for two types of massless excitations, which could be related to the two polarisations of photons. $U(1)$ gauge invariance emerges in the electrodynamic limit as rotational invariance of the above-mentioned Dreibein around the \vec{n} -axis.

Despite the small number of degrees of freedom there are further nonquantized disturbances possible. Magnetic currents as violations of the homogeneous Maxwell equations propagate with the speed of light and contribute to force fields only via their field strengths. Further we find waves in the rotational angle $\omega = 2\alpha$ with energy contributions from the potential term in the Hamiltonian. The cosmological discoveries of recent years allow attributing these two types of disturbances to dark energy and dark matter contributions.

The investigations seem to support the conjecture that the particles we find in experiments are topological solitons characterised by topological quantum numbers. They produce only spots on films and clicks in detectors. Waves seem to escape and are not directly detected. Waves could disturb the paths of particles and could contribute to a subquantum medium leading to quantum mechanics. In analogy to Couder's silicon oil drop experiments [23–26], the interference of waves created by the particle themselves with the vacuum waves could serve as a guiding wave field for particles.

If this model reproduced some features of nature, the two types of long-range forces which we find, gravitational and Coulomb forces, would be described in a geometrical manner with the degrees of freedom of space-time only. This would give a hint that particle physics could be closely related to gravitation.

Conflicts of Interest

The author declares that there are no conflicts of interest regarding the publication of this paper.

References

- [1] M. Remoissenet, *Waves Called Solitons: Concepts and Experiments*, Advanced Texts in Physics, Springer, Berlin, Germany, 2003.
- [2] C. W. Misner, K. S. Thorne, and J. A. Wheeler, *Gravitation*, W. H. Freeman, San Francisco, Calif, USA, 1973, Number Teil 3 in Gravitation.
- [3] M. Faber, “Model for topological fermions,” *Few-Body Systems*, vol. 30, no. 3, pp. 149–186, 2001.
- [4] M. Faber and A. P. Kobushkin, “Electrodynamic limit in a model for charged solitons,” *Physical Review D*, vol. 69, no. 11, Article ID 116002, 2004.
- [5] D. Borisyuk, M. Faber, and A. Kobushkin, “Electro-magnetic waves within a model for charged solitons,” *Journal of Physics A: Mathematical and Theoretical*, vol. 40, no. 3, pp. 525–531, 2007.
- [6] M. Faber, A. Kobushkin, and M. Pitschmann, “Shape vibrations of topological fermions,” *Advanced Studies in Theoretical Physics*, vol. 2, pp. 11–22, 2008.
- [7] M. Faber, “Particles as stable topological solitons,” *Journal of Physics: Conference Series*, vol. 361, no. 1, Article ID 012022, 2012.
- [8] M. Faber, “Spin and charge from space and time,” *Journal of Physics: Conference Series*, vol. 504, no. 1, Article ID 012010, 2014.
- [9] B. O. Rodrigues, “Des lois géométriques qui régissent les déplacements d’un système solide dans l’espace, et de la variation des coordonnées provenant de ces déplacements considérés indépendamment des causes qui peuvent les produire,” *Journal de Mathématiques Pures et Appliquées*, vol. 5, pp. 380–440, 1840.
- [10] T. H. R. Skyrme, “A non-linear field theory,” *Proceedings of the Royal Society A: Mathematical, Physical and Engineering Sciences*, vol. 260, pp. 127–138, 1961.
- [11] R. H. Hobart, “On the instability of a class of unitary field models,” *Proceedings of the Physical Society*, vol. 82, no. 2, pp. 201–203, 1963.
- [12] G. H. Derrick, “Comments on nonlinear wave equations as models for elementary particles,” *Journal of Mathematical Physics*, vol. 5, pp. 1252–1254, 1964.
- [13] J. D. Jackson, *Classical Electrodynamics*, Wiley, New York, NY, USA, 3rd edition, 1999.
- [14] J. Wabnig, *Interaction in the model of topological fermions [M.S. thesis]*, Technische Universität Wien, Wien, Austria, 2001.
- [15] J. Resch, *Numerische analyse an dipolkonfigurationen im modell topologischer fermionen [M.S. thesis]*, Technische Universität Wien, Wien, Austria, 2011.
- [16] D. Theuerkauf, *Charged particles in the model of topological fermions [M.S. thesis]*, Technische Universität Wien, Wien, Austria, 2016.
- [17] T. T. Wu and C. N. Yang, “Some remarks about unquantized non-abelian gauge fields,” *Physical Review D*, vol. 12, pp. 3843–3844, 1975.
- [18] L. D. Faddeev, “Quantization of solitons,” in *Proceedings of the Tbilisi Conference*, 1975.
- [19] L. D. Faddeev, “Some comments on the many-dimensional solitons,” *Letters in Mathematical Physics*, vol. 1, no. 4, pp. 289–293, 1976.
- [20] L. A. Ferreira and A. V. Razumov, “Hopf solitons and area-preserving diffeomorphisms of the sphere,” *Letters in Mathematical Physics*, vol. 55, no. 2, pp. 143–148, 2001.
- [21] L. A. Ferreira, “Exact time dependent Hopf solitons in 3 + 1 dimensions,” *Journal of High Energy Physics*, vol. 2006, 2006.
- [22] J. Markus, *Die hopfzahl in einer SU(2)-feldtheorie [M.S. thesis]*, Technische Universität Wien, Wien, Austria, 2014.
- [23] Y. Couder, E. Fort, C.-H. Gautier, and A. Boudaoud, “From bouncing to floating: Noncoalescence of drops on a fluid bath,” *Physical Review Letters*, vol. 94, no. 17, Article ID 177801, 2005.
- [24] Y. Couder and E. Fort, “Single-particle diffraction and interference at a macroscopic scale,” *Physical Review Letters*, vol. 97, no. 15, Article ID 154101, 2006.
- [25] A. Eddi, E. Fort, F. Moisy, and Y. Couder, “Unpredictable tunneling of a classical wave-particle association,” *Physical Review Letters*, vol. 102, no. 24, Article ID 240401, 2009.
- [26] E. Fort, A. Eddi, A. Boudaoud, J. Moukhtar, and Y. Couder, “Path-memory induced quantization of classical orbits,” *Proceedings of the National Academy of Sciences of the United States of America*, vol. 107, no. 41, pp. 17515–17520, 2010.

Research Article

Emerging Translational Variance: Vacuum Polarization Energy of the ϕ^6 Kink

H. Weigel

Institute for Theoretical Physics, Physics Department, Stellenbosch University, Matieland 7602, South Africa

Correspondence should be addressed to H. Weigel; weigel@sun.ac.za

Received 19 May 2017; Accepted 8 June 2017; Published 30 July 2017

Academic Editor: Ralf Hofmann

Copyright © 2017 H. Weigel. This is an open access article distributed under the Creative Commons Attribution License, which permits unrestricted use, distribution, and reproduction in any medium, provided the original work is properly cited. The publication of this article was funded by SCOAP³.

We propose an efficient method to compute the vacuum polarization energy of static field configurations that do not allow decomposition into symmetric and antisymmetric channels in one space dimension. In particular, we compute the vacuum polarization energy of the kink soliton in the ϕ^6 model. We link the dependence of this energy on the position of the center of the soliton to the different masses of the quantum fluctuations at negative and positive spatial infinity.

1. Motivation

It is of general interest to compute quantum corrections to classical field configurations like soliton solutions that are frequently interpreted as particles. On top of the wish list, we find the energies that predict particle masses. The quantum correction to the energy can be quite significant because the classical field acts as a background that strongly polarizes the spectrum of the quantum fluctuations about it. For that reason, the quantum correction to the classical energy is called vacuum polarization energy (VPE). Here, we will consider the leading (i.e., one-loop) contribution.

Field theories that have classical soliton solutions in various topological sectors deserve particular interest. Solitons from different sectors have unequal winding numbers and the fluctuation spectrum changes significantly from one sector to another. For example, the number of zero modes is linked to the number of (normalizable) zero modes that in turn arise from the symmetries that are spontaneously broken by the soliton. Of course, the pattern of spontaneous symmetry breaking is subject to the topological structure. On the other hand, the winding number is typically identified with the particle number. The prime example is the Skyrme model [1, 2] wherein the winding number determines the baryon number [3, 4]. Many properties of baryons have been studied in this soliton model and its generalization in the past [5].

More recently, configurations with very large winding numbers have been investigated [6] and these solutions were identified with nuclei. To obtain a sensible understanding of the predicted nuclear binding energies, it is, of course, important to consider the VPE, in particular when it is expected to strongly depend on the particle number. So far, this has not been attempted for the simple reason that the model is not renormalizable. A rough estimate [7] (see [8] for a general discussion of the quantum corrections of the Skyrme and further references on the topic) in the context of the H -dibaryon [9, 10] suggests that the VPE strongly reduces the binding energy of multibaryon states.

As already mentioned, one issue for the calculation of the VPE is renormalization. Another important one is, as will be discussed below, that the VPE is (numerically) extracted from the scattering data for the quantum fluctuations about the classical configuration [11]. Though this so-called *spectral method* allows for direct implementation of standard renormalization conditions, it has limitations as it requires sufficient symmetry for partial wave decomposition. This may not be possible for configurations with an intricate topological structure associated with large winding numbers.

The ϕ^6 model in $D = 1 + 1$ dimensions has soliton solutions with different topological structures [12, 13] and the fluctuations do not decouple into parity channels. The approach employed here is also based on scattering data but advances

the spectral method such that no parity decomposition is required. We will also see that it is significantly more effective than previous computations [14–16] for the VPE of solitons in $D = 1+1$ dimensions that are based on heat kernel expansions combined with ζ -function regularization techniques [17–19].

Although the ϕ^6 model is not fully renormalizable, at one-loop order, the ultraviolet divergences can be removed unambiguously. However, another very interesting phenomenon emerges. The distinct topological structures induce nonequivalent vacua that manifest themselves via different dispersion relations for the quantum fluctuations at positive and negative spatial infinity. At some intermediate position, the soliton mediates between these vacua. Since this position cannot be uniquely determined, the resulting VPE exhibits a translational variance. This is surprising since, after all, the model is defined through a local and translational invariant Lagrangian. In this paper, we will describe the emergence of this variance and link it to the different level densities that arise from the dispersion relations. To open these results for discussion (the present paper reflects the author's invited presentation at the 5th *Winter Workshop on Non-Perturbative Quantum Field Theory* based on the methods derived in [20] making some overlap unavoidable), it is necessary to review in detail the methods developed in [20] to compute the VPE for backgrounds in one space dimension that are not (manifestly) invariant under spatial reflection.

Following this introductory motivation, we will describe the ϕ^6 model and its kink solutions. In Section 3, we will review the spectral method that ultimately leads to a variant of the Krein–Friedel–Lloyd formula [21] for the VPE. The novel approach to obtain the relevant scattering data will be discussed in Section 4 and combined with the one-loop renormalization in Section 5. A comparison with known (exact) results will be given in Section 6 while Section 7 contains the predicted VPE for the solitons of the ϕ^6 model. Translational variance of the VPE that emerges from the existence of nonequivalent vacua will be analyzed in Section 8. We conclude with a short summary in Section 9.

2. Kinks in ϕ^6 Models

In $D = 1 + 1$ dimensions, the dynamics for the quantum field ϕ are governed solely by a field potential $U(\phi)$ that is added to the kinetic term

$$\mathcal{L} = \frac{1}{2} \partial_\mu \phi \partial^\mu \phi - U(\phi). \quad (1)$$

For the ϕ^6 model, we scale all coordinates, fields, and coupling constants such that the potential contains only a single dimensionless parameter a :

$$U(\phi) = \frac{1}{2} (\phi^2 + a^2) (\phi^2 - 1)^2. \quad (2)$$

From Figure 1, we observe that there are three general cases. For $a^2 > 1/2$, two degenerate minima at $\phi = \pm 1$ exist. For $0 < a^2 \leq 1/2$, an additional local minimum emerges at $\phi = 0$. Finally, for $a = 0$, the three minima at $\phi = 0$ and $\phi = \pm 1$ are degenerate. Soliton solutions connect different vacua

between negative and positive spatial infinity. For $a \neq 0$, the vacua are at $\phi = \pm 1$ and the corresponding soliton solution is [12]

$$\phi_K(x) = a \frac{X - 1}{\sqrt{4X + a^2(1 + X)^2}} \quad \text{with } X = e^{2\sqrt{1+a^2}x}. \quad (3)$$

Its classical energy is

$$E_{\text{cl}}(a) = \frac{2 - a^2}{4} \sqrt{1 + a^2} + \frac{4a^2 + a^4}{8} \ln \frac{\sqrt{1 + a^2} + 1}{\sqrt{1 + a^2} - 1}. \quad (4)$$

The case $a = 0$ is actually more interesting because two distinct soliton solutions do exist. The first one connects $\phi = 0$ at $x \rightarrow -\infty$ to $\phi = 1$ at $x \rightarrow \infty$:

$$\phi_{K_1}(x) = \frac{1}{\sqrt{1 + e^{-2x}}}, \quad (5)$$

while the second one interpolates between $\phi = -1$ and $\phi = 0$:

$$\phi_{K_2}(x) = -\frac{1}{\sqrt{1 + e^{2x}}}. \quad (6)$$

These soliton configurations are shown in Figure 2. In either case, the classical mass is $E_{\text{cl}} = 1/4 = (1/2) \lim_{a \rightarrow 0} E_{\text{cl}}(a)$. This relation for the classical energies reflects the fact that as $a \rightarrow 0$ the solution $\phi_K(x)$ disintegrates into two widely separated structures, one corresponding to $\phi_{K_1}(x)$ and the other to $\phi_{K_2}(x)$.

The computation of the VPE requires the construction of scattering solutions for fluctuations about the soliton. In the harmonic approximation, the fluctuations experience the potential

$$V(x) = \frac{1}{2} \frac{\partial^2 U(\phi)}{\partial \phi^2} \Big|_{\phi=\phi_{\text{sol}}(x)} \quad (7)$$

generated by the soliton ($\phi_{\text{sol}} = \phi_K, \phi_{K_1},$ or ϕ_{K_2}). These three potentials are shown in Figure 3. For $a \neq 0$, the potential is invariant under $x \leftrightarrow -x$. But the particular case $a \equiv 0$ is not reflection symmetric, though $x \leftrightarrow -x$ swaps the potentials generated by ϕ_{K_1} and ϕ_{K_2} . The loss of this invariance disables the separation of the fluctuation modes into symmetric and antisymmetric channels, which is the one-dimensional version of a partial wave decomposition. Even more strikingly, the different topological structures in the $a = 0$ case cause $\lim_{x \rightarrow -\infty} V(x) \neq \lim_{x \rightarrow \infty} V(x)$, which implies different masses (dispersion relations) for the fluctuations at positive and negative spatial infinity.

3. Spectral Methods and Vacuum Polarization Energy

The formula for the VPE (see (13)) can be derived from first principles in quantum field theory by integrating the vacuum matrix element of the energy density operator [22]. It is, however, also illuminative to count the energy levels when summing the changes of the zero point energies. This sum is $\mathcal{O}(\hbar)$

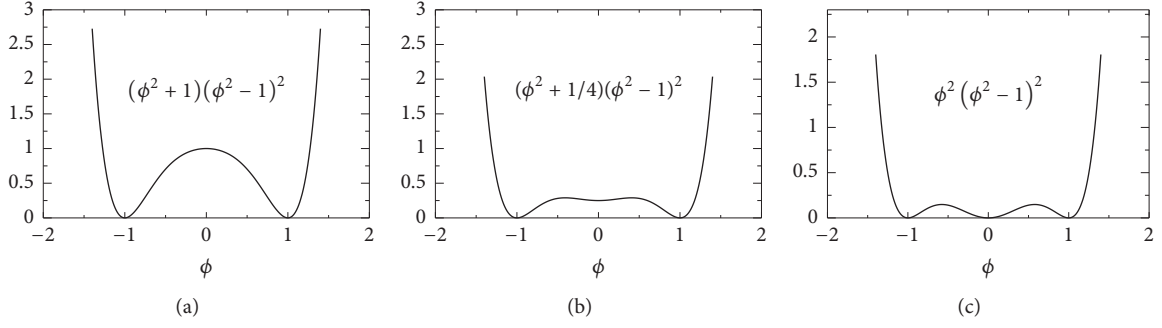


FIGURE 1: The field potential (see (2)) in the ϕ^6 model for various values of the real parameter $a = 1, 1/2, 0$ from (a) to (c).

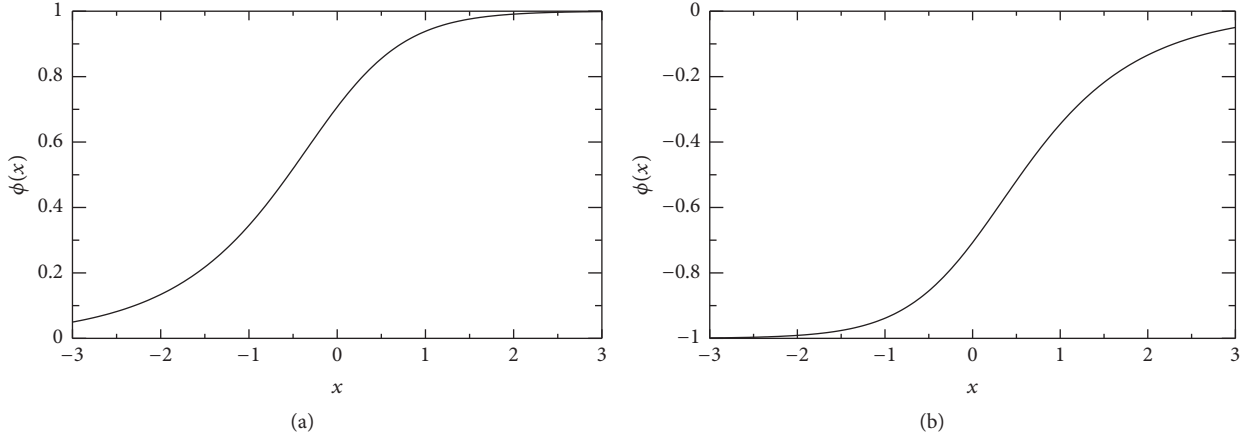


FIGURE 2: The two soliton solutions for $a = 0$: (a) see (5); (b) see (6).

and thus one-loop order ($\hbar = 1$ for the units used here). We call the single particle energies of fluctuations in the soliton type background ω_n while $\omega_n^{(0)}$ are those for the trivial background. Then, the VPE formally reads

$$E_{\text{vac}} = \frac{1}{2} \sum_n \left(\omega_n - \omega_n^{(0)} \right) \Big|_{\text{ren.}} \quad (8)$$

$$= \frac{1}{2} \sum_j \epsilon_j + \frac{1}{2} \int_0^\infty dk \omega_k \Delta \rho_{\text{ren.}}(k),$$

where the subscript indicates that renormalization is required to obtain a finite and meaningful result. On the right hand side, we have separated the explicit bound state (sum of energies ϵ_j) and continuum (integral over momentum k) contributions. The latter involves $\Delta \rho_{\text{ren.}}(k)$ which is the (renormalized) change of the level density induced by the soliton background. Let L be a large distance away from the localized soliton background. For $x \sim L$, the stationary wave function of the quantum fluctuation is a phase shifted plane wave $\psi(x) \sim \sin[kx + \delta(k)]$, where $\delta(k)$ is the phase shift (of a particular partial wave) that is obtained from scattering off the potential (see (7)). The continuum levels are counted from the boundary condition $\psi(L) = 0$ and subsequently taking the limit $L \rightarrow \infty$. The number $n(k)$ of levels with momentum less than or equal to k is then extracted from $kL + \delta(k) = n(k)\pi$. The corresponding number in the absence

of the soliton is $n^{(0)}(k) = kL/\pi$, trivially. From these, the change of the level density is computed via

$$\Delta \rho(k) = \lim_{L \rightarrow \infty} \frac{d}{dk} \left[n(k) - n^{(0)}(k) \right] = \frac{1}{\pi} \frac{d\delta(k)}{dk}, \quad (9)$$

which is often referred to as the Krein–Friedel–Lloyd formula [21]. Note that $\Delta \rho(k)$ is a finite quantity; but ultraviolet divergences appear in the momentum integral in (8) and originate from the large k behavior of the phase shift. This behavior is governed by the Born series

$$\delta(k) = \delta^{(1)}(k) + \delta^{(2)}(k) + \dots, \quad (10)$$

where the superscript reflects the power to which the potential (see (7)) contributes. Though this series does not converge (e.g., in three space dimensions, the series yields $\delta(0) \rightarrow 0$ which contradicts Levinson's theorem) for all k , it describes the large k behavior well since $\delta^{(N+1)}(k)/\delta^{(N)}(k) \propto 1/k^2$ when $k \rightarrow \infty$. Hence, replacing

$$\Delta \rho(k) \longrightarrow [\Delta \rho(k)]_N$$

$$= \frac{1}{\pi} \frac{d}{dk} \left[\delta(k) - \delta^{(1)}(k) - \delta^{(2)}(k) - \dots - \delta^{(N)}(k) \right] \quad (11)$$

produces a finite integral in (8) when N is taken sufficiently large. We have to add back the subtractions that come with

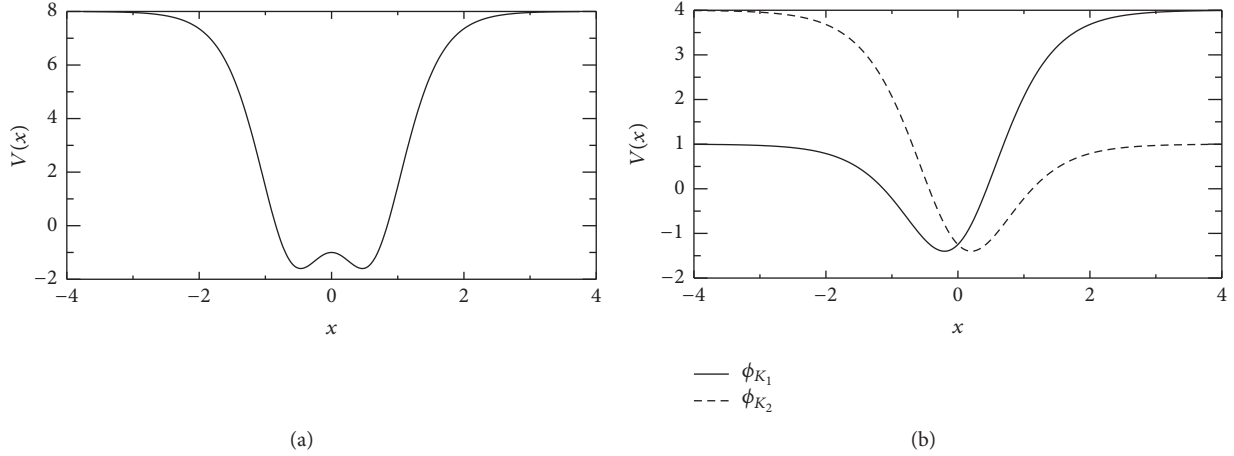


FIGURE 3: Scattering potentials for the quantum fluctuations in the ϕ^6 model. (a) Typical example for $a \neq 0$; (b) the case $a = 0$ with the two potentials generated by ϕ_{K_1} (full line) and ϕ_{K_2} (dashed line).

this replacement. Here, the spectral methods take advantage of the fact that each term in the subtraction is uniquely related

to a power of the background potential and that Feynman diagrams represent an alternative expansion scheme for the vacuum polarization energy

$$E_{\text{FD}}^N[V] = \text{diagram 1} + \text{diagram 2} + \text{diagram 3} + \dots \quad (12)$$

The diagrams in equation (12) represent Feynman diagrams for the vacuum polarization energy. Diagram 1 is a circle with a dashed line labeled $V(x)$ entering from the top and a solid line labeled $V(x)$ exiting from the bottom. Diagram 2 is a circle with a dashed line labeled $V(x)$ entering from the top and a dashed line labeled $V(x)$ exiting from the bottom. Diagram 3 is a circle with a dashed line labeled $V(x)$ entering from the top and two dashed lines labeled $V(x)$ exiting from the bottom.

The full lines are the free propagators of the quantum fluctuations and the dashed lines denote insertions of the background potential (see (7)), eventually after Fourier transformation. These Feynman diagrams are regularized with standard techniques, most commonly in dimensional regularization. They can thus be straightforwardly combined with the counterterm contribution, $E_{\text{CT}}[V]$, with coefficients fully determined in the perturbative sector of the theory. This combination remains finite when the regulator is removed.

The generalization to multiple channels is straightforward by finding an eventually momentum dependent diagonalization of the scattering matrix $S(k)$ and summing the so-obtained eigenphase shifts. This replaces $\delta(k) \rightarrow (1/2i) \ln \det S(k)$ (the proper Riemann sheet of the logarithm is identified by constructing a smooth function that vanishes as $k \rightarrow \infty$) and analogously for the Born expansion (see (10) and (11)). Since after Born subtraction the integral converges, we integrate by parts to avoid numerical differentiation and to stress that the VPE is measured with respect to the translationally invariant vacuum. We then find the renormalized VPE to be, with the sum over partial waves reinserted,

$$E_{\text{vac}}[V] = \sum_{\ell} D_{\ell} \left\{ \frac{1}{2} \sum_j (\epsilon_{\ell j} - m) \right.$$

$$\left. - \int_0^{\infty} \frac{dk}{4\pi i} \frac{k}{\sqrt{k^2 + m^2}} [\ln \det S(k)]_N \right\} + E_{\text{FD}}^N[V] + E_{\text{CT}}[V]. \quad (13)$$

Here, D_{ℓ} is the degree of degeneracy (e.g., $D_{\ell} = 2\ell + 1$ in three space dimensions). The subscript N refers to the subtraction of N terms of the Born expansion, as, for example, in (11). We stress that, with N taken sufficiently large, both the expression in curly brackets and the sum $E_{\text{FD}}^N[V] + E_{\text{CT}}[V]$ are individually ultraviolet finite and no cutoff parameter is needed [23].

4. Scattering Data in One Space Dimension

In this section, we obtain the scattering matrix for general one-dimensional problems and develop an efficient method for its numerical evaluation. This will be at the center of the novel approach to compute the VPE.

We first review the standard approach that is applicable when $V(-x) = V(x)$ (e.g., Figure 3(a)). Then, the partial wave decomposition separates symmetric $\psi_S(-x) = \psi_S(x)$ and antisymmetric, $\psi_A(-x) = -\psi_A(x)$ channels. The respective phase shifts can be straightforwardly obtained in a variant of

the variable phase approach [24] by parameterizing $\psi(x) = e^{i[kx + \beta(k, x)]}$ and imposing the obvious boundary conditions $\psi'_S(0) = 0$ and $\psi_A(0) = 0$. (The prime denotes the derivative with respect to x .) The wave equation turns into a nonlinear differential equation for the phase function $\beta(k, x)$. When solved subject to $\lim_{x \rightarrow \infty} \beta(k, x) = 0$ and $\lim_{x \rightarrow \infty} \beta'(k, x) = 0$, the scattering matrix is given by [11]

$$\frac{1}{2i} \ln \det S(k) = -2 \operatorname{Re} [\beta(k, 0)] - \arctan \frac{\operatorname{Im} [\beta'(k, 0)]}{k + \operatorname{Re} [\beta'(k, 0)]}. \quad (14)$$

Linearizing and iterating the differential equation for $\beta(k, x)$ yield the Born series (see (10)). At this point, it is advantageous to use the fact that scattering data can be continued to the upper half complex momentum plane [25, 26]. That is, when writing $k = it$, the Jost function, whose phase is the scattering phase shift when k is real, is analytic for $\operatorname{Re}[t] \geq 0$. Furthermore, the Jost function has simple zeros at imaginary $k = i\kappa_j$ representing the bound states. Formulating the momentum integral from (13) as a contour integral automatically collects the bound state contribution and we obtain a formula as simple as [11, 22]

$$E_{\text{vac}}^{(S)} = \int_m^\infty \frac{dt}{2\pi} \frac{t}{\sqrt{t^2 - m^2}} \times \left[\ln \left\{ g(t, 0) \left(g(t, 0) - \frac{1}{t} g'(t, 0) \right) \right\} \right]_N + E_{\text{FD}}^N[V] + E_{\text{CT}}[V] \quad (15)$$

for the VPE. Here, $g(t, x)$ is the nontrivial factor of the Jost solution whose $x \rightarrow 0$ properties determine the Jost function. The factor function solves the differential equation

$$g''(t, x) = 2tg'(t, x) + V(x)g(t, x), \quad (16)$$

with the boundary conditions $g(t, \infty) = 1$ and $g'(t, \infty) = 0$; iterating $g(t, x) = 1 + g^{(1)}(t, x) + g^{(2)}(t, x) + \dots$ produces the Born series.

In general, however, the potential $V(x)$ is not reflection invariant and no partial wave decomposition is applicable. Even more, there may exist different masses for the quantum fluctuations

$$m_L^2 = \lim_{x \rightarrow -\infty} V(x), \quad m_R^2 = \lim_{x \rightarrow \infty} V(x) \quad (17)$$

as it is the case for the ϕ^6 model with $a = 0$ (cf. Figure 3(b)). We adopt the convention that $m_L \leq m_R$; otherwise, we simply swap $x \rightarrow -x$. Three different cases must be considered. First, above threshold, both momenta k and $q = \sqrt{k^2 + m_L^2 - m_R^2}$

are real. To formulate the variable phase approach, we introduce the matching point x_m and parameterize

$$\begin{aligned} \psi(x) &= A(x) e^{ikx} \\ A''(x) &= -2ikA'(x) + V_p(x)A(x) \\ & \hspace{15em} x \leq x_m \\ \psi(x) &= B(x) e^{iqx} \\ B''(x) &= -2iqB'(x) + V_p(x)B(x) \\ & \hspace{15em} x \geq x_m. \end{aligned} \quad (18)$$

Observe that the *pseudopotential*

$$V_p(x) = V(x) - m_L^2 + (m_L^2 - m_R^2) \Theta(x - x_m) \quad (19)$$

vanishes at positive and negative spatial infinity. The differential equations (18) are solved for the boundary conditions $A(-\infty) = B(\infty) = 1$ and $A'(-\infty) = B'(\infty) = 0$. There are two linearly independent solutions ψ_1 and ψ_2 that define the scattering matrix $S = (s_{ik})$ via the asymptotic behaviors

$$\begin{aligned} \psi_1(x) &\sim \begin{cases} e^{ikx} + s_{12}(k) e^{-ikx} & \text{as } x \rightarrow -\infty \\ s_{11}(k) e^{iqx} & \text{as } x \rightarrow \infty, \end{cases} \\ \psi_2(x) &\sim \begin{cases} s_{22}(k) e^{-ikx} & \text{as } x \rightarrow -\infty \\ e^{-iqx} + s_{21}(k) e^{iqx} & \text{as } x \rightarrow \infty. \end{cases} \end{aligned} \quad (20)$$

By equating the solutions and their derivatives at x_m , the scattering matrix is obtained from the factor functions as

$$\begin{aligned} S(k) &= \begin{pmatrix} e^{-iqx_m} & 0 \\ 0 & e^{ikx_m} \end{pmatrix} \begin{pmatrix} B & -A^* \\ iqB + B' & ikA^* - A'^* \end{pmatrix}^{-1} \\ &\times \begin{pmatrix} A & -B^* \\ ikA + A' & iqB^* - B'^* \end{pmatrix} \begin{pmatrix} e^{ikx_m} & 0 \\ 0 & e^{-iqx_m} \end{pmatrix} \\ & \hspace{15em} \text{for } k \geq \sqrt{m_R^2 - m_L^2}, \end{aligned} \quad (21)$$

where $A = A(x_m)$, and so forth. The second case refers to $k \leq \sqrt{m_R^2 - m_L^2}$ still being real but $q = i\kappa$ becoming imaginary with $\kappa = \sqrt{m_R^2 - m_L^2 - k^2}$. The parameterization of the wave function for $x > x_m$ changes to $\psi(x) = B(x)e^{-\kappa x}$ yielding the differential equation $B''(x) = \kappa B'(x) + V_p(x)B(x)$. The scattering matrix then is a single unitary number

$$S(k) = -\frac{A(B'/B - \kappa - ik) - A'}{A^*(B'/B - \kappa + ik) - A'^*} e^{2ikx_m} \quad (22)$$

for $0 \leq k \leq \sqrt{m_R^2 - m_L^2}$.

It is worth noting that $V_p \equiv 0$ corresponds to the step function potential. In that case, the above formalism obviously yields $A \equiv B \equiv 1$ and reproduces the textbook result

$$\delta_{\text{step}}(k) = \begin{cases} (k-q)x_m, & \text{for } k \geq \sqrt{m_R^2 - m_L^2} \\ kx_m - \arctan\left(\frac{\sqrt{m_R^2 - m_L^2 - k^2}}{k}\right), & \text{for } k \leq \sqrt{m_R^2 - m_L^2}. \end{cases} \quad (23)$$

In the third regime also k becomes imaginary and we need to identify the bound states energies $\epsilon \leq m_L$ that enter (13). We define real variables $\lambda = \sqrt{m_L^2 - \epsilon^2}$ and $\kappa(\lambda) = \sqrt{m_R^2 - m_L^2 + \lambda^2}$ and solve the wave equation subject to the initial conditions

$$\begin{aligned} \psi_L(x_{\min}) &= 1, \\ \psi'_L(x_{\min}) &= \lambda, \\ \psi_R(x_{\max}) &= 1, \\ \psi'_R(x_{\max}) &= -\kappa(\lambda), \end{aligned} \quad (24)$$

where x_{\min} and x_{\max} represent negative and positive spatial infinity, respectively. Continuity of the wave function requires the Wronskian determinant

$$\psi_L(x_m)\psi'_R(x_m) - \psi_R(x_m)\psi'_L(x_m) \stackrel{!}{=} 0 \quad (25)$$

to vanish. This occurs only for discrete values λ_j that in turn determine the bound state energies $\epsilon_j = \sqrt{m_L^2 - \lambda_j^2}$ (the bosonic dispersion relation does not exclude imaginary energies that would hamper the definition of the quantum theory; this case does not occur here).

5. One-Loop Renormalization in One Space Dimension

To complete the computation of the VPE, we need to substantiate the renormalization procedure. We commence by identifying the ultraviolet singularities. This is simple in $D = 1 + 1$ dimensions at one-loop order as only the first diagram on the right hand side of (12) is divergent. Furthermore, this diagram is local in the sense that $E_{\text{FD}}^{(1)} \propto (1/\epsilon) \int dx [V(x) - m_L^2]$, where ϵ is the regulator (e.g., from dimensional regularization). Hence, a counterterm can be constructed that removes not only the singularity but also the diagram in total. This is the so-called *no tadpole* condition and implies

$$E_{\text{FD}}^{(1)} + E_{\text{CT}}^{(1)} = 0. \quad (26)$$

In the next step, we must identify the corresponding Born term in (10). To this end, it is important to note that the counterterm is a functional of the full field $\phi(x)$ that induces the background potential (see (7)). Hence, we must find the Born approximation for $V(x) - m_L^2$ rather than the one for the

pseudopotential $V_p(x)$ (see (19)). The standard formulation of the Born approximation as an integral over the potential is, unfortunately, not applicable to $V(x) - m_L^2$ since it does not vanish at positive spatial infinity. However, we note that $V(x) - m_L^2 = V_p(x) + (m_L^2 - m_R^2)\Theta(x - x_m) = V_p(x) + V_{\text{step}}(x)$ and that, by definition, the first-order correction is linear in the background and thus additive. We may therefore write

$$\begin{aligned} \delta^{(1)}(k) &= \delta_p^{(1)}(k) + \delta_{\text{step}}^{(1)}(k) \\ &= \frac{-1}{2k} \int_{-\infty}^{\infty} dx V_p(x) \Big|_{x_m} + \frac{x_m}{2k} (m_L^2 - m_R^2) \\ &= \frac{-1}{2k} \int_{-\infty}^{\infty} dx V_p(x) \Big|_0. \end{aligned} \quad (27)$$

The Born approximation for the step function potential has been obtained from the large k expansion of $\delta_{\text{step}}(k)$ in (23). The subscripts in (27) recall that the definition of the pseudopotential (see (19)) induces an implicit dependence on the (artificial) matching point x_m . Notably, this dependence disappears from the final result. This is the first step towards establishing the matching point independence of the VPE.

The integrals in $E_{\text{FD}}^{(1)}$ and $E_{\text{CT}}^{(1)}$ require further regularization when $m_L \neq m_R$. In that case, no further *finite renormalization* beyond the no tadpole condition is realizable.

6. Comparison with Known Results

Before presenting detailed numerical results for VPEs, we note that all simulations were verified to produce $S^\dagger S = \mathbf{1}$ after attaching pertinent flux factors to the scattering matrix (see (20)). These flux factors are not relevant for the VPE as they multiply to unity under the determinant in (13). In addition, the numerically obtained phase shifts (i.e., $(1/2i) \ln \det S$) have been monitored to not vary with x_m . Since this is also the case for the bound energies, the VPE is verified to be independent of the unrestricted choice for the matching point.

The VPE calculation based on (13) has been applied to the ϕ^4 kink and sine-Gordon soliton models that are defined via the potentials

$$U_K(\phi) = \frac{1}{2}(\phi^2 - 1)^2, \quad (28)$$

$$U_{\text{SG}}(\phi) = 4(\cos(\phi) - 1),$$

respectively. The soliton solutions $\phi_K = \tanh(x - x_0)$ and $\phi_{\text{SG}}(x) = 4 \arctan(e^{-2(x-x_0)})$ induce the scattering potentials

$$V_K(x) - m^2 = 6 \left[\tanh^2(x - x_0) - 1 \right], \quad (29)$$

$$V_{\text{SG}}(x) - m^2 = 8 \left[\tanh^2[2(x - x_0)] - 1 \right].$$

In both cases, we have identical dispersion relations at positive and negative spatial infinity: $m = m_L = m_R = 2$ for the dimensionless units introduced above. The simulation based on (13) reproduces the established results $E_{\text{vac}}^{(K)} = \sqrt{2}/4 - 3/\pi$ and $E_{\text{vac}}^{(\text{SG})} = -2/\pi$ [27]. These solitons break translational

invariance spontaneously and thus produce zero mode bound states in the fluctuation spectrum. In addition, the ϕ^4 kink possesses a bound state with energy $\sqrt{3}$ [27]. All bound states are easily observed using (25). The potentials in (29) are reflection symmetric about the soliton center x_0 and the method of (15) can be straightforwardly applied [11]. However, this method singles out x_0 (typically set to $x_0 = 0$) to determine the boundary condition in the differential equation and therefore cannot be used to establish translational invariance of the VPE. On the contrary, the boundary conditions for (18) are not at all sensitive to x_0 and we have applied the present method to compute the VPE for various choices of x_0 , all yielding the same numerical result.

The next step is to compute the VPE for asymmetric background potentials that have $m = m_L = m_R$. For the lack of a soliton model that produces such a potential, we merely consider a two-parameter set of functions

$$V_p(x) \longrightarrow V_{R,\sigma}(x) = Axe^{-x^2/\sigma^2} \quad (30)$$

for the pseudopotential in (18). Although (15) is not directly applicable, it is possible to relate $V_{R,\sigma}(x)$ to the symmetric potential

$$\begin{aligned} V_R(x) &= A \left[(x+R) e^{-(x+R)^2/\sigma^2} - (x-R) e^{-(x-R)^2/\sigma^2} \right] \\ &= V_R(-x) \end{aligned} \quad (31)$$

and apply (15). In the limit $R \rightarrow \infty$, interference effects between the two structures around $x = \pm R$ disappear, resulting in twice the VPE of (30). The numerical comparison is listed in Table 1. Indeed, the two approaches produce identical results as $R \rightarrow \infty$. The symmetrized version converges only slowly for wide potentials (large σ) causing obstacles for the numerical simulation that do not at all occur in the present approach.

7. Vacuum Polarization Energies in the ϕ^6 Model

We first discuss the VPE for the $a \neq 0$ case. A typical background potential is shown in Figure 1(a). Obviously, it is reflection invariant and thus the method based on (15) is applicable. In Table 2, we also compare our results to those from the heat kernel expansion of [15] since, to our knowledge, it is the only approach that has also been applied to the asymmetric $a = 0$ case in [14]. Not surprisingly, the two methods based on scattering data agree within numerical precision for all values of a . The heat kernel results also agree for moderate and large a ; but for small values, deviations of the order of 10% are observed. The heat kernel method relies on truncating the expansion of the exact heat kernel about the heat kernel in the absence of a soliton. Although in [15] the expansion has been carried out to the eleventh(!) order, leaving behind a very cumbersome calculation, this does not seem to provide sufficient accuracy for small a .

We are now in the position to discuss the VPE for $a = 0$ associated with the soliton $\phi_{K_1}(x)$ from (5). The potentials for the fluctuations and the resulting scattering data are shown in

Figure 4. By construction, the pseudopotential jumps at $x_m = 0$. However, neither the phase shift nor the bound state energy (the zero mode is the sole bound state) depends on x_m . As expected, the phase shift has a threshold cusp at $\sqrt{m_R^2 - m_L^2} = \sqrt{3}$ and approaches $\pi/2$ at zero momentum. This is consistent with Levinson's theorem in one space dimension [28] and the fact that there is only a single bound state. In total, we find significant cancellation between the bound state and continuum contributions

$$E_{\text{vac}} = -0.5 + 0.4531 = -0.0469. \quad (32)$$

The result $-0.1264\sqrt{2} = -0.1788$ (the factor $\sqrt{2}$ is added to adjust the datum from [14] to the present scale) of [14] was estimated relative to $V_\alpha(x) = (3/2)[1 + \tanh(\alpha x)]$ for $\alpha = 1$. Our results for various values of α are listed in Table 3. These results are consistent with $V_\alpha(x)$ turning into a step function for large α . For the particular value $\alpha = 1$, our relative VPE thus is $\Delta E_{\text{vac}} = -0.0469 - 0.1660 = -0.2129$. In view of the results shown in Table 2, especially for small a , these data match within the validity of the approximations applied in the heat kernel calculation.

8. Translational Variance

So far, we have computed the VPE for the ϕ^6 model soliton centered at $x_0 = 0$. We have already mentioned that there is translational invariance for the VPE of the kink and sine-Gordon solitons. It is also numerically verified for the asymmetric background (see (30)). In those cases, the two vacua at $x \rightarrow \pm\infty$ are equivalent and $q = k$ in (20). When shifting $x \rightarrow x + x_0$, the transmission coefficients (s_{11} and s_{22}) remain unchanged relative to the amplitude of the incoming wave while the reflection coefficients (s_{12} and s_{21}) acquire opposite phases. Consequently, $\det S$ is invariant. For unequal momenta, this invariance forfeits and the VPE depends on x_0 . This is reflected by the results in Table 4 in which we present the VPE for $V_\alpha(x) = (3/2)[1 + \tanh(\alpha(x + x_0))]$ and the ϕ^6 model soliton $1/\sqrt{1 + e^{-2(x+x_0)}}$. Obviously, there is a linear dependence of the VPE on x_0 with the slope insensitive to specific structure of the potential. This insensitivity is consistent with the above remark on the difference between the two momenta. Increasing x_0 shifts the vacuum with the bigger mass towards negative infinity, thereby removing states from the spectrum and hence decreasing the VPE.

The effect is immediately linked to varying the width of a symmetric barrier potential with height $m_R^2 - m_L^2 = 3$:

$$V_{\text{SB}}^{(x_0)}(x) = 3\Theta\left(\frac{x_0}{2} - |x|\right). \quad (33)$$

For this potential, the Jost solution (see (16)) can be obtained analytically [20] and the VPE has the limit

$$\lim_{x_0 \rightarrow \infty} \frac{E_{\text{vac}}[V_{\text{SB}}^{(x_0)}]}{x_0} \approx -0.102, \quad (34)$$

which again reveals the background independent slope observed above.

TABLE 1: The R dependent data are half the VPE for the symmetrized potential, (31) computed from (15). The data in the column “*present*” list the results obtained from (13) for the original potential (see (30)).

R	1.0	1.5	2.0	2.5	3.0	3.5	Present
$A = 2.5, \sigma = 10$	-0.0369	-0.0324	-0.0298	-0.0294	-0.0293	-0.0292	-0.0293
R	4.0	5.0	6.0	7.0	8.0	9.0	Present
$A = 0.2, \sigma = 4.0$	-0.0208	-0.0188	-0.0170	-0.0161	-0.0158	-0.0157	-0.0157

TABLE 2: Different methods to compute the VPE of the ϕ^6 soliton for $a \neq 0$.

a	0.001	0.01	0.05	0.1	0.2	1.0	1.5
Heat kernel ([15])	-1.953	-1.666	-1.447	-1.349	-1.239	-1.101	-1.293
Parity sep. (equation (15))	-2.145	-1.840	-1.595	-1.461	-1.298	-1.100	-1.295
Present (equation (13))	-2.146	-1.841	-1.596	-1.462	-1.297	-1.102	-1.297

TABLE 3: VPE for background potential $V_\alpha(x)$ defined in the main text. The entry “*step*” gives the VPE for the step function potential $V(x) = 3\Theta(x)$ using (23) and its Born approximation from (27) for $x_m = 0$.

α	1.0	2.0	5.0	10.0	30.0	Step
E_{vac}	0.1660	0.1478	0.1385	0.1363	0.1355	0.1355

TABLE 4: The VPE as a function of the position of the center of the potential for V_α and the ϕ^6 model soliton. ΔE_{vac} is the difference between the VPEs of the latter and V_1 .

x_0	E_{vac}				
	-2	-1	0	1	2
$\alpha = 5$	0.341	0.240	0.139	0.037	-0.064
$\alpha = 2$	0.351	0.250	0.148	0.046	-0.057
$\alpha = 1$	0.369	0.267	0.166	0.064	-0.038
ϕ^6	0.154	0.053	-0.047	-0.148	-0.249
ΔE_{vac}	-0.215	-0.214	-0.213	-0.212	-0.211

Having quantitatively determined the translation variance of the VPE, it is tempting to subtract $E_{\text{vac}}[V_{\text{SB}}^{(x_0)}]$. Unfortunately, this is not unique because x_0 is not the unambiguous center of the soliton. For example, employing the classical energy density $\epsilon(x)$ to define the position of the soliton $1/\sqrt{1 + e^{-2(x-\bar{x})}}$, which is formally centered at \bar{x} , as an expectation value leads to

$$x_s = \frac{\int dx x \epsilon(x)}{\int dx \epsilon(x)} = \bar{x} + \frac{1}{2}. \quad (35)$$

This changes the VPE by approximately 0.050. This ambiguity also hampers the evaluation of the VPE as half that of a widely separated kink–antikink pair

$$\phi_{K\bar{K}}(x) = [1 + e^{2(x-\bar{x})}]^{-1/2} + [1 + e^{-2(x+\bar{x})}]^{-1/2} - 1 \quad (36)$$

similar to the approach for (31). The corresponding background potential V_B is shown in Figure 5. For computing the VPE, the large contribution from the constant but nonzero

potential in the regime $|x| \leq \bar{x}$ should be eliminated. The above considerations lead to

$$\frac{1}{2} \lim_{\bar{x} \rightarrow \infty} \{E_{\text{vac}}[V_B] - 2E_{\text{vac}}[V_{\text{SB}}^{(2\bar{x})}]\} = -0.170, \quad (37)$$

$$\frac{1}{2} \lim_{\bar{x} \rightarrow \infty} \{E_{\text{vac}}[V_B] - 2E_{\text{vac}}[V_{\text{SB}}^{(2x_s)}]\} = -0.120.$$

When the VPE from $V_{\text{SB}}^{(2(\bar{x}+1.2))}$ is subtracted, the main result (see (32)) is matched. Eventually, this can be used to define the center of the soliton.

Now, we also understand why the VPE for $a \neq 0$ diverges as $a \rightarrow 0$ (cf. Table 2). In that limit, kink and antikink structures separate and the “vacuum” in between produces an ever-increasing contribution (in magnitude).

Finally, we discuss the link between the translational variance and the Krein–Friedel–Lloyd formula (see (9)). We have already reported the VPE for the step function potential when $x_m = 0$. We can also consider $x_m \rightarrow \infty$:

$$\frac{E_{\text{vac}}[V_{\text{step}}^{(x_m)}]}{|x_m|} \rightarrow -\text{sign}(x_m) \left[\int_0^{\sqrt{3}} \frac{dk}{4\pi} \frac{2k^2 - 3}{\sqrt{k^2 + 1}} + \int_{\sqrt{3}}^{\infty} \frac{dk}{4\pi} \frac{2k^2 - 2k\sqrt{k^2 - 3} - 3}{\sqrt{k^2 + 1}} \right] \approx 0.101 \text{sign}(x_m), \quad (38)$$

reproducing the linear dependence on the position from above. Formally, that is, without Born subtraction, the integral (see (38)) is dominated by

$$\begin{aligned} & \int \frac{dk}{2\pi} \frac{k}{\sqrt{k^2 + 1}} [k - \sqrt{k^2 - 3}] \\ & \sim \int \frac{dk}{2\pi} \sqrt{k^2 + 1} \frac{d}{dk} [\sqrt{k^2 - 3} - k] \\ & = \int \frac{dk}{2\pi} \sqrt{k^2 + 1} \frac{d}{dk} [q - k]. \end{aligned} \quad (39)$$

Essentially, this is that part of the level density that originates from the different dispersion relations at positive and negative spatial infinity.

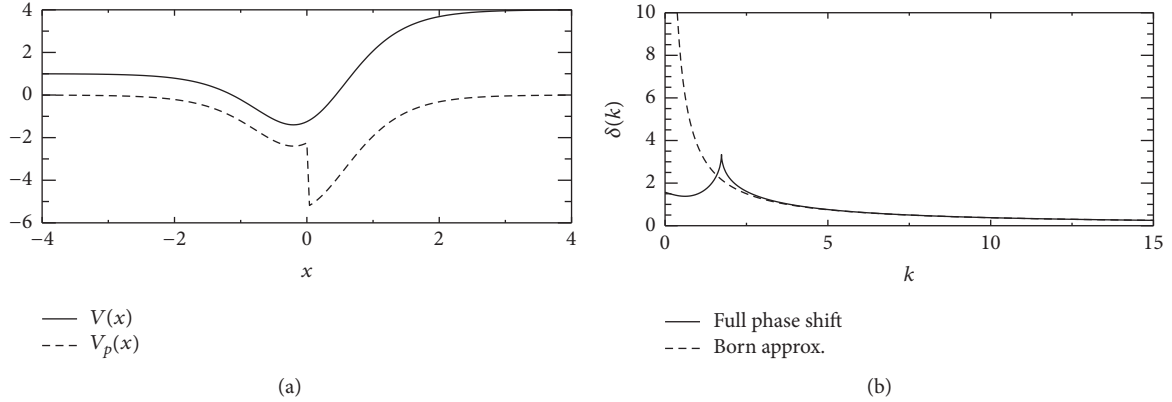


FIGURE 4: (a) Potential (V) and pseudopotential (V_p) for fluctuations about a ϕ^6 soliton with $a = 0$. The pseudopotential is shown for $x_m = 0$. (b) Resulting phase shift, that is, $(1/2i) \ln \det S$ (full line), and its Born approximation (dashed line).

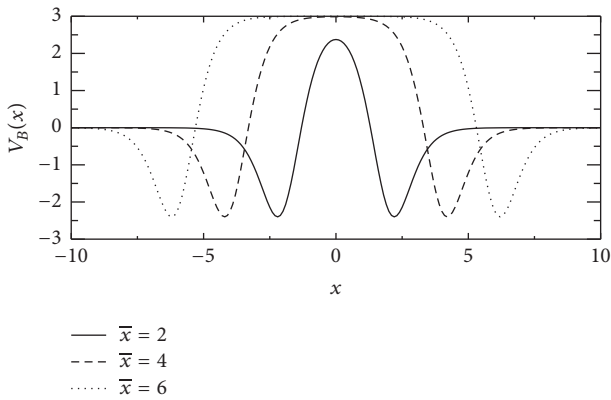


FIGURE 5: Background potential for the kink–antikink pair (see (36)) for different separation instances.

9. Conclusion

We have advanced the spectral methods for computing vacuum polarization energies (VPEs) to also apply to static localized background configurations in one space dimension that do not permit a parity decomposition for the quantum fluctuations. The essential progress is the generalization of the variable phase approach to such configurations. Being developed from spectral methods, it adopts their amenities, as, for example, an effective procedure to implement standard renormalization conditions. A glimpse at the bulky formulas for the heat kernel expansion (alternative method to the problem) in [14–16] immediately reveals the simplicity and effectiveness of the present approach. The latter merely requires numerically integrating ordinary differential equations and extracting the scattering matrix thereof (cf. (18) and (21)). Heat kernel methods are typically combined with ζ -function regularization. Then, the connection to standard renormalization conditions is not as transparent as for the spectral methods, though that is problematic only when nonlocal Feynman diagrams require renormalization, that is, in larger

than $D = 1 + 1$ dimensions or when fermion loops are involved.

We have verified the novel method by means of well-established results, as, for example, the ϕ^4 kink and sine-Gordon solitons. For these models, the approach directly ascertains translational invariance of the VPE. Yet, the main focus was on the VPE for solitons in ϕ^6 models because its soliton(s) may connect inequivalent vacua leading to background potentials that are not invariant under spatial reflection. This model is not strictly renormalizable. Nevertheless, at one-loop order, a well-defined result can be obtained from the no tadpole renormalization condition although no further finite renormalization is realizable because the different vacua yield additional infinities when integrating the counterterm. The different vacua also lead to different dispersion relations for the quantum fluctuations and thereby induce translational variance for a theory that is formulated by an invariant action. We argue that this variance is universal, as it is not linked to the particular structure of the background and can be related to the change in the level density that is basic to the Krein–Friedel–Lloyd formula (see (9)).

Besides attempting a deeper understanding of the variance by tracing it from the energy momentum tensor, future studies will apply the novel method to solitons of the ϕ^8 model. Its elaborated structure not only induces potentials that are reflection asymmetric but also leads to a set of topological indexes [29] that are related to different particle numbers. Then, the novel method will progress the understanding of quantum corrections to binding energies of compound objects in the soliton picture. Furthermore, the present results can be joined with the interface formalism [30], which augments additional coordinates along which the background is homogeneous, to explore the energy (densities) of domain wall configurations [31].

Disclosure

This work was presented at the 5th Winter Workshop on Non-Perturbative Quantum Field Theory, Sophia-Antipolis (France), March 2017.

Conflicts of Interest

The author declares that there are no conflicts of interest regarding the publication of this paper.

Acknowledgments

The author is grateful to the organizers for providing this worthwhile workshop. This work is supported in parts by the NRF under Grant 109497.

References

- [1] T. H. R. Skyrme, "A non-linear field theory," *Proceedings of the Royal Society A: Mathematical, Physical and Engineering Sciences*, vol. 260, pp. 127–138, 1961.
- [2] T. H. Skyrme, "The origins of Skyrmions," *International Journal of Modern Physics A. Particles and Fields. Gravitation. Cosmology*, vol. 3, no. 12, pp. 2745–2751, 1988, (Article reconstructed by I. Aitchison).
- [3] E. Witten, "Baryons in the $1/N$ expansion," *Nuclear Physics B*, vol. 160, no. 1, pp. 57–115, 1979.
- [4] G. S. Adkins, C. R. Nappi, and E. Witten, "Static properties of nucleons in the Skyrme model," *Nuclear Physics, Section B*, vol. 228, no. 3, pp. 552–566, 1983.
- [5] H. Weigel, vol. 743 of *Lecture Notes in Physics*, 2008.
- [6] D. T. J. Feist, P. H. C. Lau, and N. S. Manton, "Skyrmions up to baryon number 108," *Physical Review D*, vol. 87, Article ID 085034, 2013.
- [7] F. G. Scholtz, B. Schwesinger, and H. B. Geyer, "The Casimir energy of strongly bound $B = 2$ configurations in the Skyrme model," *Nuclear Physics, Section A*, vol. 561, no. 4, pp. 542–556, 1993.
- [8] F. Meier and H. Walliser, "Quantum corrections to baryon properties in chiral soliton models," *Physics Reports*, vol. 289, no. 6, pp. 383–450, 1997.
- [9] R. L. Jaffe, "Perhaps a stable dihyperon," *Physical Review Letters*, vol. 38, p. 195, 1977, (Erratum: *Physical Review Letters* vol. 38, p. 617, 1977).
- [10] A. P. Balachandran, A. Barducci, F. Lizzi, V. G. J. Rodgers, and A. Stern, "Doubly strange dibaryon in the chiral model," *Physical Review Letters*, vol. 52, no. 11, pp. 887–890, 1984.
- [11] N. Graham, M. Quandt, and H. Weigel, *Spectral Methods in Quantum Field Theory*, vol. 777 of *Lecture Notes in Physics*, Springer, Berlin, Germany, 2009.
- [12] M. A. Lohe, "Soliton structures in P_2 ," *Physical Review D*, vol. 20, no. 12, pp. 3120–3130, 1979.
- [13] M. A. Lohe and D. M. O'Brien, "Soliton mass corrections and explicit models in two dimensions," *Physical Review. D. Particles and Fields. Third Series*, vol. 23, no. 8, pp. 1771–1780, 1981.
- [14] A. Alonso Izquierdo, W. Garcia Fuertes, M. A. Gonzalez Leon, and J. Mateos Guilarte, "Generalized zeta functions and one-loop corrections to quantum kink masses," *Nuclear Physics. B*, vol. 635, no. 3, pp. 525–557, 2002.
- [15] A. Alonso Izquierdo and J. M. Guilarte, "One-loop kink mass shifts: a computational approach," *Nuclear Physics B*, vol. 852, no. 3, pp. 696–735, 2011.
- [16] A. Alonso-Izquierdo and J. Mateos Guilarte, "On a family of (1+1)-dimensional scalar field theory models: kinks, stability, one-loop mass shifts," *Annals of Physics*, vol. 327, no. 9, pp. 2251–2274, 2012.
- [17] E. Elizalde, *Ten Physical Applications of Spectral Zeta Functions*, vol. 35 of *Lecture Notes in Physics*, Springer, Berlin, Germany, 1995.
- [18] E. Elizalde, S. D. Odintsov, A. Romeo, A. A. Bytsenko, and S. Zerbini, *Zeta Regularization Techniques with Applications*, World Scientific Publishing, River Edge, NJ, USA, 1994.
- [19] K. Kirsten, "Spectral functions in mathematics and physics," *AIP Conference Proceedings*, vol. 484, no. 1, p. 106, 1999.
- [20] H. Weigel, "Vacuum polarization energy for general backgrounds in one space dimension," *Physics Letters B*, vol. 766, pp. 65–70, 2017.
- [21] J. S. Faulkner, "Scattering theory and cluster calculations," *Journal of Physics C: Solid State Physics*, vol. 10, no. 23, pp. 4661–4670, 1977.
- [22] N. Graham, R. L. Jaffe, V. Khemani, M. Quandt, M. Scandurra, and H. Weigel, "Calculating vacuum energies in renormalizable quantum field theories: a new approach to the Casimir problem," *Nuclear Physics B*, vol. 645, no. 3, pp. 49–84, 2002.
- [23] E. Farhi, N. Graham, P. Haagenen, and R. L. Jaffe, "Finite quantum fluctuations about static field configurations," *Physics Letters B*, vol. 427, no. 3-4, pp. 334–342, 1998.
- [24] R. Calegero, *Variable Phase Approach to Potential Scattering*, Academic Press, New York, NY, USA, 1967.
- [25] R. G. Newton, *Scattering Theory of Waves and Particles*, Springer, New York, NY, USA, 2nd edition, 1982.
- [26] K. Chadan and P. C. Sabatier, *Inverse Problems in Quantum Scattering Theory*, Texts and Monographs in Physics, Springer, New York, NY, USA, 2nd edition, 1989.
- [27] R. Rajaraman, *Solitons and Instantons*, North-Holland, Amsterdam, The Netherlands, 1982.
- [28] G. Barton, "Levinson's theorem in one dimension: heuristics," *Journal of Physics. A. Mathematical and General*, vol. 18, no. 3, pp. 479–494, 1985.
- [29] V. A. Gani, V. Lensky, and M. A. Lizunova, "Kink excitation spectra in the (1+1)-dimensional," *Journal of High Energy Physics*, vol. 2015, article 147, 2015.
- [30] N. Graham, R. L. Jaffe, M. Quandt, and H. Weigel, "Quantum energies of interfaces," *Physical Review Letters*, vol. 87, Article ID 131601, 2001.
- [31] A. Parnachev and L. G. Yaffe, "One-loop quantum energy densities of domain wall field configurations," *Physical Review D*, vol. 62, Article ID 105034, 2000.

Research Article

Radiative Decay Widths of Ground and Excited States of Vector Charmonium and Bottomonium

Hluf Negash¹ and Shashank Bhatnagar²

¹Department of Physics, Samara University, P.O. Box 132, Samara, Ethiopia

²Department of Physics, University Institute of Sciences, Chandigarh University, Mohali 140413, India

Correspondence should be addressed to Hluf Negash; h2002hluf@yahoo.com

Received 26 January 2017; Accepted 14 May 2017; Published 20 June 2017

Academic Editor: Thierry Grandou

Copyright © 2017 Hluf Negash and Shashank Bhatnagar. This is an open access article distributed under the Creative Commons Attribution License, which permits unrestricted use, distribution, and reproduction in any medium, provided the original work is properly cited. The publication of this article was funded by SCOAP³.

We study the radiative decay widths of vector quarkonia for the process of $J/\psi(nS) \rightarrow \eta_c(nS)\gamma$ and $\Upsilon(nS) \rightarrow \eta_b(nS)\gamma$ (for principal quantum numbers $n = 1, 2, 3$) in the framework of Bethe-Salpeter equation under the covariant instantaneous ansatz using a 4×4 form of BSE. The parameters of the framework were determined by a fit to the mass spectrum of ground states of pseudoscalar and vector quarkonia, such as η_c , η_b , J/ψ , and Υ . These input parameters so fixed were found to give good agreements with data on mass spectra of ground and excited states of pseudoscalar and vector quarkonia, leptonic decay constants of pseudoscalar and vector quarkonia, two-photon decays, and two-gluon decays of pseudoscalar quarkonia in our recent paper. With these input parameters so fixed, the radiative decay widths of ground (1S) and excited (2S, 3S) states of heavy vector quarkonia (J/Ψ and Υ) are calculated and found to be in reasonable agreement with data.

1. Introduction

Studies on mass spectra and decays of heavy quarkonia ($c\bar{c}$ and $b\bar{b}$) have become a hot topic in recent years, due to observation of many new states at various high energy accelerators at BABAR, Belle, CLEO, and BES-III collaborations [1–4]. All this has opened up new challenges in theoretical understanding of heavy hadrons and provide an important tool for exploring the structure of these simplest bound states in QCD and for studying the nonperturbative (long distance) behavior of strong interactions.

As regards the dynamical framework, to investigate these properties is concerned; many nonperturbative approaches, such as lattice QCD [5], chiral perturbation theory [6], QCD sum rules [7], heavy-quark effective theory [8], NRQCD [9], dynamical-equation based approaches like Schwinger-Dyson equation and Bethe-Salpeter equation (BSE) [10–15], and potential models [16] have been proposed to deal with the long distance property of QCD.

Bethe-Salpeter equation (BSE) [11, 15, 17–19] is a conventional approach in dealing with relativistic bound state problems. From the solutions, we can obtain useful information

about the inner structure of hadrons, which is also crucial in treating hadronic decays. The BSE framework which is firmly rooted in field theory provides a realistic description for analyzing hadrons as composite objects. Despite its drawback of having to input model-dependent kernel, these studies have become an interesting topic in recent years, since calculations have shown that BSE framework using phenomenological potentials can give satisfactory results as more and more data are being accumulated. The BSE is frequently adopted as starting point of QCD inspired models, due to the fact that this equation has a firm base in quantum field theory.

In a recent work [20, 21], we employed a 4×4 representation for two-body ($q\bar{q}$) BS amplitude for calculating both the mass spectra and the transition amplitudes for various processes. However, the price one pays in this approach is to solve a coupled set of Salpeter equations for both pseudoscalar and vector quarkonia. However, in [21], we explicitly showed that these coupled Salpeter equations can indeed get decoupled in the heavy-quark approximation, leading to mass spectral equations with analytical solutions for both masses, as well as eigenfunctions for all the ground and excited states of pseudoscalar and vector $c\bar{c}$ and $b\bar{b}$ systems

in an approximate harmonic oscillator basis. These analytical forms of eigenfunctions for ground and excited states so obtained were used to evaluate the transition amplitudes for different processes in [21]. Thus, in [21], we had calculated the mass spectrum, weak decay constants, two-photon decay widths and two-gluon decay widths of ground (1S) and radially excited (2S, 3S, ...) states of pseudoscalar charmonium and bottomonium such as η_c and η_b , as well as the mass spectrum and leptonic decay constants of ground state (1S) and excited (2S, 1D, 3S, 2D, 4S, and 3D) states of vector charmonium and bottomonium such as J/ψ and Υ , using this formulation of 4×4 Bethe-Salpeter equation under covariant instantaneous ansatz (CIA). Our results were in good agreement with data (wherever available) and other models. However, in all the above processes, the quark antiquark loop involved a single hadron-quark vertex, which was simple to handle.

However for the transitions such as $V \rightarrow P + \gamma$, the process requires calculation of triangle quark-loop diagram involving two hadron-quark vertices and is difficult to evaluate in BSE-CIA, which gives rise to complexities in amplitudes. However in [22, 23], they demonstrated an explicit mathematical procedure for handling such problems in 4×4 representation of BSE. Thus, in the present work, we will precisely apply an instantaneous formalism employing 4×4 BSE under CIA for transitions involving the process, $V \rightarrow P\gamma$, where such problems do not enter in the calculations of [21].

This paper is organized as follows. In Section 2, we give the formulation of 4×4 BSE under CIA. In Section 3, we give the derivation of the hadronic process $V \rightarrow P + \gamma$ in the framework of 4×4 BSE under CIA and calculate its radiative decay widths. The numerical results for radiative decay widths of the processes are worked out. Section 4 is reserved for discussions and conclusion.

2. Formulation of BSE under CIA

We give a short derivation of Salpeter equations in this section, giving only the main steps. The 4D BSE for $q\bar{q}$ comprising equal mass fermionic quarks of momenta $p_{1,2}$ and masses $m_1 = m_2 (=m)$, respectively, is written in 4×4 representation as

$$\begin{aligned} & (\not{p}_1 - m_1) \Psi(P, q) (\not{p}_2 + m_2) \\ &= \frac{i}{(2\pi)^4} \int d^4 q' K(q, q') \Psi(P, q'), \end{aligned} \quad (1)$$

where the 4×4 BS wave function is sandwiched between the inverse propagators of the quark and the antiquark, whose individual momenta $p_{1,2}$ are related to the internal momentum q and total momentum P of hadron of mass M as $p_{1,2\mu} = (1/2)P_\mu \pm q_\mu$. We further decompose the internal momentum, q_μ , as the sum of its transverse component, $\hat{q}_\mu = q_\mu - (q \cdot P)P_\mu/P^2$ (which is orthogonal to total hadron momentum P_μ), and the longitudinal component, $\sigma P_\mu = (q \cdot P)P_\mu/P^2$ (which is parallel to P_μ). Thus, $q_\mu = (M\sigma, \hat{q})$, where the transverse component, \hat{q} , is an effective 3D vector, while the longitudinal component, $M\sigma$, plays the role of the time

component. The 4D volume element in this decomposition is $d^4 q = d^3 \hat{q} M d\sigma$. To obtain the 3D BSE and the hadron-quark vertex, use an ansatz on the BS kernel K in (1) which is assumed to depend on the 3D variables $\hat{q}_\mu, \hat{q}'_\mu$ as

$$K(q, q') = K(\hat{q}, \hat{q}'). \quad (2)$$

Hence, the longitudinal component, $M\sigma$ of q_μ , does not appear in the form $K(\hat{q}, \hat{q}')$ of the kernel and we define 3D wave function $\psi(\hat{q})$ as

$$\psi(\hat{q}) = \frac{i}{2\pi} \int M d\sigma \Psi(P, q). \quad (3)$$

Substituting (3) in (1), with definition of kernel in (2), we get a covariant version of Salpeter equation

$$\begin{aligned} & (\not{p}_1 - m_1) \Psi(P, q) (\not{p}_2 + m_2) \\ &= \int \frac{d^3 \hat{q}'}{(2\pi)^3} K(\hat{q}, \hat{q}') \psi(\hat{q}'), \end{aligned} \quad (4)$$

and the 4D BS wave function can be written as

$$\Psi(P, q) = S_F(p_1) \Gamma(\hat{q}) S_F(-p_2), \quad (5)$$

where

$$\Gamma(\hat{q}) = \int \frac{d^3 \hat{q}'}{(2\pi)^3} K(\hat{q}, \hat{q}') \psi(\hat{q}') \quad (6)$$

plays the role of hadron-quark vertex function. Following a sequence of steps given in [20, 21], we obtain four Salpeter equations:

$$\begin{aligned} (M - 2\omega) \psi^{++}(\hat{q}) &= -\Lambda_1^+(\hat{q}) \Gamma(\hat{q}) \Lambda_2^+(\hat{q}), \\ (M + 2\omega) \psi^{--}(\hat{q}) &= \Lambda_1^-(\hat{q}) \Gamma(\hat{q}) \Lambda_2^-(\hat{q}), \end{aligned} \quad (7)$$

$$\psi^{+-}(\hat{q}) = \psi^{-+}(\hat{q}) = 0$$

with the energy projection operators, $\Lambda_j^\pm(\hat{q}) = (1/2\omega_j)[\not{P}\omega_j/M \pm I(j)(m_j + \not{\hat{q}})]$, $\omega_j^2 = m_j^2 + \hat{q}^2$, and $I(j) = (-1)^{j+1}$, where $j = 1, 2$ for quarks and antiquarks, respectively. The projected wave functions, $\psi^{\pm\pm}(\hat{q})$, in Salpeter equations are obtained by the operation of the above projection operators on $\psi(\hat{q})$ (for details see [20, 21]) as

$$\psi^{\pm\pm}(\hat{q}) = \Lambda_1^\pm(\hat{q}) \frac{\not{P}}{M} \psi(\hat{q}) \frac{\not{P}}{M} \Lambda_2^\pm(\hat{q}). \quad (8)$$

To obtain the mass spectral equation, we have to start with the above four Salpeter equations and solve the instantaneous Bethe-Salpeter equation. However, the last two equations do not contain eigenvalue M and are thus employed to obtain constraint conditions on the Bethe-Salpeter amplitudes associated with various Dirac structures in $\psi(\hat{q})$, as shown in detail in [21]. The framework is quite general so far. In fact the above four equations constitute an eigenvalue problem that should lead to evaluation of mass spectra of pseudoscalar and vector charmonium and bottomonium states such as η_c ,

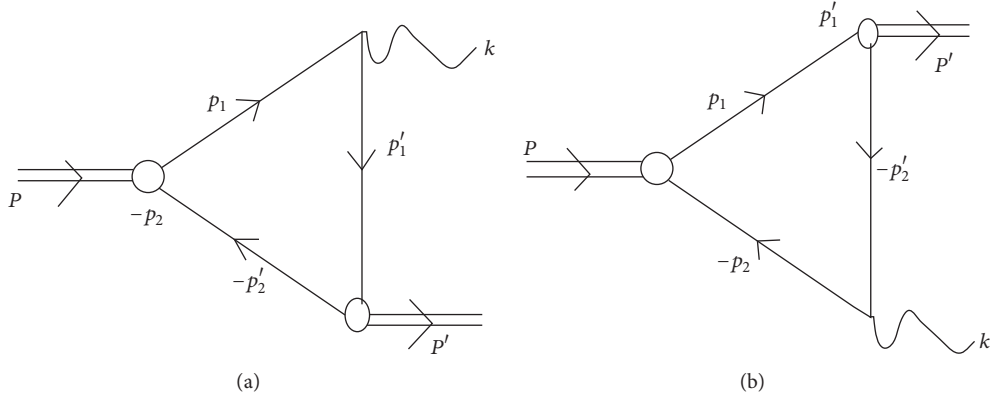


FIGURE 1: Feynman diagram for the first and second figures corresponding to the quark and antiquark emitting the photon, respectively, for the transition $V \rightarrow P\gamma$.

η_b , J/ψ , and Υ (see [21]). The numerical results [21] of mass spectra of P and V quarkonia participating in the radiative decays studied in this paper are listed in Section 3. We now give details of calculation of decay widths for the process, $V \rightarrow P + \gamma$, in the next section.

3. Electromagnetic Transition of $V \rightarrow P + \gamma$

The lowest order, Feynman diagrams for the process, $V \rightarrow P\gamma$, are given in Figure 1, where $V(1^{--})$ and $P(0^{+-})$ are vector and pseudoscalar quarkonia, respectively. The second diagram is obtained from the first one by reversing the directions of internal fermionic lines.

The electromagnetic transition amplitude M_{fi} , corresponding to Figures 1(a) and 1(b), is given by the one-loop momentum integral as in [23, 31, 32]:

$$M_{fi} = -ie_q \int \frac{d^4 q}{(2\pi)^4} \cdot \text{Tr} [\bar{\Psi}_P(P', q') \not{\epsilon} \Psi_V(P, q) S_F^{-1}(-p_2) + \bar{\Psi}_P(P', q') S_F^{-1}(p_1) \Psi_V(P, q) \not{\epsilon}], \quad (9)$$

where P and P' are momenta of the initial and final hadrons, respectively, p_1 , p'_1 , $-p_2$, and $-p'_2$ are initial and final momenta of the quark and antiquark, respectively, k is the momentum of the outgoing photon, and Ψ_P and Ψ_V are the 4D BS wave functions of pseudoscalar and vector quarkonia involved in the process and are expressed as $\Psi_P(P, q) = S_F(p_1)\Gamma(\hat{q})S_F(-p_2)$ and $\bar{\Psi}_P(P', q') = S_F(-p'_2)\Gamma(\hat{q}')S_F(p'_1)$. e_q is the electric charge of quarks. ϵ_μ is the polarization vector of the emitted photon. We have used the momentum relations $P = p_1 + p_2$, $P' = p'_1 + p'_2$, $k = P - P'$, and $p_2 = p'_2$ for first diagram. However for second diagram, the last momentum relation is $p_1 = p'_1$, while the other relations are the same as in first diagram. Here, the second term (coming from

Figure 1(b)) in (9) gives the same contribution as the first term (coming from Figure 1(a)), and hence we can write M_{fi} as

$$M_{fi} = -2ie_q \int \frac{d^4 q}{(2\pi)^4} \text{Tr} [\bar{\Psi}_P(P', q') \not{\epsilon} \Psi_V(P, q) S_F^{-1}(-p_2)] \quad (10)$$

with an overall multiplicative factor of 2.

This equation can be reduced to 3D forms by defining the 3D wave function, $\psi(\hat{q}) = (i/2\pi) \int M d\sigma \Psi(P, q)$. Thus, one can write the instantaneous Bethe-Salpeter form for the electromagnetic transition amplitude between two bound states as (see [33])

$$M_{fi} = -\frac{2e_q}{M} \int \frac{d^3 \hat{q}}{(2\pi)^3} \cdot \text{Tr} \{ \not{P} \bar{\psi}_P^{++}(\hat{q}') \not{\epsilon} \psi_V^{++}(\hat{q}) - \not{P} \bar{\psi}_P^{--}(\hat{q}') \not{\epsilon} \psi_V^{--}(\hat{q}) \}, \quad (11)$$

where we resolve the amplitude corresponding to the first term (i.e., Figure 1(a)) in the previous equation into $++$ and $--$ components, where the dominant contribution comes from the $++$ components, while the contribution from the $--$ components is less than 1 percent [34]. Thus we can, to a good approximation, write the total amplitude for the process $V \rightarrow P\gamma$ in terms of only the $++$ components as

$$M_{fi} = -\frac{2e_q}{M} \int \frac{d^3 \hat{q}}{(2\pi)^3} \text{Tr} \{ \not{P} \bar{\psi}_P^{++}(\hat{q}') \not{\epsilon} \psi_V^{++}(\hat{q}) \}, \quad (12)$$

where $\hat{q}' = \hat{q} + (1/2)\hat{P}'$ and M is the mass of the initial quarkonia. The relativistic BS wave function of $P(0^{+-})$ meson bound state is taken as in [21]:

$$\psi_P(\hat{q}') = N'_P \left[M' + \not{P}' + \frac{\hat{q}' \not{P}'}{m} \right] \gamma_5 \phi_P(\hat{q}'), \quad (13)$$

where P' is the momentum of the final state P -quarkonia, N'_P is the BS normalization of the final state P -quarkonia, and M' is the mass of the final state P -quarkonia.

The relativistic BS wave function of $V(1^{--})$ quarkonium can ultimately be written as in [21]:

$$\begin{aligned} \psi_V(\hat{q}) &= N_V \left[M \not{\epsilon} + \hat{q} \cdot \epsilon \frac{M}{m} + \not{\epsilon} \not{P} + \frac{\not{P} \hat{q} \cdot \epsilon}{m} - \frac{\not{P} \not{\epsilon} \hat{q}}{m} \right] \phi_V(\hat{q}). \end{aligned} \quad (14)$$

Here, ϵ is the polarization vector of the vector quarkonia and N_V is the BS normalizer of the initial state quarkonia. We wish to mention that (13) above is obtained by starting from the most general expression for $\Psi(P, q)$ in Eq. (17) of [21]. The general decomposition of instantaneous wave function in the center of mass frame of dimensionality M is given in Eq. (18) of [21]. This instantaneous wave function $\Psi^P(\hat{q})$ is put into the last two Salpeter equations, and the constraint conditions on the amplitudes (given in Eq. (19) of [21]) are obtained. We thus obtain Eq. (20) of [21]. This is then put into the first two Salpeter equations to obtain the two coupled equations (Eq. (21) of [21]). Solving them simultaneously leads to (13) of present paper (which is Eq. (23) in [21]), written in terms of ϕ_P . Similarly we obtain $\Psi_V(\hat{q})$ in (14) written in terms of ϕ_V . These scalar functions $\phi_{P,V}(\hat{q})$ satisfy the harmonic oscillator equation, Eq. (37) of [21], whose solutions are worked out by using the power series method in Eq. (37)–(41) of [21], with plots of these wave functions given in Figures 1-2 (for P -quarkonia) and Figures 3-4 (for V quarkonia) in [21]. Thus we want to mention that the complete 2-fermion wave functions, $\Psi_{P,V}(\hat{q})$, are ultimately expressed in terms of summation over various Dirac structures multiplying a single scalar function $\phi_{P,V}(\hat{q})$, whose detailed algebraic expressions (Gaussian functions) are not approximations, but are obtained as analytic solutions of the algebraic form of the mass spectral equations for P and V quarkonia (with the complete spectrum written down in terms of principal quantum number N in Eq. (35)-(36) of [21]) in an approximate harmonic oscillator basis.

The projected wave function for positive energy, $\psi^{++}(\hat{q})$, is obtained by the operation of projection operators on $\psi_P(\hat{q})$ and $\psi_V(\hat{q})$, respectively, as in (8):

$$\begin{aligned} \psi_P^{++}(\hat{q}') &= \Lambda_1^+(\hat{q}') \frac{\not{P}'}{M'} \psi_P(\hat{q}') \frac{\not{P}'}{M'} \Lambda_2^+(\hat{q}') \\ \psi_V^{++}(\hat{q}) &= \Lambda_1^+(\hat{q}) \frac{\not{P}}{M} \psi_V(\hat{q}) \frac{\not{P}}{M} \Lambda_2^+(\hat{q}), \end{aligned} \quad (15)$$

where $\Lambda_{1,2}^+(\hat{q}) = (1/2\omega)[(\not{P}/M)\omega \pm m \pm \hat{q}]$, $\Lambda_{1,2}^+(\hat{q}') = (1/2\omega')[(\not{P}'/M')\omega' \pm m \pm \hat{q}']$, are called projection operators and $\omega^2 = m^2 + \hat{q}^2$ and $\omega'^2 = m^2 + \hat{q}'^2$. The relativistic positive energy wave function of equal mass pseudoscalar quarkonia in the center of mass system can be expressed as

$$\begin{aligned} \psi_P^{++}(\hat{q}') &= \frac{N'_P \phi_P(\hat{q}')}{2} \gamma_5 \left\{ M' \left[\frac{m^2}{\omega'^2} + \frac{m}{\omega'} - \frac{\hat{q}'^2}{m\omega'} \right] \right. \\ &\quad \left. - \not{P}' \left[\frac{m^2}{\omega'^2} + \frac{m}{\omega'} \right] + \hat{q}' \not{P}' \left[\frac{m}{\omega'^2} + \frac{1}{\omega'} \right] \right\}. \end{aligned} \quad (16)$$

And the relativistic positive energy wave function of equal mass vector quarkonia in the center of mass system can be written as

$$\begin{aligned} \psi_V^{++}(\hat{q}) &= \frac{N_V \phi_V(\hat{q})}{2} \left\{ M \left[\frac{m^2}{\omega^2} - \frac{m}{\omega} + \frac{\hat{q}^2}{m\omega} \right] \not{\epsilon} + M \hat{q} \right. \\ &\quad \cdot \epsilon \left[\frac{m}{\omega^2} - \frac{1}{\omega} \right] + \left[\frac{m^2}{\omega^2} - \frac{m}{\omega} \right] \not{\epsilon} \not{P} + \hat{q} \cdot \epsilon \left[\frac{m}{\omega^2} - \frac{1}{\omega} \right] \not{P} \\ &\quad \left. - \left[\frac{m}{\omega^2} - \frac{1}{\omega} \right] \not{P} \not{\epsilon} \hat{q} + \frac{\hat{q} \cdot \epsilon}{m\omega} \not{\epsilon} \not{P} - \frac{M \hat{q} \cdot \epsilon}{m\omega} \not{\epsilon} \right\}. \end{aligned} \quad (17)$$

The conjugate of $\psi_P^{++}(\hat{q}')$ is evaluated from $\bar{\psi}_P^{++}(\hat{q}') = \gamma^0 (\psi_P^{++})^\dagger \gamma^0$, after a sequence of steps is expressed as

$$\begin{aligned} \bar{\psi}_P^{++}(\hat{q}') &= -\frac{N'_P \phi_P(\hat{q}')}{2} \gamma_5 \left\{ M' \left[\frac{m^2}{\omega'^2} + \frac{m}{\omega'} - \frac{\hat{q}'^2}{m\omega'} \right] \right. \\ &\quad \left. - \not{P}' \left[\frac{m^2}{\omega'^2} + \frac{m}{\omega'} \right] + \not{P}' \hat{q}' \left[\frac{m}{\omega'^2} + \frac{1}{\omega'} \right] \right\}. \end{aligned} \quad (18)$$

Now, if we evaluate the total transition amplitude using (12), (17), and (18), we get

$$M_{fi} = -\frac{e_q N'_P N_V}{2M} \int \frac{d^3 \hat{q}}{(2\pi)^3} \phi_P(\hat{q}') \phi_V(\hat{q}) [\text{TR}], \quad (19)$$

where

$$\begin{aligned} [\text{TR}] &= \text{Tr} \left\{ -\gamma_5 \not{P} \not{P}' \left[\frac{m^2}{\omega'^2} + \frac{m}{\omega'} \right] \right. \\ &\quad \cdot \left[M \left[\frac{m^2}{\omega^2} - \frac{m}{\omega} + \frac{\hat{q}^2}{m\omega} \right] \not{\epsilon} \not{\epsilon}' - \left[\frac{m}{\omega^2} - \frac{1}{\omega} \right] \not{\epsilon} \not{P} \not{\epsilon}' \hat{q} \right. \\ &\quad \left. - \frac{M \hat{q} \cdot \epsilon}{m\omega} \not{\epsilon} \hat{q} \right] + \gamma_5 \not{P} \not{P}' \hat{q}' \left[\frac{m}{\omega'^2} + \frac{1}{\omega'} \right] \left[M \hat{q} \right. \\ &\quad \left. \cdot \epsilon \left[\frac{m}{\omega^2} - \frac{1}{\omega} \right] \not{\epsilon}' + \left[\frac{m^2}{\omega^2} - \frac{m}{\omega} \right] \not{\epsilon} \not{\epsilon}' \not{P} + \frac{\hat{q} \cdot \epsilon}{m\omega} \not{\epsilon} \not{P} \right] \left. \right\}. \end{aligned} \quad (20)$$

Evaluating trace over the gamma matrices, one can obtain the expression:

$$\begin{aligned} [\text{TR}] &= -4M\epsilon_{\mu\nu\alpha\beta} P_\mu P'_\nu \epsilon_\alpha \epsilon'_\beta \left[\frac{m}{\omega'^2} + \frac{1}{\omega'} \right] \\ &\quad \cdot \left[\frac{m^3}{\omega^2} - \frac{m^2}{\omega} + \left(\frac{m}{\omega^2} - \frac{1}{\omega} \right) \hat{q} \cdot \hat{q}' \right], \end{aligned} \quad (21)$$

where P and P' are momenta of the initial (V) and final (P) quarkonia, respectively. One can rewrite the transition amplitude after evaluation of the gamma matrices as

$$\begin{aligned} M_{fi} &= 2e_q N'_P N_V \int \frac{d^3 \hat{q}}{(2\pi)^3} \phi_P(\hat{q}') \phi_V(\hat{q}) \left[\frac{m}{\omega'^2} + \frac{1}{\omega'} \right] \\ &\quad \cdot \left[\frac{m^3}{\omega^2} - \frac{m^2}{\omega} + \left(\frac{m}{\omega^2} - \frac{1}{\omega} \right) \hat{q} \cdot \hat{q}' \right] \\ &\quad \cdot \epsilon_{\mu\nu\alpha\beta} P_\mu P'_\nu \epsilon_\alpha \epsilon'_\beta. \end{aligned} \quad (22)$$

The decay width for $V \rightarrow P\gamma$ can be expressed as (see [32])

$$\Gamma_{V \rightarrow P\gamma} = \frac{|\vec{P}'|}{8\pi M^2} |M_{fi}|^2; \quad (23)$$

$$|\vec{P}'| = \frac{1}{2M} [M^2 - M'^2].$$

From (22) for total amplitude, M_{tot} , one can obtain

$$|M_{fi}|^2 = |f(\hat{q})|^2 (\epsilon_{\mu\nu\alpha\beta} P_\mu P'_\nu \epsilon_\alpha \epsilon_\beta)^2 \quad (24)$$

$$= (M^4 + 10M^2 M'^2 + M'^4) |f(\hat{q})|^2,$$

where

$$f(\hat{q}) = 2e_q N'_P N_V \int \frac{d^3 \hat{q}'}{(2\pi)^3} \phi_P(\hat{q}') \phi_V(\hat{q}) \left[\frac{m}{\omega'^2} + \frac{1}{\omega'} \right] \quad (25)$$

$$\cdot \left[\frac{m^3}{\omega^2} - \frac{m^2}{\omega} + \left(\frac{m}{\omega^2} - \frac{1}{\omega} \right) \hat{q} \cdot \hat{q}' \right].$$

One can obtain the expression of the decay rate of heavy quarkonia for the process, $V \rightarrow P\gamma$, as

$$\Gamma_{V \rightarrow P\gamma} = \frac{1}{64\pi} \left[M^3 + \frac{M'^4}{M} - M'^2 M - \frac{M'^6}{M^3} \right]^3 |f(\hat{q})|^2. \quad (26)$$

M' and M are the masses of the pseudoscalar heavy quarkonia (η_c, η_b) and vector heavy quarkonia ($J/\psi, \Upsilon$), respectively. In the expression for $f(\hat{q})$, N_V and N'_P are the BS normalizers for heavy vector and pseudoscalar quarkonia, respectively, which are given in a simple form as in [21]:

$$N_V = \left[16mM_V \int \frac{d^3 \hat{q}}{(2\pi)^3} \frac{\hat{q}^2}{\omega^3} \phi_V^2(\hat{q}) \right]^{-1/2}, \quad (27)$$

$$N'_P = \left[\frac{16M_P}{m} \int \frac{d^3 \hat{q}'}{(2\pi)^3} \frac{\hat{q}'^2}{\omega'} \phi_P^2(\hat{q}') \right]^{-1/2}.$$

The ground state (1S) wave function and the radial wave functions for the 2S and 3S excitations for initial heavy vector quarkonia are written as in Eq. (41) of [21]:

$$\phi_V(1S, \hat{q}) = \frac{1}{\pi^{3/4} \beta_V^{3/2}} e^{-\hat{q}^2/2\beta_V^2},$$

$$\phi_V(2S, \hat{q}) = \left(\frac{3}{2} \right)^{1/2} \frac{1}{\pi^{3/4} \beta_V^{3/2}} \left(1 - \frac{2\hat{q}^2}{3\beta_V^2} \right) e^{-\hat{q}^2/2\beta_V^2}, \quad (28)$$

$$\phi_V(3S, \hat{q}) = \left(\frac{15}{8} \right)^{1/2} \frac{1}{\pi^{3/4} \beta_V^{3/2}} \left(1 - \frac{20\hat{q}^2}{15\beta_V^2} + \frac{4\hat{q}^4}{15\beta_V^4} \right) e^{-\hat{q}^2/2\beta_V^2}$$

TABLE 1: Input parameters of BSE-CIA framework.

C_0	ω_0 (GeV)	Λ (GeV)	A_0	m_c (GeV)	m_b (GeV)
0.210	0.150	0.200	0.010	1.490	5.070

TABLE 2: β_P and β_V values for ground state and excited states of $\eta_c, \eta_b, J/\psi$, and Υ (in GeV) in present calculation (BSE-CIA).

1^- state	β_V	0^- state	β_P
$J/\psi(1S)$	0.2466	$\eta_c(1S)$	0.3486
$\psi(2S)$	0.2442	$\eta_c(2S)$	0.3454
$\psi(3S)$	0.2420	$\eta_c(3S)$	0.3422
$\Upsilon(1S)$	0.5066	$\eta_b(1S)$	0.7165
$\Upsilon(2S)$	0.5018	$\eta_b(2S)$	0.7097
$\Upsilon(3S)$	0.4972	$\eta_b(3S)$	0.7032

and the ground state (1S) wave function and the radial wave functions for the 2S and 3S excitations for final heavy pseudoscalar quarkonia are written as in Eq. (41) of [21]:

$$\phi_P(1S, \hat{q}') = \frac{1}{\pi^{3/4} \beta_P^{3/2}} e^{-\hat{q}'^2/2\beta_P^2},$$

$$\phi_P(2S, \hat{q}') = \left(\frac{3}{2} \right)^{1/2} \frac{1}{\pi^{3/4} \beta_P^{3/2}} \left(1 - \frac{2\hat{q}'^2}{3\beta_P^2} \right) e^{-\hat{q}'^2/2\beta_P^2}, \quad (29)$$

$$\phi_P(3S, \hat{q}') = \left(\frac{15}{8} \right)^{1/2} \frac{1}{\pi^{3/4} \beta_P^{3/2}} \left(1 - \frac{20\hat{q}'^2}{15\beta_P^2} + \frac{4\hat{q}'^4}{15\beta_P^4} \right) e^{-\hat{q}'^2/2\beta_P^2},$$

where $\hat{q}' = \hat{q} + (1/2)|\vec{P}'|$ and $|\vec{P}'| = (M_V/2)(1 - M_P^2/M_V^2)$.

The inverse range parameters for pseudoscalar and vector meson, respectively, are $\beta_P = (4(m\omega_{\hat{q}\hat{q}'}^2/\sqrt{1+2A_0(N+3/2)}))^{1/4}$ and $\beta_V = (2(m\omega_{\hat{q}\hat{q}'}^2/\sqrt{1+2A_0(N+3/2)}))^{1/4}$ and are dependent on the input kernel and contain the dynamical information, and they differ from each other only due to spin-spin interactions.

We had recently calculated the mass spectrum of ground and excited states of P and V quarkonia in [21]. The input parameters employed in this calculation that were fit from the mass spectrum of ground state pseudoscalar and vector quarkonia in [21] are given in Table 1.

The numerical values of inverse range parameters β_P and β_V for various P and V quarkonia in the radiative transitions studied in this paper are listed in Table 2.

We had fixed the input parameters by studying the mass spectra for P and V quarkonia for a number of states. However in Tables 3 and 4, we list only the spectra of the quarkonia for which we have done calculations of radiative decay widths in this paper.

Numerical Results. We use the same input parameters listed in Table 1, to calculate the decay widths for the process $V \rightarrow P + \gamma$. The results of radiative decay widths of our model are listed in Table 5.

TABLE 3: Masses of ground and radially excited states of η_c and η_b (in GeV) in present calculation (BSE-CIA) along with experimental data and their masses in other models.

	BSE - CIA	Expt. [4]	Pot. model [24]	QCD sum rule [7]	LQCD [25]	Re. P. model [26]
$M_{\eta_c(1S)}$	2.9509	2.983 ± 0.0007	2.980	3.11 ± 0.52	3.292	2.981
$M_{\eta_c(2S)}$	3.7352	3.639 ± 0.0013	3.600		4.240	3.635
$M_{\eta_c(3S)}$	4.4486		4.060			3.989
$M_{\eta_b(1S)}$	9.0005	9.398 ± 0.0032	9.390	9.66 ± 1.65	7.377	9.398
$M_{\eta_b(2S)}$	9.7215	9.999 ± 0.0028	9.947		8.202	9.990
$M_{\eta_b(3S)}$	10.4201		10.291			10.329

TABLE 4: Masses of ground and radially excited states of heavy vector quarkonium, J/ψ and Υ , in BSE-CIA along with their masses in other models and experimental data (all units are GeV).

	BSE - CIA	Expt. [4]	Rel. Pot. model [26]	Pot. model [24]	BSE [27]	LQCD [28]
$M_{J/\psi(1S)}$	3.0974	3.0969 ± 0.000011	3.096	3.0969	3.0969	3.099
$M_{\psi(2S)}$	3.6676	3.6861 ± 0.00034	3.685	3.6890	3.686	3.653
$M_{\psi(3S)}$	4.1945	4.03 ± 0.001	4.039	4.1407	4.065	4.099
$M_{\Upsilon(1S)}$	9.6719	9.4603 ± 0.00026	9.460	9.4603	9.460	
$M_{\Upsilon(2S)}$	10.1926	10.0233 ± 0.00031	10.023	9.9814	10.029	
$M_{\Upsilon(3S)}$	10.6979	10.3552 ± 0.00005	10.355	10.3195	10.379	

TABLE 5: Radiative decay widths of equal mass heavy vector quarkonium of ground state (1S) and radially excited states (2S, 3S) in present calculation (BSE-CIA) along with their decay widths in other models and experimental data (all values are in unit of Kev).

Transition	Our work	Expt. [4]	LFM [29]	PM [30]
$\Gamma_{J/\psi(1S) \rightarrow \eta_c(1S)\gamma}$	2.0054	1.5687 ± 0.011	1.67 ± 0.05	1.8
$\Gamma_{\psi(2S) \rightarrow \eta_c(2S)\gamma}$	0.5709	0.2093 ± 0.002		0.4
$\Gamma_{\psi(3S) \rightarrow \eta_c(3S)\gamma}$	0.2984			
$\Gamma_{\Upsilon(1S) \rightarrow \eta_b(1S)\gamma}$	0.3387		$0.043^{+0.09}_{-0.03}$	0.001
$\Gamma_{\Upsilon(2S) \rightarrow \eta_b(2S)\gamma}$	0.1053			0.0002
$\Gamma_{\Upsilon(3S) \rightarrow \eta_b(3S)\gamma}$	0.0781			

4. Discussions and Conclusion

We have employed a 3D reduction of BSE (with a 4×4 representation for two-body ($q\bar{q}$) BS amplitude) under covariant instantaneous ansatz (CIA) and used it for calculating the amplitudes and decay widths for ground and radially excited states of vector (J/Ψ and Υ) quarkonia in the process, $V \rightarrow P + \gamma$.

The numerical values of decay widths calculated in this BSE framework for (1S, 2S, 3S) states of J/ψ and Υ are shown in Table 5. The numerical calculation in this work has been done using Mathematica. We first fit our parameters to the ground state masses of η_c , η_b , J/ψ , and Υ . Using the input parameters (along with the input quark masses) listed in Table 1, we obtained the best fit to these ground state masses. The same set of parameters above was used to calculate the masses of all the other (excited) states of η_c , η_b , J/ψ , and Υ , as well as the leptonic decay constants of these states. Two-photon as well as two-gluon decay widths of η_c and η_b were further studied (see our recent paper [21]).

The results obtained for decay width of ground and radially excited states of J/ψ and Υ are somewhat on the higher side in comparison to central values of data for these states,

which might be probably due to the absence of the negative energy part employed in (11), where we have considered only the positive energy part (as in [34] employed earlier for heavy mesons). However, from Table 5, a wide range of variation of radiative decay widths of $J/\Psi(1S)$ and $\Psi(2S)$ states in different models can be observed. However, the important thing is that our radiative decay width values for vector quarkonia show a marked decrease as one goes from 1S to 3S state for J/ψ and Υ , which is again in conformity with data and other models. We have also given our predictions for radiative decay widths of $\Psi(3S)$, $\Upsilon(1S)$, $\Upsilon(2S)$, and $\Upsilon(3S)$ states, for which data is currently not yet available. The aim of doing this study was to mainly test our analytic forms of wave functions in (28)-(29) obtained as solutions of mass spectral equations in an approximate harmonic oscillator basis obtained analytically from the 4×4 BSE as our starting point (that had so far given good predictions for leptonic decays of P and V quarkonia and the two-photon and the two-gluon decays of P -quarkonia [21]), to the single photon radiative decays of V quarkonia. This would in turn lead to validation of our approach, which provides a much deeper insight than the purely numerical calculations in 4×4 BSE approach that are prevalent in the literature.

In the process of arriving at analytic solution of spectra by solving the coupled Salpeter equations, we have worked in approximate harmonic oscillator basis, also employing approximation $\omega \sim m$ for heavy quarks. We do concede that some numerical accuracy has been lost in the process, but at the same time we have obtained a much deeper understanding of the mass spectra of quarkonia, where the equations are expressible in terms of the principal quantum number N . We wish to mention that to the best of our knowledge we have not encountered any work in 4×4 representation of BSE that treats this problem analytically. On the contrary all the other 4×4 approaches adopt a purely numerical approach of solving the coupled set of Salpeter equations, which may enhance the numerical accuracy, but this is at the expense of a deeper understanding of the spectral problem. We further wish to mention that the correctness of our approximations can be judged by the fact that our plots of wave functions obtained analytically for various states of P and V quarkonia [21] are very similar to the corresponding plots of wave functions of various states of these quarkonia obtained by purely numerical approach in [13].

We are also not aware of any other BSE framework, involving 4×4 BS amplitude, with all the Dirac structures incorporated (in fact many works use only the leading Dirac structure), that treats these problems analytically and uses the algebraic forms of wave functions derived analytically from mass spectral equation for calculation of various transitions. To the best of our knowledge, all the other 4×4 BSE approaches treat this problem numerically after obtaining the coupled set of equations.

Conflicts of Interest

The authors declare that they have no conflicts of interest.

References

- [1] B. Aubert, M. Bona, Y. Karyotakis et al., "Evidence for the $\eta_b(1S)$ Meson in Radiative $Y(2s)$ Decay," *Physical Review Letters*, vol. 103, Article ID 161801, 2009, (BaBar collaboration).
- [2] K.-F. Chen, W.-S. Hou, I. Adachi et al., "Observation of an enhancement in $e^+e^- \rightarrow Y(1S)\pi^+\pi^-$, $Y(2S)\pi^+\pi^-$, and $Y(3S)\pi^+\pi^-$ production near $\sqrt{s} = 10.89$ GeV," *Physical Review D - APS Physics*, vol. 82, (Belle Collaboration), Article ID 091106, 2010.
- [3] K. W. Edwards, R. Janicek, P. M. Patel et al., "Study of B Decays to Charmonium States: $B \rightarrow \eta_c K$ and $B \rightarrow \chi_{c0} K$," *Physical Review Letters*, vol. 86, no. 30, 2001, (CLEO collaboration).
- [4] K. Olive, K. Agashe, and C. Amsler, "Review of particle physics," *Chinese Physics C*, vol. 38, no. 9, Article ID 090001, 2014, (Particle Data Group).
- [5] C. McNielle, C. T. H. Davies, E. Follana, K. Hornbostel, and G. P. Lepage, "Heavy meson masses and decay constants from relativistic heavy quarks in full lattice QCD," *Physical Review D*, vol. 86, 16 pages, 2012, (HPQCD Collaboration).
- [6] J. Gasser and H. Leutwyler, "Chiral perturbation theory to one loop," *Annals of Physics*, vol. 158, no. 1, pp. 142–210, 1984.
- [7] E. Veli Veliev, K. Azizi, H. Sundu, and N. Aksit, "Investigation of heavy-heavy pseudoscalar mesons in thermal QCD sum rules," *Journal of Physics G*, vol. 39, Article ID 015002, 2012.
- [8] M. Neubert, "Heavy-quark symmetry," *Physics Reports*, vol. 245, 259 pages, 1994.
- [9] G. T. Bodwin, E. Braaten, and G. P. Lepage, "Rigorous QCD analysis of inclusive annihilation and production of heavy quarkonium," *Physical Review D*, vol. 51, article 1125, p. 1125, 1995.
- [10] C. H. L. Smith, "A relativistic formulation of the quark model for mesons," *Annals of Physics*, vol. 53, 521 pages, 1969.
- [11] A. N. Mitra and B. M. Sodermark, "A dynamical principle for 3D–4D interlinkage in Salpeter-like equations," *Nuclear Physics A*, vol. 695, no. 1-4, pp. 328–352, 2001.
- [12] R. Alkofer and L. von Smekal, "The infrared behaviour of QCD Green's functions: confinement, dynamical symmetry breaking, and hadrons as relativistic bound states," *Physics Reports A: Review Section of Physics Letters*, vol. 353, no. 5-6, pp. 281–465, 2001.
- [13] C.-H. Chang and G. L. Wang, "Spectrum for heavy quarkonia and mixture of the relevant wave functions within the framework of Bethe-Salpeter equation," *Science in China G*, vol. 53, 2010, G53.
- [14] R. Ricken, M. Koll, D. Merten, B. Metsch, and H. Petry, "A relativistic quark model for mesons with an instanton-induced interaction," *The European Physical Journal A*, vol. 9, p. 221, 2000.
- [15] A. N. Mitra and S. Bhatnagar, "A hadron-quark vertex function: interconnection between 3D and 4D wave functions," *International Journal of Modern Physics A*, vol. 7, p. 121, 1992.
- [16] S. Patel, P. C. Vinodkumar, and S. Bhatnagar, "Decay rates of charmonia within a quark-antiquark confining potentials," *Chinese Physics C*, vol. 40, no. 5, Article ID 053102, 2016.
- [17] A. N. Mitra, "QCD motivated BSE-SDE framework for quark dynamics under Markov-Yukawa transversality- a unified view of qq-bar and qqq systems," *Proceedings of the Indian National Science Academy*, vol. 65, p. 527, 1999.
- [18] S. Bhatnagar, D. S. Kulshreshtha, and A. N. Mitra, "How big are the decay constants f_p of heavy-light mesons?" *Physics Letters B*, vol. 263, no. 3-4, pp. 485–490, 1991.
- [19] S. Bhatnagar, J. Mahecha, and Y. Mengesha, "Relevance of various Dirac covariants in hadronic Bethe-Salpeter wave functions in electromagnetic decays of ground state vector mesons," *Physical Review D*, vol. 90, Article ID 014034, 2014.
- [20] H. Negash and S. Bhatnagar, "Mass spectrum and leptonic decay constants of ground and radially excited states of η_c and η_b in a Bethe-Salpeter equation framework," *International Journal of Modern Physics E*, vol. 24, no. 4, Article ID 1550030, 2015.
- [21] H. Negash and S. Bhatnagar, "Spectroscopy of ground and excited states of pseudoscalar and vector charmonium and bottomonium," *International Journal of Modern Physics E*, vol. 25, Article ID 1650059, 29 pages, 2016.
- [22] C.-H. Chang, J.-K. Chen, and G.-L. Wang, "Instantaneous formulation for transitions between two instantaneous bound states and its gauge invariance," *Communications in Theoretical Physics*, vol. 46, no. 3, pp. 467–480, 2006.
- [23] C.-H. Chang, J.-K. Chen, and G.-L. Wang, "The instantaneous formulations for bethe salpeter equation and radiative transitions between two bound-states," <https://arxiv.org/abs/hep-th/0312250>.
- [24] K. B. V. Bhagyesh, A. P. Kumar, and J. Monterio, "Heavy quarkonium spectra and its decays in a nonrelativistic model with Hulthen potential," *Journal of Physics G: Nuclear and Particle Physics*, vol. 38, no. 8, Article ID 085001, 2011.

- [25] T. Burch, C. DeTar, M. Di Pierro et al., “Quarkonium mass splittings in three-flavor lattice QCD,” *Physical Review D*, vol. 81, Article ID 034508, 2010.
- [26] D. Ebert, R. N. Faustov, and V. O. Galkin, “Spectroscopy and Regge trajectories of heavy quarkonia in the relativistic quark model,” *Physics of Atomic Nuclei*, vol. 76, no. 12, pp. 1554–1562, 2013.
- [27] G.-L. Wang, “Decay constants of heavy vector mesons in relativistic Bethe–Salpeter method,” *Physics Letters B*, vol. 633, 2006.
- [28] T. Kawanai and S. Sasaki, “Potential description of the charmonium from lattice QCD,” *AIP Conference Proceedings*, September 2016.
- [29] H.-M. Choi, “Decay constants and radiative decays of heavy mesons in light-front quark model,” *Physical Review D*, Article ID 073016, 2007.
- [30] S. F. Radford and W. W. Repko, “Potential model calculations and predictions for heavy quarkonium,” *Physical Review D - Particles, Fields, Gravitation and Cosmology*, vol. 75, no. 7, Article ID 074031, 2007.
- [31] N. N. Singh and A. N. Mitra, “Hadronic transition amplitudes under null-plane Bethe–Salpeter dynamics,” *Physical Review D*, vol. 38, no. 5, article 1454, pp. 1454–1468, 1988.
- [32] E. Mengesha and S. Bhatnagar, “Radiative decays of equal mass vector mesons in a Bethe–Salpeter equation framework,” *International Journal of Modern Physics E*, vol. 21, Article ID 1250084, 2012.
- [33] G.-H. Wang and G.-L. Wang, “Radiative E1 decays of X(3872),” *Physics Letters B*, vol. 9, no. 4, 9 pages, 2011.
- [34] T. Wang, G.-L. Wang, Y. Jiang, and W.-L. Ju, “EM Decay of X(3872) as the $1^1D_2(2^-)$ charmonium,” *Journal of Physics G: Nuclear and Particle Physics*, vol. 2013, 2013.

Research Article

On the Emergence of the Coulomb Forces in Quantum Electrodynamics

Jan Naudts

Physics Department, University of Antwerp, Universiteitsplein 1, 2610 Antwerpen, Belgium

Correspondence should be addressed to Jan Naudts; jan.naudts@uantwerpen.be

Received 6 April 2017; Accepted 16 May 2017; Published 6 June 2017

Academic Editor: Thierry Grandou

Copyright © 2017 Jan Naudts. This is an open access article distributed under the Creative Commons Attribution License, which permits unrestricted use, distribution, and reproduction in any medium, provided the original work is properly cited. The publication of this article was funded by SCOAP³.

A simple transformation of field variables eliminates Coulomb forces from the theory of quantum electrodynamics. This suggests that Coulomb forces may be an emergent phenomenon rather than being fundamental. This possibility is investigated in the context of reducible quantum electrodynamics. It is shown that states exist which bind free photon and free electron fields. The binding energy peaks in the long-wavelength limit. This makes it plausible that Coulomb forces result from the interaction of the electron/positron field with long-wavelength transversely polarized photons.

1. Introduction

Quantum electrodynamics (QED), although very successful, is *not* a mathematically rigorous theory. Several difficulties have to be resolved or circumvented during the search for a consistent theory. One of them is the excess number of degrees of freedom in the description of the electromagnetic fields. In this context, the approach of Gupta [1] and Bleuler [2] is well known. An alternative is found in the work of Creutz [3]. He uses a unitary transformation which yields wave functions which do not undergo Coulomb forces. In quantum chromodynamics, the light cone gauge is used because then only transverse gluons remain [4]. In the present work, the assumption is that only transverse photons exist and that the number of degrees of freedom of the electromagnetic field is two. The argument of Creutz is used in opposite direction to define field operators which satisfy the Maxwell equations in presence of Coulomb forces.

Recently, Verlinde [5, 6] developed a cosmological theory in which gravity forces are emergent forces, in the sense that they are produced by other, more fundamental, forces of nature. A similar statement is investigated here for the role of Coulomb forces in QED. Not only are the degrees of freedom of the electromagnetic field limited to two, but also the Hamiltonian does not contain a Coulomb potential.

Further mathematical problems of QED disappear if one abandons the axiom that representations of the canonical commutation and anticommutation relations must be irreducible. This reducible QED is studied in the work of Czachor and collaborators (see [7–9] and references given in these papers). This formalism can be simplified along the lines worked out by the author in a series of papers [10–12].

The reduction of the representation involves an integration over three-dimensional wave vectors. At fixed wave vector, the system is purely quantum mechanical and consists of a pair of harmonic oscillators at each position in space-time to cover transversely polarized photons. A 16-dimensional Hilbert space describes the different states of an electron-positron field.

The mediation of Coulomb forces by transverse photons can be understood by analogy with the polaron problem of Solid State Physics. The polaron [13] is a state binding an electron with quantized lattice vibrations. In a polarized medium, the electric field of the electron is completely screened by redistribution of charges in its vicinity. The remaining interactions between electron and medium result in an attractive force between pairs of polarons. In some situations, it is strong enough to form bipolarons.

The present work shows that a free electron field can form a bound state with transversely polarized photons to form

a dressed electron field. By analogy with the polaron case, one can then expect that dressed electrons interact with each other and that Coulomb forces can be explained in this way.

The next section introduces a transformation of field variables which adds Coulomb forces to transverse photons interacting with a charge field. The new field variables form what is called here the emergent picture of QED. They satisfy the full Maxwell equations. Section 3 highlights some aspects of reducible QED. Section 4 discusses the proof of the existence of bound states of transverse photons in interaction with the electron field. The final section gives a short discussion of what actually has been achieved.

2. The Emergent Picture

In [3], the temporal gauge, also called Weyl gauge or Hamiltonian gauge, is used. A unitary transformation \widehat{V} is defined by a generator $\widehat{T}(\mathbf{x})$ through

$$\widehat{V} = \exp\left(i \int d^3\mathbf{x} \widehat{T}(\mathbf{x})\right). \quad (1)$$

The generator is of the form

$$\widehat{T}(\mathbf{x}) = \frac{q}{4\pi} \int d^3\mathbf{y} \widehat{\mathbf{A}}(\mathbf{x}) \cdot \frac{\mathbf{x} - \mathbf{y}}{|\mathbf{x} - \mathbf{y}|^3} \widehat{j}_0(\mathbf{y}). \quad (2)$$

Here, q is the elementary unit of charge. Bold characters are used to indicate 3-vectors. The result of [3], in the context of standard QED, is that

$$\widehat{V} \nabla \cdot \widehat{\mathbf{E}} \widehat{V}^{-1} = \nabla \cdot \widehat{\mathbf{E}} - q \widehat{j}_0, \quad (3)$$

where $\widehat{\mathbf{E}}(x)$ are the electric field operators. If they satisfy Gauss's law in the presence of a charge distribution $\widehat{j}_0(\mathbf{x})$, then $\widehat{V} \widehat{\mathbf{E}} \widehat{V}^{-1}$ satisfies Gauss's law in absence of charges.

In the present work, the trick of [3] is directly applied to define new electric field operators:

$$\begin{aligned} \widehat{E}''_{\alpha}(x) &= \widehat{E}'_{\alpha}(x) \\ &+ \frac{\mu_0 c}{4\pi} \frac{\partial}{\partial x^{\alpha}} \int d\mathbf{y} \frac{1}{|\mathbf{x} - \mathbf{y}|} \widehat{U}(-x^0) \widehat{j}^0(\mathbf{y}, 0) \widehat{U}(x^0). \end{aligned} \quad (4)$$

Here, $\widehat{U}(x^0) = \exp(-ix^0 \widehat{H}/\hbar c)$ is the time evolution of the interacting system. The new operators are marked with a double prime to distinguish them from the operators of the noninteracting system and those of the interacting system. The latter are denoted with a single prime. One verifies immediately that Gauss' law is satisfied:

$$\sum_{\alpha} \frac{\partial}{\partial x^{\alpha}} \widehat{E}''_{\alpha}(x) = -\mu_0 c \widehat{j}^{0\prime}(x). \quad (5)$$

The second term of (4) is the Coulomb contribution to the electric field. The curl of this term vanishes. Hence, it is obvious to take

$$\widehat{B}''_{\alpha}(x) \equiv \widehat{B}'_{\alpha}(x). \quad (6)$$

This implies the second of the four equations of Maxwell, stating that the divergence of $\widehat{B}''_{\alpha}(x)$ vanishes. Also the fourth equation, absence of magnetic charges, follows immediately because $\widehat{E}''(x)$ and $\widehat{E}'(x)$ have the same curl. Faraday's law remains to be written as

$$(\nabla \times \widehat{B}''(x))_{\alpha} - \frac{1}{c} \frac{\partial}{\partial x^0} \widehat{E}''_{\alpha}(x) = -\mu_0 \widehat{j}''_{\alpha}(x) \quad (7)$$

with

$$\widehat{j}''_{\alpha}(x) = -\frac{1}{\mu_0 c} \frac{\partial}{\partial x^0} (\widehat{E}''_{\alpha}(x) - \widehat{E}'_{\alpha}(x)). \quad (8)$$

Finally, take $\widehat{j}''_0(x) = \widehat{j}'_0(x)$. A short calculation shows that the newly defined current operators $\widehat{j}''_{\mu}(x)$ satisfy the continuity equation.

One concludes that a formalism of QED is possible which does not postulate the existence of longitudinal or scalar photons. Two pictures coexist: the original Heisenberg picture and what is called here the *emergent* picture. In both pictures, the time evolution of all operators is the same, but the definition of the electromagnetic field operators differs. In the original description, only transversely polarized photons exist. On the other hand, the field operators of the emergent picture satisfy the full Maxwell equations, including Coulomb forces.

3. Reducible QED

A dominant characteristic of reducible QED, in the version used here, is that many expressions look familiar from standard QED, except that integrations over the wave vector are missing. They are postponed to the evaluation of quantum expectation values. As a consequence, field operators depend on both position x in spacetime and wave vector \mathbf{k} in \mathbb{R}^3 . For instance, the electromagnetic potential operators are defined by

$$\begin{aligned} \widehat{A}_{\alpha}(x) &= \frac{1}{2} \lambda \varepsilon_{\alpha}^{(H)}(\mathbf{k}^{\text{ph}}) \left[e^{-ik_{\mu}^{\text{ph}} x^{\mu}} \widehat{a}_{\text{H}} + e^{ik_{\mu}^{\text{ph}} x^{\mu}} \widehat{a}_{\text{H}}^{\dagger} \right] \\ &+ \frac{1}{2} \lambda \varepsilon_{\alpha}^{(V)}(\mathbf{k}^{\text{ph}}) \left[e^{-ik_{\mu}^{\text{ph}} x^{\mu}} \widehat{a}_{\text{V}} + e^{ik_{\mu}^{\text{ph}} x^{\mu}} \widehat{a}_{\text{V}}^{\dagger} \right]. \end{aligned} \quad (9)$$

Here, \widehat{a}_{H} , $\widehat{a}_{\text{H}}^{\dagger}$, \widehat{a}_{V} , and $\widehat{a}_{\text{V}}^{\dagger}$ are the creation and annihilation operators of horizontally, respectively, vertically polarized photons. The dispersion relation of the photon is $k_0^{\text{ph}} = |\mathbf{k}^{\text{ph}}|$ as usual. $\varepsilon_{\alpha}^{(H)}(\mathbf{k}^{\text{ph}})$ and $\varepsilon_{\alpha}^{(V)}(\mathbf{k}^{\text{ph}})$ are polarization vectors. The parameter λ is introduced for dimensional reasons.

A consequence of the missing integration over the wave vector is that equal-time fields become noncommutative. For instance, a calculation starting from (9) shows that

$$\begin{aligned} &[\widehat{A}_{\alpha}(\mathbf{x}, 0), \widehat{A}_{\beta}(\mathbf{y}, 0)] \\ &= \frac{i\lambda^2}{2} F_{\alpha, \beta}(\mathbf{k}^{\text{ph}}) \sin(\mathbf{k}^{\text{ph}} \cdot (\mathbf{x} - \mathbf{y})), \end{aligned} \quad (10)$$

where $F(\mathbf{k}^{\text{ph}})$ projects onto the plane orthogonal to \mathbf{k}^{ph} . If the integration over \mathbf{k}^{ph} is executed, then the standard result of vanishing equal-time commutators follows.

Another feature of the theory is that wave functions are properly normalized for each wave vector separately. For instance, if ψ describes an electron/positron field, then $\psi_{\mathbf{k}}$ is a wave function in the \mathbf{k} th Fock space and satisfies $\langle \psi_{\mathbf{k}} | \psi_{\mathbf{k}} \rangle = 1$ for each value of \mathbf{k} . Superpositions of wave functions with different wave vector are allowed. The general wave function is therefore of the form

$$\psi_{\mathbf{k}} = \sum_{X \subset \{1,2,3,4\}} \sqrt{\rho_X(\mathbf{k})} |X\rangle \quad \text{for any } \mathbf{k}. \quad (11)$$

The set X selects one of the 16 possible states of an electron/positron field. The empty set \emptyset refers to the vacuum state $|\emptyset\rangle$. Normalization requires that

$$\sum_{X \subset \{1,2,3,4\}} \rho_X(\mathbf{k}) = 1 \quad \text{for any } \mathbf{k}. \quad (12)$$

Ultraviolet divergences are avoided by requiring that $\rho_X(\mathbf{k})$ with $X \neq \emptyset$ vanishes for large values of $|\mathbf{k}|$. Similarly, the general wave function of the free electromagnetic field is of the form

$$\psi_{\mathbf{k}^{\text{ph}}} = \sum_{m,n=0}^{\infty} \sqrt{\rho_{m,n}(\mathbf{k}^{\text{ph}})} e^{i\phi(m,n)} |m,n\rangle. \quad (13)$$

Normalization requires that

$$\sum_{m,n=0}^{\infty} \rho_{m,n}(\mathbf{k}^{\text{ph}}) = 1 \quad \text{for any } \mathbf{k}^{\text{ph}}. \quad (14)$$

The Dirac currents $\hat{j}^{\mu}(x)$ are defined in terms of Dirac spinors $\hat{\psi}_r(x)$ which satisfy a free Dirac equation (see [11] for details). The Dirac equation is only used to define currents $\hat{j}^{\mu}(x)$ in absence of interaction with the electromagnetic fields. No interacting Dirac equation is considered. Instead, the interactions between the free field operators are described by the usual interaction Hamiltonian in a Heisenberg picture. See (17) below.

4. Bound States

Let \hat{b}_1^{\dagger} denote the creation operator for an electron with spin up. An example of a realistic electron field is described by

$$\psi^{\text{el}} = e^{i\chi(\mathbf{k})} \sqrt{1 - \rho^{\text{el}}(\mathbf{k})} |\emptyset\rangle + \sqrt{\rho^{\text{el}}(\mathbf{k})} \hat{b}_1^{\dagger} |\emptyset\rangle. \quad (15)$$

Similarly, a realistic wave function for a horizontally polarized photon is

$$\psi^{\text{ph}} = \sqrt{\rho^{\text{ph}}(\mathbf{k}^{\text{ph}})} \hat{a}_H^{\dagger} |\emptyset\rangle + \sqrt{1 - \rho^{\text{ph}}(\mathbf{k}^{\text{ph}})} |\emptyset\rangle. \quad (16)$$

The Hamiltonian is the usual one, with interaction part

$$\hat{H}^I = \int d\mathbf{x} \hat{j}^{\mu}(\mathbf{x}, 0) \hat{A}_{\mu}(\mathbf{x}, 0). \quad (17)$$

Assume that $\rho^{\text{el}}(-\mathbf{k}^{\text{el}}) = \rho^{\text{el}}(\mathbf{k}^{\text{el}})$. Then the average interaction energy of a product state $\psi = \psi^{\text{ph}} \psi^{\text{el}}$ vanishes for symmetry

reasons. However, there exist entangled wave functions which lower the total energy.

Choose, for instance, an entangled wave function of the form

$$\begin{aligned} \psi_{\mathbf{k}^{\text{ph}}, \mathbf{k}} = & \left[\tau(\mathbf{k}^{\text{ph}}, \mathbf{k}) \hat{a}_H^{\dagger} + 1 - \tau(\mathbf{k}^{\text{ph}}, \mathbf{k}) \right] \\ & \cdot \sqrt{\rho(\mathbf{k}^{\text{ph}}) \rho^{\text{el}}(\mathbf{k})} \hat{b}_1^{\dagger} |\emptyset\rangle \\ & + \sqrt{1 - \rho(\mathbf{k}^{\text{ph}}) \rho^{\text{el}}(\mathbf{k})} |\emptyset\rangle, \end{aligned} \quad (18)$$

where $\tau(\mathbf{k}^{\text{ph}}, \mathbf{k})$ equals either 1 or 0. Assume in addition that the electron density $\rho^{\text{el}}(\mathbf{k})$ has a Gaussian shape. Then an explicit calculation shows that the binding energy peaks for long-wavelength horizontally polarized photons with wave vector \mathbf{k}^{ph} in principle direction 1 (see [12] for detailed calculations). Moreover, the total energy is lower than that of the free electron. One concludes that there exist states binding an electron field and a transversely polarized photon field.

5. Discussion

In a theory with only transverse photons and no Coulomb forces, a simple transformation of the field variables, given by (4), introduces new variables which satisfy the full Maxwell equations. The new variables form what is called here the emergent picture of QED. The time evolution of operators is the same in the emergent picture as in the original Heisenberg picture. Hence, one can avoid introducing Coulomb forces if one does not want to have them.

Is this transformation more than a mathematical trick? A plausible explanation of the physics behind this transformation is that long-wavelength transverse photons produce effective forces between different parts of the electron/positron field. The expectation is that these effective forces coincide with what is known as Coulomb forces.

Investigation of the scenario sketched above starts with a mathematical proof that transverse photons do interact with the electron/positron field and even can form bound states. This proof is given in the context of reducible QED because this formalism allows for a mathematically rigorous treatment. Details of the proof are found elsewhere [12]. The next thing to do is an analysis of the time evolution of these bound states. This analysis is still missing.

Conflicts of Interest

The author declares that there are no conflicts of interest regarding the publication of this paper.

References

- [1] S. N. Gupta, "Theory of longitudinal photons in quantum electrodynamics," *Proceedings of the Physical Society. Section A*, vol. 63, no. 7, article no. 301, pp. 681–691, 1950.
- [2] K. Bleuler, "Eine neue methode zur Behandlung der longitudinalen und skalaren photonen," *Helvetica Physica Acta*, vol. 23, pp. 567–586, 1950.

- [3] M. Creutz, "Quantum electrodynamics in the temporal gauge," *Annals of Physics*, vol. 117, no. 2, pp. 471–483, 1979.
- [4] S. J. Brodsky, H.-C. Pauli, and S. S. Pinsky, "Quantum chromodynamics and other field theories on the light cone," *Physics Reports. A Review Section of Physics Letters*, vol. 301, no. 4-6, pp. 299–486, 1998.
- [5] E. Verlinde, "On the origin of gravity and the laws of Newton," *Journal of High Energy Physics*, vol. 4, p. 29, 2011.
- [6] E. P. Verlinde, "Emergent Gravity and the Dark Universe," <https://arxiv.org/abs/1611.02269>.
- [7] M. Czachor, "Non-canonical quantum optics," *Journal of Physics. A. Mathematical and General*, vol. 33, no. 45, pp. 8081–8103, 2000.
- [8] M. Czachor and J. Naudts, "Regularization as quantization in reducible representations of CCR," *International Journal of Theoretical Physics*, vol. 46, no. 1, pp. 73–104, 2007.
- [9] M. Czachor and K. Wrzask, "Automatic regularization by quantization in reducible representations of CCR: Point-form quantum optics with classical sources," *International Journal of Theoretical Physics*, vol. 48, no. 9, pp. 2511–2549, 2009.
- [10] J. Naudts, "Reducible Quantum Electrodynamics. I. The Quantum Dimension of the Electromagnetic Field," <https://arxiv.org/abs/1506.00098>.
- [11] J. Naudts, "Reducible Quantum Electrodynamics. II. The charged states of the vacuum," <https://arxiv.org/abs/1510.02640>.
- [12] J. Naudts, "Reducible Quantum Electrodynamics. III. The emergence of the Coulomb forces," <https://arxiv.org/abs/1703.04952>.
- [13] J. T. Devreese and A. S. Alexandrov, "Fröhlich polaron and bipolaron: recent developments," *Reports on Progress in Physics*, vol. 72, no. 6, p. 066501, 2009.